Similar coils introduce a vacuum field labelled HS5-7 with interchanged poloidal positions of the stagnation points on the separatrix and the O-points of the edge islands. In Fig. 9, an enlarged detail is given of several closed field lines, where one of them is rational with $\iota = \frac{15}{16}$, the 'ergodic' separatrix, and one of the five $\iota = 1$-islands. Near the edge of the island, a sub-structure with 8 clusters is visible. The radial 'spokes' demonstrate an internal rotational transform $\iota_{island} \approx 1/7$ within the island, relative to the transform $\iota = 1$ of the O-points. The average radius of the island is about 15 % of the minor radius of the separatrix. There are 5 separate magnetic islands which are changed to one closed island of slightly smaller size at reduced $\iota = 5/6$. One can anticipate the use of such magnetic islands for edge control of the plasma.

From the Helias system 4978 with four field periods two slightly different coil systems, HS4-11 and HS4-12 are derived, which serve as a basis for technical studies concerning flexibility and feasibility. The configurations differ in the sign of shear. The parameter ranges attainable in their vacuum fields are similar, e.g. a variation of 20 % in rotational transform, either by using different currents in radially split coils which shifts the effective current radially, see right part of Fig. 10 , or by a 10 % variation of the toroidal field component by superimposing the field of planar TF-coils. Then the extreme ι-values can be attained at larger fields than those shown in the figure. Further details on the two options for ι-variation are given in [15]. The radial position of the magnetic axis can be shifted by 2 to 3 % of the average major radius by vertical fields of about $\pm$ 1 % of B_o . An accessible parameter range within these numbers is considered as reasonable for experimental purposes. It is to be noted, however, that parameter variations often are interrelated, and that the aspect ratio is increased at low-valued rational ι at the plasma edge, due to the presence of the magnetic island chains.

Because of the finite size of the superconducting coils and the need of a cryostat the distance between plasma and first wall (dashed line in Fig. 10) becomes rather small. Sufficient decoupling of plasma and wall requires a minimum distance of more than 10 cm which in 5-period Helias configurations is more difficult to realize than in 4-period cases. For this reason the dimensions of Wendelstein VII-X have been increased to $R_o =$ 6.5 m with a reduced magnetic field of 3 T. The behaviour of the neutrals in the boundary region is being studied with the Monte Carlo code DEGAS.

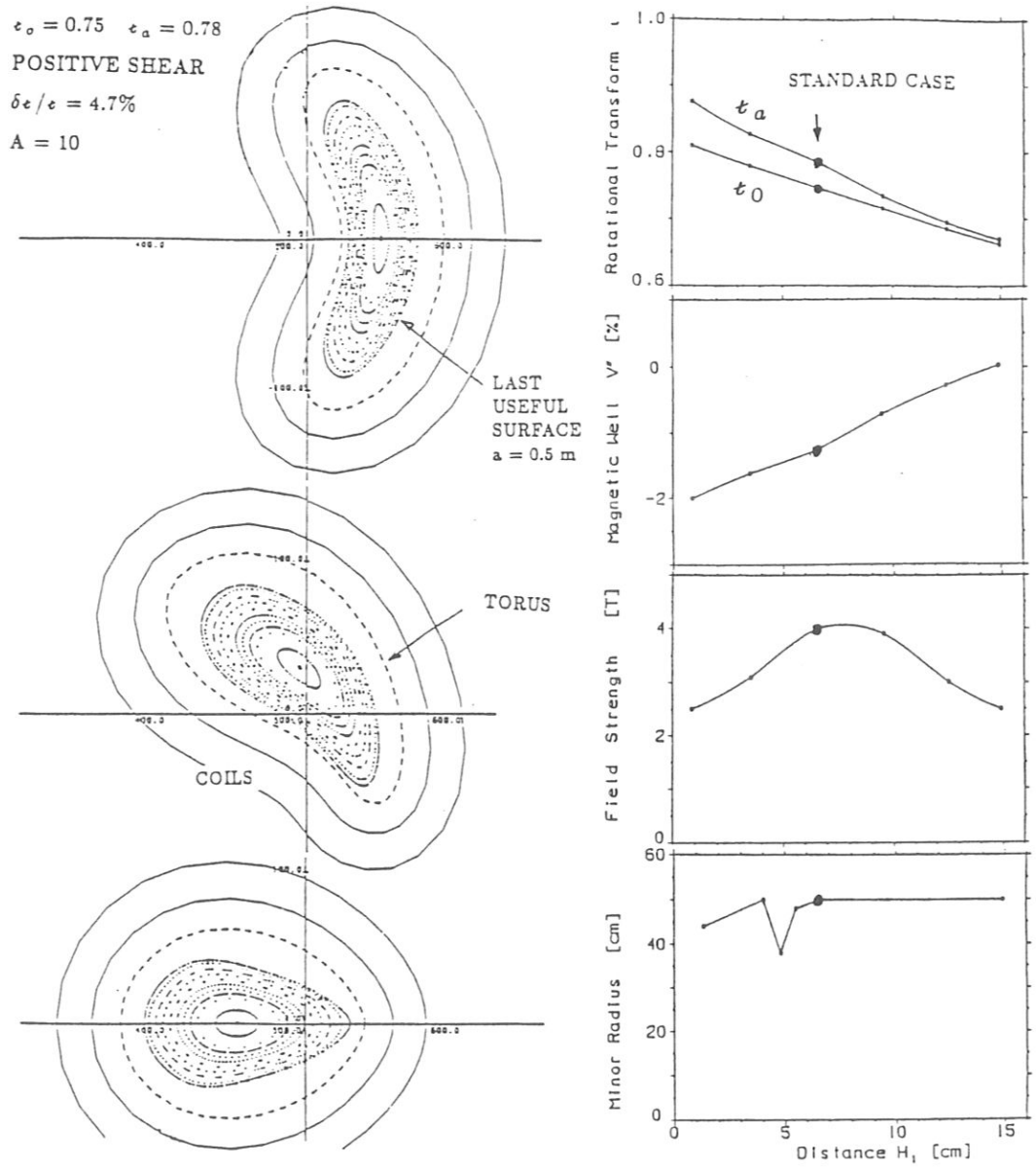

Fig. 10 : Left part: Vacuum magnetic field of the HS4-12, shown in three toroidal planes with contours of a tentative torus (dashed), and the envelope of the modular coils.
Right part : parameter range attainable by radial shift H_1 of the effective minor radius of the coils.

7. Engineering Aspects of Helias Coil Systems

Engineering aspects have been studied mainly for the coils of HS4-12 and HS5-8 with 12 coils per field period, having major radii of 5 and 6.5 m, average fields of 4 and 3 T, current densities of 40 and 50 MA/m^2, and coil aspect ratios A_c of 5.0 and 5.3, respectively. In Fig. 11 the coils of HS5-8 are shown along with the resulting net coil forces in the radial and vertical directions. They exhibit a helical structure, according to that of the magnetic axis. A maximum net coil force of approximately 4 MN is obtained. Local coil forces are directed radially and laterally, depending on the current density and the coil shape. These components can be comparable. Integrating the coil forces over one field period results in purely radial forces. This follows from the toroidal geometry. Several load cases are considered, according to differing currents in the two radial layers of the coils at differing ι-values. In the smaller system HS4-12 nearly the same net coil force is obtained [15].

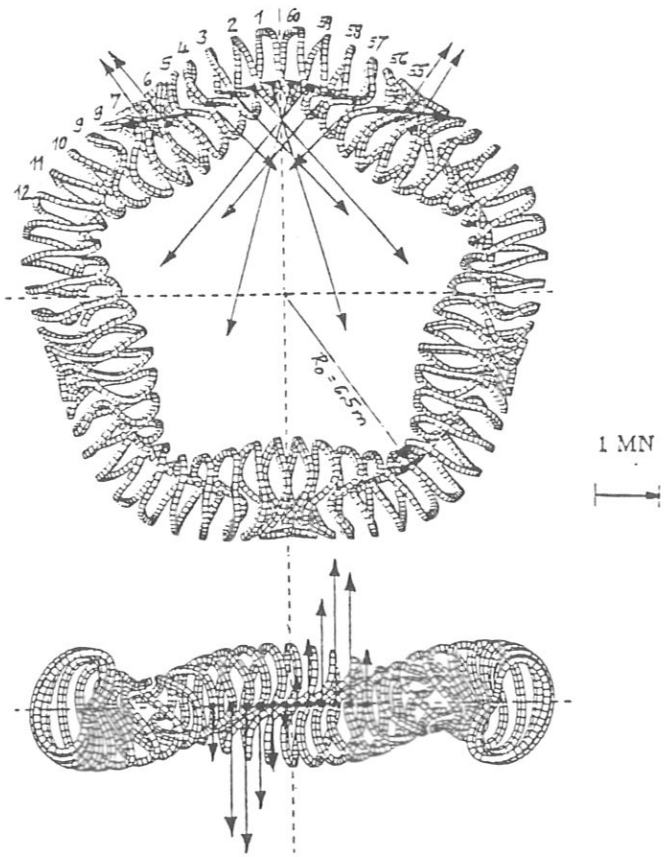

Fig. 11 : Coil system of HS5-8 with radial and vertical net coil forces.

The electromechanical stresses in the coils are calculated with the finite element code SAP V(2), taking the orthotropic material data of the EURATOM LCT-coil. A system of mutual coil support is being optimized. It consists of a coil housing and an intercoil structure. The complete structure of one field period, as shown in Fig. 12, is treated in the finite-element code, subjected to the force density present in the coil elements. This force density is produced by the whole system of 48 'double-layer' modular coils. Several load cases are studied. In non-planar twisted coils all components of the stress tensor are important.

In HS4-12, the largest stress values amount to a maximum von-Mises stress of about $\sigma_{vM} \approx 110$ MPa , and a maximum shear stress of about 1/3 of this value. More information and local values of the stresses are given in [15]. Although the shear stresses are large, the design looks feasible.

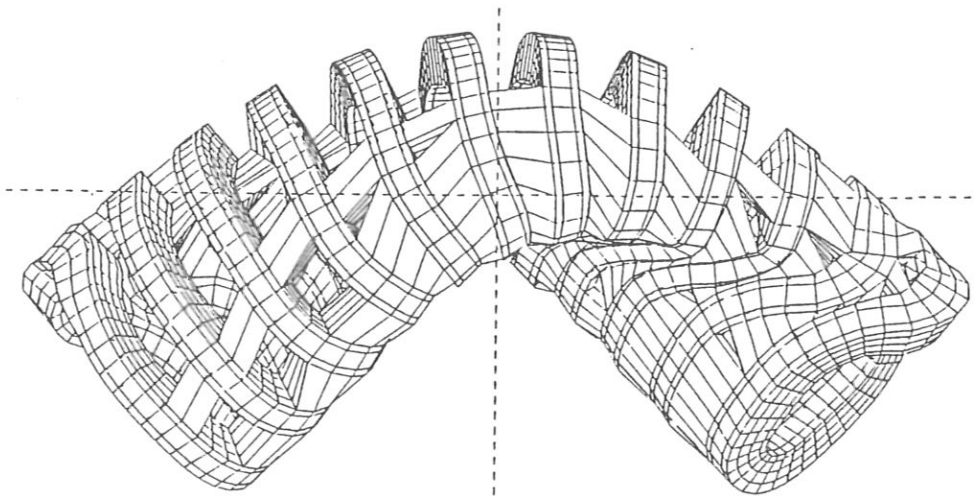

Fig. 12 : System of mutual coil support for HS4-12.

5. Summary and Conclusions

The optimization of the advanced stellarator has led to the Helias concept, where, as a consequence of the small Pfirsch-Schlüter currents, the Shafranov-shift is small and no longer limits the equilibrium-β as in standard stellarators. – Stability-β limits of $\langle\beta\rangle = 5\ \%$ or more in Helias configurations are determined by resistive interchange and ideal ballooning modes; the limit tends to increase with the number of field periods around the torus. – For this reason and taking technical constraints into account, a Helias configuration with five field periods has been chosen for Wendelstein VII-X , the future stellarator experiment in Garching. – How much the β-limits in Helias configurations are reduced by non-ideal MHD effects has still to be investigated. – Progress in the field of Helias configurations has been achieved by the discovery of quasi-helically symmetric systems, which have the favourable property of confining trapped particles extremely well, thus leading to very small neoclassical losses and good confinement of α-particles in reactor-sized systems. – The plateau bootstrap current can be made very small in the linked mirror type Helias systems with 4 field periods, whereas in quasi-helical configurations it remains finite and flows opposite to the bootstrap current envisaged in tokamaks. Intermediate systems with reduced bootstrap current at 5 field periods, as described above, are being further optimized. – The physics in the boundary region of Helias configurations is a critical issue, since stochasticity can determine this region, and magnetic islands can be present depending on the ι-value there. The structure of the magnetic field near the separatrix has been analysed, however an appropriate plasma model including transport of impurities remains to be developed for this region. – Methods for finding modular coils for optimized stellarator configurations are well established. Starting from the NESCOIL code, finite modular coils can be constructed for any Helias configuration. The small distance between the modular coils and the plasma boundary is a critical issue, particularly for systems with small size. Therefore for experimental application a careful optimization of coil shape, current density and overall dimensions of the device has to be done. In the case of Wendelstein VII-X an acceptable solution has been found. – For experimental flexibility a sufficiently broad accessible range of magnetic field parameters, like field strength, rotational transform, depth of the magnetic well, and axis position has been demonstrated, considering two alternative methods for ι-variation. – The net electromagnetic coil forces in modular Helias systems are inhomogeneous with components in all directions. Local lateral forces within a single coil can be as large as the radial components, requiring an optimized support structure. As described above and in the reference cited, this force inhomogeneity is not a serious obstacle, and the stresses within the coils can be kept within technical limits when utilizing an optimized support structure.

In summary : Helias configurations have been optimized in many respects and show convincing advantages over standard stellarators. The theoretical understanding with respect to stability and transport has come to a point where the concrete planning of a new experiment at the required size appears appropriate and justified.

References

[1] NÜHRENBERG, and J., ZILLE, R., Phys. Letters **114A** (1986) 129.

[2] W VII-AS TEAM, private communication.

[3] DOMMASCHK, W. et al., 'Physics Studies for Advanced Stellarators', Plasma Physics and Contr. Nucl. Fusion Research 1986, Eleventh Conf. Proc., IAEA 1987, II, 383.

[4] PALUMBO, D., Il Nuovo Cimento **X53B** (1968) 507;
and LORTZ, D., and NÜHRENBERG, J., 'Omnigenous Stellarators', Proc. Sherwood Meeting, Austin/Texas (1981), 3B48.

[5] HARMEYER, E., et al., 'Modular Stellarators with Improved Confinement Properties', Proc. 14^{th} Eur. Conf., Madrid 1987, Europhysics Conf. Abstracts, **11D** I 411.

[6] NÜHRENBERG, J. and ZILLE, R., Phys. Letters A **129** (1988) 113.

[7] NÜHRENBERG, J., and ZILLE, R., 'Equilibrium and Stability of Low-Shear Stellarators', Theory of Fusion Plasmas, Eds. A. Bondeson, E. Sindoni, and F. Troyon, Varenna, Italy, EUR 11336EN (1988) 3 - 23.

[8] HARMEYER, E., et al., Plasma Physics and Contr. Nucl. Fusion Research 1984, Proc. 10^{th} Int. Conf., London 1984, IAEA 1985 III 363.

[9] RODRIGUEZ-SOLANO, E., and K.C. SHAING, K.C., Phys. Fluids **30** (1987) 527.

[10] SHAING, K.C., and CALLEN, J.D., Phys. Fluids **26** (1983) 3315.

[11] LOTZ, W., NÜHRENBERG, J., Phys. Fluids (1988).

[12] LOTZ, W., NÜHRENBERG, J., and SCHLÜTER, A., J. Comput. Physics **73** No.1 (1987) 73.

[13] BEIDLER, C.D., et al., Phys. Rev. Lett. **58** (1987) 1745.

[14] MERKEL, P., 'Applications of the Neumann Problem to Stellarators: Magnetic Surfaces, Coils, Free-Boundary Equilibrium, Magnetic Diagnostics', Theory of Fusion Plasmas, Eds. A. Bondeson, E. Sindoni, and F. Troyon, Varenna, Italy, EUR 11336EN (1988) 25 - 46.

[15] HARMEYER, E., et al., 'Magnetic Field, Force and Stress Calculations for Modular Helias Coil Systems', paper A31, Proc. 15^{th} Symp. on Fus. Techn., Utrecht 1988, to be published.

Plasma Physics and Controlled Fusion, Vol. 30, No. 3, pp. 283 to 291, 1988
Printed in Great Britain.

0741-3335/88$3.00+ .00
IOP Publishing Ltd. and Pergamon Press plc.

STUDIES ON ELECTRON CYCLOTRON HEATING AT THE WENDELSTEIN VII-A/AS STELLARATORS

U. GASPARINO, H. MAASSBERG, M. TUTTER, WVII-A TEAM*
Max-Planck-Institut für Plasmaphysik, Association EURATOM-IPP D-8046 Garching, FRG

ECRH GROUP†
Institut für Plasmaforschung der Universität Stuttgart D-7000 Stuttgart 80, FRG

(*Received* 2 *September* 1987)

Abstract—The absorption of ECF power launched nearly perpendicular to the magnetic field, ECF current drive and generation of suprathermal electrons is analysed using a 3-D ray tracing code in combination with a simplified Fokker–Planck solution for which the ECF energy source function is estimated by means of quasilinear theory. Results are compared with W VII-A experimental data of ECF current drive and electron cyclotron emission.

1. INTRODUCTION

PLASMA heating with waves in the electron cyclotron frequency range (ECF) is basically understood. Considerable agreement was achieved between theoretical predictions based on simple ray tracing calculations and experimental data for power absorption for both fundamental (*o*-mode) and 2nd harmonic (*x*-mode) heating in the Wendelstein VII-A stellarator (ERCKMANN *et al.*, 1986) where the ECF power was launched from the low field side. There are, however, strong experimental indications for ECF current drive as well as for degraded absorption due to quasi-linear effects (deviation of the electron distribution function from the Maxwellian). These problems must be described on the basis of the kinetic theory (Fokker–Planck equation). Consequently, Fokker–Planck codes were developed for simplified models in the last years (e.g. KARNEY, 1986), however, a consistent description of particle and energy transport, ECF energy source and collisional interaction is missing up to now. In this paper, we describe power deposition, current drive and deviation of the electron distribution from the Maxwellian in a simplified way.

For the nearly shearless W VII-AS stellarator, ECF current drive will play an important role for the control of the current density profile. In the low shear W VII-A, optimum confinement was found in close neighbourhood to rational values of the rotational transform, ι, whereas the confinement was strongly degraded at rational values of ι (WOBIG *et al.*, 1986). Small pressure driven currents (bootstrap current) can significantly affect the rotational transform profile and, consequently, the confinement. ECF driven currents can be localized to the pressure gradient region where the maximum bootstrap current is expected and thus reduce the influence of pressure driven currents on the rotational transform profile. An estimate of current density

*G. Cattanei, D. Dorst, A. Elsner, K. Engelhardt, V. Erckmann, G. Grieger, P. Grigull, H. Hacker, H. J. Hartfuß, H. Jäckel, R. Jaenicke, J. Junker, M. Kick, H. Kroiss, G. Kühner, C. Mahn, G. Müller, W. Ohlendorf, F. Rau, H. Renner, H. Ringler, F. Sardei, A. Weller, H. Wobig, E. Würsching, M. Zippe.
†W. Kasparek, G. A. Müller, E. Räuchle, P. G. Schüller, K. Schwörer, M. Thumm.

profiles is described for W VII-A ECF discharges based on measured density and temperature profiles.

BASIC FORMALISM

The local ECF power deposition is estimated by means of a Hamiltonian 3-D ray tracing code which is based on the cold plasma dispersion relation and an absorption coefficient for general angle of propagation (relativistic Doppler shifted resonance condition). With the local power deposition and $k_{\|}$-spectrum from the ray tracing code (based on Maxwellian), the flux surface averaged quasi-linear tensor element, $Q_{\perp\perp}$ (all other terms can be neglected), is calculated for different radii. Then, the flux surface averaged electron distribution function, f, is estimated by means of Fokker–Planck equation with electron heat conduction included for stationary conditions

$$S^l(f) = C(f) + S^{ql}(f) \quad \text{with} \quad S^{ql}(f) = \frac{1}{v_\perp}\frac{\partial}{\partial v_\perp} v_\perp Q_{\perp\perp}\frac{\partial f}{\partial v_\perp},$$

where C is the usual collision operator based on Maxwellian background (where $C(f_{\max})$ gives the energy transfer to the ions), S^{ql} the quasi-linear energy source and S^l the energy loss in velocity space (the velocity space integration of $v^2 \cdot S^l(f)$ leads to the flux surface averaged electron heat conduction). For almost all ECF heated discharges in W VII-A, radiation losses can be neglected (typically less than 20%). Within the neoclassical theory, electron transport is related to the deviation of the electron distribution function from the Maxwellian and is determined by the Fokker–Planck equation in full phase space. Generally, the neoclassical transport may be modified by both the particle and energy source functions on the flux surface, an experimental indication for enhanced transport due to ECF heating was given by RINGLER *et al.* (1986). However, a self-consistent solution of the Fokker–Planck equation in full phase space is not possible at the present time. As in W VII-A the electron heat conduction within the gradient region was mainly determined by anomalous transport, we assume the following convective form of the energy loss term: $S^l(f) \propto (v^2 - \langle v^2 \rangle) \cdot f$. The magnitude of this energy loss is determined by the energy balance for stationary conditions as well as for small (adiabatic) time dependence. Due to the large aspect ratio ($A = 20$) and the very small helical field ripple ($\leqslant 2\%$) of W VII-A, the toroidal and poloidal dependences are neglected for the flux surface average, this approximation is justified for collisionalities within the plateau regime. Then, the Fokker–Planck equation is iteratively solved in spherical co-ordinates using Legendre polynomial expansion in $v_{\|}/v$, straight forward integration of the collision operator in v and numerical differencing of f in S^{ql}. By this procedure, the electron distribution function, f, is calculated for each magnetic surface separately. Finally, the electron cyclotron emission (ECE) can be simulated by means of the 3-D ray tracing code based on the calculated distribution function.

ECF POWER DEPOSITION

In this section, the calculated ECF power deposition profile is compared with experimental data which were estimated by means of the ECE electron temperature measurements. A fast ECE superhet-receiver ($\approx$ 14 kHz sampling rate) was used at 8 frequencies corresponding to 8 plasma radii (4 frequencies for 2nd harmonic

heating at $B_0 \approx 1.25$ T). During ECF power modulation experiments as well as immediately after switch off, the line density, $\int n_e \mathrm{d}l$, was unaffected. For these conditions, changes of the energy content measured by the diamagnetic signal could be described by temporal variations of the electron temperature profile. This is consistent with the general finding that the particle confinement time was large compared to the energy confinement time. Then, the absorbed power density at the time t_0, where the gyrotron was switched off, is approximately given by

$$p_{\mathrm{ECF}}(r) \approx \frac{3}{2} n_e(r) \left\{ \left(\frac{\partial T(r,t)}{\partial t} \right)_{t<t_0} - \left(\frac{\partial T(r,t)}{\partial t} \right)_{t>t_0} \right\}.$$

The plasma density $n_e(r)$ was measured by Thomson scattering, and the ECE temperature was calibrated to the Thomson data; the error for the estimation of p_{ECF} is typically less than 20%. Furthermore, the total ECF power absorbed was estimated from the diamagnetic signal immediately after the r.f.-source was switched off, the temporal resolution however, is determined by the sampling rate of less than 3 kHz leading to a lower limit for the absorbed power.

At low densities [central density $n_e(0) < 0.5 \cdot n_{e\,\mathrm{cutoff}}$], the power deposition profile is mainly determined by the location of the resonant magnetic field. The horizontal shift of the resonance layer is given by $x_{\mathrm{res}} \simeq (B_0/B_{\mathrm{res}} - 1)R$, where B_{res} is the resonant magnetic field (2.5 T or 1.25 T for 70 GHz) and R is the major radius (200 cm). The diameter of the ECF beam, which was about 5 cm, determines the power deposition profile for resonant magnetic field on axis. In the ray tracing code, the far-field approach was used for describing the power profile of the ECF beam, this assumption may result in a slightly more peaked power deposition profile. However, highly localized power deposition leads to a flattening of the electron distribution function at the resonance condition $\omega_{\mathrm{ECF}} - l\omega_{ce}(v) - k_{\parallel} v_{\parallel} \approx 0$, and less power is absorbed in comparison to a Maxwellian distribution. This quasi-linear effect becomes important for low densities and is believed to be the reason for the decreased heating efficiency found experimentally [for $n_e(0) < 10^{13}$ cm^{-3}, see ERCKMANN *et al.*, (1986)]. In Fig. 1(a), the absorbed ECF power density calculated by the ray tracing code based on the Maxwellian distribution is plotted (solid curve) for an ECF heated discharge (fundamental o-mode at 70 GHz and $n_e(0) = 1.18\ 10^{13}$ cm^{-3}, see Table 1) with the resonance layer shifted outside ($x_{\mathrm{res}} = 3.2$ cm). The ECF power deposition profile in Fig. 1(a) determined from the response of the ECE temperature on the fast r.f.-power switch-off (circles) corresponds to about 95 kW total power absorbed, this is in good agreement with the value obtained from the diamagnetic signal. However, the absorbed power density is decreased by less than 20% for the central part ($r < 2.5$ cm) of the deposition profile due to the quasi-linear flattening of the electron distribution function.

For higher plasma densities, ECF wave deflection becomes important leading to a broadening of the power deposition profile in comparison to the low density case. In Fig. 1(b), the absorbed ECF power density (from ray tracing code) is shown (solid curve) for fundamental o-mode at 70 GHz and $n_e(0) = 3.9\ 10^{13}$ cm^{-3} $\simeq 0.64 \cdot n_{e\,\mathrm{cutoff}}$ with resonance close to magnetic axis. The experimentally determined ECF power deposition profile in Fig. 1(b) corresponds to 103 kW total power absorbed, the value obtained from the diamagnetic signal is about 120 kW and is used as input

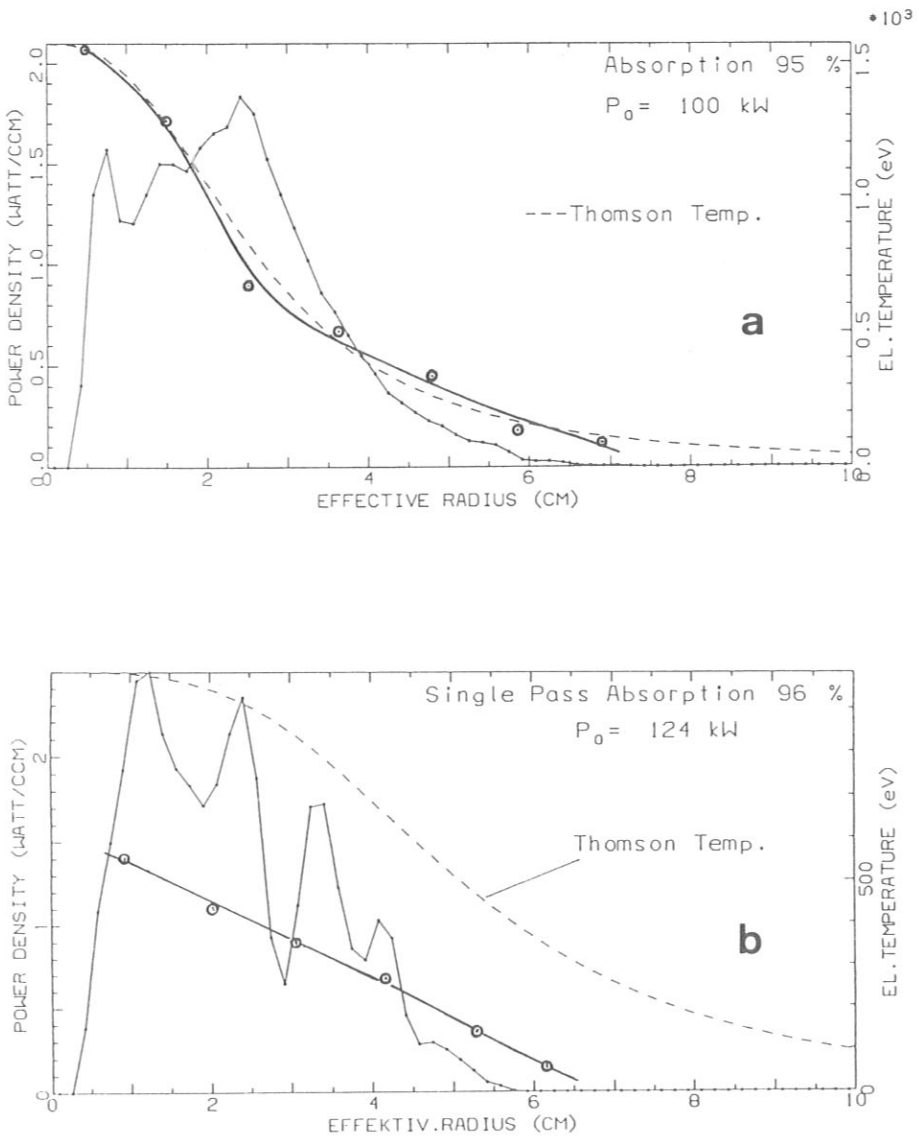

FIG. 1.—Absorbed power density vs effective plasma radius from ray tracing code based on Maxwellian distribution (solid line) and from ECE electron temperature (circles) for lower density ($n_e(0) = 1.18\ 10^{13}$ cm $^{-3}$) in Fig. 1(a) and for higher density ($n_e(0) = 3.9\ 10^{13}$ cm^{-3}) in Fig. 1(b).

power for the ray tracing code. For these high densities, density fluctuations may result in stronger deflection of the ECF beam and to a broader deposition profile [see HANSEN *et al.* (1987)]. For most of the ECF heated discharges in W VII-A with resonance close to the magnetic axis, however, the electron density and consequently the deflection of the ECF waves was smaller leading both to strongly peaked power deposition and electron temperature profiles.

ECF CURRENT DRIVE

Because the ECF power was launched nearly perpendicular ($\approx 92°$) to the magnetic field in W VII-A, the current drive efficiency was expected to be rather small. The pulse duration of the ECF discharges was limited to less than 100 ms, the L/R time of W VII-A was about 50 ms. Consequently, the total current driven by the ECF power absorption, by the plasma pressure (bootstrap current) and by the small self-induced loop voltage could not reach stationary conditions. A separation of these different current components is not possible on the basis of only experimental data. However, ECF current drive was strongly indicated in the experiments: (i) by the influence of the angle of a pivoted mirror on the inner torus wall on the total current ($k_{\parallel}$-spectrum of the reflected ECF power) and (ii) by the current evolution after plasma generation at very low densities (negligible bootstrap current for low energy content) depending on the position of the resonance layer.

On the basis of the quasi-linear theory, we analyse, in this section, discharges with different positions of the resonance layer for densities $n_e(0) > 10^{13}$ cm^{-3}, the data of the Thomson scattering diagnostic are used for the electron density and temperature profiles. A positive current increasing in time was measured for the discharges where the resonance layer was at the plasma center or shifted to the high field side. For the case of outward shifted resonance layer (increased B_0), the total current was negative in the first part of the discharges with lower energy content and became positive with increasing energy content. Here, the analysis is carried out for the later phase of all discharges of Table 1.

TABLE 1.—COMPARISON OF CURRENT DRIVE CALCULATIONS WITH EXPERIMENTAL DATA

Shots	B_0 (T)	r_{res} (cm)	$T_e(0)$ (eV)	$n_e(0)$ (10^{13} cm^{-3})	P_{ECF} (kW)	Z_{eff}	I_B (A)	I_{ECF} (A)	I_{exp} (A)	U_{bal} (V)	U_{exp} (V)
62060 82	2.57	5.6	795	1.56	75	3	480	−260	−280	−0.10	−0.07 ± 0.05
61760 88	2.54	3.2	1570	1.18	100	3	840	−220	515	−0.02	−0.0 ± 0.05
61968 96	2.46	−3.2	680	1.87	70	1.5	680	30	805	+0.01	−0.03 ± 0.05
63402 21	1.280	4.8	292	2.29	105	3	230	− 10	140	−0.03	−0.03 ± 0.03
63459 73	1.255	0.8	791	2.06	130	3	1230	120	1015	−0.05	−0.04 ± 0.03
63432 50	1.220	−4.8	503	1.78	130	2.5	920	250	1050	−0.03	−0.02 ± 0.03

The bootstrap current density, j_B, is estimated using a formula for axisymmetric magnetic field (HINTON *et al.*, 1972) which is simplified for the conditions of W VII-A with the large aspect ratio ($A = 20$) and the very small helical field ripple for collisionalities within the plateau regime:

$$j_B \simeq -\frac{r}{R^2 B_0}\frac{n_e T_e}{\nu_e^B}\sqrt{\frac{T_e}{m_e}}\cdot 2.87\cdot\left\{\left(1+\frac{T_i}{Z_{\text{eff}}T_e}\right)\frac{n'_e}{n_e}+2.29\frac{T'_e}{T_e}+1.5\frac{T'_i}{Z_{\text{eff}}T_e}\right\}$$

with ν_e^B being the Braginski collision frequency. The ion temperature is of the order of 100 eV for the discharges discussed in this section. The ohmic current density is calculated using Spitzer resistivity. These estimates, however, depend on the value of Z_{eff} for which a value of 3 was assumed (the experimental estimates were rather uncertain for these types of discharges). Z_{eff} was reduced for two cases in order to get a better fit of the bootstrap current as the leading contribution to the measured

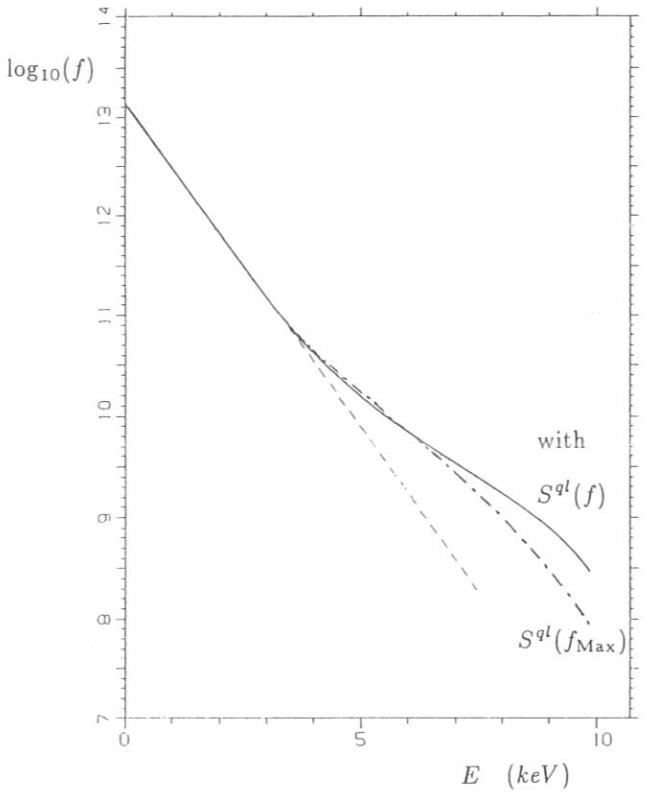

FIG. 2.—Electron energy spectrum estimated from quasi-linear Fokker–Planck equation at $r = 3$ cm (shots 62060–82 in Table 1).

total current. The additional ohmic current is estimated by means of the necessary loop voltage U_{bal} for balancing the difference. Due to the uncertainties in Z_{eff}, this comparison of the quasi-linear theory with the experimental data in Table 1 should be judged with some care. Nevertheless, the agreement of the calculated currents and the measured total current is satisfactory. For the assumed values of Z_{eff}, U_{bal} is of the order of the measured loop voltage U_{exp} which is rather unaccurate due to strong temporal disturbances. For both types of discharges (fundamental *o*-mode at $B_0 \approx 2.5$ T and 2nd harmonic *x*-mode at $B_0 \approx 1.25$ T), the bootstrap current, I_B, is the leading contribution. The ECF driven current, I_{ECF}, depends sensitively on the position of the resonance layer and compensates partially the bootstrap current I_B if the resonance is shifted outside (higher B_0). For fundamental *o*-mode (1st line in Table 1), this case is outlined in more detail.

As in this example the electron temperature close to the resonance layer is rather low, the single pass absorption is only of the order of 20% and wall reflection (3 transits) of the ECF wave was taken into account in the ray tracing code leading to power absorption of about 75 kW ($\approx 60\%$). Inside of the resonance layer (at higher magnetic field corresponding to the smaller radii), the ECF power is mainly absorbed by the tail of the electron distribution function leading to rather strong anisotropy and current drive, quasi-linear effects become important. In Fig. 2, the electron energy spectrum is shown (solid line) in comparison to the result where only $S^{ql}(f_{\mathrm{max}})$ is

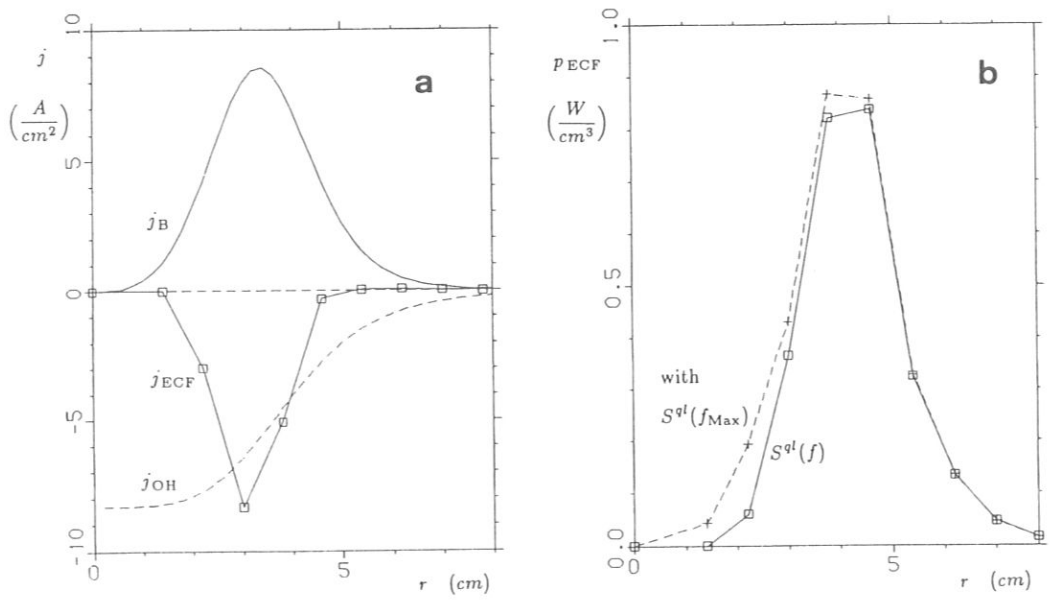

FIG. 3.—ECF driven (j_{ECF}), bootstrap (j_B) and ohmic (j_{OH}) current density in plot *a* and absorbed power density (p_{ECF}) in plot *b* versus the effective plasma radius for shots 62060–82.

used as the ECF power source function in the Fokker–Planck equation (dash–dot line). For the distribution function, f, the gradient $\partial f/\partial v_\perp$ is decreased for higher energies resulting in smaller ECF power absorption. This is shown in Fig. 3(b) (solid line) where the absorbed power density is significantly decreased at smaller radii (the total absorption is reduced by about 7%), here, we found the maximum ECF current drive efficiency [see Fig. 3(a)]. For these conditions (maximum current drive at r = 3 cm), the deviation of the electron distribution function from the Maxwellian, $f_1 = f - f_{max}$, is shown in Fig. 4, the asymmetry of this distribution indicates the high current drive efficiency. As shown in Table 1, the quasi-linear effects influenced the current density typically up to 30% whereas the local ECF power absorption was decreased by less than 20%. Furthermore, the ECF power deposition leads to pressure anisotropies which are typically larger than 1%.

In the electron cyclotron emission (ECE) from the low field side, strong indications of suprathermal electron populations were found for rather low densities (< 1.5 10^{13} cm^{-3}, see HARTFUSS *et al.*, 1985) when the resonance layer was shifted outside: strong emission was found at down-shifted frequencies corresponding to radii outside of the plasma. This finding is qualitatively consistent with quasi-linear calculations (see Fig. 2). However, the fraction of suprathermal electrons turned out to be too small to explain quantitatively the measured ECE signals without multiple wall reflection of the ECE. This is supported by the degree of polarization of the ECE (measured at the opposite toroidal position to the ECF launching) which was found to be fairly low indicating multiple wall reflection. Analogous to the problem of the absorption of the remains of the injected ECF power, multiple wall reflection of the ECF waves must be taken into account in future ray tracing calculations for these critical conditions.

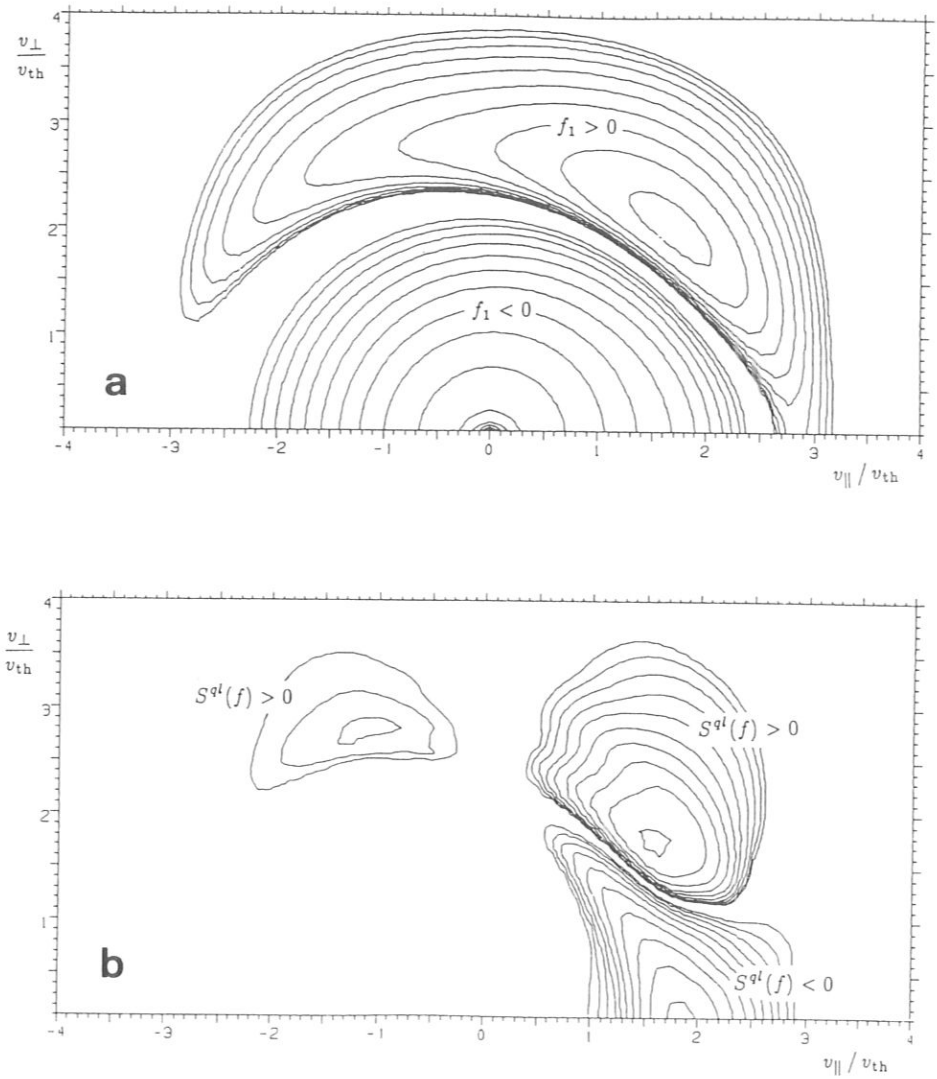

FIG. 4.—Deviation of the electron distribution function from the Maxwellian, $f_1 = f - f_{max}$ (plot *a*), and quasi-linear ECF energy source, $S^{ql}(f)$ (plot *b*), estimated from the quasi-linear Fokker Planck equation at $r = 3$ cm (compare Fig. 2).

CONCLUSIONS

The absorption of ECF wave power and the current drive described by quasi-linear theory (Fokker–Planck equation) based on a 3-D ray tracing code was found to be in rather good agreement with experimental data of the Wendelstein VII-A stellarator. In detail, the deviation of the electron distribution function from the Maxwellian can lead to degradation of the local ECF power absorption which must be taken into account in ray tracing calculations. It was shown that local ECF current drive is qualified to modify the current density profile. The ECF current drive as a tool for counteracting the bootstrap current is an important aspect for nearly shearless configurations as the W VII-AS stellarator for which a rather advanced ECF power launching system (with mirrors pivotally attached in poloidal as well as in toroidal direction) was developed.

Acknowledgement—The authors would like to acknowledge the helpful suggestions of the referee.

REFERENCES

ERCKMANN V. *et al.* (1986) *Plasma Phys. Contr. Fusion* **28** (9A), 1277.
HANSEN F. R. *et al.* (1987) *Proceedings of the 14th European Conference on Controlled Fusion and Plasma Physics*, ECA Vol. 11D-III, p. 972.
HARTFUß H. J. *et al.* (1985) *Proceedings of the 5th International Workshop on Electron Cyclotron Emission and Electron Cyclotron Heating*, San Diego, GA-A18294, p. 37.
HINTON F. L. *et al.* (1972) *Phys. Rev. Lett.* **29**, 698.
KARNEY C. F. F. (1986) *Comput. Phys. Rep.* **4**, 183.
RINGLER H. *et al.* (1986) *IAEA Conf. on Plasma Phys. and Contr. Nucl. Fusion Res., Kyoto*, IAEA-CN-47/D-V-1.
WOBIG H. *et al.* (1986) *IAEA Conf. on Plasma Phys. and Contr. Nucl. Fusion Res., Kyoto*, IAEA-CN-47/D-I-2.

EFFECT OF TEARING MODES ON TEMPERATURE AND DENSITY PROFILES AND ON THE PERPENDICULAR TRANSPORT IN THE W VII-A STELLARATOR

R. JAENICKE, W VII-A TEAM*
Max-Planck-Institut für Plasmaphysik,
Euratom–IPP Association,
Garching bei München,
Federal Republic of Germany

ABSTRACT. In the ohmically heated W VII-A stellarator, the behaviour of which is similar to that of a medium sized tokamak, the additional shearless external rotational transform ι_0 ($\Delta\iota_0/\iota_0 < 1\%$, $\iota = 1/q$) improves the stability properties and allows stationary and reproducible helium discharges with large amplitude tearing modes to be produced for $0.10 \lesssim \iota_0 \lesssim 0.15$. Discharges of this type are used to study, by means of Thomson scattering, the modification of electron temperature and density profiles by large amplitude tearing modes. The two-dimensional shapes of the profiles found experimentally can be attributed to the magnetic islands predicted by tearing mode theory. These shapes are further used to define an effective, locally enhanced radial transport coefficient $\kappa_{\perp,e}$ in a one-dimensional heat transport code. In this way, the measured temperature profiles can be reproduced quite well and the energy confinement time of discharges with tearing mode activity can be predicted quantitatively. The transport model is used to investigate the explicit dependence of $\kappa_{\perp,e}$ on the plasma current and to study the importance of plasma current driven instabilities for the energy confinement in the W VII-A stellarator as well as in tokamaks.

1. INTRODUCTION

The electron heat transport in ohmically heated helium discharges in the W VII-A stellarator [1] ($R_0 = 200$ cm, $a \approx 10$ cm, $B_0 \approx 3.5$ T) has been treated in Ref. [2]. There, it was shown from local measurements that in a low density regime characterized by small amplitude tearing modes the local electron heat conduction coefficient $\kappa_{\perp,e} = n_e\chi_e$ is approximately given by the heat diffusivity:

$$\chi_{e,an} \approx 3 \times 10^{18} \frac{1}{n_e T_e^{2/3}} \left(\frac{cm^2}{s}\right) \qquad (1)$$

where n_e is the electron density in cm^{-3} and T_e is the electron temperature in eV. At sufficiently low n_e and T_e, this anomalous electron heat diffusivity can be larger than the neoclassical value by up to three orders of magnitude. In addition, the possible dependence of χ_e on other parameters (toroidal field B_0, plasma current I_{pl}, rotational transform ι) was investigated. New results for the dependence of χ_e on I_{pl} led to a revised interpretation of the older experimental findings; these are presented in this paper.

In Ref. [2] it was also stated that for ohmically heated plasmas the empirical relationship expressed in Eq. (1) is no longer applicable in a high density regime characterized by the presence of large amplitude tearing modes. It was suggested that tearing modes are responsible for the observed deterioration in confinement. This hypothesis was examined in detail in the following years, with the result that it is now possible to make quantitative predictions about the effect of tearing modes on the effective perpendicular heat transport. This paper presents additional measurements together with their application to the energy balance equation.

In Ref. [3] it was concluded that the ion heat transport in ohmically heated discharges in W VII-A is approximately neoclassical. This estimate could be

* W VII-A Team: D. Dorst, A. Elsner, G. Grieger, P. Grigull, V. Erckmann, H. Hacker, H.J. Hartfuß, H. Jäckel, R. Jaenicke, J. Junker, M. Kick, H. Kroiss, K.Krusch, G. Kühner, C. Mahn, S. Marlier, G. Müller, W. Ohlendorf, F. Rau, H. Renner, H. Ringler, F. Sardei, M. Tutter, A. Weller, H. Wobig, E. Würsching, M. Zippe.

confirmed by numerically solving the ion heat balance equation.

Tearing modes, as a plasma current driven instability, as well as sawtooth oscillations are well known from tokamaks. They occur also in the ohmically heated W VII-A stellarator [4], the behaviour of which is generally quite similar to that of a medium sized tokamak. However, in Section 2 it is shown that the almost shearless rotational transform modifies the tearing mode behaviour in such a way that the production of large amplitude tearing modes is possible in stationary discharges for an intermediate range of ι_0. The results of profile measurements in the presence of these large amplitude tearing modes, which were obtained by a new experimental method, are presented in Section 3 together with their interpretation.

Energy balance equations including tearing mode effects are used in Section 4 to reproduce measured electron temperature profiles and to calculate the global energy confinement time τ_E. The dependence of τ_E on the measured tearing mode amplitude is analysed in detail for a density scan and a plasma current scan. The plasma current scan can also be used to investigate the explicit dependence of χ_e on I_{pl} as well as the question of whether the plasma current is the energy source driving the anomalous transport mechanism. The W VII-A stellarator is especially suited for such an investigation since the Ohmic heating current can be varied over a wide range, including cases with $q(a) < 2$ and the case of no net current when Ohmic heating is replaced by electron cyclotron resonance heating and neutral beam heating.

A summary and conclusions are presented in Section 5. The results obtained from tearing mode produced magnetic islands are extrapolated to investigations of the influence of magnetic islands on the transport in currentless discharges in W VII-A. The energy transport of these discharges with no Ohmic heating current has been published elsewhere [5, 6].

2. PROPERTIES OF THE OHMICALLY HEATED W VII-A IN COMPARISON WITH TOKAMAKS

The dimensions of W VII-A [1] and the plasma parameters achieved with Ohmic heating [3] are similar to those of a medium sized tokamak, except for the small plasma radius (a = 10 cm), which results in a rather large aspect ratio (A = 20) and a rather limited Ohmic heating capability.

In an ohmically heated stellarator, part of the poloidal field is produced by an external helical winding. The resulting external helical fields lead to an external rotational transform ι_0; in the case of W VII-A, this is constant over the radius and therefore has no shear (Fig. 1). This property of W VII-A is the one which makes it so similar to tokamaks when Ohmic heating is applied. The Ohmic heating current makes a second contribution to the poloidal field and to the rotational transform. To first order, these two contributions can be added up, to give the total rotational transform, $\iota(r) = 1/q(r)$. This simple additive law makes the use of ι convenient in ohmically heated stellarators; the

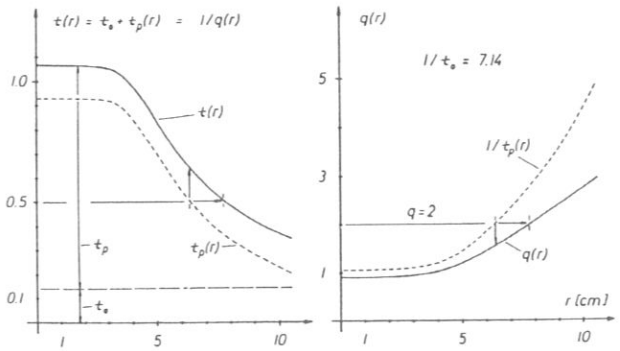

FIG. 1. Radial profiles of rotational transform $\iota(r)$ (left side) and safety factor $q(r) = 1/\iota(r)$ (right side) for a typical helium discharge in the W VII-A stellarator: $B_0 = 3.5$ T, $\iota_0 = 0.14$, plasma current $I_{pl} = 20$ kA, $\int ndl = 8.3 \times 10^{14}$ cm^{-2}. $\iota_p(r)$ is the contribution to $\iota(r)$ by the Ohmic current.

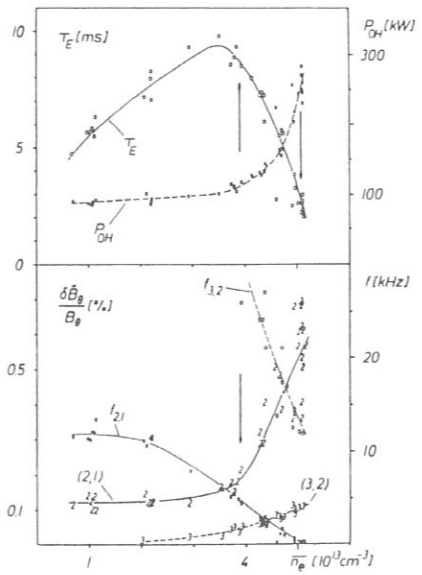

FIG. 2. Energy confinement time τ_E, Ohmic heating power p_{OH} (upper part), and frequency and relative poloidal field fluctuation amplitude of the observed tearing modes (lower part) as functions of the line averaged electron density. The parameters of this helium discharge are: $B_0 = 3.5$ T, $\iota_0 = 0.14$, $I_{pl} = 20$ kA, $q(a) = 2.9$. The arrows indicate the discharges treated in detail in Section 4.2.

corresponding q-profiles are shown on the right-hand side of Fig. 1 for comparison. These q-profiles are very similar to those in tokamaks, since W VII-A also has the $q = 1$ or $\iota = 1$ condition in the centre because of sawtooth oscillations (maximum current density proportional to $B_0 (1-\iota_0)/R_0$). Only the shear is, on the average, somewhat smaller as a result of the additional external transform in W VII-A.

Although the external rotational transform ι_0 is usually much smaller than the contribution ι_p made by the plasma current, it can nevertheless result in essential differences in the discharge behaviour, especially concerning the plasma stability. There are two main reasons for this (for further details, see Ref. [4]):

(a) The helical fields are fixed in space since they are produced by external current windings. This improves the positional stability of the plasma, as illustrated by the fact that a vertical field is not necessarily required for horizontal plasma equilibrium. The improved positional stability also helps prevent current disruptions, for which the loss of the horizontal plasma equilibrium plays an important role [4].

(b) The external rotational transform ι_0 is a tool for varying almost independently the relation between the radial position of a resonant magnetic surface and the plasma parameters in its vicinity. Increasing ι_0 means that a rational magnetic surface is shifted towards larger radii (Fig. 1), where the current density gradient becomes smaller and smaller, thus making tearing modes stable. In Ref. [4], it was demonstrated that for ι_0 0.15 the m = 2, n = 1 (for short, (2, 1)) tearing mode is stabilized. Somewhat below this stability limit, the largest amplitudes of tearing modes are observed for high density discharges (compare Fig. 5, Ref. [4]).

Such a situation is illustrated in Fig. 2, where the measured poloidal field fluctuation is shown as a function of the electron density for an external rotational transform just below the stability limit. The plasma current was kept constant during this density scan, and each point in this figure corresponds to some time interval within a stationary discharge. Although the tearing mode amplitudes are large at high densities, the use of helium as working gas leads to stationary and reproducible discharges. This kind of discharge is therefore especially well suited to studying the effects of large amplitude tearing modes.

When the tearing mode amplitudes increase, the energy confinement time τ_E drops considerably at high densities, partly as a result of the increased impurity radiation (upper part of Fig. 2). This behaviour is very similar to the time evolution of these parameters just before a current disruption. Therefore, we believe that this high amplitude tearing mode regime is not accessible in a tokamak under stationary conditions.

The striking correlation between the drop of τ_E and the increase of the tearing mode amplitudes (Fig. 2) leads to the question of what the relation between the two events is, especially whether the tearing modes cause the observed deterioration of the energy confinement. Before this question can be answered, the influence of tearing modes on the (effective) radial transport must be known quantitatively. This problem is treated in Section 4.1.

3. TEMPERATURE AND DENSITY PROFILES IN THE PRESENCE OF TEARING MODES

According to theory, the tearing mode instability perturbs the magnetic field in such a way that magnetic islands are formed [7]. As a consequence of island formation, the transport parallel to the field can, at

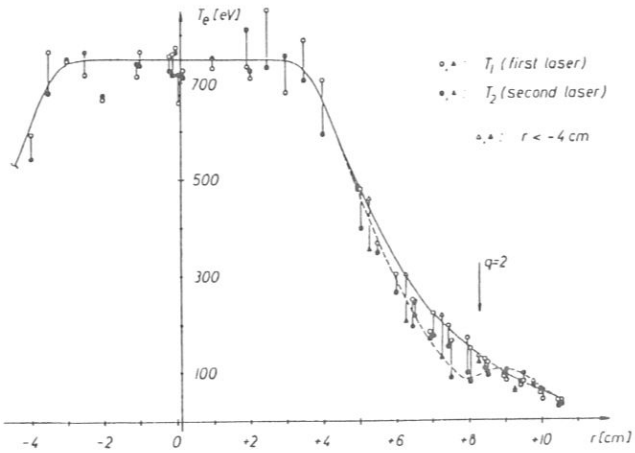

FIG. 3. Electron temperatures measured by Thomson scattering, with two lasers triggered at different poloidal positions of the (2, 1) tearing mode islands. The open symbols correspond to a cut through the x-points of the islands, the closed symbols to a cut through the o-points. A complete profile was measured, but all further points for the left side are shown by triangles on the right side. For clarity, error bars have been omitted. Two profile points measured during one shot are connected by a vertical line. The parameters of the helium discharge are: $B_0 = 3.6$ T, $\epsilon_0 = 0.083$, $I_{pl} = 27$ kA, $q(a) = 2.9$, $\int ndl = 4.6 \times 10^{14}$ cm^{-2}, $\delta\dot{B}_\theta/B_\theta = 0.46\%$ (measured at $r = 15.9$ cm), $f = 5$ kHz. In addition to the (2, 1) mode, a small (3, 2) mode with $\delta\dot{B}_\theta/B_\theta = 0.01\%$ was found.

least partly, short-circuit the perpendicular transport across the island. In the limiting case of infinitely large transport coefficients parallel to the magnetic field, all magnetic surfaces, and therefore also the closed surfaces within an island, must be surfaces of, for example, constant temperature and density. Thus, the same temperature and density should occur twice when taking a profile across an island, and the profiles should become two-dimensional quantities with local plateaus at certain poloidal positions.

Although this assumption is commonly used and although there is experimental evidence that it is correct (see, for example, Ref. [8]), we tried to measure the poloidal variation of the electron temperature and density profiles in discharges with large amplitude tearing modes. A Thomson scattering diagnostic was used with two lasers focused along the same chord through the centre of the plasma. In this way, it was possible to measure local temperatures and densities at one (variable) radial position, at two different times during each shot.

The poloidal position of the tearing mode islands with respect to the laser beams can be determined from the absolute phase of the Mirnov coil oscillations. Thus, the Pockels cell of the first laser was triggered depending on the phase of a Mirnov coil signal, for example in an island position corresponding to a profile cut through the x-points of the island. The second laser was fired half an oscillation time later, resulting in a cut through the o-points (magnetic axis of the islands), where the broadest plateaus are to be expected. The typical time interval between the two measurements was 100 μs, which is short in relation to transport times, and therefore the change of plasma parameters during that short time interval should be negligible. In this way, two extreme profile shapes could be measured during a series of reproducible discharges. A first result was published in Ref. [2] and further examples were presented in Ref. [9].

3.1. Experimental results

One of the best electron temperature profile measurements obtained in this way is shown in Fig. 3. The discharge chosen was one with an almost pure (2,1) mode, a relative poloidal field fluctuation amplitude of 0.5% and a q = 2 surface not too close to the plasma boundary. Measurements taken by the first laser (open symbols in Fig. 3) correspond to a maximum

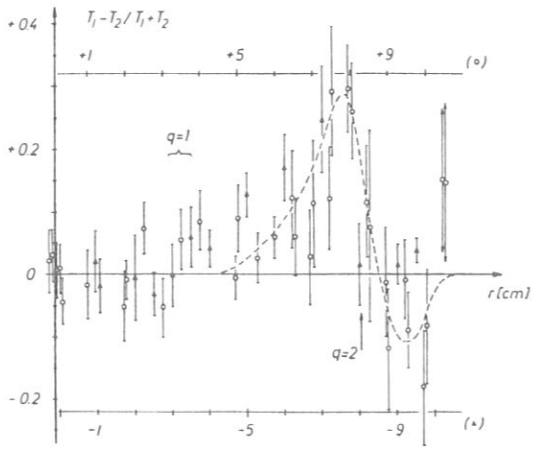

FIG. 4. Relative temperature differences between the temperature pairs connected by vertical lines in Fig. 3. The broken line was fitted by hand.

of the poloidal field and result in a cut through the x-points of the islands, in accordance with tearing mode theory.

Figure 4 illustrates the relative differences of the two temperature measurements taken during one shot. This plot shows more clearly that a systematic difference between the two temperatures exists only in the vicinity of the resonant q = 2 surface. The broken line in this figure is a measure of the relative temperature difference. This temperature difference was used to calculate in Fig. 3 from the solid line (fitted by hand) the broken line which represents the profile cut through the o-point or across the island. Therefore, by identifying the local minimum in this broken line as the position of the inner separatrix and assuming T_e = const on the island magnetic surfaces, we can derive a temperature island width or temperature plateau width w_T which is approximately 2 cm. This value can be compared with the magnetic island width w_0 (maximum width of the magnetic separatrix), which is approximately 2.3 cm, as determined from a field line tracing code (see Section 4.1); this is somewhat larger than the temperature island width.

In the same manner, we treated a discharge with higher plasma current, corresponding to $q(a) < 2$, where the (3,2) mode was the dominating tearing mode. The uneven structure of this mode could be clearly demonstrated.

Another example is shown in Fig. 5. This profile applies to discharges with the highest density shown in Fig. 2 and is characterized by a rotating (3,2) mode and an almost stationary or non-rotating (2, 1) mode ($f_{2,1} \rightarrow 0$). From the absolute phase of the m = 2 component of the Mirnov coil signals, it can be concluded that the (2,1) island locks in such a posi-

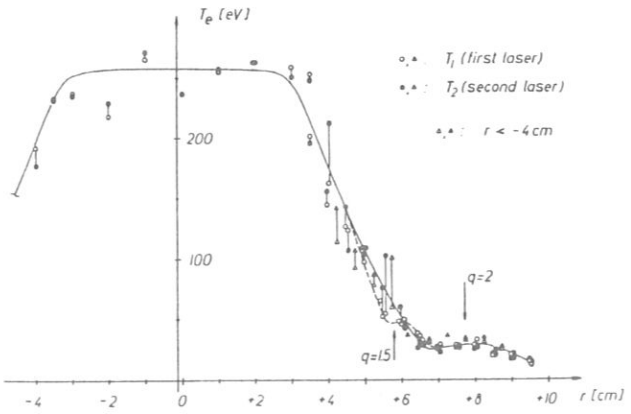

FIG. 5. Plot of electron temperatures similar to Fig. 3, but for another set of plasma parameters: $B_0 = 3.5$ T, $\epsilon_0 = 0.14$, $I_{pl} = 20$ kA, $\int ndl = 10.8 \times 10^{14}$ cm^{-2} ($\bar{n}_e = 5.1 \times 10^{13}$ cm^{-3}, compare with Fig. 2). The uneven (3,2) mode was used for the phase locking of the two profile cuts: the open symbols correspond to a cut through the o-points of the (3, 2) island. The mode data are: (3, 2) mode: $\delta\dot{B}_\theta/B_\theta = 0.096\%$, $f = 13$ kHz, and (2, 1) mode: $\delta\dot{B}_\theta/B_\theta = 0.5\%$, $f \approx 0$.

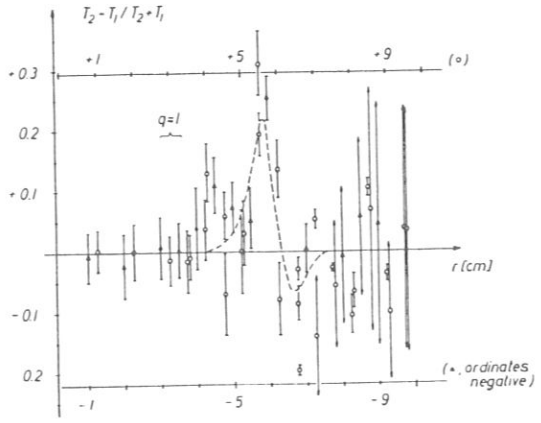

FIG. 6. Relative temperature differences between the temperature pairs of Fig. 5, taken during one shot. Because of the uneven structure of the (3,2) mode, the ordinates for $r < 0$ were drawn with a negative sign.

tion that the Thomson scattering diagnostic measures a profile almost exactly through the o-point. As a result, there is a plateau in the vicinity of the q = 2 surface, which can be clearly seen in Fig. 5, and the temperatures measured there are independent of the time of the measurement. The rotating (3,2) mode was used for phase locking of the Thomson scattering diagnostic. The derived relative temperature differences are shown in Fig. 6. These temperature differences are again used to calculate the relative profile shape of the o-point cut through the (3, 2) island in Fig. 5. The resulting temperature plateau of $w_0 \approx 0.5$ cm is just above the experimental error and is much smaller than the magnetic island width of $w_0 \approx 1.4$ cm. In the case of the locked (2, 1) islands, w_T is equal to w_0 within the error bars.

In the density profiles, tearing mode effects could be observed only for very small rotation frequencies. For the density scan shown in Fig. 2, the modulation of the line density signal with the (2,1) mode frequency was more than 1% only for frequencies below 5 kHz. A plateau in the density profiles was clearly shown by Thomson scattering only at the highest density or for almost vanishing rotation frequency of the (2,1) mode (Fig. 7). This density plateau is again around the q = 2 surface and has the same size and the same radial position as the simultaneously observed temperature plateau (Fig. 5).

3.2. Interpretation of the experimental results

Summarizing the experimental results of Section 3.1, we can say that local plateaus were always found in the temperature profiles of discharges with large amplitude tearing modes and that the radial position of these plateaus always agreed with the corresponding resonant magnetic surface. Usually, the measured temperature plateau width w_T is, however, smaller than the calculated magnetic island width w_0, and this deviation is the larger the higher the rotation frequency of the island. A density plateau could be found only in the limiting case of vanishing rotation frequency.

It seems that at higher rotation frequencies the transport parallel to the field lines is not fast enough to compete with the island motion. The resulting relaxation process is similar to the time lag of the current in an LR circuit with an AC voltage and can be approximately described by the same mathematical formalism. This means that, for example, the plateau width in the temperature profile can be approximately calculated from

$$w_T = w_0 \frac{1}{(1 + \omega_*^2 \tau_T^2)^{1/2}} \tag{2}$$

where the relaxation time τ_T is given by

$$\tau_T = \frac{3}{2} \frac{L_\parallel^2}{\pi^2 \chi_{\parallel,e}} \tag{3}$$

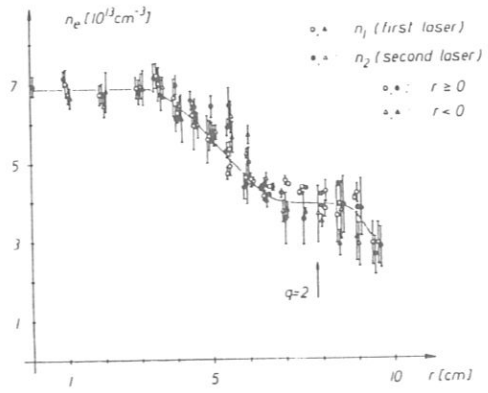

FIG. 7. Density profile for the discharge conditions of Fig. 5. The curve was fitted by hand.

$L_\parallel$ is the length of a field line connecting the inner side with the outer side, around an island, which requires N toroidal revolutions. N can be derived from field line calculations. It is around 3 in the island centre and between 5 and 20 for field lines close to the island separatrix. ω_* is the relative rotation frequency of the electrons with respect to the island. Such a relative motion must exist, otherwise the electron temperature would always be constant on magnetic surfaces as long as the heat flux parallel to the field, $q_\parallel$, is sufficiently larger than that perpendicular to the field, $q_\perp$.

$$\frac{q_\parallel}{q_\perp} = \frac{\chi_{\parallel,e}\, w_0}{\chi_{e,an} L_\parallel} = f(T_e^{3,2}) \gg 1$$

This condition requires $T_e > 6$ eV and is satisfied in all cases considered here.

ω_* remains an unknown quantity. If we assume the transport parallel to the field to be classical, it is the only unknown quantity and can be calculated in cases where w_T has been measured. The result is

$$\omega_* = 0.25 \ldots 0.9 \cdot 2\pi f_{2,1}$$

or ω_* is roughly half the frequency observed with the Mirnov coils, which is close to the diamagnetic drift frequency of the electrons.

When the same formalism is applied to particle transport, the only difference is that the relaxation time is given by

$$\tau_n = \frac{L_\parallel^2}{\pi^2 D_\parallel} \approx \left(\frac{m_i}{m_e}\right)^{1/2} \cdot \tau_T$$

which is roughly two orders of magnitude larger than the temperature relaxation time. The ions will move only slowly compared with the islands or even in the opposite direction in the case of the diamagnetic drift. Thus, ω_* will again be close to the frequency observed with the Mirnov coils. Consequently, effects of tearing modes on the density profiles should be observable only at much smaller frequencies, in agreement with the experimental results (see previous section).

4. EFFECT OF TEARING MODES ON THE ENERGY TRANSPORT

4.1. Energy balance equations including tearing mode effects

Measurements of the two-dimensional shape of the electron temperature profiles in the presence of tearing modes afford a good basis for quantitatively evaluating the influence of tearing modes on the radial heat transport. The energy balance equations are solved in cylindrical geometry and in the simplest possible form:

$$-\frac{1}{r}\frac{d}{dr}\left(r\kappa_{\perp,e}\frac{dT_e}{dr}\right) = p_{OH}(r) - p_{ei}(r) - p_{rad}(r) \qquad (4)$$

$$-\frac{1}{r}\frac{d}{dr}\left(r\kappa_{\perp,i}\frac{dT_i}{dr}\right) = p_{ei}(r) \qquad (5)$$

The heat fluxes are assumed to be proportional to the temperature gradients, which introduces effective transport coefficients $\kappa_{\perp,e}$ and $\kappa_{\perp,i}$.

The electrons are heated by Ohmic heating ($p_{OH}(r)$) and they exchange energy by Coulomb collisions with the ions ($p_{ei}(r)$). They are cooled by impurity radiation ($p_{rad}(r)$), as measured at one toroidal position with bolometers. Measured electron density profiles are used in the calculation. Ions are essential for the electron energy balance only at high densities. Charge exchange losses are negligible in helium discharges. Neoclassical heat conduction with an anomaly factor of the order of one is assumed. Tearing mode effects on the ion heat transport are neglected.

For the electrons, the anomalous heat diffusivity of Eq. (1) is used as a basis:

$$\kappa_{\perp,e} = n_e \chi_{e,an} = 3 \times 10^{18} \frac{1}{T_e[eV]^{2/3}} \left[\frac{1}{cm \cdot s}\right]$$

Tearing modes are assumed to enhance the effective radial heat transport locally. Therefore, $\kappa_{\perp,e}$ is increased by an artificial factor of 100 (which forces the temperature gradient to become almost zero) within a radial region of $0.7 w_T$ around the corresponding rational magnetic surface. The temperature plateau width w_T is taken from the experiment or calculated

from Eq. (2). The factor 0.7 takes into account the poloidal variation of the width of the island separatrix. In addition, $\kappa_{\perp,e}$ has to be increased gradually towards the centre to reproduce the flat profiles observed inside the $q = 1$ surface as a result of sawtooth oscillations.

Electron temperature profiles calculated in this way agree quite well with measured electron temperatures for discharges with small tearing mode islands or with a single large island ($w_0/a \approx 0.2$). However, this model is not applicable in cases where several tearing modes are unstable at the same time and where the islands are large and close enough to each other. It is well known [10] that, under these circumstances, interactions between islands with different helicities occur because of radial overlapping of the perturbation functions and cause field line ergodization.

Taking field line ergodization quantitatively into account in a transport model is a complicated two- or even three-dimensional problem. Attempts to solve this problem have been published for example in Refs [11, 12], but, to date, a satisfactory theory for the local enhancement of the perpendicular heat transport does not exist for cases where magnetic islands, ergodic field lines and unperturbed regions coexist [12]. In W VII-A, we found empirically that the measured electron temperatures can be reproduced quite well in cases with ergodic field lines if $\kappa_{\perp,e}$ is additionally increased by a rather small factor (2.5) inside the ergodic regions. A similar enhancement factor was measured in the plasma boundary of the TEXT tokamak made ergodic by external perturbation fields [13].

Therefore, before solving the energy balance equation (4), we have to investigate the magnetic field for ergodic field lines. The radial dependence of the magnetic field perturbation caused by tearing modes is calculated from the perturbed helical flux function by using a straightforward extension of the code described in Ref. [4]. This perturbation function is calibrated by the measured poloidal field fluctuation and is linearly superimposed on the cylindrical poloidal field of the plasma current together with the external rotational transform. The resulting perturbed field is applied to a field line tracing code. If ergodic regions are found, $\kappa_{\perp,e}$ is enhanced additionally by the factor of 2.5 inside the ergodic region.

From the measured density profile and the calculated temperature profiles it is possible to calculate the total energy content W and the Ohmic heating power P_{OH} for a given plasma current and with $Z_{eff}(r) = \text{const} \approx 2$. The global energy confinement time is then defined as

$$\tau_E = \frac{W}{P_{OH}}$$

This value can be compared with experimental values for which the energy content is measured by a diamagnetic coil and the Ohmic heating power is given by the measured loop voltage and the plasma current.

Equation (4) can also be used to estimate the change in the temperature profiles and hence the change in τ_E when the tearing mode induced temperature plateaus and ergodic regions are omitted. The resulting change in the impurity radiation is extrapolated either from discharges with smaller tearing mode amplitudes or simply by recalibrating the radiation profile with $P_{rad}(0)/P_{OH} = \text{const}$. This is not without problems, since almost 50% of the Ohmic heating power is lost by impurity radiation.

If very simple assumptions are made, Eq. (4) can also be solved analytically, with and without temperature plateaus [10, 14]. The resulting ratio of τ_E with and without tearing mode islands is

$$\tau_E/\tau_{E0} = 1 - \frac{w_0}{a}\,\frac{4r_s^3}{a^3}$$

where r_s is the radius of the corresponding resonant magnetic surface around which the island is assumed to extend symmetrically. A comparison with the more exact calculation used in this paper shows that this simple expression overestimates the effect of tearing mode islands on energy confinement.

The radial heat transport model described above will be applied to several discharges with measured electron temperature and density profiles. This will allow the validity of the model to be checked and the effect of tearing modes on the global energy confinement to be quantitatively studied under various discharge conditions.

4.2. Dependence of τ_E on electron density

The dependence of the energy confinement time τ_E on the electron density for a standard helium discharge in W VII-A is shown in Fig. 2. To check the hypothesis that the decreasing τ_E at high densities is due to the enhanced tearing mode activity, the energy confinement time was calculated for two densities (indicated by arrows in Fig. 2), with allowance for tearing mode effects: (a) at about the maximum of τ_E ($\bar{n}_e \approx 3.9 \times 10^{13}$ cm^{-3}) and (b) at the highest achievable

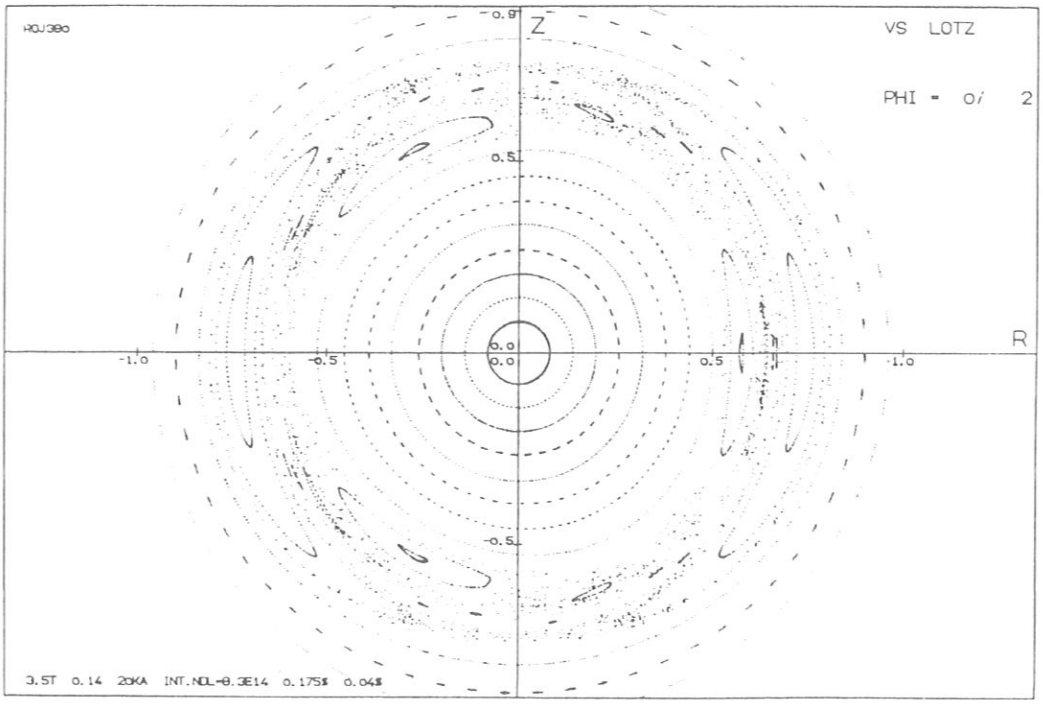

FIG. 8. Magnetic surfaces for the discharge parameters of Fig. 2 at $\bar{n}_e = 3.9 \times 10^{13}$ cm^{-3}, calculated in cylindrical geometry. The following fluctuation amplitudes, measured at $r = 15.9$ cm, were used for calibrating the tearing mode perturbations: $\delta\hat{B}_0/B_0\,(2,1) = 0.175\%$, $\delta\hat{B}_\theta/B_\theta\,(3,2) = 0.04\%$. There are secondary islands between the (2,1) and (3,2) islands.

density, which is given by the available loop voltage ($\bar{n}_e \approx 5.1 \times 10^{13}$ cm^{-3}).

Figure 8 shows the result of a field line calculation for case (a). Although, in this case, two tearing modes are unstable at the same time, there is almost no interaction between them. Only the regions close to the x-points of the islands are slightly ergodic, but no field lines exist which surround and connect the two islands. Evidently, closed magnetic surfaces still exist between the two islands, and it is in this region where the most stable magnetic surface ($\iota = 0.62$) has to be expected according to the KAM theorem [15]. Ergodic regions can therefore be neglected in the calculation.

Corresponding to the rather high rotation frequencies (5 and 30 kHz for the (2,1) and the (3,2) mode, respectively) and the rather small electron temperatures, the widths of the tearing mode induced temperature plateaus are rather small according to Eq. (2). They lead to rather small steps in the calculated electron temperature profile (Fig. 9) because of the assumed discontinuous dependence of $\kappa_{\perp,e}(r)$ when Eq. (4) is integrated. When a discharge is simulated without tearing modes by omitting

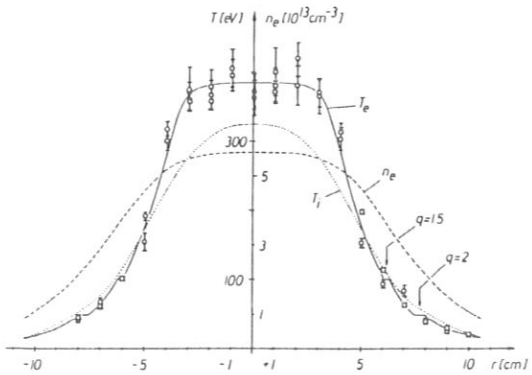

FIG. 9. Measured electron temperatures and measured electron density profile (fitted function) for the magnetic field configuration of Fig. 8. Also shown is the calculated electron temperature profile, where the two steps are the result of the assumed local enhancement of $\kappa_{\perp,e}$ due to the (3,2) and (2,1) tearing mode islands. The ion temperature profile (dotted line) calculated with neoclassical ion heat conduction agrees quite well with the central value measured by charge exchange on H^0 minority ions (≈ 350 eV [3]).

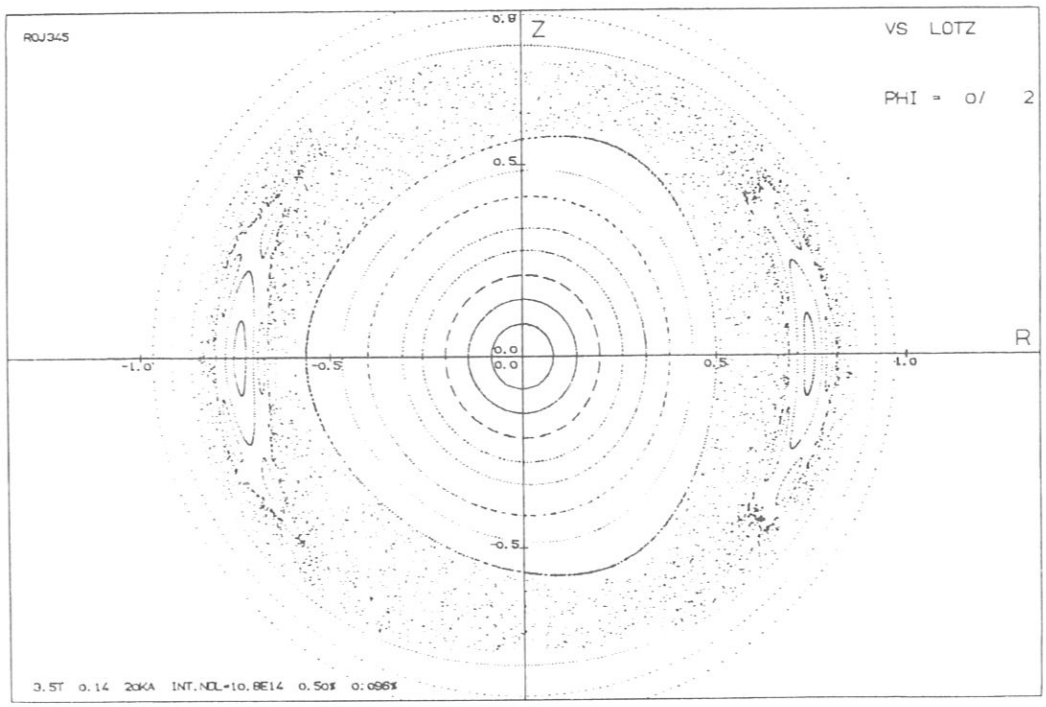

FIG. 10. Magnetic surfaces for the discharge parameters of Fig. 2 at the highest achievable density: $\bar{n}_e = 5.1 \times 10^{13}$ cm^{-3}. The (2,1) mode with $\delta\hat{B}_\theta/B_\theta = 0.5\%$ and the (3,2) mode with $\delta\hat{B}_\theta/B_0 = 0.096\%$ produce a broad region with ergodic field lines.

the two T_e plateaus, the average electron temperature is only slightly increased and τ_E increases by only 13%. The effect of tearing modes on the global energy confinement is thus still small, but the ergodic island separatrices together with the fact that τ_E has already passed through its maximum could indicate that this effect is becoming important.

At the higher density, case (b), the tearing mode amplitudes are considerably increased. The measured electron temperature and density profiles with the almost locked (2,1) mode and the rotating (3,2) mode are shown in Figs 5 and 7, respectively. The corresponding field line calculation presented in Fig. 10 indicates that a broad ergodic region now exists. Single field lines covering this region ergodically surround the islands in part and cross the whole ergodic region between the inner and outer boundaries typically within within 20 to 100 toroidal revolutions. The (3,2) island has no longer closed magnetic surfaces, but its existence can be demonstrated by following single field lines

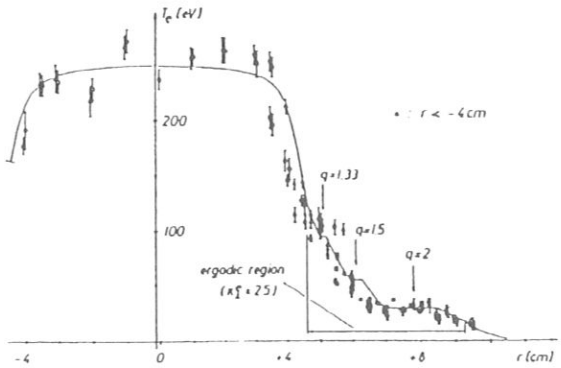

FIG. 11. Measured electron temperatures (compare with Fig. 5) together with the calculated profile for the field configuration of Fig. 10. In addition to the local enhancement of $\kappa_{\perp,e}$ leading to plateaus at the radial position of the tearing mode islands, a moderate enhancement of $\kappa_{\perp,e}$ in the estimated ergodic region was used in the calculation.

become steeper and steeper outside the q = 1 surface. This in turn destabilizes tearing modes in this region [4]. At first, the amplitude of the (2, 1) mode increases again and then higher order modes, such as the (3,2) mode and (4,3) mode, appear (Fig. 12) as the corresponding resonant surfaces are shifted towards the limiter or, in the case of q = 2, even beyond the limiter.

Taking into account the observed tearing modes together with ergodic regions, the transport model of Section 4.1 again yields good agreement between measured and calculated electron temperature profiles (Fig. 13). Thus, at high plasma currents, the effective radial heat transport inside the q = 1 surface can be considered to be almost infinite. In the rather small remaining region outside q = 1, it is locally enhanced by tearing modes, resulting in significantly reduced global energy confinement.

At these large currents the loop voltage is almost proportional to I_{pl}, which means that the plasma resistance is nearly independent of I_{pl}. Consequently, the average electron temperature and also the total energy content are almost constant, whereas P_{OH} is proportional to I_{pl}^2. The energy confinement time τ_E therefore roughly scales with $1/I_{pl}^2$ at high currents. This scaling is compared with the drift parameter scaling, $\tau_E \sim 1/\zeta \sim \bar{n}_e \sqrt{\bar{T}_e}/I_{pl}$ [2], commonly used in ohmically heated stellarators about ten years ago. Normalized to the measured τ_E at 25 kA, this scaling is shown as a dotted line in Fig. 12.

Although the behaviour of τ_E shows some similarity to the drift parameter scaling, we argue that the deviations are large enough to be significant. We believe that the effective radial heat transport can be described entirely by a perpendicular heat conduction coefficient $\kappa_{\perp,e}$ which does not depend explicitly on I_{pl}, together with a local enhancement of $\kappa_{\perp,e}$ due to current driven instabilities (sawtooth oscillations and tearing modes). A re-examination of the dependence of $\chi_{e,an}$ on I_{pl} reported in Ref. [2], distinguishing more carefully between discharges with and without tearing mode activity, confirmed the above statement [17].

5. SUMMARY AND CONCLUSIONS

The possibility of producing large amplitude tearing modes in stationary and reproducible helium discharges in the ohmically heated W VII-A stellarator has been used to study the two-dimensional shapes of electron temperature and density profiles in the presence of tearing modes. The Thomson scattering diagnostic was phase locked to the Mirnov coil oscillations to measure profile cuts through the x-points and o-points of the tearing mode induced magnetic islands. Local 'plateaus' were found to extend around the o-points or the centre of the islands, as expected from theory.

Usually, the width of these temperature plateaus is, however, smaller than the width of the magnetic islands determined from the measured poloidal field fluctuations. This difference can be understood on the basis of classical transport parallel to the field if, in addition, a relative motion of the islands with respect to the electrons is allowed for. According to such a model, the local plateau width and the magnetic island width coincide only in the limit of vanishing rotation frequency, as observed in experiments.

In accordance with the experimental results, tearing mode effects are taken into account in a one-dimensional transport model. To simulate the contribution of parallel heat conduction, an effective perpendicular heat conductivity is defined; this is strongly enhanced across part of the closed magnetic surfaces within islands. In addition, a moderate enhancement in regions with ergodic field lines is needed to reproduce the measured electron temperature profiles sufficiently well.

This transport model, based on local transport properties, is used to study the effect of tearing modes on the global energy confinement time τ_E. It can be shown that single tearing mode islands cause only a small reduction of τ_E, even for large islands with $w_0/a \approx 0.20$. One of the reasons for this is the inverse dependence of p_{OH} on T_e, which counteracts a strong change in the temperature profile. For strong effects (e.g. a reduction of τ_E to 1/3), several large amplitude tearing modes are required; these lead to field line ergodization in a substantial radial region. It is questionable whether such a strong deterioration of the confinement (leading to a total reduction of τ_E to 1/5, according to Fig. 2) can be observed in a tokamak with only Ohmic heating under stationary conditions, since a tokamak will become unstable and finally disrupt before the tearing modes reach the large amplitudes required.

According to our model, the heat transport (assumed to be proportional to the temperature gradient) in the ohmically heated W VII-A stellarator can be described as a superposition of two additional contributions on the neoclassical transport, which itself is negligible in W VII-A within the parameter range accessible with Ohmic heating alone: (a) the anomalous heat diffusivity $\chi_{e,an}$ and (b) a local enhancement of the effective radial transport; this is due to current driven instabilities.

The anomalous heat diffusivity determines the transport in discharges with small or even vanishing tearing mode activity. This anomalous diffusivity depends on the local density and temperature (see Eq. (1)), but not explicitly on the plasma current. Consequently, it is very unlikely that this anomalous transport mechanism, which is so far unexplained, is driven by the plasma current.

This result is further confirmed by experiments in the W VII-A stellarator where the Ohmic current is entirely switched off and where the plasma is heated by ECRH and neutral beam heating only. An equivalent transport analysis (using the same transport coefficients together with power deposition profiles for ECRH and neutral beam heating) can describe the measured electron temperature profiles in these currentless discharges within the error bars as long as the anomalous transport coefficient is sufficiently large compared to neoclassical values [5, 6, 18], since its contribution becomes smaller with growing density and temperature.

Plasma current driven instabilities lead to a further enhancement of the effective radial transport. In the case of sawtooth oscillations, the contribution of these instabilities is restricted mainly to the region inside the $q = 1$ surface. Outside $q = 1$, tearing modes enhance the transport locally, especially in the vicinity of low-order rational magnetic surfaces. This effect is due to the existence of magnetic islands and should be independent of the mechanism which produces the islands.

Therefore, as far as the effect of magnetic islands on confinement is concerned, the results deduced from tearing mode experiments should be transferable to discharges in a currentless stellarator. In a low shear vacuum field, even rather small external field perturbations produce magnetic islands on low order resonant magnetic surfaces. In fact, in W VII-A, the achievable energy content for a given heating power shows minima as a function of ϵ_0 which differ by factors of two to five from the maxima [18, 19]. In the present study, a similar reduction factor was found which is due to tearing mode islands. In Ref. [18] an attempt was made to explain this dependence of W on ϵ_0 in more detail by investigating the stability of the vacuum field surfaces in W VII-A against external field perturbations.

ACKNOWLEDGEMENTS

The authors would like to thank Dr. D. Biskamp for useful discussions and Dr. W. Lotz for his help with the field line calculations. The excellent support of the W VII-A technical staff is also gratefully acknowledged.

REFERENCES

[1] W VII-A TEAM, in Plasma Physics and Controlled Nuclear Fusion Research 1976 (Proc. 6th Int. Conf. Berchtesgaden, 1976), Vol. 2, IAEA, Vienna (1977) 81.
[2] W VII-A TEAM, NI GROUP, in Plasma Physics and Controlled Nuclear Fusion Research 1980 (Proc. 8th Int. Conf. Brussels, 1980), Vol. 1, IAEA, Vienna (1981) 173.
[3] W VII-A TEAM, in Plasma Physics and Controlled Nuclear Fusion Research 1978 (Proc. 7th Int. Conf. Innsbruck, 1978), Vol. 2, IAEA, Vienna (1979) 265.
[4] W VII-A TEAM, Nucl. Fusion **20** (1980) 1093.
[5] GRIEGER, G., W VII-A TEAM, et al., Plasma Phys. Controll. Fusion **28** (1986) 43.
[6] CATTANEI, G., DORST, D., ELSNER, A., et al., in Plasma Physics and Controlled Nuclear Fusion Research 1982 (Proc. 9th Int. Conf. Baltimore, 1982), Vol. 2, IAEA, Vienna (1983) 241.
[7] BATEMAN, G., in MHD Instabilities, MIT Press, Cambridge, MA (1978) 192.
[8] SAUTHOFF, N.R., VON GOELER, S., STODIEK, W., Nucl. Fusion **18** (1978) 1445.
[9] W VII-A TEAM, Bull. Am. Phys. Soc. **26** (1981) 892, 2U12.
[10] CALLEN, J.D., WADDELL, B.V., CARRERAS, B., et al., in Plasma Physics and Controlled Nuclear Fusion Research 1978 (Proc. 7th Int. Conf. Innsbruck, 1978), Vol. 1, IAEA, Vienna (1979) 415.
[11] RECHESTER, A.B., ROSENBLUTH, M.N., Phys. Rev. Lett. **40** (1978) 38.
[12] REBUT, P.H., BRUSATI, M., Plasma Phys. Controll. Fusion **28** (1986) 113.
[13] WOOTTON, A.J., BENGTSON, R.D., BOEDO, J.A., et al., in Plasma Physics and Controlled Nuclear Fusion Research 1986 (Proc. 11th Int. Conf. Kyoto,1986), Vol. 1, IAEA, Vienna (1987) 187.
[14] CALLEN, J.D., AZUMI, M., Bull. Am. Phys. Soc. **23** (1978) 885, 8T7.
[15] MAC KAY, R.S., Physica, **D 7** (1983) 283.
[16] W VII-A TEAM, in Controlled Fusion and Plasma Physics (Proc. 9th Eur. Conf. Oxford, 1979), Contributed Papers (1979) 4.
[17] W VII-A TEAM, Bull. Am. Phys. Soc. **26** (1981) 891, 2U11.
[18] WOBIG, H., MAASSBERG, H., RENNER, H., W VII-A TEAM, ECRH GROUP, NI GROUP, in Plasma Physics and Controlled Nuclear Fusion Research 1986 (Proc. 11th Int. Conf. Kyoto, 1986), Vol. 2, IAEA, Vienna (1987) 369.
[19] W VII-A TEAM, NI GROUP, PELLET INJECTION GROUP, in Plasma Physics and Controlled Nuclear Fusion Research 1984 (Proc. 10th Int. Conf. London, 1984), Vol. 2, IAEA, Vienna (1985) 371.

(Manuscript received 11 January 1988
Final manuscript received 25 July 1988)

INITIAL OPERATION OF THE WENDELSTEIN 7AS ADVANCED STELLARATOR

H. Renner, W7AS Team, NBI Group, ICF Group, ECRH Group

Max-Planck-Institut für Plasmaphysik,
EURATOM Association, D-8046 Garching, FRG

W7AS

E. Anabitarte[1], E. Ascasibar[1], S. Besshou[2], R. Brakel, R. Burhenn, G. Cattanei, A. Dodhy, D. Dorst, A. Elsner, K. Engelhardt, V. Erckmann, D. Evans, U. Gasparino, G. Grieger, P. Grigull, H. Hacker, H. Hailer[6], H.J. Hartfuss, H. Jäckel, R. Jaenicke, S. Jiang[3], J. Junker, M. Kick, H. Kroiss, G. Kuehner, I. Lakicevic, H. Maassberg, C. Mahn, R. Martin[1], G. Müller, H. Münch, A. Navarro[1], M. Ochando[1], W. Ohlendorf, M. Petrov[4], F. Rau, H. Renner, H. Ringler, J. Saffert, J. Sanchez[1], J. Sapper, A.V. Saposhnikov[5], F. Sardei, I.S. Sbitnikova[5], I. Schoenewolf, K. Schwoerer[6], F. Tabares[1], M. Tutter, A. Weller, H. Wobig, E. Würsching, M. Zippe.

NBI (Neutral Beam Injection Heating)

J.H. Feist, K. Freudenberger, R.C. Kunze, W. Ott, F.-P. Penningsfeld, E. Speth (Technology Division), W. Melkus (ZTE).

ECF (Electron Cyclotron Frequency Heating)

W. Kasparek, G.A. Müller, P.G. Schüller, M. Thumm, R. Wienecke (IPF Stuttgart).

ICF (Ion Cyclotron Frequency Heating)

J. Bäumler, W. Becker, F. Braun, R. Fritsch, F. Hofmeister, A. Murphy, J.M. Noterdaeme, S. Puri, F. Ryter, H. Wedler, F. Wesner (Technology Division).

---

1) Guest from CIEMAT, Madrid
2) Guest from Kyoto University
3) Guest from Southwestern Institute of Physics, Leshan, China
4) Guest from Ioffe Institute, Leningrad
5) Guest from General Physics Institute, Moscow
6) Guest from IPF, University of Stuttgart

ABSTRACT

The first plasma experiments on the W7AS advanced stellarator were conducted in October 1988, after magnetic surface mapping. The characteristics of the device are described. During the first phase of operation, 70 GHz ECF was used to generate and heat a "currentless" plasma which was maintained in quasi-steady state for typically 0.5 s. Effects of the magnetic configuration on the confinement and measures to deal with the observed plasma current (bootstrap current and ECF-driven current) were investigated. Preliminary results of transport analysis are presented and compared with predictions of transport models.

1. INTRODUCTION

Essential progress has been made with stellarators in the last few years /1/: (1) properties favourable to plasma stability and particle and energy transport have been demonstrated experimentally in "currentless operation" by means of powerful non-ohmic heating, (2) theoretical understanding of basic physics problems in stellarators and development of adapted numerical codes allow further improvement of confinement with optimized magnetic configurations, (3) the engineering of modular coil systems promises the realization of optimized magnetic devices even with the large dimensions necessary for reactors.

The W7AS "Advanced Stellarator" will partially allow experimental investigation of the optimization concept and the underlying theoretical models. As the secondary currents in the nonaxisymmetric magnetic configuration designed for W7AS are reduced /2/, this device will be dealing with a reduced Shafranov shift. Another effect achieved by the same measures is optimization of the particle drift orbits. Appropriate shaping of the magnetic surfaces has enabled the difference between the magnetic surfaces and the drift orbits of the passing particles to be reduced by a factor of 2, so that the collisional losses in the Pfirsch-Schlüter and plateau regimes are expected to be reduced. In the designing of W7AS, as an upgrade version of the former W7A, limits to optimization were set as a result of adapting to existing hardware. It was practically only the magnetic coil system and the vessel that were renewed. The improved equipment for heating includes ECF (electron cyclotron heating), NBI (neutral beam injection heating), ICF (ion cyclotron heating) and will favour more flexible operation of the device.

1.1 CHARACTERISTICS OF THE W7AS MAGNETIC FIELD

The configuration of W7AS with m = 5 periods, equivalent to 5 toroidally linked mirrors, is produced by a system of modular coils. Each period consists of 9 nonplanar (modular field) coils and 2 planar (toroidal field, TF) coils/3/. A schematic of the coil system is illustrated in fig. 1. The rotational transform, position of the magnetic axis, separatrix, shear, magnetic ripple and magnetic well are given by the arrangement and shape of the modular coils. In addition, these magnetic parameters can be varied for flexibility by superposing toroidal and vertical fields. The β-limit for equilibrium as compared with that in a conventional stellarator is increased to $\beta(0) \leq 4.5$ %. A small magnetic well is produced to guarantee stability. The stability limit of W7AS is expected to be $\beta \sim 2$ %. More modern advanced configurations, such as HELIAS /4/, promise higher β-limits of up to 5 %.

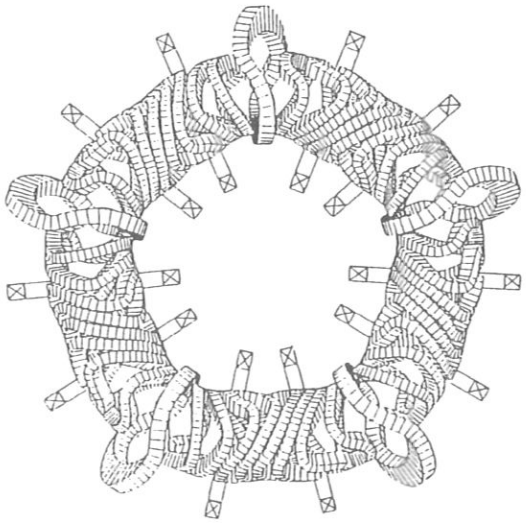

Wendelstein Stellarator W 7 AS

The cross-section of the magnetic surfaces is toroidally asymmetric: at the position of the large modular coils ($\phi = 36^{o}$) the magnetic surface it is elliptical. There is a strong field gradient in the radial direction. These magnetic field configurations are favourable for heating under magnetic resonance conditions: ECF and ICF. At the other plane of symmetry ($\phi = 0^{o}$) the cross-section of the magnetic surfaces is triangular. The gradient of the magnetic field at this position is rather small and points radially inward. To interpret local measurements with diagnostics this complex geometry has to be taken into account.

Fig. 1: Schematic of the magnet system of W7AS: 45 nonplanar modular field coils and 10 planar toroidal field coils.

Transformation of spatial coordinates to magnetic coordinates of the magnetic surfaces is mandatory. At finite β, corrections to the vacuum field configuration have to be calculated as functions of the plasma pressure profile on the basis of MHD codes. It is thus possible to obtain a 1-dimensional description of the plasma parameters.

The following table presents comparative data of W7A and W7AS:

	W7A conventional stellarator (planar toroidal field coils and helical windings)	W7AS advanced stellarator (nonplanar modular and planar field coils)
symmetry	$\ell = 2$, $m = 5$	$m = 5$
rotational transform at the centre	0.1 - 0.6 (shear ≤ 1 %)	0.39 for $B_{TF} = 0$ 0.25 - 0.6 for $\|B\|_{TF} \leq 0.5$ T
geometry: R a (m)	2.0 0.1	2.0 0.2
toroidal field (T)	3.5	3
field ripple ΔB/B (peak-to-peak)	0.03	0.09 on axis 0.3 on last surface
magnetic well ΔV'/V'	-0.03	+0.01 to -0.015
β(0)-limit for equilibrium (%)	2	4.5

1.1.2 HEATING

Three different heating methods are already installed at W7AS: ECF, NBI and ICF. Figure 2 illustrates the arrangement of the main components and the diagnostics of the first experimental phase. Local power deposition and independent heating of electrons and ions will be applied to perform detailed investigations of how the confinement is influenced by the temperature ratio T_i/T_e, temperature and density profiles, electric fields and trapped particles under conditions of distorted energy distributions. In addition, the OH transformer of W7A is still operational and is being used with small loop voltages, $U_L \leq 0.5$ V, to control the plasma current, which is generated by the heating mechanism or by plasma pressure anisotropy.

ECF at 70 GHz

After neutral gas filling the application of ECF is essential for "currentless operation" of stellarators to replace ohmic heating. At W7AS the ECF system is designed to feed a power of up to 1 MW (4 70 GHz VARIAN gyrotrons: 200 kW per unit, pulse duration 3 s; 1 VARIAN pulsed gyrotron: 200 kW, pulse duration 0.1 s) to the plasma. The heating is restricted to 1.25 T with x-mode irradiation at the second harmonic to a cut-off density $n < 3 \times 10^{19}$ m^{-3}. At a main field of 2.5 T the density limit is increased to $n < 6 \times 10^{19}$ m^{-3}. In cooperation with the ECF Group of IPF Stuttgart, we developed a sophisticated transmission line consisting of optimized components: bends, mode converters, filters, k-spectrometer /5/. At the end of the transmission line a completely polarized, almost divergence-free beam is generated which quasioptically penetrates the plasma. The use of moveable mirrors allows the interaction region of the beam with the plasma to be geometrically selected. By tuning the magnetic field it is thus possible to achieve local power deposition and even local current drive by varying the angle of incidence of the wave vector component $k_{parallel}$.

Fast modulation of the ECF power allows excitation of heat waves for investigation of local transport. Within the accessible density range and with the expected electron temperatures, $T_e < 3$ keV, ECF heating will be of interest to explore transport at low collisionality. In these parameter ranges strong effects due to the magnetic ripple of W7AS will contribute to transport. Higher β will be achieved at higher densities, $n \sim 10^{20}$ m^{-3}. Gyrotrons with 140 GHz will therefore be used in the future. A pulsed gyrotron (140 GHz, 200 kW, 0.1 s, developed by KfK Karlsruhe) will soon become available. It will be used to achieve high-β conditions in W7AS at high density. It will also be suitable as a diagnostic tool for generating heat waves.

Wendelstein Stellarator W 7 AS

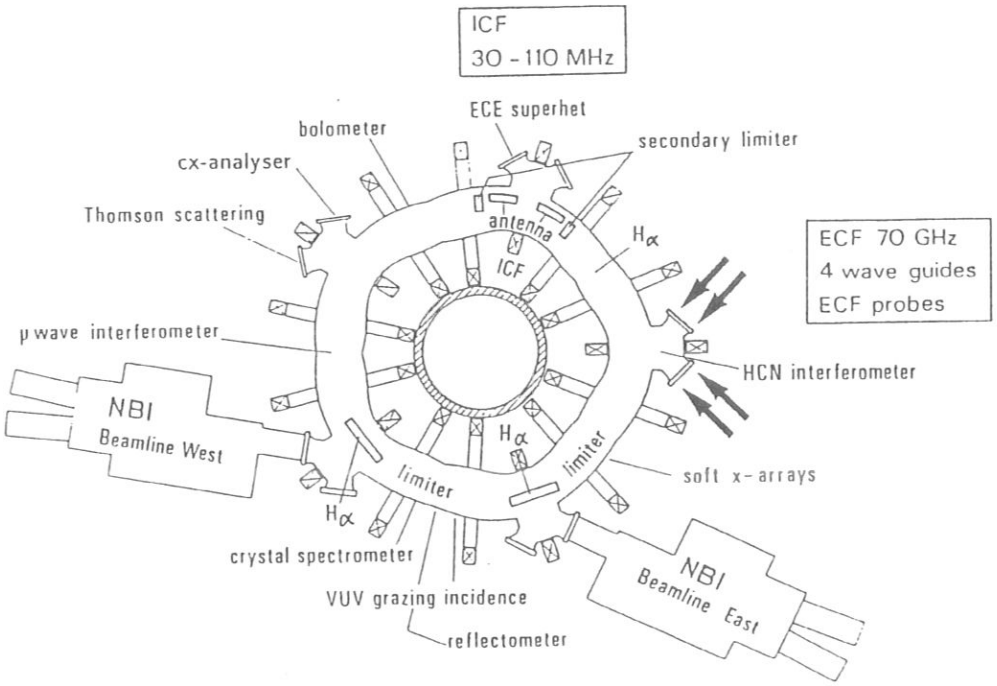

Fig. 2: W7AS device: diagnostics of the first phase of experiments and heating.

NBI

A target plasma generated by ECF is subjected in the subsequent discharge phase to NBI (neutral beam injection) or ICF (ion cyclotron frequency) to maintain and heat it at a density exceeding the cut-off density for ECF. Fast density increase will be achieved by pellet injection. Tangential NBI with a power of up to 1.5 MW (H^0 : 45 keV, >1 s) is installed at W7AS /6,7/. In view of the long interaction length of 2 m, the heating efficiency should be improved even at low densities, $n \geq 1 \times 10^{19}$ m^{-3}.

Two beamlines will be used for co- and counter-injection, whereas the present use of one beam injector yields unbalanced current drive. During the first experiments with one injector, currents of up to 5 kA were observed at $n \leq 4 \times 10^{19}$ m^{-3} and T_i, $T_e \sim$ 0.2 keV. At the low field of 1.25 T a power of up to 750 kW was applied and the discharge was maintained by NBI alone for 0.3 s.

An increase of the power to 3 MW is already being prepared, but demonstration of successful density and impurity control is a prerequisite for handling this power.

ICF

For ion cyclotron heating a flexible experimental antenna system (30 - 110 MHz, 1.5 MW, 0.5 s) is installed at W7AS. Two classical loops with a Faraday shield allow variation of the k-spectra to investigate the coupling to the target plasma in the rather complicated magnetic geometry of W7AS /8/. The results that will be obtained for the coupling efficiency and impurity handling will determine whether an antenna system developed for high power, 4 MW, and long pulse operation, 3 s, will be used in a next step.

1.2 AIMS OF THE EXPERIMENT

The experiments on the W7AS advanced stellarator have the following aims:
- to produce "currentless" plasmas and optimize the heating for three different heating methods
- to investigate the equilibrium and stability limits of the device as functions of the magnetic parameters and pressure profiles
- to describe local transport and determine the effect of magnetic ripple (i.e. trapped particles) on electric fields
- to study impurity sources and transport as functions of the plasma parameters and boundary conditions (ergodization and island formation) to find possibilities for impurity and density control in stationary operation
- to demonstrate the optimization principle and provide a data base for further development of the advanced stellarator concept.

2. START OF THE W7AS EXPERIMENT

By May 1988 assembly of the coils and vessel had almost been completed. After final tests the existence and quality of the magnetic surfaces of the vacuum field were investigated during the period May 18 to July 7, 1988. This was followed by completion of the components inside the vessel: limiters, carbon tiles, antenna for ECF and ICF, and installations for diagnostics. Conditioning of the vessel began in September 1988. Baking of the vessel at 150° C, DC glow discharges with H_2 and He gas, continuous 50 Hz ohmic discharges at low fields of up to 0.4 T and pulse cleaning with ohmic heating at a field of 1.25 T were applied. A base pressure of less than 4×10^{-8} mbar is maintained with a pumping speed of 5,000 litres/s at the vessel. First plasma experiments were performed on October 4, 1988, by using 70 GHz ECF at the second harmonic with the field of 1.25 T for plasma generation and heating. Even with He as working gas the recycling coefficient stays below 1, so that density control by external gas flow using a system of piezoelectric valves operated in a feedback loop controlled by the line density is applied. Wall gettering with Ti has been prepared, but not yet activated.

2.1 MODE OF OPERATION

Up to now data from 3,000 shots have been accumulated. Activities were concentrated on investigations of plasmas generated by ECF applications. Mostly, two gyrotrons with a total incident power of 400 kW and a typical pulse duration of 0.5 s were used. The microwave beams are launched at the completely polarized $HE_{1,1}$ mode: At the magnetic field of 1.25 T (2,800 shots) the polarization is reversed for x-mode irradiation, whereas at 2.5 T (300 shots) o-mode irradiation is appropriate. Without any preionization, the plasma is generated from a neutral gas filling in the vessel.

2.2 DIAGNOSTICS AND DATA ACQUISITION

The experiment started with an almost complete set of diagnostics, planned for the first phase of experiments:
- mass spectrometer, controllable gas flux
- Thomson scattering system for measurements along a vertical line at the location of an elliptically shaped magnetic surface
- ECE superhet
- reflectometry (in cooperation with CIEMAT, Madrid)
- ECF probes for monitoring the incident and absorbed power and control of the beam divergence
- bolometers
- soft X-ray cameras
- charge exchange analyzers (Leningrad)
- H_{alpha} arrays
- interferometry
- magnetic and electrical measurements: Rogowski coils, flux loops, diamagnetic coils
- spectroscopy: crystal spectrometer, VUV grazing incidence spectrometer
- instrumented limiters, Langmuir probes
- targets for deposition of impurities
- CCD cameras, TV monitors

Almost complete information on the plasma parameters with temporal and spatial resolution was available from the beginning of the experiments. Data handling is done with local μVAX subunits. Relevant data are accumulated by the central VAX 750 computer and transferred to the coumputer centre at IPP. Synoptical data analysis of the whole data file (with a present content of 2 Mbyte per shot) is made possible by the IBM system at the computer centre. Local data of the individual diagnostics can be analyzed on the subunits. These units are also available for control of diagnostics.

3. FIRST RESULTS

3.1 MAGNETIC SURFACE MAPPING

The new W7AS stellarator is intended as a pilot activity for the design and engineering of future modular coil systems. The Dommaschk potentials for the selected magnetic configuration served as starting point for computing the magnetic surfaces of W7AS.

The 5 x 9 nonplanar modular coils tailored to the geometric requirements (large ports for tangential injection, orientation of ports for diagnostic purposes) were manufactured to an accuracy of 10^{-3} m. They were positioned with the same precision. In operation of the magnet system the coils have to withstand strong interacting forces.

The magnetic surface mapping measurements were of course made at a low magnetic field of 0.2 T, not at the operating field of 1.25 T or 2.5 T. The existence of magnetic surfaces and the agreement of the actual magnetic parameters with the design values were therefore extensively studied by magnetic surface mapping. Two different methods were applied, both of them using a directed electron beam source that can be positioned on an arbitrary magnetic surface in the poloidal cross-section. Besides the standard technique, which determines the position of electrons in transit by means of a capacitive probe, a faster optical method was developed in cooperation with IPF Stuttgart /9/: To localize the electrons in transit, a fluorescent rod is swept across a poloidal cross-section. Images of the spots where electrons hit the rod and stimulate emission of light are taken with a CCD camera and combined by means of an image processor into a picture of a few magnetic surfaces relating to the particular positions of the electron gun. These surfaces were measured at the toroidal plane $\phi = 0^{o}$ for various values of the ratio of the currents flowing in the modular coils and toroidal field coils. Figure 3 shows a collection of magnetic surfaces around the value of the rotational transform $\iota = 1/2$. If the rotational transform value 1/2 is excluded, unperturbed magnetic surfaces are obtained close to $= 1/2$. Otherwise, as expected for configurations with small shear, large islands are produced, even for field deviations within the proposed tolerances for the assembly of the magnet system. The last closed magnetic surface at higher values of the transform is given by a magnetic separatrix. This separatrix is normally determined by one of the 5/n resonances, which are a consequence of the 5 periods of the configuration and the pentagonal shape of the magnetic axis.

Analysis of the different measurements of the vacuum field shows excellent agreement with the design values of the magnetic parameters of a separatrix at higher transform. No corrections of the magnetic field are needed, although small errors (geometry, uncompensated bus-bars) are manifested by the observed islandization at rational values of the rotational transform: 1/2, 1/3, 2/3, 2/5 etc. Far from low-order resonances there are unperturbed, nested magnetic surfaces, and with the low shear in W7AS such resonances can be excluded across the plasma cross-section. Those regions promising optimal particle confinement are thus made accessible by appropriately selecting the magnetic parameters. At low transform values of less than 0.39 complete magnetic flux surfaces extending to the maximal aperture of the limiter $a = 0.19$ m are realized.

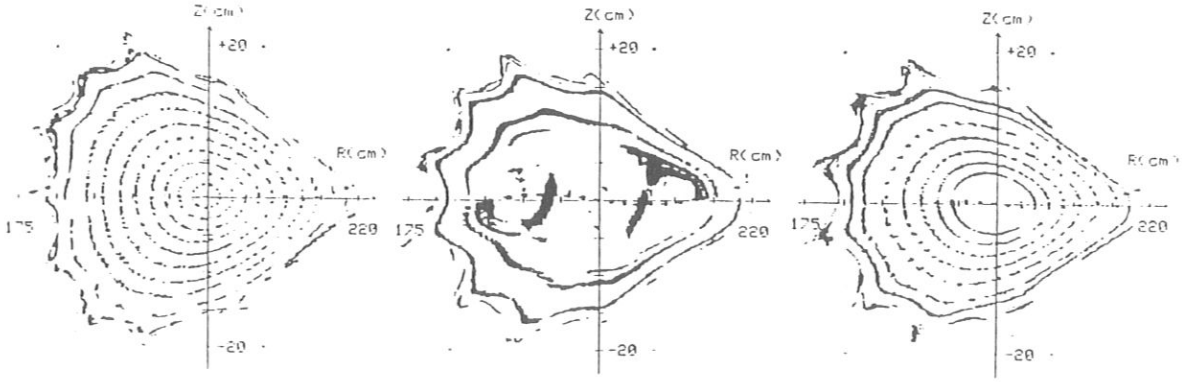

rotational transform 0.468 rotational transform 0.50 rotational transform 0.51

Fig. 3: Measured magnetic surfaces for different ratios of the currents in the modular coils and toroidal field coils: values of the rotational transform, 0.468, 0.50, 0.51.

3.2 PLASMA EXPERIMENTS

The initial plasma experiments were aimed at exploring the performance of the stellarator and the accessible ranges of parameters, at studying the confinement as a function of the parameters of the magnetic field, and at making full use of the flexible ECF launching system. Owing to the restrictions on the density the maximal achievable $\beta(0)$ is close to 0.5 %.

3.2.1 PARAMETER RANGE FOR ECF AT 70 GHz

At present, plasma experiments in W7AS are restricted by the amount of power available and the density limits for the application of 70 GHz. Mostly, two gyrotrons were operated with a total power $P_N < 400$ kW : By irradiating with the second-harmonic extraordinary mode at the main field of 1.25 T it was possible to maintain plasmas in the quasi-steady state with averaged densities $n < 2 \times 10^{19}\ m^{-3} < n_{cutoff} = 3 \times 10^{19}\ m^{-3}$, electron temperatures $T_e \geq 1$ keV and ion temperatures $T_i \sim 0.2$ keV. The single-path power absorption, as monitored by the ECF probes, approaches 100 % during the stationary phase. The high heating efficiency agrees with results from ray-tracing calculations based on experimental density and temperature profiles and is consistent with the transient temperature decay measured by ECE diagnostics after switching off the incident power. The typical energy replacement time for these discharges is about 5 ms and is reduced with increasing temperature. In operation at the fundamental mode with the magnetic field of 2.5 T the parameters can be increased to $n < 4 \times 10^{19}\ m^{-3} < n_{cutoff} = 6 \times 10^{19}\ m^{-3}$, $T_e \leq 2$ keV and $T_i \sim 0.4$ keV. The maximal energy replacement time at high density is evaluated as 15 ms with slightly reduced heating efficiencies of 90 %. The data base, especially for the field of 2.5 T, is very small and improvements are expected. Suprathermal electrons with energies about 10 times the thermal energies are only observed at very low densities. Figure 4 demonstrates the extent of the parameter regime for the rotational transform 0.34 when operating with 1 and 2 gyrotrons at 1.25 T and 2.5 T: The energy content is plotted versus the line density. To obtain the line-averaged density the given value has to be divided by the diameter $2a = 0.32$ m.

Both the measured radiative plasma losses and the calculated collisional power transfer from electrons to ions are in the range of less than 40 kW and thus rather small. A first estimate of the impurity content, based on spectroscopic measurements, soft X-ray data, and bolometric measurements, typically leads to oxygen and carbon concentrations of the order of 2 - 3 %. Iron concentrations seem almost negligible but can increase to 0.03 %.

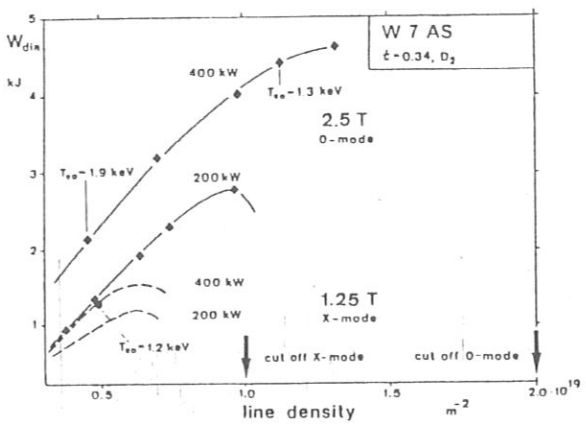

Fig. 4: Parameter range for 70 GHz ECF heating with rotational transform 0.34 and net plasma current I_p = 0 by means of an induced control voltage: Energy content W as measured by diamagnetic loops versus line density for different incident power levels, x-mode at 1.25 T, o-mode at 2.5 T. The central electron temperatures are marked. Plasma radius a = 0.16 m.

Tuning the magnetic field and geometric adjustment of the mirrors (fig. 5) can be used to modify the power deposition profiles and consequently the electron temperature profiles. An example of the influence on the temperature profiles is given in fig. 6. The case of off-axis heating was achieved by shifting the resonance zone of the interacting beam and plasma vertically upwards to 0.13 m.

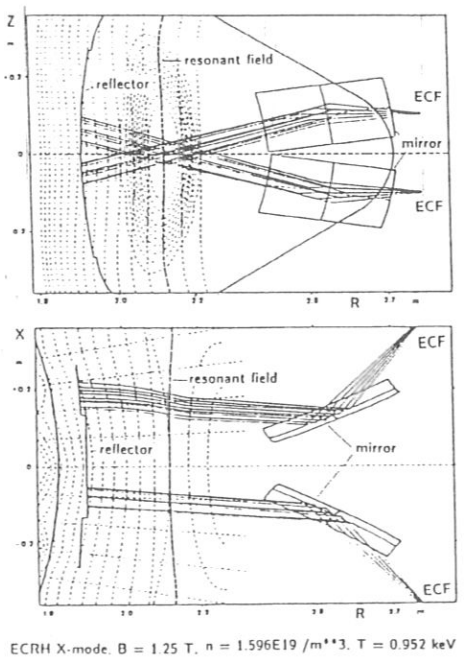

Fig. 5: Geometry of the ECF launching system and ray-tracing calculations for the vertical (Z,R) and horizontal (X,R) planes: the mirrors are adjusted for central deposition Z = 0 and with small $k_{parallel}$ components of the beams. The contour of the resonant field is indicated.

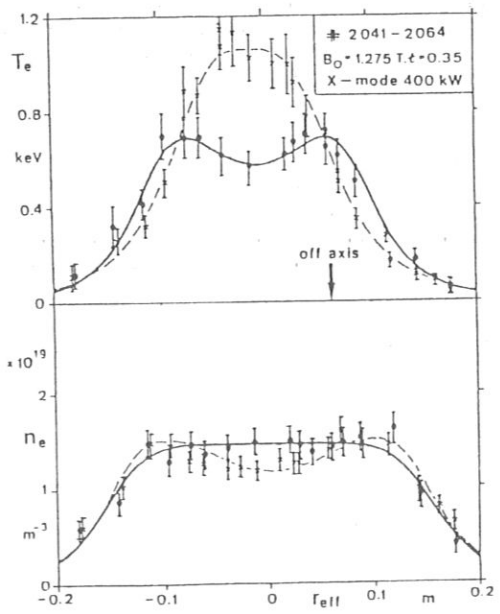

Fig. 6: Measured profiles of density and temperature for central (Z = 0) power deposition (crosses) and off-axis (Z = 0.13 m) deposition (spots). Note that the plasma parameters relate to the effective radius.

3.2.2 EFFECTS OF THE ROTATIONAL TRANSFORM CONFIGURATION ON CONFINEMENT

The low-shear W7A /11,12/ exhibited a strong influence of the magnetic configuration on the confinement. Similar effects were expected in W7AS. Systematic studies of the global confinement properties of W7AS as functions of the magnetic parameters were initiated. To minimize the contribution that currents generated by the heating method make to the magnetic configuration, almost perpendicular injection of the ECF wave vector and central power deposition were chosen. The rotational transform was varied shot by shot by changing the currents fed to the modular coils and the toroidal field coils. Figure 7 presents the energy content obtained versus the boundary value of the transform, which was calculated for the last closed magnetic surface, being determined either by the position of the limiter (z_L = 0.275 m) at low rotational transform or by the separatrix at high transform. At the rotational transforms investigated, ranging from 0.24 to 0.65, the effective plasma radius is slightly reduced from a = 0.18 m to 0.15 m. The energy content is derived from the diamagnetic signals during the quasistationary phase of discharges with a pulse duration of 0.4 s. Because of the almost constant absorbed heating power of $P_N \leq$ 200 kW (1.25 T) the energy replacement time is proportional to the given energy content. The line density is fixed at 1.5 x 10^{19} m^{-3} by gas feed.

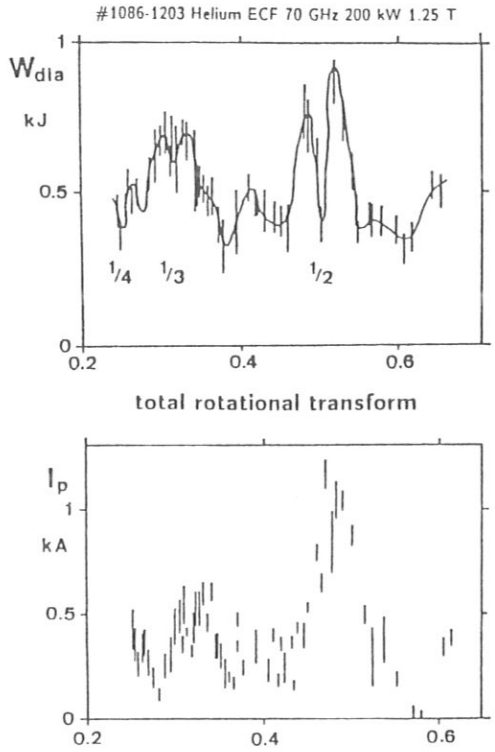

Fig. 7: Energy content versus the boundary value of the rotational transform: the line density is kept constant at 4 x 10^{19} m^{-3}. The observed stationary currents are correlated. Time window: 0.10 - 0.15 s.

Like the confinement in W7A, that in W7AS is strongly dependent on the particular value of the rotational transform: Reduced confinement is observed to be associated with low-order rational values of the rotational transform, ι = 1/4, 1/3, 1/2, 2/3, at the plasma edge. Every value 5/n should also be avoided. Close to these "resonances" optimal confinement is found. As shown by the vacuum field measurements, the system of nested magnetic surfaces can easily be destroyed even by small error fields of the order of 10^{-3} T at rational values of the transform; the rotational transform configuration appears to be robust far from rational values. The formation of magnetic islands and ergodic regions and the onset of convective cells consequently enhance the plasma loss by particle transport. Convection becomes particularly important in low-temperature discharges when islands are located at the plasma edge. Relatively large plasma currents are observed, which appear to be correlated to the energy content and become almost stationary after several 100 ms. The current density distribution modifies the profile of the rotational transform and contributes additively to the boundary value: at the field of 1.25 T it increases the boundary value by $\Delta\iota$ = 0.014 I_p, I_p being the plasma current in kA. The observed plasma current is found to be in agreement with the expected bootstrap current and changes direction as the magnetic field is inverted. Parameter studies based on measured profiles support this conclusion and will be presented later.

In order to study the effect of the plasma current on the confinement, the temporal development of a discharge for two different cases, "free current" and controlled net current (I_p = 0), has to be investigated. Figure 8 shows the corresponding temperature profiles measured by ECE diagnostics and the relevant global parameters, confined energy, plasma current and plasma loop voltage. The transient behaviour of the discharge, with relatively long time constants as expected on the resistive time

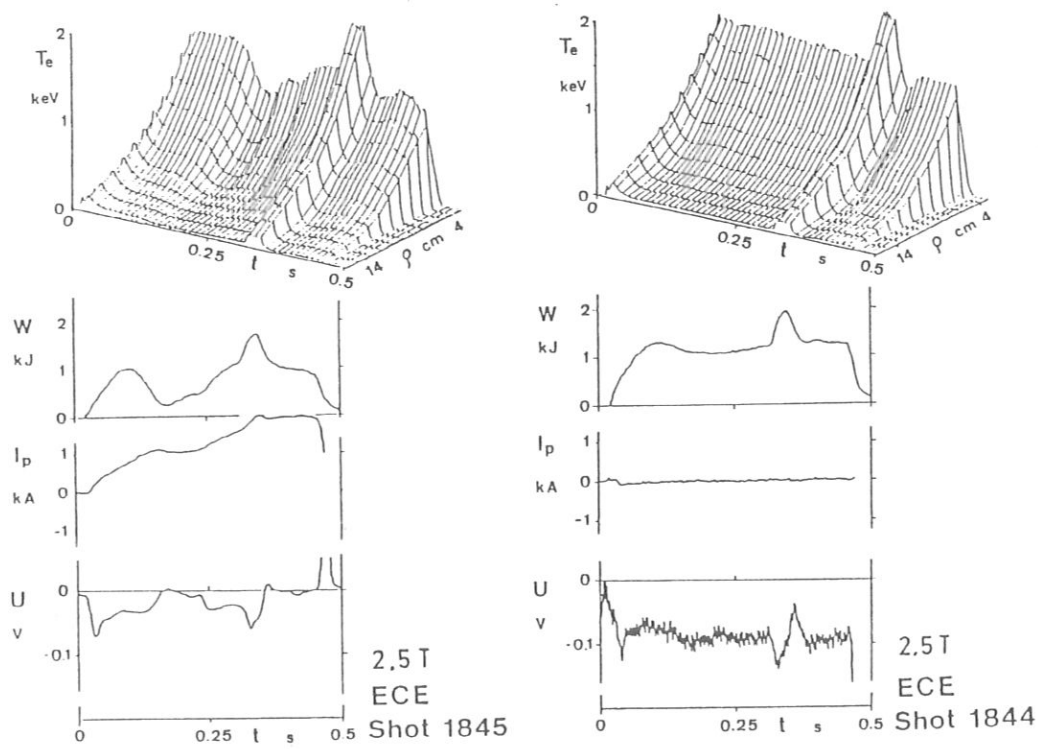

Fig. 8: Electron temperature profiles obtained by means of ECE and global parameters: energy content, plasma current, and loop voltage during discharges with free current (shot 1845) and with current control I_p = 0 by means of the ohmic transformer (shot 1844). The second gyrotron is switched on for a short pulse at the discharge time 0.32 s. The line density is controlled at 5×10^{18} m^{-3}.

scale, is demonstrated by varying the net current which affects the confinement in the form of perturbations of the temperature profiles. The vacuum field was adjusted to a rotational transform close to 1/3 and small negative shear. The perturbations may be associated with resonant magnetic surfaces and the shift of their position across the plasma radius with varying plasma current. Good confinement can be maintained by controlling the plasma current and adjusting the rotational transform.

In order to introduce shear by shaping the current density profiles experiments with induced currents of up to 5 kA were performed . Figure 9, like fig. 7, presents data from discharges at -1.25 T in the vicinity of rotational transforms close to 1/2. Three cases with induced currents -5 kA, 0 kA, and +5 kA were considered. For the bootstrap current distribution a maximal current density is expected at high gradients of pressure and especially temperature. In contrast, the current distribution of the induced current is determined by the plasma conductivity profile.

The case with +5 kA introduces an induced current in the direction opposite to the bootstrap current, so that overcompensating the local current densities will establish strong, positive shear. The energy content now shows a rather weak dependence on the boundary rotational transform value. Probably as a consequence of the increased shear and the reduced extent of the associated islands, the discharge can be maintained even at ι = 1/2. However, maximum confinement is obtained in the case of low shear with I_p = 0 close to 1/2. A critical influence of the current density distribution on the confinement is indicated in the last case of -5 kA, where, with an induced current additive to the bootstrap current, the shear may become negative.

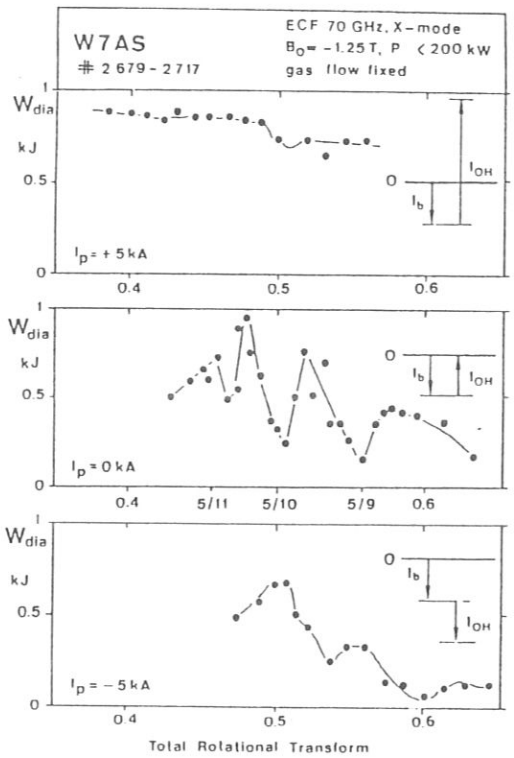

Fig. 9: Energy content W (measured with diamagnetic coil) versus the total rotational transform, which is the boundary value. The parameter is the plasma current I_p = +5 kA, 0 kA and net -5 kA. The direction of the induced current I_{OH} and bootstrap current I_b is given for each case. Note the inverted magnetic field: -1.25 T.

These experiments clearly demonstrate the influence of resonances. Improved confinement therefore requires configurations which exclude resonances from the confinement space. The destruction of the confinement seems so far to be caused by loss of equilibrium rather than by MHD instabilities. In practice, control of the boundary conditions is mandatory. Effects due to internal resonances are also observed. Such perturbations should be controlled by local current density shaping, especially at higher $\beta > 0.5$ %, when finite β-effects will become important.

3.2.3 CURRENT DRIVE BY ECF

The ECF launching system allows local current drive by varying the angle of the incident wave to adjust wave vector components that are parallel to the field. A proof-of-principle experiment allowed the possibilities of this method to be studied. At 1.25 T a target plasma was produced by central deposition with one gyrotron, and a second beam was launched at various angles of incidence. To avoid perturbations due to the shift of the rotational transform by currents, the plasma current was controlled by means of the OH transformer. The dependence of the loop voltage on the angle of incidence can be used to evaluate the current drive efficiency. An optimum current drive efficiency of 20 A/kW was evaluated for the plasma parameters $n \sim 1.5 \times 10^{19}$ m^{-3} and $T_e \sim 1.2$ keV with an angle of 18^o to the perpendicular to the magnetic axis. The theoretical current drive efficiency based on a quasilinear diffusion tensor (computed with a ray-tracing code) in combination with a Fokker-Planck solution or with a simple Spitzer function convolution /13/ agrees fairly well with the experimental data /14/. This promising result in turn stimulated an experiment for current control by ECF. As shown in fig. 10, when the angle is adjusted to 10^o compensation of the bootstrap current is possible even for different power levels. The corresponding values for the bootstrap current were estimated on the basis of the profiles (fig. 11): 56 A for a central temperature of 0.3 keV and a power of 90 kW, 660 A for 0.8 keV and 200 kW, 1.33 kA for 1 keV and 400 kW.

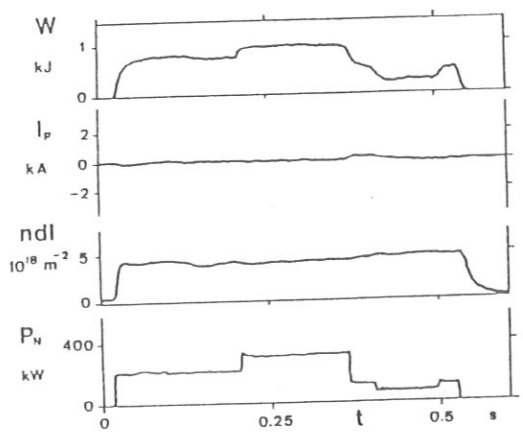

Fig. 10: EC current drive experiment profile(shot 2362): energy content, net plasma current, controlled line density and incident ECF power versus time. The net plasma current is controlled by ECF current drive. Central deposition and angle of incidence adjusted at 10^{o} to the axis normal.

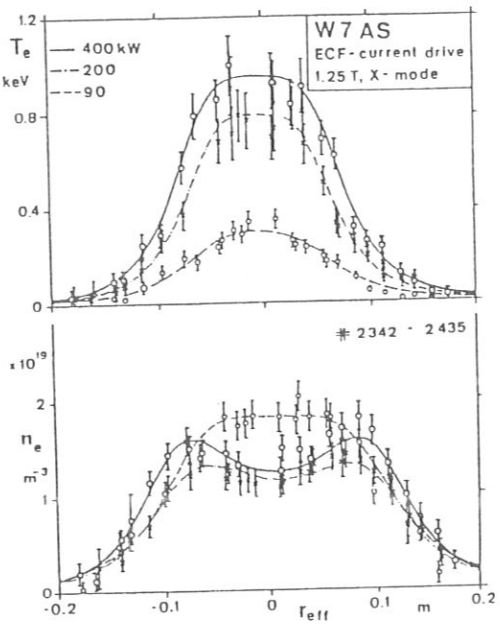

Fig. 11: Temperature and density profiles for ECF powers of of 400 kW, 200 kW and 90 kW. Power deposition as shown in Fig. 10.

3.2.4 TRANSPORT STUDIES

Thomson scattering yields accurate density and temperature profiles. Almost hollow density profiles were observed in cases with strong temperature gradients and high heating power (see fig. 9). The temperature profiles with central power deposition are rather narrow compared with the density profiles. Under conditions for optimal confinement at boundary values of the rotational transform, 0.34, 0.47, and 0.52, quasistationary discharges are maintained. The coherent data set, namely the profiles of the plasma radiation density, electron density, and electron and ion temperatures, was used for a first description of the transport. The quality and the reliability of the data, accumulated from a sequence of up to 40 shots, depends mainly on accurate control of the machine parameters and may be further improved.

ELECTRON HEAT CONDUCTION

In the ECF discharge density range investigated the radiation losses and the collisional power transfer from electrons to ions are small. Therefore, the energy balance is dominated by the electron heat conduction term. Up to 75 % of the gyrotron power is assumed to be absorbed, this being consistent with ray-tracing calculations and the ECE data. The ECF power deposition profiles are adapted to the beam width and centred with respect to the resonance condition. The power loss terms are estimated by an average oxygen radiation model renormalized to the bolometer data and the collisional power transfer.

As an example the parameters of a discharge at 2.5 T and rotational transform 0.34 are given in fig. 12. Two gyrotrons (≤370 kW) are used for heating with central power deposition. The energy content determined from diamagnetic signals is 4.5 kJ. The evaluated experimental electron heat conductivity is compared with theoretical predictions based on the DKES code /15/. The DKES code is based on the monoenergetic drift kinetic equations in magnetic flux coordinates for each particle species, with radial electric fields included. For given density and temperature profiles in the real, nonaxisymmetric magnetic configuration of W7AS it is possible to calculate the radial electric field, the particle and energy fluxes and the bootstrap current under the condition of ambipolarity. The data for anomalous transport, as empirically derived for W7A, are also plotted. The information is completed by adding the local radiative power densities. The total power measured by bolometer is 35 kW. Some estimates for the radiation with assumed impurity concentrations almost consistent with the spectroscopic data are included.

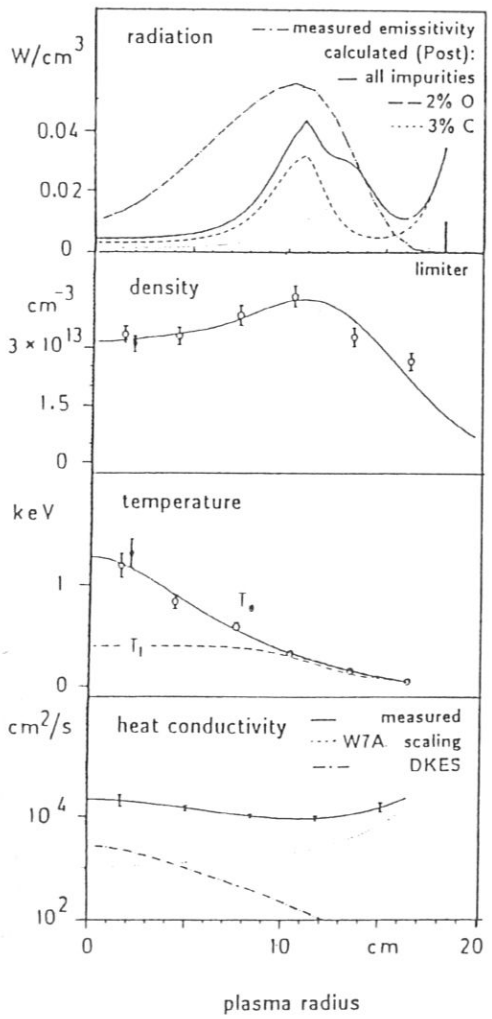

So far all profiles analyzed for various ECF heating powers, magnetic parameters and densities, and a temperature range 0.5 to 2 keV exhibit a similar radial dependence of the heat conductivity. In the inner part of the plasma up to a radius a/2 the predicted heat conductivity values are a factor 2 - 5 lower than the experimental data. At the boundary, however, a significant increase of the transport is indicated /16/. So far, regions with electron temperatures $T_e < 0.2$ keV always become distorted. The onset of convection and destruction of the configuration are probably responsible for the high energy losses.

Fig. 12: Transport analysis for discharges with ECF o-mode operation (400 kW) at 2.5 T (at discharge time 0.32 s for shots 1965 - 1972). The profiles of the plasma radiation, electron density, electron and ion temperatures and electron heat conductivity are presented. The evaluated radiative power densities are compared with corona equilibrium calculations for assumed impurity concentrations. In the density and temperature profiles the blank circles refer to the outer major radius side, shaded circles to the minor radius side of the magnetic surfaces. The experimental electron heat conductivity is compared with values obtained by transport models: DKES calculations, empirical W7A scaling.

PARTICLE TRANSPORT

Some discharges were analyzed to get information about the particle fluxes. DEGAS code calculations /17/ and H_{alpha} measurements were combined to estimate the particle balance and describe the neutral particle profiles /18/. For a discharge with a density $n \sim 1.5 \times 10^{19}\ m^{-3}$, a temperature $T_e \sim 1$ keV, and an energy replacement time of 3 ms the refuelling rate inside the separatrix is $\Gamma = 2.5 \times 10^{20}$ ions/s. This corresponds to a particle confinement time of 36 ms. In the gradient region the neoclassical particle flux is consistent with the flux derived from the DEGAS code. However, towards the plasma boundary a strong anomaly is found, being described by a diffusion coefficient equal to 1/10 of the electron heat conduction there (fig. 13).

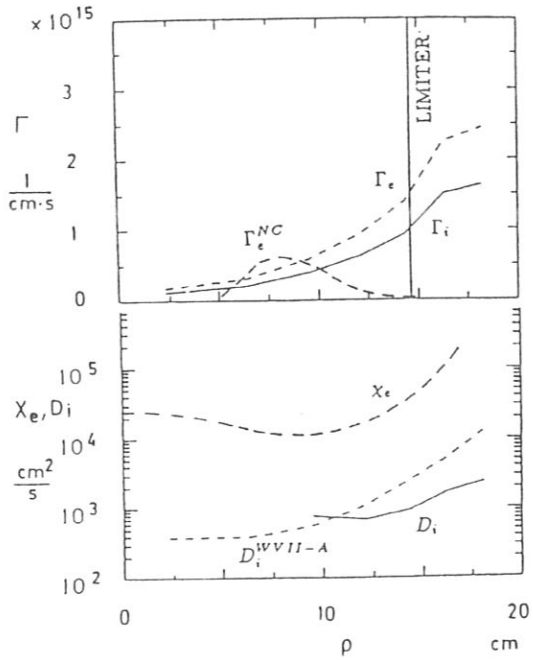

Fig. 13: Comparison of fluxes determined from analysis of the particle balance and those expected on the basis of the DKES code. At the boundary, the diffusion coefficient D_i is evaluated and compared with the value obtained from the anomalous W7A scaling. The experimental heat conductivity is derived for a discharge with a power of 200 kW, a magnetic field of 1.25 T, rotational transform 0.53, OH current control (shots 1294-1313).

BOOTSTRAP CURRENT

A conclusive picture of the origin and scaling of the observed plasma current is essential because of the influence of the current density profile on the rotational transform. Current density profiles with values of the order of 10 A/cm² are not measurable. Some measured temperature profiles, if the current is compensated by induced currents, show local flattening, probably correlated to the position of resonances. The current density distribution may therefore be checked by means of local temperature perturbations. Current density distributions for the bootstrap current were derived on the basis of the pressure profiles by using both the neoclassical model for axisymmetric systems (Hazeltine-Hinton) /19/ and the DKES code as adopted for W7AS. The axisymmetric model typically predicts currents a factor of about 2 as large as those of the DKES code. Figure 14 presents results for a case with OH current control. The current density distribution is plotted for the bootstrap current and the compensating OH current relating to the conductivity profile for an assumed impurity factor $Z_{eff} = 3$. The integrated value for the bootstrap current is 1.3 kA (DKES) and the OH current for the loop voltage $U_L = -0.085$ V is -2.26 kA. For the absolute values agreement within a factor 2 seems reasonable. A further, more detailed discussion of effects due to suprathermal electrons and their confinement and to, on the other hand, the observed transport anomaly may clarify the discrepancy. The following table summarizes some global data for different discharges. In most cases the net plasma current was controlled at $I_p = 0$ in stationary operation, compensated either by induced voltages (OH) or by ECF current drive. For some discharges with free-running current a direct comparison of the net plasma current (I_p) and the calculated bootstrap current (I_b) is possible. A critical parameter in this comparison is the value of Z_{eff}, which was estimated consistently with the radiation measurements.

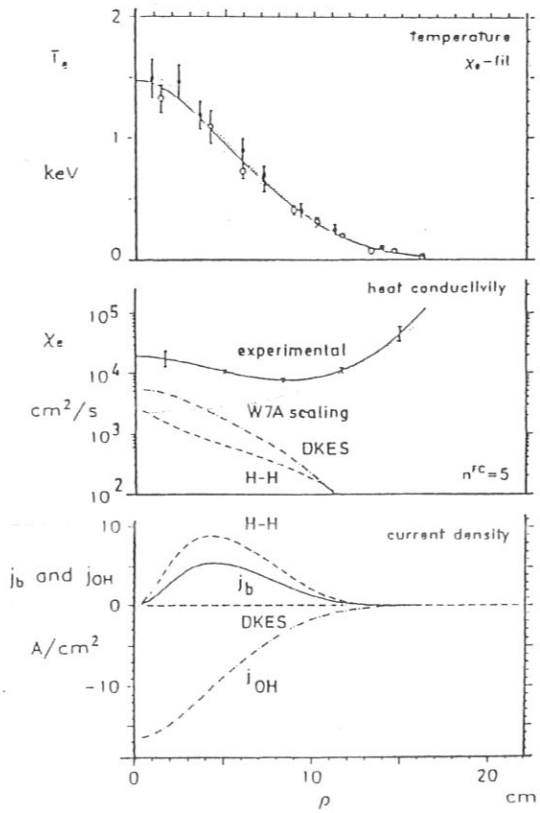

Fig. 14: Transport analysis of shots 1802-1802: Calculations of the current density profiles for the bootstrap current, j_b, and the compensating current, j_{OH}, assuming an induced voltage of 0.08 V and an impurity factor of 3. Blank and shaded circles as in Fig. 12. H-H Hazeltine-Hinton.

For cases with free current the table gives the measured steady-state plasma current (I_p). In the case of current control by OH, the ohmic current (I_{OH}) has to be calculated for the measured loop voltage (U_L). In the case of ECF current control only the calculated bootstrap current is documented.

70 GHz ECF
analysis based on Thomson: n, T_e profiles

$n_e \leq 2$ E19 m^{-3}, $Z_{eff} = 3$

shot	B(T)	transform	P_N(kW)	T_{eo}(keV)	W(kJ)	I_b(kA) DKES	I_p(kA)	$-I_{OH}$(kA)	$-U_L$(V)
906	1.256	0.53	400	0.75	1.3	0.9	1.2		
1147	1.256	0.31	200	0.5	0.6	0.7	0.7		
1680	1.275	0.53	200	1.15	1.0	1.3	0	3.0	0.13
1727	1.275	0.53	400	1.45	1.2	2.2	0	3.76	0.11
1802	2.55	0.34	200	1.5	1.4	1.2	0	2.2	0.08
1899	2.55	0.34	400	1.7	1.95	1.9	0	3.7	0.08
2041	1.275	0.34	400	1.2	1.55	1.8	0	2.75	0.095
2065	1.275	0.34	200	0.7	1.0	0.4	0	0.9	0.075
2269	1.270	0.34	400	1.15	1.45	1.9	0		ECF
2299	1.270	0.34	200	0.9	1.1	0.9	0		ECF
2342	1.27	0.345	400	1.0	1.0	1.33	0		ECF
			200	0.8	0.75	0.66	0		ECF
			90	0.3	0.35	0.06	0		ECF

$n_e \leq 4$ E19 m^{-3}, $Z_{eff} = 2$, O-mode

1965	2.55	0.34	400	1.3	4.5	1.4	0	2.6	0.07

In the case of current compensation by OH a rather smooth ι profile can be obtained as a consequence of the broad current density profiles relating to the conductivity distribution. Compensation of the bootstrap current by ECF current drive introduces a localized current sheath associated with the power deposition, which is beneficial for local shaping of the profile. This is demonstrated by the example given in fig. 15. The discharge is already described in the previous section and the temperature profile is plotted in fig. 11. The calculated current density profiles of both the bootstrap current and the ECF-driven current /14/ are included for comparison. The ECF current, according to the calculations, is larger than the estimated bootstrap current. The amplitude of this calculated ECF current is therefore normalized to make the net plasma current zero as experimentally observed.

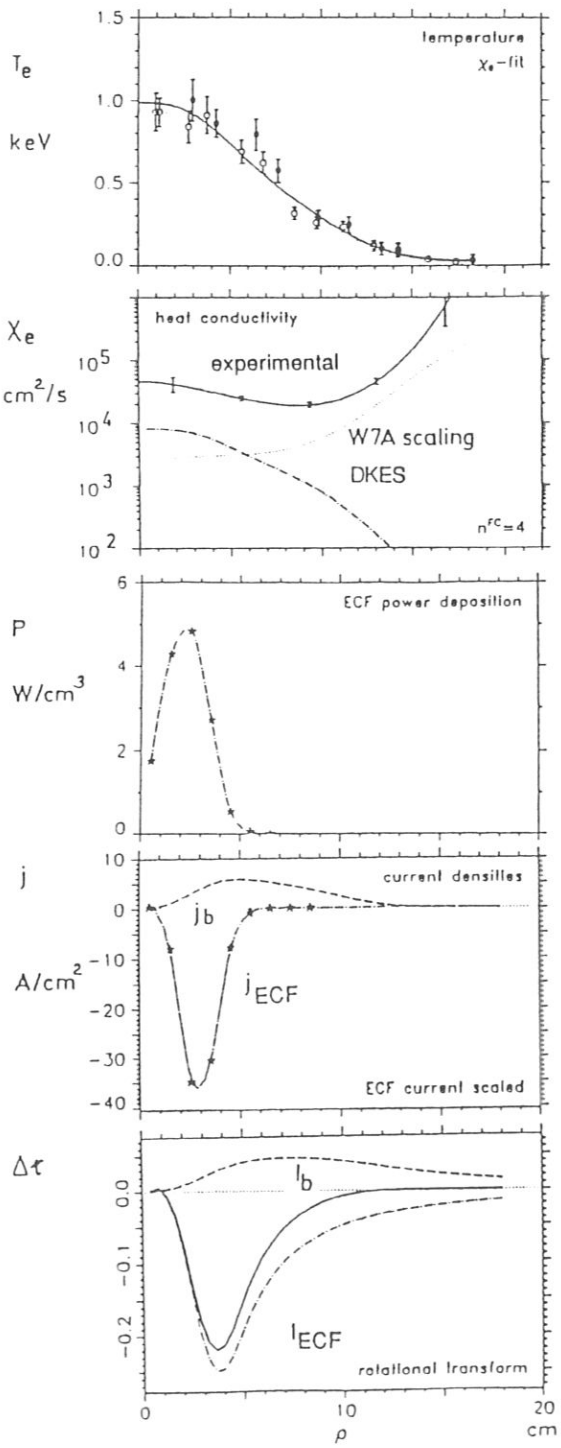

Fig. 15: Transport analysis of shots 2342 - 2365: Calculations of the bootstrap current density for the discharge of fig. 10. The power deposition profile is given from ray-tracing calculations. The current density contribution to the rotational transform is estimated locally.

4. SUMMARY AND CONCLUSIONS

The new W7AS advanced stellarator is in operation. The magnetic configuration was developed according to an optimization principle with reduced secondary currents and was realized with a set of 45 modular coils. Extensive studies of the vacuum field show excellent agreement of the measured magnetic parameters with the design values. Especially, field errors could be kept within a tolerance of 10^{-3}, so that unperturbed, nested magnetic surfaces are established far from low-order rational values of the transform ("resonances"). No corrections are needed. Toroidal fields and vertical fields are superposed to allow wide variation of the magnetic parameters and hence flexible adjustment of the magnetic configuration to the requirements of the experiment.

The plasma is generated and heated by applying ECF at 70 GHz. In cooperation with IPF Stuttgart a rather sophisticated launching system was developed. Focused beams (HE_{11} mode) are quasioptically guided by moveable mirrors. The measured losses of the optimized transmission line, including the conversion losses to the final HE_{11} mode, are less than 10 %. Variable power deposition and current drive are thus achieved by varying the $k_{parallel}$ wave vector components. Experiments with the 2nd-harmonic x-mode at the magnetic field of 1.25 T and with the fundamental o-mode at 2.5 T using two gyrotrons (up to 400 kW) produced electron temperatures of up to 2 keV within the accessible density range. Measurements of the single-path absorption are in good agreement with ray-tracing calculations and show heating efficiencies close to 1. Nevertheless, the absorption mechanism needs further studies to clarify the power deposition at the boundary and the role of suprathermal electrons.

Systematic studies of the confinement as a function of the magnetic configuration for the accessible range of $\beta \leq 0.5$ % at the field of 1.25 T found behaviour similar to that observed in W7A: deterioration of the confinement is associated with the existence of low-order resonant surfaces in the confinement space. Control of the boundary value of the rotational transform, far from resonances, and sufficiently low shear are necessary for optimal confinement. During discharges with long pulse duration, more than 0.2 s, a bootstrap current, strongly dependent on the temperature profiles and additive to the rotational transform of the vacuum field, becomes stationary at values of up to 3 kA. Control of the net current for stationary conditions with good confinement was successfully applied by two different methods: voltages induced by means of an OH transformer and ECF current drive. Even fine tuning of the current density profiles by local ECF current drive seems possible and may be necessary to attain higher β-values.

The theoretical values of the neoclassical bootstrap current calculated by means of the DKES code (drift kinetic equation solver by S.P. Hirshman, W.I. Rij) on the basis of the measured density and temperature profiles were roughly consistent with the experimental observations in W7AS. The modification of the magnetic configuration by the bootstrap current is especially large in the low-field case and in the region of high temperature gradients. Operation at a high field may be favourable because then, according to the scaling for the bootstrap current, the amplitude will be diminished. In addition, the contribution of the related poloidal field to the transform scales as 1/B.

More detailed studies of the bootstrap current are certainly required: For further development of the advanced stellarator concept it will be necessary to take into account the bootstrap current and consider countermeasures, probably by means of an appropriately shaped magnetic configuration.

Some preliminary studies of the electron heat conduction have been discussed. Under conditions of optimal confinement, which were established at particular values of the rotational transform close to 1/3 and 1/2 by current control, the energy balance was evaluated on the basis of measured density and temperature profiles. For almost all discharges, irrespective of the heating power, the experimental values of the electron heat conductivity were in the range of 0.7 to 2 m^2/s at the radius a/2. Towards the centre a slight increase is observed, but a strong increase is seen at the boundary. Especially at the boundary, significant discrepancies in relation to the theoretical predictions of the DKES code occur. Additional losses have to be assumed in the boundary region. So far the plasma confinement with temperatures $T_e <$ 200 eV may be rather fragile.

Estimates of the particle confinement based on H_{alpha} measurements and DEGAS code simulations indicate for some discharges consistency with neoclassical predictions for the particle flux in the plasma gradient region and anomalous fluxes at the plasma edge ($D \sim 1/10\ \chi_e$). Extension of the parameter range in future experiments will certainly help to clarify these phenomena.

Up to now, radiation and impurities in ECF discharges do not seem to be very important. Control of impurity sources and impurity transport will be studied during the next phase of experimentation and may become problematic with full use of the installed power on W7AS towards higher densities.

REFERENCES

/1/ Carreras et al., "Progress in Stellarator/Heliotron Research", Nuclear Fusion Vol. 28 (1988), p. 1613

/2/ Brossmann, U., Dommaschk, W., et al., "Concept of an Advanced Stellarator", Plasma Physics and Controlled Nuclear Fusion Research (Proc. 9th Conf. Baltimore 1982), Vol. 3, IAEA, Vienna (1983), p. 141

/3/ Sapper, J. et al., "Engineering problems of WENDELSTEIN 7AS", Transactions 8th Int. Conf. Structural Mechanics in Reactor Technology, Amsterdam (1985), N, p. 15

/4/ Nührenberg, J., Zille, R., Physics Letters 114 A (1986), p. 129

/5/ "Microwave technology and tests of the 70 GHz/1 MW long-pulse ECRH system on W7AS", Kasparek, W., et al.. Proc. 15th Symp. on Fusion Technology (SOFT), Utrecht (1988), B 19.

/6/ Lister, G.G., et al., Proc. 11th Europ. Conf. on Contr. Fusion and Plasma Physics, Aachen (1983), vol. II, p. 323

/7/ Feist, J.H., et al., Proc. 4th Symp. on Heating in Toroidal Plasmas, Rome (1984), EUR 9341 EN, p. 1051

/8/ Wesner, F., et al., Proc. 5th Symp. on Fusion Technology, Utrecht (1988)

/9/ Hailer, H., et al., Contr. Fusion and Plasma Physics, Madrid (1987), Proc. 14th Europ. Conf., Vol. I, p. 423

/10/ Jaenicke, R., et al., 16th Europ. Conf. on Controlled Fusion and Plasma Physics, Venice (1989), P8 B3

/11/ Renner, H., Proc. Workshop on Basic Physical Processes of Toroidal Fusion Plasmas, Varenna (1985), EUR 10418 EN, Brussels 81986), Vol. II, p. 479

/12/ Grieger, G., et al., Plasma Physics and Contr. Fusion, 28 1A (1986), p.43

/13/ Gasparino, U., et al., Plasma Physics and Contr. Fusion, 30 (1988), p. 283

/14/ Gasparino, U., et al., 16th Europ. Conf. on Controlled Fusion and Plasma Physics, Venice (1989), P8 B4

/15/ Hirshman, S.P. et al., Phys. of Fluids 29 (1986), p. 2951

/16/ Maassberg, H. et al., 16th Europ. Conf. on Controlled Fusion and Plasma Physics, Venice (1989), P8 B5

/17/ Heifetz, D.B. et al., J. Comp. Physics 46 (1982), p. 309

/18/ Sardei, F., et al., 16th Europ. Conf. on Controlled Fusion and Plasma Physics, Venice (1989), P8 B6

/19/ Hazeltine, R.D., Hinton, F.L., Revue of Mod. Physics 48 (1976), p. 241

STELLARATOR WENDELSTEIN VII-AS: PHYSICS AND ENGINEERING DESIGN

STELLARATOR SYSTEMS

KEYWORDS: *stellarator, modular coils, Wendelstein VII-AS*

JÖRG SAPPER and HERMANN RENNER
Max-Planck-Institut für Plasmaphysik, Boltzmannstrasse 2
D-8046 Garching bei München, Federal Republic of Germany

Received August 21, 1989
Accepted for Publication August 24, 1989

The advanced stellarator Wendelstein VII-AS at the Max-Planck-Institut für Plasmaphysik, Garching, Federal Republic of Germany, is a medium-sized experimental machine with the following properties and aims:

1. *a broadly optimized magnetic configuration with improved plasma equilibrium and smaller neoclassical transport losses compared to classical stellarators*
2. *operation with net-current-free plasma*
3. *field generation with a modular set of coils instead of the conventional helix/toroidal field coil system*
4. *good access for plasma heating methods, e.g., neutral beam injection, electron cyclotron heating, and ion cyclotron heating.*

The physics characteristics and the engineering design of the experiment as well as results from the initial operation period are reported.

INTRODUCTION

Stellarators are an alternative line to tokamaks in the field of toroidal confinement systems for fusion machines. In contrast to tokamaks, they allow net-current-free plasma operation and are, therefore, inherently suitable for continuous performance in a reactor. In the last few years, essential progress has been made with stellarators[1]:

1. Properties favorable to transport and stability have been demonstrated experimentally in "currentless operation" by means of powerful nonohmic heating.

2. Theoretical understanding of the basic physics in stellarators and development of numerical codes have allowed further improvement of confinement with optimized magnetic configurations.

3. The engineering of modular coil systems promises to realize optimized magnetic devices even with the large dimensions necessary for reactors.

The Wendelstein VII-AS advanced stellarator (W VII-AS) will experimentally investigate a particular optimization concept and the guiding theoretical models. By reducing the secondary currents, the nonaxisymmetric magnetic configuration designed for W VII-AS (Ref. 2) will have a greatly reduced Shafranov shift. Another effect achieved by the same means is optimization of the particle drift orbits. By appropriate shaping of the magnetic surfaces, the difference between the drift orbits of the passing particles and the magnetic surfaces has been reduced by a factor of 2, so a reduction of the collisional losses in the Pfirsch-Schlüter and plateau regimes is expected. For the design of W VII-AS, as an upgraded version of the Wendelstein VII-A (W VII-A), limits to optimization were set by existing hardware. Essentially only the magnetic coil system and the vessel were new. The improved equipment for heating includes electron cyclotron heating (ECH), neutral beam injection (NBI), and ion cyclotron heating (ICH), which allow more flexible operation of the device.

The aims of the experiments on W VII-AS are the following:

1. to produce "currentless" plasmas and to optimize the heating for three different heating methods
2. to investigate the equilibrium and stability limits of the device as a function of the magnetic configuration parameters and the pressure profile
3. to describe local transport and to determine the effect of magnetic ripple, trapped particles, and electric fields

4. to study impurity sources and transport as functions of the plasma parameters and the boundary conditions (ergodization and island formation) for possible impurity and density control in stationary operation
5. to demonstrate the optimization principle and to provide a data base for further development of the advanced stellarator concept.

PHYSICS CHARACTERISTICS OF W VII-AS

Magnetic Field

The configuration of W VII-AS with $m = 5$ periods, similar to five toroidally linked mirrors, is produced by a system of modular coils. Each period consists of nine individually shaped nonplanar coils.[3] The coil system is illustrated in Fig. 1. A superimposed

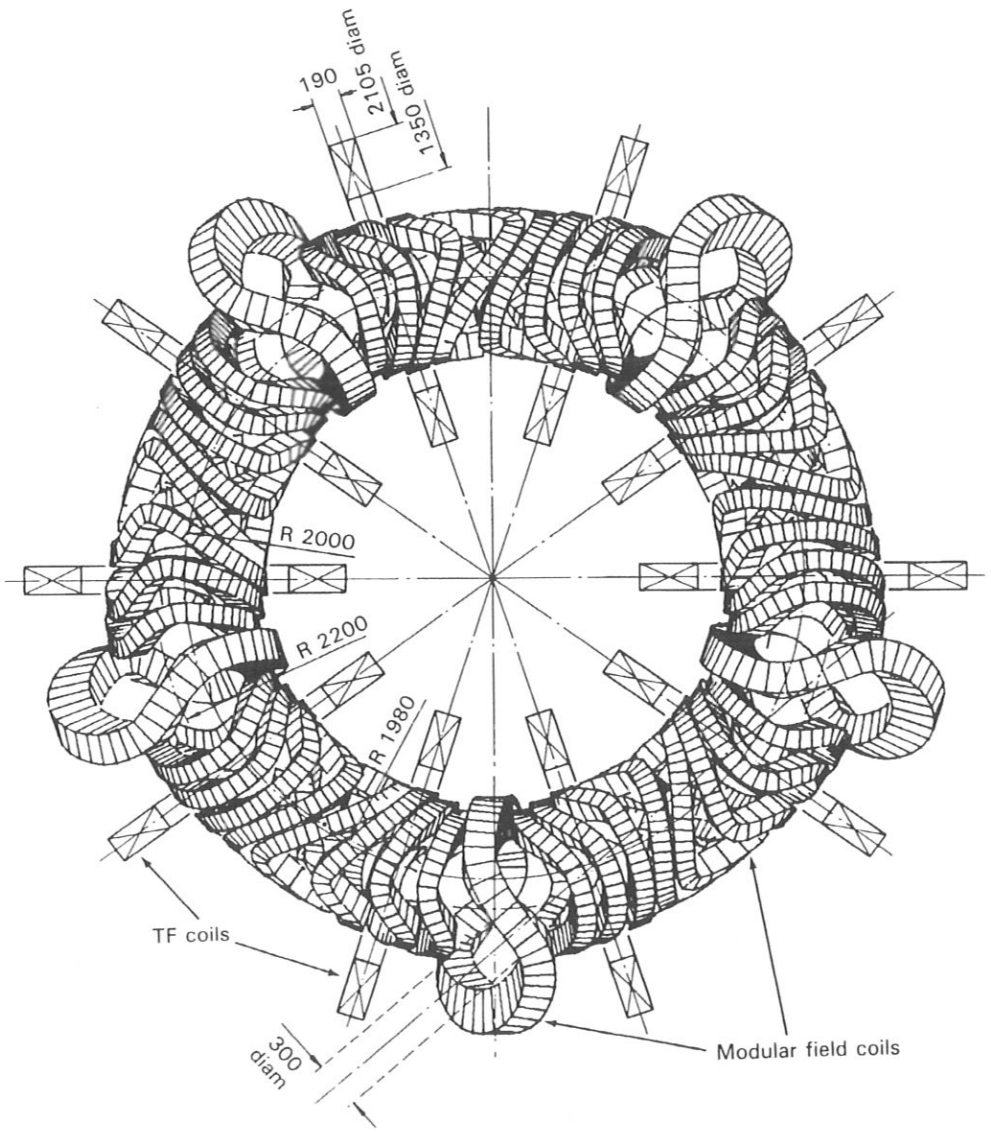

Fig. 1. Schematic of the magnetic system of W VII-AS showing modular coils and planar TF coils. All dimensions are in millimetres.

toroidal field (TF) and vertical field are used to modify the magnetic configuration parameters for flexibility: rotational transform, position of the magnetic axis, separatrix, shear, magnetic ripple, magnetic well, and others. Otherwise, these are fixed by the shape and arrangement of the modular coils alone. The beta limit for equilibrium is increased over that for a conventional stellarator [to $\beta(0) \leq 4.5\%$]. A small magnetic well is provided to guarantee stability. The stability limit of W VII-AS is expected to be $\beta(0) \sim 2\%$. More modern advanced stellarator configurations, such as the Helical Advanced Stellarator,[4] promise higher beta limits (up to 5%).

The W VII-AS has a moderate-transform, low-shear, and magnetic-well-stabilized stellarator configuration. Table I is a comparison of W VII-A and W VII-AS. The low shear makes it possible to avoid low-order resonant values of the transform entirely by careful control of the transform profiles. Magnetic configuration flexibility has to be provided to counteract finite-beta plasma effects. Control of the net plasma current and the magnetic configuration is mandatory. Transform, shear, and magnetic well can be modified by particular compositions of the field components—the toroidal field, the field of the modular coils, and the vertical field—over a limited range, even during the pulse. Current control is possible by a small induced voltage and even locally by ECH current drive. The optimization introduces magnetic mirrors, which influence transport at conditions approaching low collisionality. For investigation of transport, independent current feeds to particular modular coils allow variation of the magnetic ripple, changing the fraction of trapped particles.

Heating

Three different heating methods are installed on W VII-AS. Figure 2 illustrates the arrangement of the main components and the diagnostics for the first experimental phase. Local power deposition and independent heating of electrons and ions will be applied to perform detailed investigations of how the confinement is influenced by the temperature ratio T_i/T_e, pressure profiles, electric fields, and trapped particles under conditions of distorted energy distributions. In addition, the ohmic heating (OH) transformer of W VII-AS is being used with small loop voltages, $U_L \leq 0.5$ V, to control the plasma current that is generated by the heating mechanism or by plasma pressure.

ECH at 70 GHz

Starting with neutral gas filling, the use of ECH to replace OH is essential for currentless operation of stellarators. The W VII-AS ECH system is designed to feed a power of up to 1 MW to the plasma (four Varian gyrotrons, 200 kW per unit, pulse duration 3 s; one Varian pulsed gyrotron, pulse duration 0.1 s). The heating is restricted at 1.25 T and X-mode irradiation at the second harmonic with a cutoff density $n < 3 \times 10^{19}$ m^{-3}. At the main field of 2.5 T and O-mode irradiation, the density limit is increased to $n < 6 \times 10^{19}$ m^{-3}. In cooperation with the ECH group of the Institut für Plasmaforschung, Stuttgart, a sophisticated transmission line consisting of optimized components including bends, mode converters, filters, and a k-spectrometer was realized.[5] The plasma is irradiated quasi-optically by focused, completely polarized beams. The use of movable mirrors allows the interaction region of the beam with the plasma to be geometrically selected. Thus, in addition to tuning of the magnetic field, local power deposition and even local current drive by variation of $k_\parallel$ are possible. Fast modulation of the ECH power allows excitation of heat waves for investigation of local transport. Within the accessible density range and with the expected electron temperatures ($T_e < 3$ keV), ECH will be used to explore transport at low collisionality. In this range of parameters, strong effects due to the magnetic ripple of W VII-AS will contribute to transport. Higher beta will be achieved at higher densities ($n \sim 10^{20}$ m^{-3}). Therefore, gyrotrons at 140 GHz will be used in the future. A pulsed gyrotron (140 GHz, 200 kW, 0.1 s, developed by Kernforschungszentrum Karlsruhe) will soon become available. It will be used for diagnostics, for example, for generation of heat waves and for approaching high-beta conditions in W VII-AS at high density.

NBI

Starting with a target plasma generated by ECH, NBI and radio-frequency at the ion cyclotron frequencies (ICH) are being used to maintain plasmas at densities exceeding the cutoff density for ECH. A fast density increase will be achieved by pellet injection. In contrast to W VII-A, tangential injection with a power of up to 1.5 MW (H^0: 45 keV, >1 s) is installed on W VII-AS (Refs. 6 and 7). In view of the long interaction length of 2 m, the heating efficiency should be improved even at low densities ($n \geq 1 \times 10^{19}$ m^{-3}). Two beamlines are used for co- and counterinjection, and unbalanced injection will be possible for current drive. A power increase to 3 MW is being prepared, but demonstration of successful density and impurity control is a prerequisite.

ICH

A flexible experimental antenna system (30 to 110 MHz, 1.5 MW, 0.5 s) is installed on W VII-AS for ICH. Two classical loops with a Faraday shield allow variation of the k spectra to investigate the coupling to the target plasma in the rather complicated magnetic geometry of W VII-AS (Ref. 8). Depending on the results of the coupling efficiency and impurity handling, an antenna system developed for high-power (4-MW), long-pulse (3-s) operation may be used in a next step.

TABLE I

Characteristics of W VII-AS and W VII-A

	W VII-A Conventional Stellarator	W VII-AS Advanced Stellarator, Modular Coils
Symmetry	$l = 2$, $m = 5$	$m = 5$
Rotational transform at the center	0.1 to 0.6 (shear $\leq$ 1%)	0.39 0.25 to 0.6 (by $\Delta B_{tor} \leq 0.5$ T)
Geometry: R, a (m)	2.0, 0.1	2.0, 0.2
Toroidal field on axis (T)	3.5	3
Field ripple, $\Delta B/B$	0.03	0.09 on axis 0.3 on last surface
Magnetic well, $\Delta V'/V'$	-0.03	$+0.01$ to -0.015
Beta limit for equilibrium (%)	2	4.5
Heating		
ECH	70-GHz, 200-kW, 0.1-s polarized HE_{11}	70-GHz, 1-MW, 3-s quasi-optical, polarized HE_{11} 140 GHz, 0.2 MW, 0.1 s (1990)
ICH	30 to 110 MHz, 500 kW	30 to 110 MHz, 1.5 MW
NBI	H^0: 30-kV, 0.8-MW, 0.2-s injection 6 deg to perpendicular	H^0: 45-kV, 1.6-MW, 1-s tangential co- and counterinjection

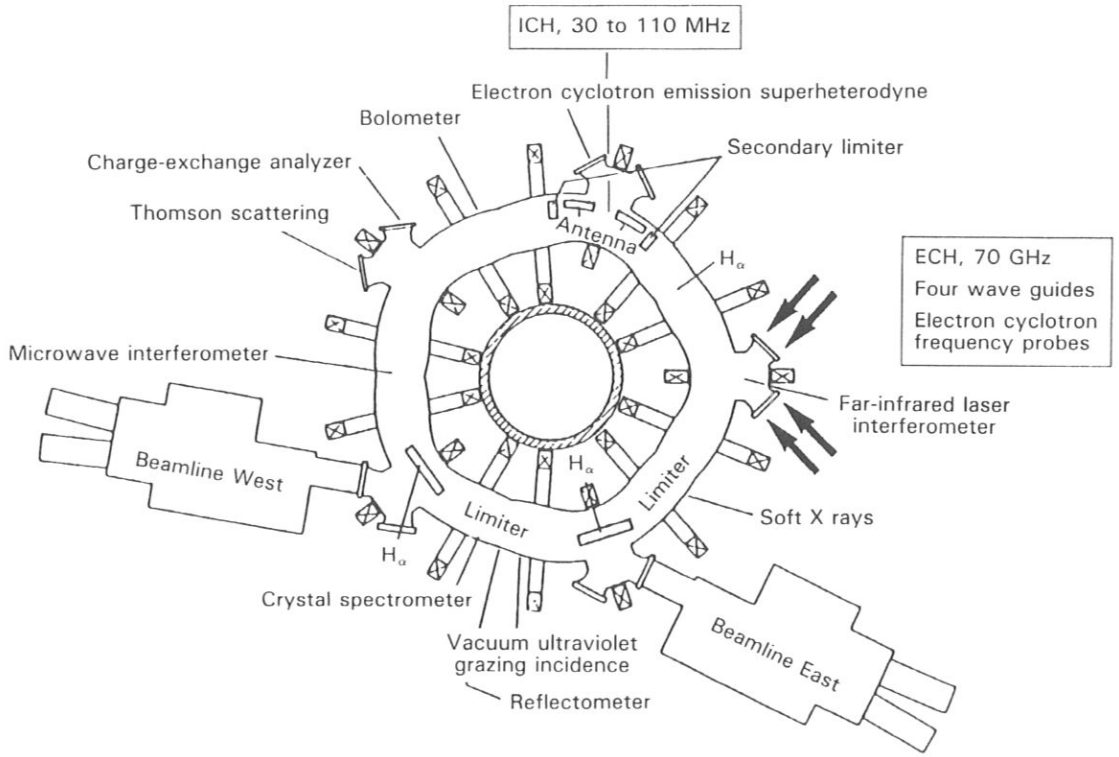

Fig. 2. W VII-AS device showing diagnostics for the first phase of experiments and the installed external plasma heating equipment.

ENGINEERING DESIGN OF W VII-AS

The W VII-AS (Ref. 9) (see Fig. 3) is an upgraded version of the earlier W VII-A stellarator. The following technical aims were factored into its design:

1. field generation with a modular set of poloidally closed coils instead of the conventional helix/TF coil system
2. improved access for plasma heating methods, e.g., NBI, ECH, and ICH
3. increased plasma size in an adequate vacuum vessel.

An analysis of the necessary steps toward a stellarator device of reactor size showed that the underlying principles of the advanced stellarator concept should first be tested in a device of the size of W VII-AS before taking the next step to a considerably larger machine. The fastest and most economical way was to upgrade the W VII-A device.

Components of the Confinement System

The most characteristic design feature of the W VII-AS device is the modular set of 45 nonplanar coils. This coil set replaces the TF coils and the helix of a conventional stellarator. The combination of helical and poloidal currents in the same coils produces the nonplanar shape of the coils. The coil set can be divided into five periods, allowing modular design of the machine. Ten planar TF coils are added to the modular system for increased experimental flexibility. The combination of currents in the two coil systems allows a variation of the rotational transform ι from 0.25 to 0.6 (where 0.39 is the standard value) at B_T = 2.5 T. A wide parameter range is accessible by varying the vertical field or current in separately fed, enlarged modular coils (allowing access for tangential NBI). The technical data of the machine are given in Table II.

A new kind of circumferential and vertical force appears in nonplanar coils. The force is distributed irregularly along the coil body, so detailed computational analysis is needed to show tensile and shear stresses in the coil cross section. An optimized supporting concept

TABLE II

Technical Data of the W VII-AS Coil Systems

	Normal Coils	Enlarged Coils
Modular coil system		
Nominal current, I (kA)	37	37
Nominal voltage, U_N (kV)	3.3	
Excitation/flattop voltage, U (kV)	4.0/2.5	
Total resistance, R_W (20°C) (mΩ)	60	
Inductance, L (mH)	60	
Time constant, τ (s)	1.0	
Stored energy, W_{mag} (flattop) (MJ)	60.0	
Pulse duration, t_p (equivalent rectangular current) (s)	5	
Flattop duration, t_{FT} (s)	≧3	
Number of coils	40	5
Number of windings per coil	16	40
Overall diameter of one coil (m)	1.3	1.7
Copper cross section per turn (mm^2)	930	
Cooling medium	H_2O in hollow conductors	
Temperature rise per pulse, $\Delta\Theta$ (K)	≦50	
Interval between pulses (min)	3	
Magnetic field on the axis (T)	2.5 for all combinations with toroidal field	
Additional TF coil system		
Nominal current, I (kA)	43	
Nominal voltage, U_N (kV)	1.2	
Total resistance, R_Ω (mΩ)	6	
Inductance, L (mH)	4	
Time constant, τ (s)	0.66	
Number of coils	10 (modified W VII-A coils)	
Number of windings per coil	12	
Magnetic field on the axis, B_{tor} (T)	±0.5	

in the lateral and radial directions minimizes the stresses. Figures 4 and 5 show the finite element model and the stresses typical for a W VII-AS nonplanar coil.[10,11]

The coils, encased in a dividable support shell with resin-filled pads, can slide partially in the structure to avoid transmission of the thermal expansion to the structure (see Fig. 6). A new winding manufacturing method had to be developed to minimize the initial winding tension and, hence, the tendency for the coils

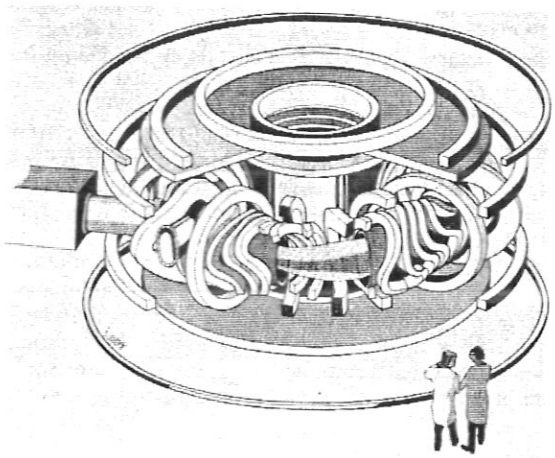

Fig. 3. Schematic of W VII-AS.

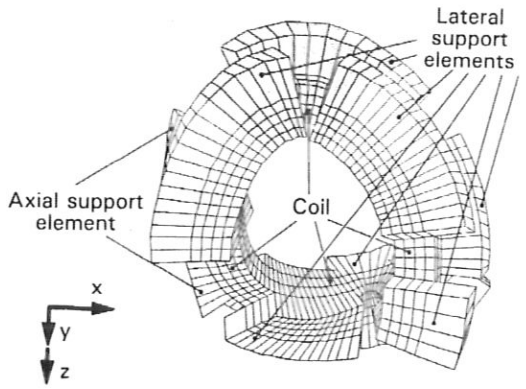

Fig. 4. Finite element model of a nonplanar coil with support elements.

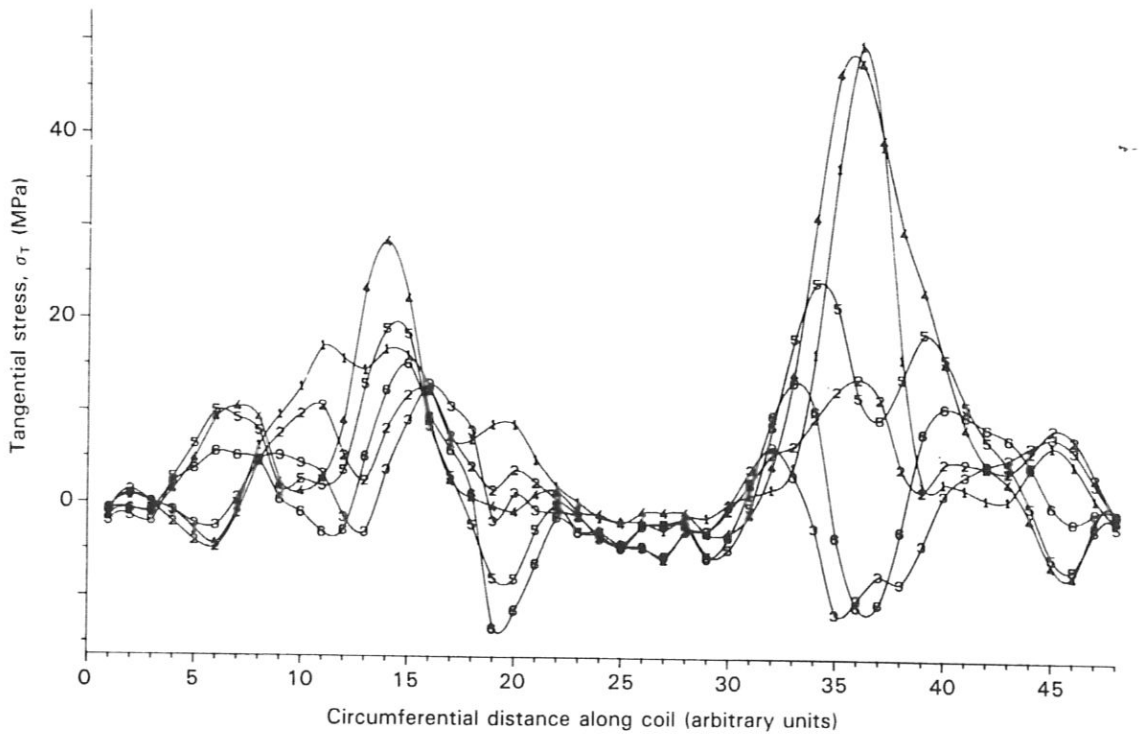

Fig. 5. Stress distribution along the circumference of a coil for six cross sections of the coil.

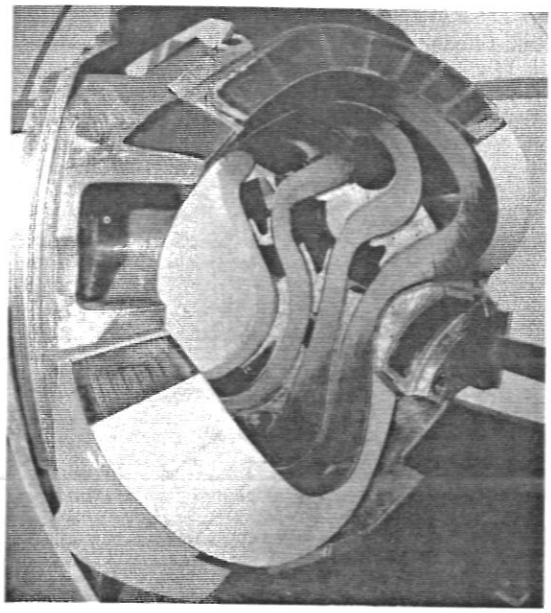

Fig. 6. Assembled half-module of W VII-AS.

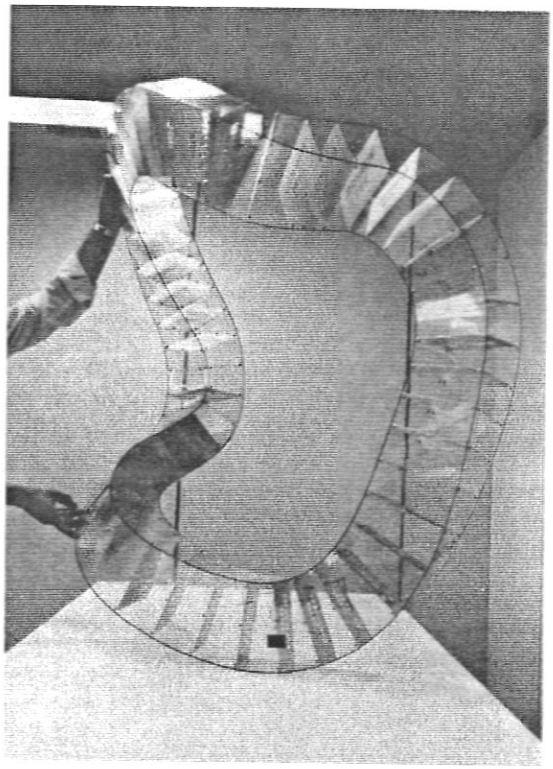

Fig. 7. Master model for a nonplanar coil.

to spring back into a planar shape. The use of stranded copper wires and a resin impregnation treatment was sufficient. The coil shape is fixed by a splittable mold, which was produced from a master model. Thus, high reproducibility of geometrical accuracy is guaranteed for each of the five different coils in a module (see Figs. 7, 8, and 9).

The shape of the plasma column of W VII-AS (see Fig. 10) is influenced by the optimized confinement field, and its cross section varies from a triangle at $\varphi = 0$ deg to a vertical ellipse at $\varphi = 36$ deg. It is also five times periodic. In contrast to a classical stellarator, the vacuum vessel is free of magnetic forces. It, therefore, is fabricated from stainless steel sheet with a relatively small wall thickness (12 mm). The ideal contour of the vacuum vessel follows the inner surface topology of the coils, as shown in Fig. 11. Actually, the vacuum vessel is split into five flange-connected modules and has sections with enlarged cross sections and ports to give good access for NBI. Figure 12 shows a finite element model of the vacuum vessel. Figure 13 shows an assembled vacuum vessel module on the machine bed for testing.

Manufacturing the vacuum vessel requires a practical approach for obtaining a nearly ideal shape. A good method is to subdivide the vacuum vessel into circumferential sections from which the surface can be unrolled into a plane. Thus, the welding and bending techniques for tubular machinery can be used. Figure 14 shows an inside view of a section of the vacuum vessel and its welding seams.

Assembly of the W VII-AS device, beginning with the coils and the structural shell halves and ending with pumping of the torus and first current tests, took 1 yr and was completed in May 1988. The device assembly procedure also made use of the modularity. First, the coils were inserted into half-shells of the modular field structure, exactly positioned, and then fixed with resin-filled pads, as shown in Figs. 4 and 6. Then the torus segments were fitted axially into the modules and the modules were completed by bolting the shells and welding the torus segments from the inside. Also, the ports were assembled at that time. Final assembly of the device on its base was managed by radially shifting the completed modules to a central support tube. Closing and final positioning of all parts were done with bolts (see Fig. 15).

The last work to be done on the magnet system before commissioning was assembly of the busbar systems, the poloidal field coils, and the cooling water distribution and piping equipment. The completed device is shown in Fig. 16.

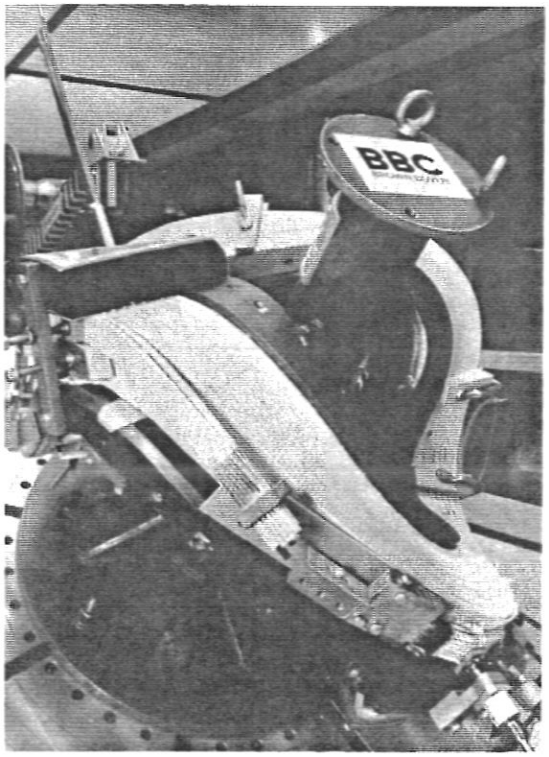

Fig. 8. Winding device and mold for a nonplanar coil.

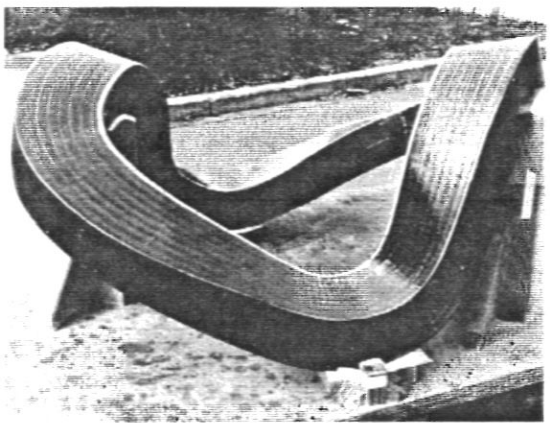

Fig. 9. Impregnated and cured coil.

INITIAL OPERATION OF THE W VII-AS EXPERIMENT

The existence and quality of the magnetic surfaces of the vacuum field were investigated during the period from May 18 to July 7, 1988. Figure 17 shows a collection of magnetic surfaces, measured in the toroidal plane $\varphi = 0$ deg, as the ratio of the current in the modular coils to that in the TF coils is varied around the value of the rotational transform $\iota = \frac{1}{2}$. If the value of $\iota = \frac{1}{2}$ is excluded, unperturbed magnetic surfaces are obtained close to $\iota = \frac{1}{2}$. Otherwise, as expected for a configuration with small shear, large islands are produced, even for field deviations within the proposed tolerances for the assembly of the magnet system. The last closed magnetic surface at higher values of the transform is given by a magnetic separatrix. This separatrix is normally determined by one of the 5/n resonances, which are a consequence of the five periods of the configuration and the pentagonal shape of the magnetic axis. At low transforms ($\iota <$ 0.39), complete surfaces up to the maximum aperture

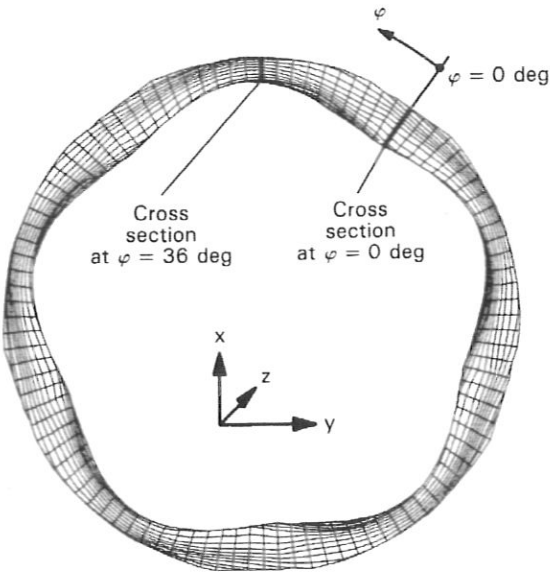

Fig. 10. Top view of the plasma surface.

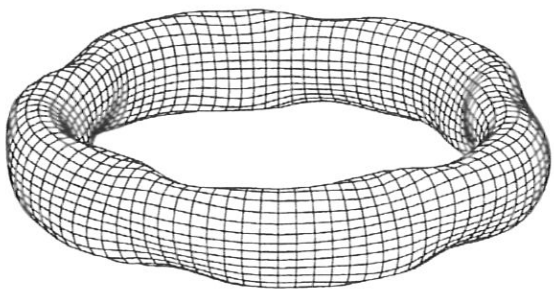

Fig. 11. Ideal vacuum vessel.

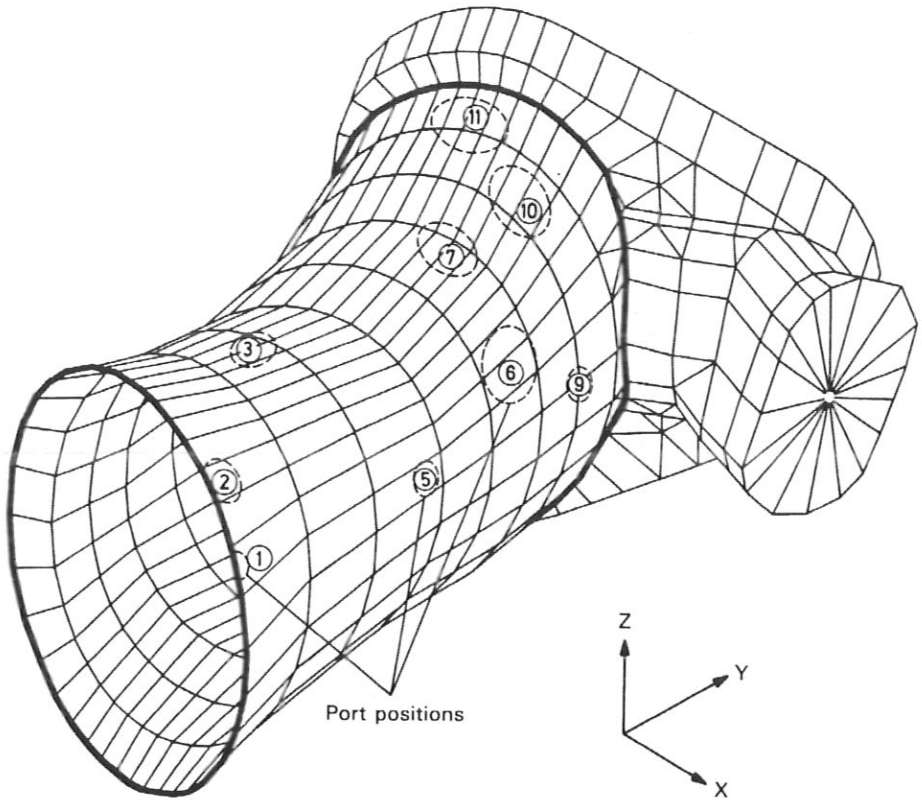

Fig. 12. Finite element mesh for a half-module of the actual vacuum vessel.

of the limiter ($a = 0.19$ m) are obtained. Analysis of the different measurements of the vacuum field shows excellent agreement with the design parameters, such as rotational transform, shear, position of the magnetic axis, and formation of a separatrix at higher transform. No corrections of the magnetic field are needed, although small errors (geometry, uncompensated busbars) are indicated by the observed islands at rational values of the rotational transform: $\frac{1}{2}$, $\frac{1}{3}$, $\frac{2}{3}$, $\frac{2}{5}$, etc. These measurements were followed by completion of the components inside the vacuum vessel: limiters, carbon tiles, antennas for ECH and ICH. Installation of the diagnostics followed. Conditioning of the vacuum vessel began in September 1988. Baking of the vacuum vessel at 150°C, dc glow discharges with H_2 and helium gas, continuous 50-Hz ohmic discharges at low field ($B_0 \leq 0.4$ T), and pulse cleaning with OH at full field were applied. A base pressure $p < 4 \times 10^{-8}$ mbar was maintained with a pumping speed of 5000 ℓ/s at the vessel.

The first plasma experiments were performed on October 4, 1988, with a field of 1.25 T using 70-GHz ECH at the second harmonic for plasma generation and heating. Even with helium as the working gas, the recycling coefficient remains below 1, so the density is controlled by an external gas feed using a system of piezoelectric valves operated in a feedback loop related to the line density. Wall gettering with titanium, carbonization, or boronization by a glow discharge is being prepared, but have not yet been used.

Diagnostics and Data Acquisition

The experiment started with an almost complete set of diagnostics planned for the first operation phase (see Table III). A set of improved diagnostics (active charge-exchange measurements, neutron counting, soft X-ray cameras, bolometer cameras, particle detector and probe arrays, microwave scattering, multichannel Thomson scattering for profile measurements, and Doppler shift measurements to determine plasma rotation and electric fields) is under construction and will be in operation at the end of 1989.

Almost complete information on plasma parameters with temporal and spatial resolution was available

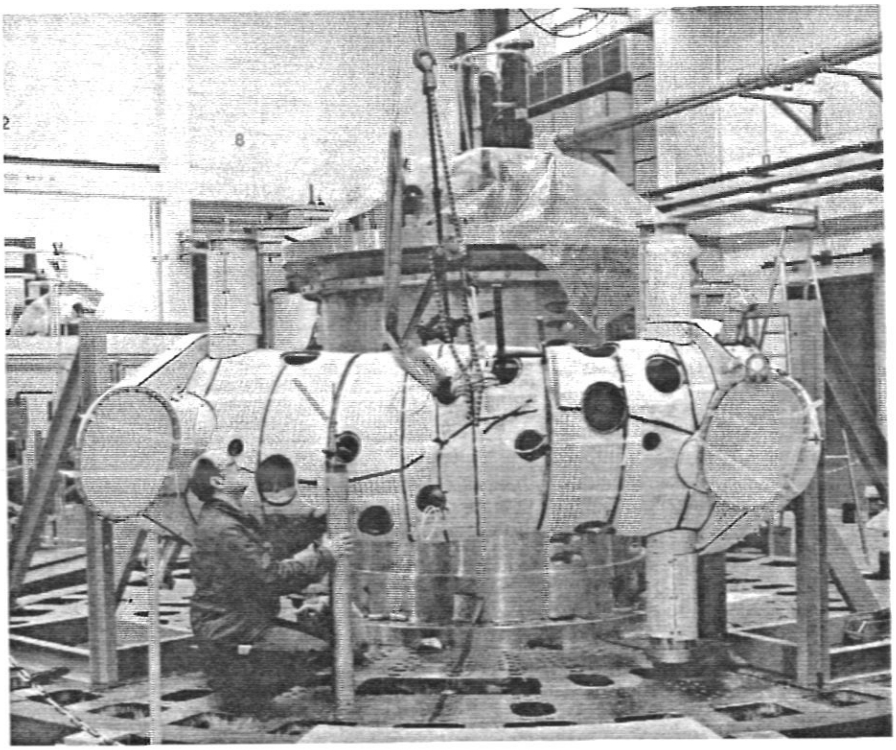

Fig. 13. Preassembly of a vacuum vessel module with thermal insulation.

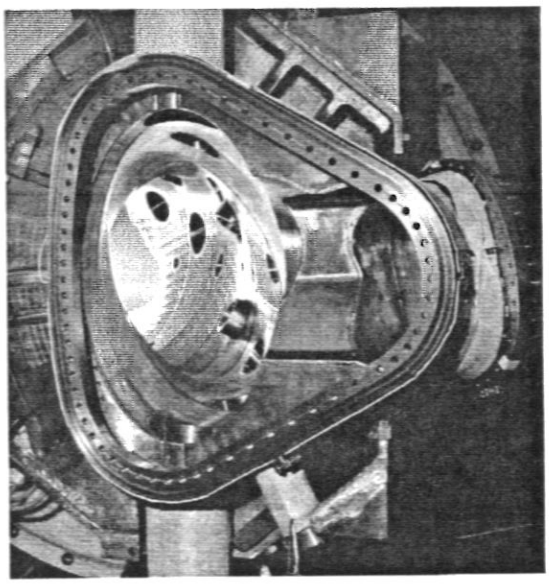

Fig. 14. Inside view of the vacuum vessel showing port penetrations and the connecting flange.

TABLE III

Diagnostics for the First Experimental Period on W VII-AS

Mass spectrometer, controllable gas flux
Magnetic and electric measurements: Rogowski coils, flux loops, diamagnetic coils
Electron cyclotron frequency probes for monitoring the incident and absorbed microwave power and control of the beam divergence
Thomson scattering system for measurements along a vertical line at the location of an elliptically shaped magnetic surface
Electron cyclotron emission superheterodyne
Reflectometry (in cooperation with CIEMAT)
Bolometers
Soft X-ray cameras
Charge-exchange analyzers (Leningrad)
H_α arrays
Interferometry
Spectroscopy: crystal spectrometer, vacuum ultraviolet grazing incidence spectrometer
Instrumented limiters, Langmuir probes
Targets for deposition of impurities
Charge-coupled device cameras, television monitors

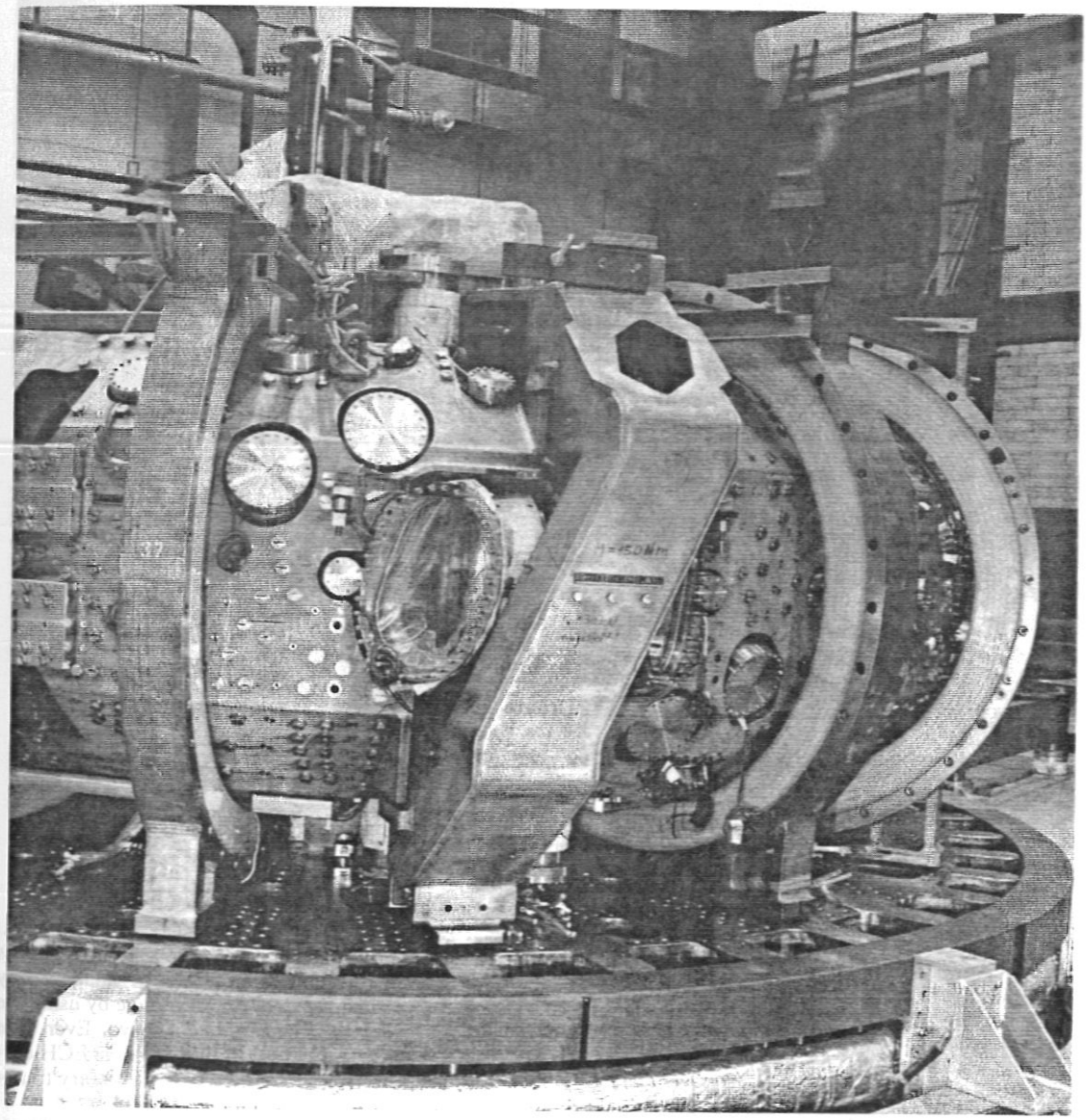

Fig. 15. Modular assembly on the machine base.

from the beginning of the experiments. Data handling is carried out with local microVAX subunits. Relevant data are accumulated by the central VAX 750 computer and transferred to the computer center. Synoptical data analysis relating to the whole data file (currently 2 Mbyte/shot) is made possible by the IBM system at the computer center. Local data from the individual diagnostics can be analyzed on the subunits. These units are also available for control of diagnostics.

First Experimental Results

The plasma is generated and heated by application of ECH at 70 GHz. Focused beams (HE_{11} mode) are quasi-optically guided by movable mirrors, allowing variable power deposition and current drive through variation of the $k_{\parallel}$ component. Experiments with the second harmonic X mode at a magnetic field of 1.25 T and with fundamental O mode at 2.5 T using 2 gyrotrons ($P_N < 400$ kW) produced electron temperatures

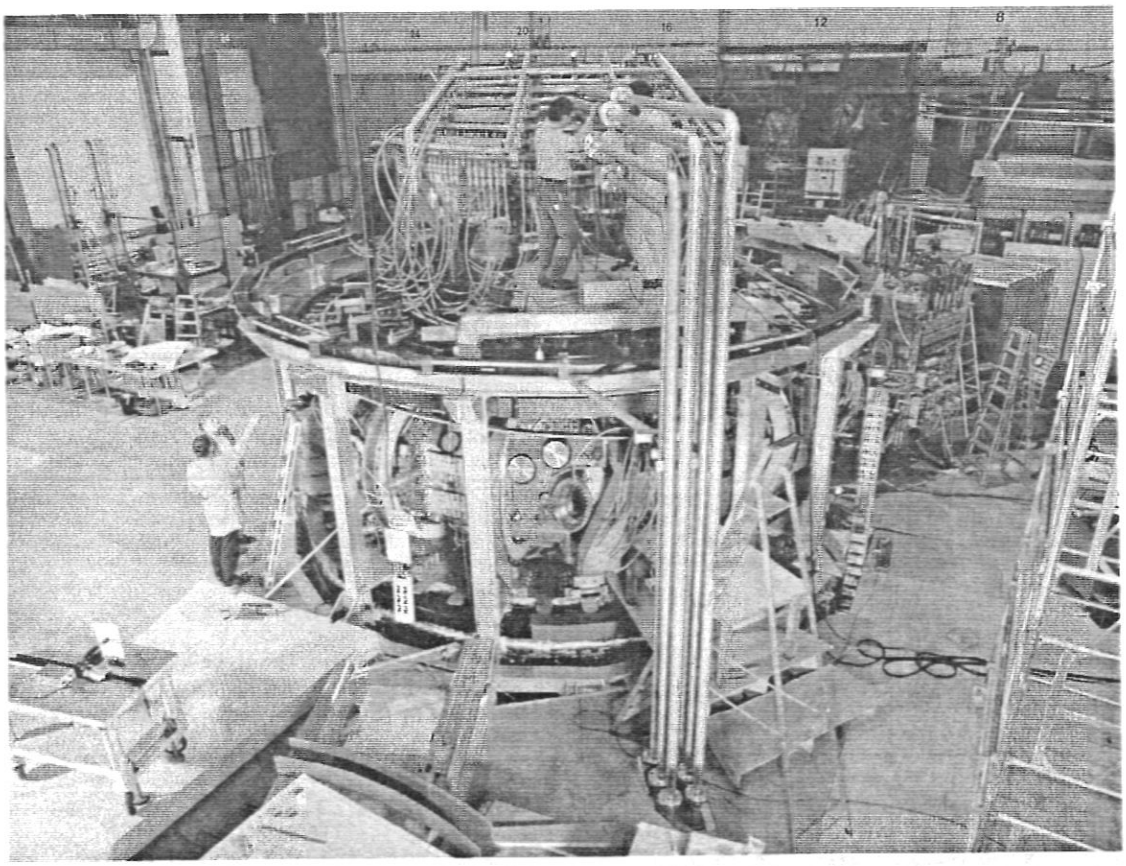

Fig. 16. The assembled W VII-AS system.

of up to 2 keV within the accessible density range $n < n_{cutoff}$: $n_{cutoff} = 3 \times 10^{19}$ m^{-3} for X mode at 1.25 T and $n_{cutoff} < 6 \times 10^{19}$ m^{-3} for O mode at 2.5 T. Measurements of the single-path absorption are in good agreement with ray-tracing calculations and show heating efficiencies close to 1. Nevertheless, the absorption mechanism needs further study to clarify the power deposition at the boundary and to define the role of suprathermal electrons.

Systematic studies of the confinement as a function of the magnetic configuration for the accessible range of $\beta \leq 0.5\%$ at 1.25 T showed behavior similar to that observed on W VII-A: Deterioration of the confinement is associated with the existence of low-order resonant surfaces in the confinement region. Control of the boundary value of the rotational transform far from resonances and sufficiently low shear are necessary for optimum confinement. During discharges with long pulse duration (>200 ms), a bootstrap current, which is strongly dependent on the temperature profiles and adds to the rotational transform of the vacuum field, becomes stationary at values of up to 3 kA. Control of the net current for stationary conditions with good confinement was successfully achieved by two different methods: an induced voltage by using the OH transformer and ECH current drive. Even fine tuning of the current density profile by local ECH current drive seems possible and may be necessary to approach higher beta.

The theoretical values of the neoclassical bootstrap current, calculated by means of the Drift Kinetic Equation Solver (DKES) code[12] on the basis of the measured density and temperature profiles, were roughly consistent with the experimental observations in W VII-AS. The modification of the magnetic configuration by the bootstrap current is especially large for low field and high-temperature gradients.

Under conditions of optimal confinement, which were established at particular values of the rotational transform close to $\frac{1}{3}$ and $\frac{1}{2}$ by current control, the energy balance was evaluated on the basis of measured density and temperature profiles. For almost all

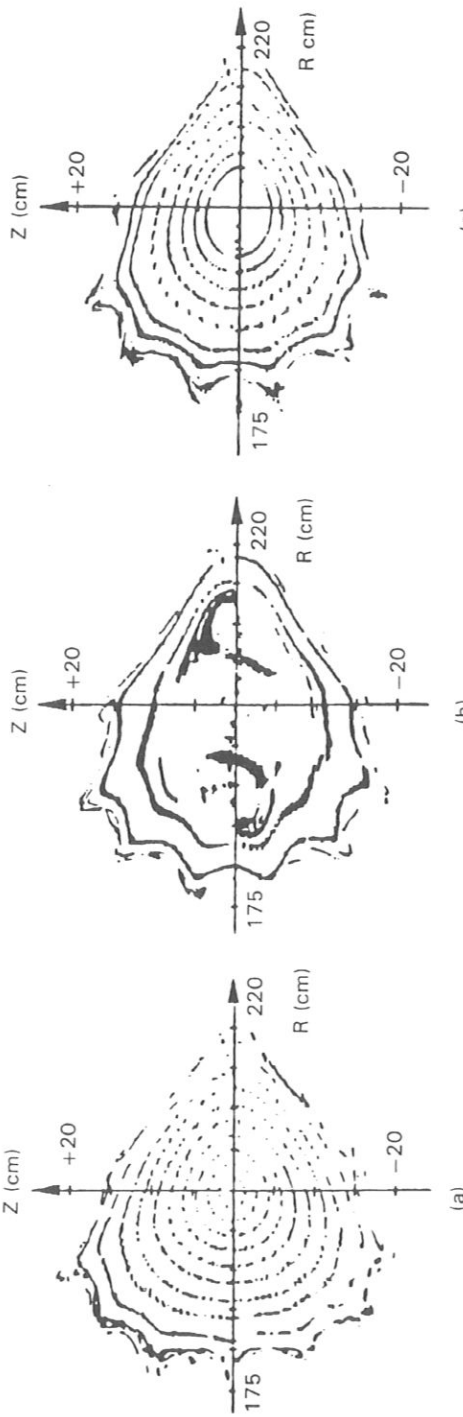

Fig. 17. Magnetic surfaces of W VII-AS for rotational transform $\iota \approx \frac{1}{2}$, measured for various values of the current ratio I_{tor} (toroidal field)/I_{mod} (modular field): (a) $\iota = 0.468$, (b) $\iota = 0.50$, and (c) $\iota = 0.51$.

discharges with different heating powers, the experimental values of the electron heat conductivity at the radius $a/2$ were in the range of 0.7 to 2 m^2/s. A slight increase is observed toward the center, but a strong increase is seen at the boundary. In particular, significant discrepancies in relation to the theoretical predictions of the DKES code occur at the boundary, and additional losses have to be assumed in the boundary region. Estimates of the particle confinement based on H_α measurements and DEGAS code simulations indicate, for some particular discharges, consistency with neoclassical predictions for the particle flux in the plasma gradient region and anomalous fluxes at the plasma edge ($D \sim \frac{1}{10}\ \chi_e$). Up to now, radiation and impurities do not seem to be very important in ECH discharges. Control of impurity sources and impurity transport will be studied during the next phase of experimentation and may become problematic with full use of the installed heating power on W VII-AS at higher densities.

ACKNOWLEDGMENTS

The authors thank the W VII-AS crew (technicians, engineers, experimentalists, and theoreticians) for the work done during the construction and operation of the experiment.

REFERENCES

1. B. A. CARRERAS, G. GRIEGER, J. H. HARRIS, J. L. JOHNSON, J. F. LYON et al., "Progress in Stellarator/Heliotron Research: 1981–1986," *Nucl. Fusion*, **28**, 1613 (1988).

2. U. BROSSMANN, W. DOMMASCHK, F. HERRNEGGER, G. GRIEGER, F. RAU, H. RENNER, H. RINGLER, J. SAPPER, A. SCHLÜTER, and H. WOBIG, "Concept of an Advanced Stellarator," *Proc. 9th Int. Conf. Plasma Physics and Controlled Nuclear Fusion Research*, Baltimore, Maryland, September 1–8, 1982, Vol. 3, p. 141, International Atomic Energy Agency (1983).

3. J. SAPPER, R. MATHIS, and I. SCHOENEWOLF, "Engineering Problems of Wendelstein W VII-AS," *Trans. 8th Int. Conf. Structural Mechanics in Reactor Technology*, Amsterdam, Netherlands, 1985, p. 15, Balkema, Boston.

4. J. NÜHRENBERG and R. ZILLE, "Stable Stellarators with Medium β and Aspect Ratio," *Phys. Lett.*, **114A**, 129 (1986).

5. W. KASPAREK, H. KUMRIC, G. A. MÜLLER, P. G. SCHÜLLER, M. THUMM, and V. ERCKMANN, "Microwave Technology and Tests of the 70 GHz/1 MW Long

Pulse ECRH-System on W VII-AS," *Proc. 15th Symp. Fusion Technology*, Utrecht, Netherlands, September 19–23, 1988, p. 490, Pergamon Press.

6. G. G. LISTER, F. P. PENNINGSFELD, W. OTT, and E. SPETH, "Neutral Beam Injection Studies for W VII-AS Using the 3-D Computer Code FAFNER," *Proc. 11th European Conf. Controlled Fusion and Plasma Physics*, Aachen, FRG, June 8–10, 1983, Vol. II, p. 323, European Physical Society.

7. J. H. FEIST, K. FREUDENBERGER, J. KOLOS, P. MIKOLAJCZAK, W. OTT, P. J. SCHNEIDER, E. SPETH, and G. WULFF, "Long Pulse Injector Design for ASDEX and Wendelstein VII-AS," *Proc. 4th Int. Symp. Heating in Toroidal Plasmas*, Rome, Italy, March 21–28, 1984, p. 1051.

8. F. WESNER, J. M. NOTERDAEME, J. BÄUMLER, W. BECKER, F. BRAUN, R. FRITSCH, P. GRIGULL, F. HOFMEISTER, A. B. MURPHY, and H. WEDLER, "The ICRH Technical System for Wendelstein VII-AS," *Proc. 15th Symp. Fusion Technology*, Utrecht, Netherlands, September 19–23, 1988, p. 475, Pergamon Press.

9. U. BROSSMANN, F. KERL, W. MELCHIOR, S. MUKHERJEE, J. SAPPER, and B. SOMBACH, "Modular Mechanical Design of the Advanced Stellarator Wendelstein W VII AS," *Proc. 12th Symp. Fusion Technology*, Jülich, FRG, September 13–17, 1982, Vol. 2, p. 915, Pergamon Press, Oxford (1983).

10. U. BROSSMANN, F. KERL, S. MUKHERJEE, J. SAPPER, and B. SOMBACH, "Modular Design of the Advanced Stellarator W VII AS—Engineering Details," *Proc. 10th Symp. Fusion Engineering*, Philadelphia, Pennsylvania, December 5–9, 1983, p. 1569, Institute of Electrical and Electronic Engineers.

11. R. MATHIS and J. SAPPER, "Application of Finite-Element Methods to the Design of a Torus-Shaped Magnetic Confinement System for Fusion Experiments," *Proc. Int. Conf. Computational Techniques and Applications*, Sydney, Australia, 1987, p. 461, North-Holland Publishing Company, Amsterdam (1988).

12. S. P. HIRSHMAN, K. C. SHAING, W. I. van RIJ, C. O. BEASLEY, Jr., and E. C. CRUME, Jr., "Plasma Transport Coefficients for Nonsymmetric Toroidal Confinement," *Phys. Fluids*, **29**, 2951 (1986).

ELECTRON CYCLOTRON RESONANCE HEATING TRANSMISSION LINE AND LAUNCHING SYSTEM FOR THE WENDELSTEIN VII-AS STELLARATOR

STELLARATOR SYSTEMS

KEYWORDS: *electron cyclotron resonance heating, stellarator, microwaves*

V. ERCKMANN and THE WENDELSTEIN VII-AS TEAM
Max-Planck-Institut für Plasmaphysik, Association Euratom
8046 Garching, Federal Republic Of Germany

W. KASPAREK, G. A. MÜLLER, P. G. SCHÜLLER, and M. THUMM *Universität Stuttgart, Institut für Plasmaforschung*
7000 Stuttgart 80, Federal Republic of Germany

Received April 10, 1989
Accepted for Publication June 29, 1989

A 70-GHz electron cyclotron resonance heating (ECRH) system (4 × 0.2 MW for 3 s and 0.2 MW for 0.1 s) has been installed on the Wendelstein VII-AS stellarator for plasma buildup, heating, and current drive. Five commercially available gyrotrons, each delivering 0.2-MW radio-frequency (rf) output power, serve as the ECRH sources. The microwaves are transmitted to the stellarator by conventional oversized waveguides, and they convert the gyrotron output mode to a linearly polarized Gaussian free-space mode, which is launched to the plasma at arbitrary poloidal and toroidal angles by a quasi-optical launcher. The transmission line and launching system as well as the related rf diagnostics are discussed in detail. Experimental results on heating and current drive obtained with various kinds of microwave launching are presented.

I. INTRODUCTION

Radio-frequency (rf) heating of magnetically confined fusion plasmas in the electron cyclotron frequency range (20 to 110 GHz) with rf power in the megawatt range has become a well-established heating method for both stellarators and tokamaks.[1-6] The attractiveness of electron cyclotron resonance heating (ECRH) is based on physical as well as technical arguments.

From the physical point of view, the narrow power deposition profiles together with the almost complete rf absorption at sufficiently high electron temperatures have both been well proven theoretically as well as experimentally. This offers the experimental possibility of electron temperature profile shaping and allows ECRH application as a diagnostic tool for electron heat transport studies.[7] The proper shaping of electron temperature profiles may become a crucial condition for achieving H-mode transition in tokamaks and for minimizing heat transport losses in both stellarators and tokamaks. Increasing attention is also given to the current drive capability of ECRH with respect to compensation of small net plasma currents (i.e., bootstrap current) in stellarators or to steady-state operation of tokamaks.

From the technical point of view, a major advantage of ECRH compared with other rf heating methods is that no launching structure close to the plasma surface is necessary to excite plasma waves. Therefore, no impurity problem is introduced by antenna material in contact with the plasma boundary layer. Proper launching of the electron cyclotron waves is obtained simply by free-space irradiation of the plasma. The port size per unit power can be kept comparatively small due to the high power density of the rf beam (up to 100 MW/m^2). This feature may become increasingly important for the next generation of machines, where tritium contamination and blanket requirements introduce additional technical and safety constraints on the application of different heating methods.

There is, however, still a lack of continuous wave rf sources at higher frequencies (100 to 200 GHz), which would increase the density limit (the cutoff density) toward the 10^{20} m^{-3} range, and higher rf power per unit (0.5 to 1 MW/unit), which would allow building the multimegawatt heating systems that are required for the next generation of fusion machines.

A 1-MW ECRH system at 70 GHz (corresponding

to a resonant magnetic field of 2.5 T for first harmonic heating or 1.25 T for second harmonic heating) has been installed on the Wendelstein VII-AS stellarator (W VII-AS). A highly flexible launcher allows a wide variety of ECRH investigations such as on- and off-axis heating at ordinary and extraordinary wave polarization as well as current drive under arbitrary angles of incidence of the rf beam. A technical description of the transmission line and launcher as well as the related diagnostics is given in Sec. II together with an outline of the transmission line that is under construction for a planned 140-GHz ECRH system. Some illustrative experimental results obtained during the first period of plasma operation are given in Sec. III.

II. rf TRANSMISSION LINE AND LAUNCHER

II.A. 70-GHz Transmission Line

The rf power is generated by five commercially available Varian gyrotrons, each delivering 200-kW output power at 70 GHz in the circular symmetric TE_{02} mode. Four out of the five tubes have continuous wave capability and are located ~50 m from the stellarator in a separate hall. The microwaves are transmitted to the stellarator by separate circular oversized waveguides and are finally combined at one poloidal plane by a quasi-optical launcher. A schematic of the complete transmission line is given in Fig. 1.

The TE_{02} gyrotron output mode is converted to the low-loss TE_{01} mode after a corrugated 90-deg bend with a curvature that is optimized for preserving the TE_{02} mode. The TE_{01} mode is then used for long distance transmission in a 63.5-mm-i.d. circular waveguide to minimize wave damping. After a second 90-deg bend, which is optimized for TE_{01} mode propagation, this mode is first converted to the almost linearly polarized TE_{11} mode and finally to the HE_{11} hybrid mode, which has an almost perfect linear polarization (98%) and couples well to the fundamental Gaussian free-space mode if radiated from an open-ended waveguide. All mode converters and bends are built at a reduced diameter of 27.8-mm i.d. to obtain reasonably sized elements (typically 1 to 2 m long) and high mode purity. Therefore, the waveguides have to be tapered down and up at each bend and mode converter by means of mode-preserving nonlinear waveguide diameter tapers. The final HE_{11} section of the transmission line consists of a circumferentially corrugated circular waveguide, which is the normal-mode waveguide for such hybrid modes. The HE_{11} mode is transmitted through a commercially available double-disk sapphire window with FC-75 face cooling, mounted in a 63.5-mm-i.d. corrugated waveguide. This window serves to separate the stellarator vacuum from the transmission line, which is operated under atmospheric pressure. The HE_{11} mode is finally radiated from an open-ended circular corrugated waveguide section inside the vacuum chamber.

II.B. Launcher and rf Diagnostics

Whereas the transmission to the stellarator and the conversion of the gyrotron output mode to the desired linearly polarized wave is performed with conventional oversized waveguide techniques, the beam launching is achieved with a quasi-optical mirror system inside the vacuum vessel.

As seen from Fig. 2, each rf beam hits a movable focusing mirror and can be directed into the plasma at arbitrary poloidal and toroidal angles with respect to the orientation of the stellarator magnetic field. Figure 3 shows a pair of launching mirrors during installation in the torus port.

The curvature of the mirror surface is chosen to position the beam waist with plane phase fronts in the plasma center (normal incidence). An additional segmented graphite mirror is installed at the inner torus wall opposite the four launching mirrors, which reflects the nonabsorbed fraction of the incident waves back to the plasma in a well-defined polarization.

One section of this mirror rotates the incident wave polarization by 90 deg. By illuminating this mirror section, an incident ordinary mode is reflected back toward the plasma as an extraordinary wave and vice versa. The central part of the mirror preserves the polarization of the incident wave. The mirror during installation on the vacuum vessel wall is shown in Fig. 4. An array of 38 single-mode waveguides is embedded in the central section, which allows a direct measurement of the rf beam quality with respect to beam divergence and cross polarization (with no plasma), as well as a measurement of the single-pass absorption and beam deflection in the presence of a plasma. The contour plot of one rf beam shown in Fig. 5 is obtained by sweeping the beam across one of the pickup waveguides. The beam was found to be very close to the calculated Gaussian radiation pattern; the cross polarization is typically $<3\%$.

II.C. Mode Analysis and Power Measurement

The purity of the different modes propagating in the waveguides is measured by inserting a wavenumber spectrometer[8] in the various waveguide sections of each line. This k spectrometer allows *in situ* high-power measurement of the full TE- and TM-mode spectra present in the waveguide and, consequently, optimization of the whole transmission system with respect to the different mode mixtures emitted by the individual gyrotrons. In cases where the gyrotrons emitted an unacceptably high number of unwanted modes (mainly TE_{01}, up to 15%), the transmission lines were matched to the particular TE_{01}/TE_{02} mode mixture by specially designed mode converters capable of converting this mixture to a pure TE_{01} mode. Typical TE-mode spectra measured at two positions in the TE_{01} section of the transmission line are shown in Fig. 6; the purity of the desired mode is typically 97%.

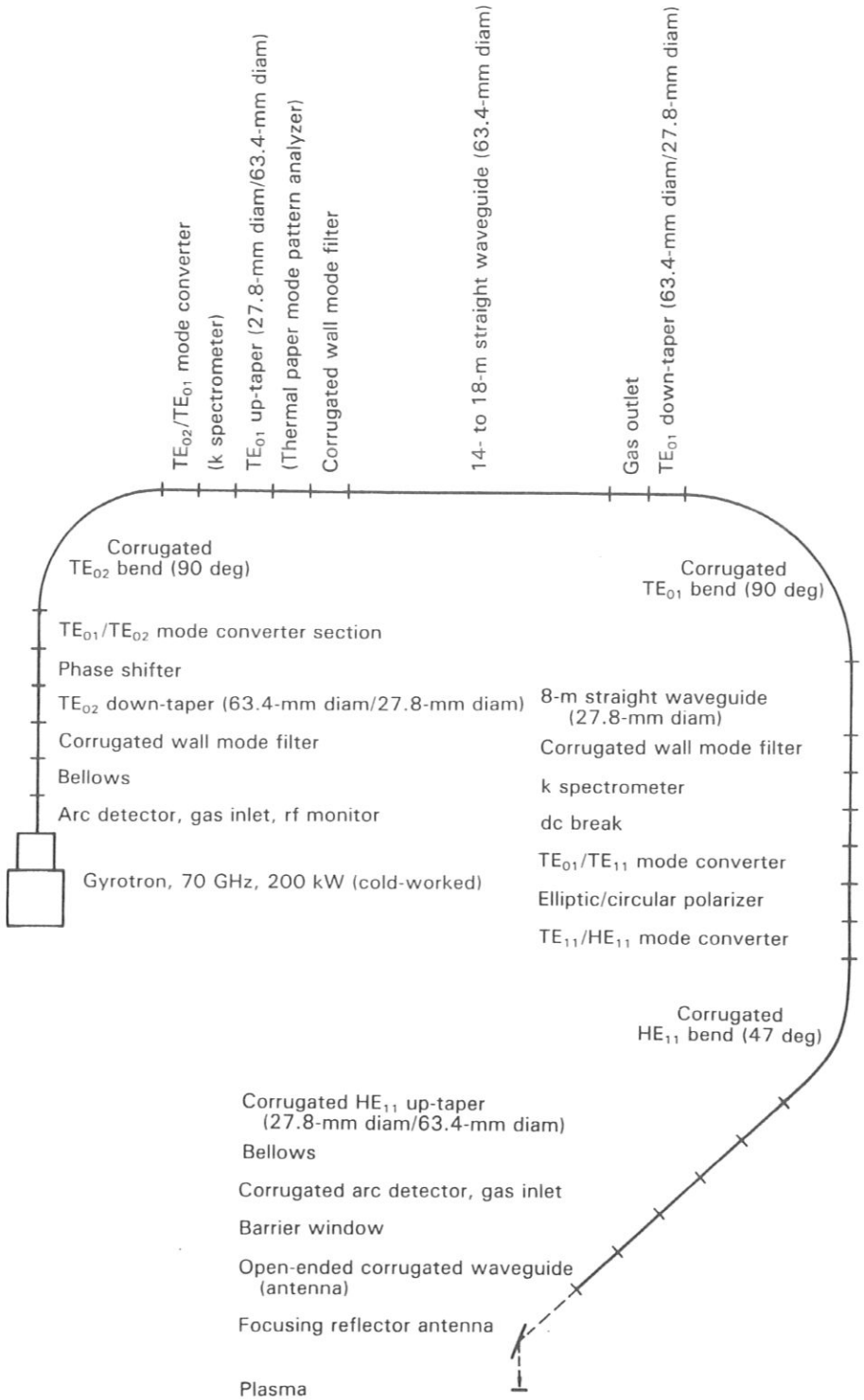

Fig. 1. Schematic of a 70-GHz transmission line in operation at W VII-AS.

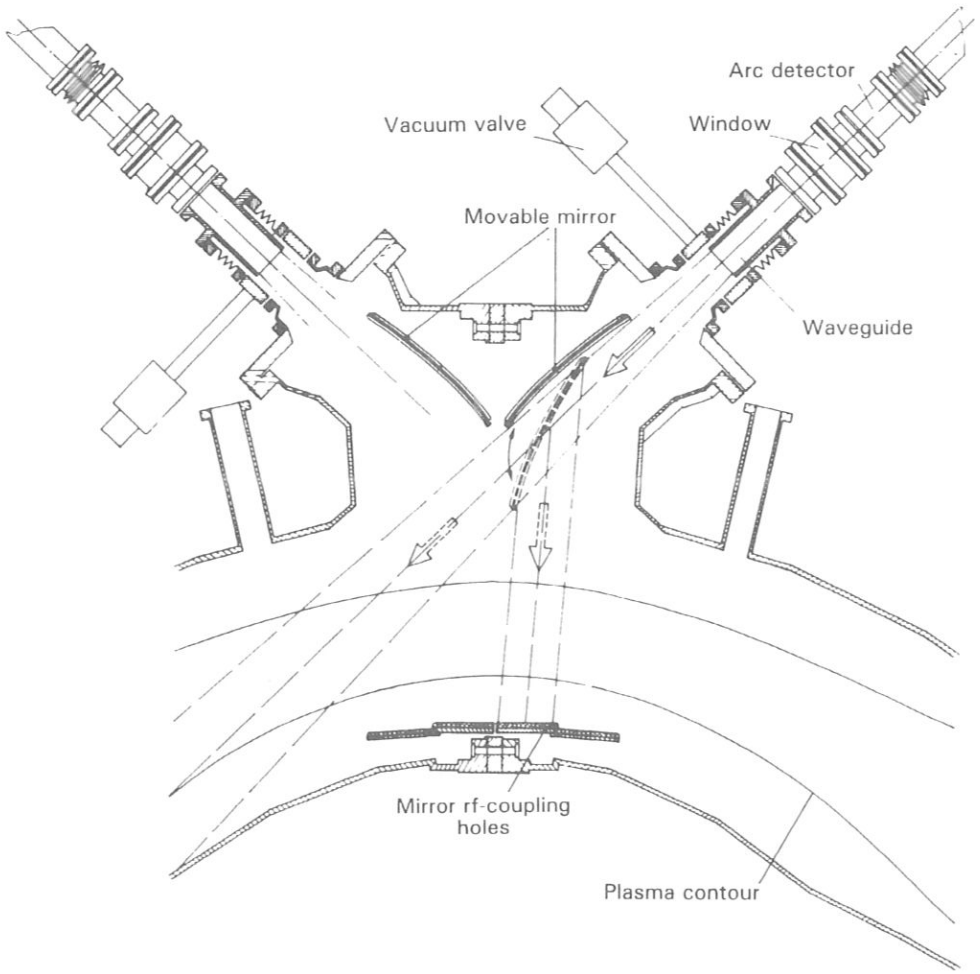

Fig. 2. Horizontal cut through the W VII-AS vacuum vessel slightly above the torus midplane. Two rf transmission lines are fed at each tangential port.

Since the mode composition at the torus end of the transmission line was known, the *k* spectrometer signal for the dominant TE_{01} mode was calibrated with a matched calorimetric load and then used as a direct *in situ* power measurement.

A relative calibration of the sensitivity of the waveguide array at the high-field-side mirror was achieved by sweeping one of the rf beams across the array and adjusting the attenuation of each channel to the level of one arbitrarily chosen reference channel.

II.D. 140-GHz Transmission Line

A pilot ECRH experiment at 140 GHz (0.2 MW, 0.1 s) is under preparation that will operate with the nominal W VII-AS magnetic field at second harmonic resonance and can be run together with the 70-GHz system described in Sec. II.A. At 140 GHz, the cutoff density for plasma operation is shifted to twice the value at 70 GHz (1.2×10^{20} m^{-3}).

In contrast to the 70-GHz transmission line, the 140-GHz transmission line will be built as a pure quasi-optical open system. Such quasi-optical systems theoretically provide the high power capability required for future rf sources in the power range from 0.5 to 1 MW per gyrotron and are well adapted to the 2-mm wavelength of the microwaves. This short wavelength would require enlarging the various mode converters necessary for a conventional oversized waveguide system to an intolerable size because the waveguide diameter can no longer be reduced at the given high power density.

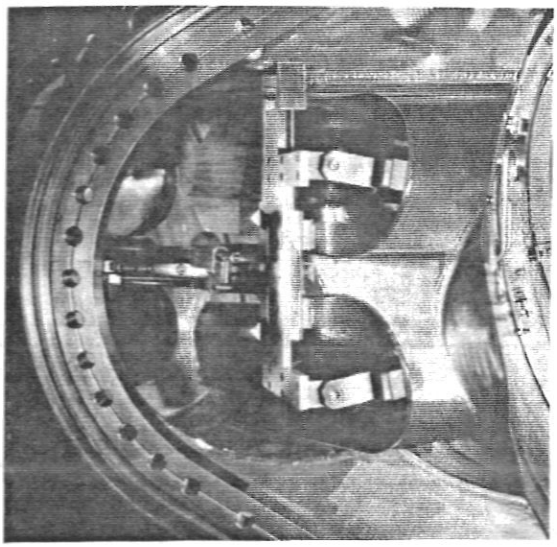

Fig. 3. View from inside the vacuum chamber toward the rear side of a pair of launching mirrors.

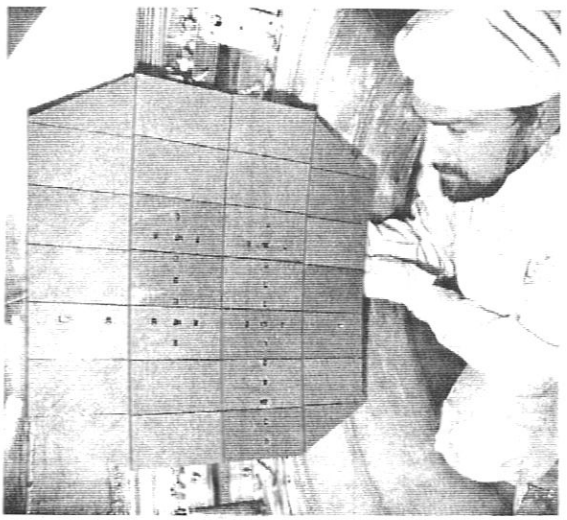

Fig. 4. Front view of the mirror mounted at the inner vessel wall. The diagnostic single-mode waveguide array is embedded in the graphite tiles of the mirror.

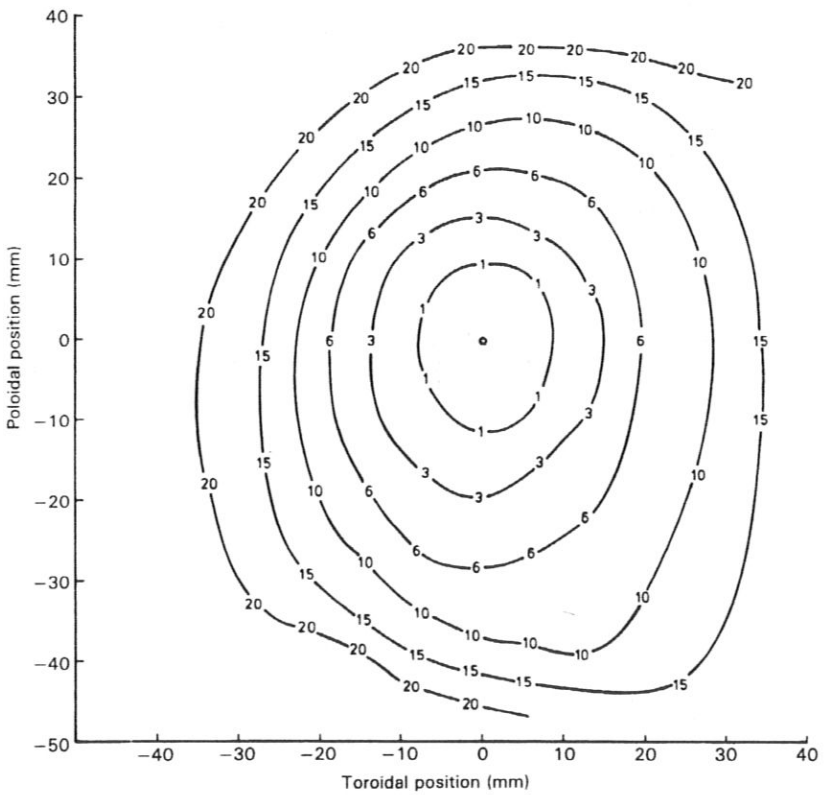

Fig. 5. Contours of constant power (in decibels) of an rf beam incident on the inner mirror.

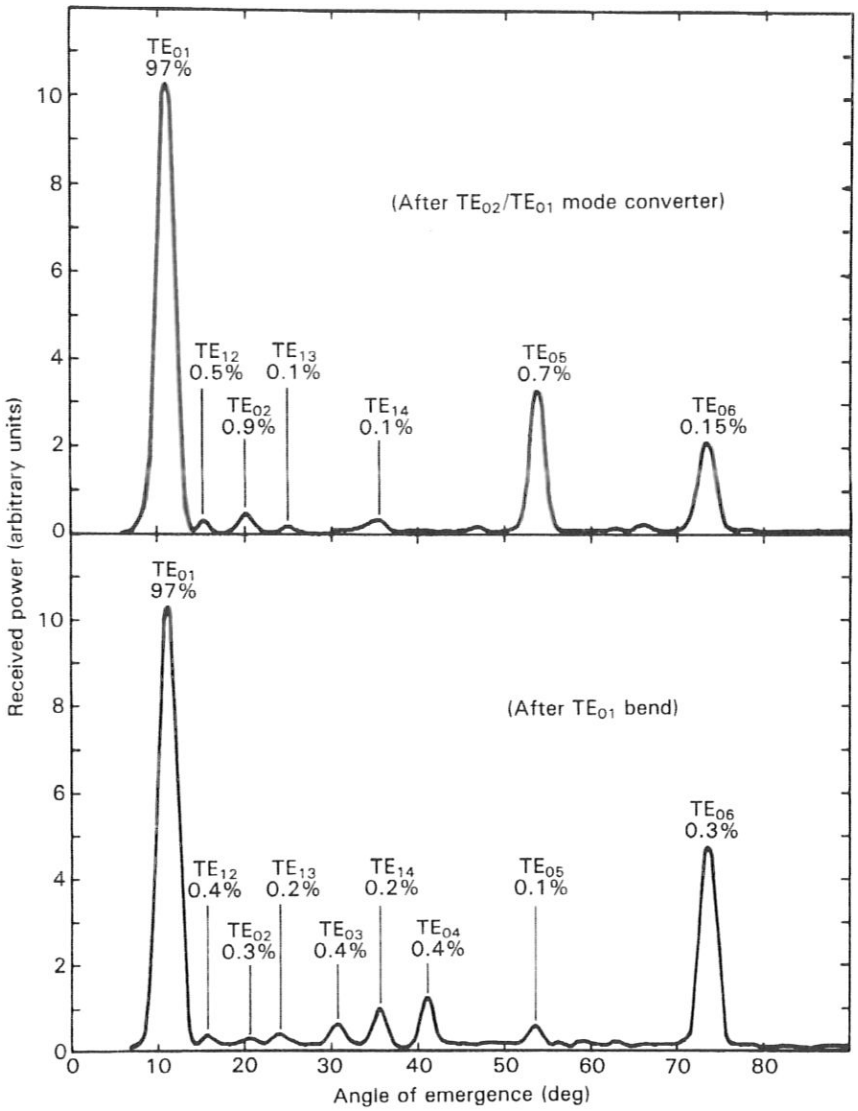

Fig. 6. TE mode spectra propagating at different positions along the TE_{01} section of the transmission line: (top) gyrotron end and (bottom) torus end after a 35-m waveguide run. The spectra are obtained at full-power operation.

In such a beam waveguide, the microwaves are guided from the rf source to the plasma by a proper arrangement of mirrors. The gyrotron output mode, which may be TE_{03} or, more likely, a high-order whispering gallery mode, for example a $TE_{12,2}$ mode, will be transformed to a circular symmetric, linearly polarized Gaussian free-space mode by a Vlasov converter[9] in combination with properly shaped imaging mirrors. The efficiency of such Vlasov converters is not high enough at present (typically 80%) and intense investigations are under way to improve the efficiency.

The Gaussian beam generated by the Vlasov converter will be fed to a beam waveguide consisting of at least three ellipsoidal reflectors that guide the beam toward the stellarator vacuum vessel and simultaneously perform proper focusing at the plasma center in the extraordinary mode. An in-vessel launcher will be used

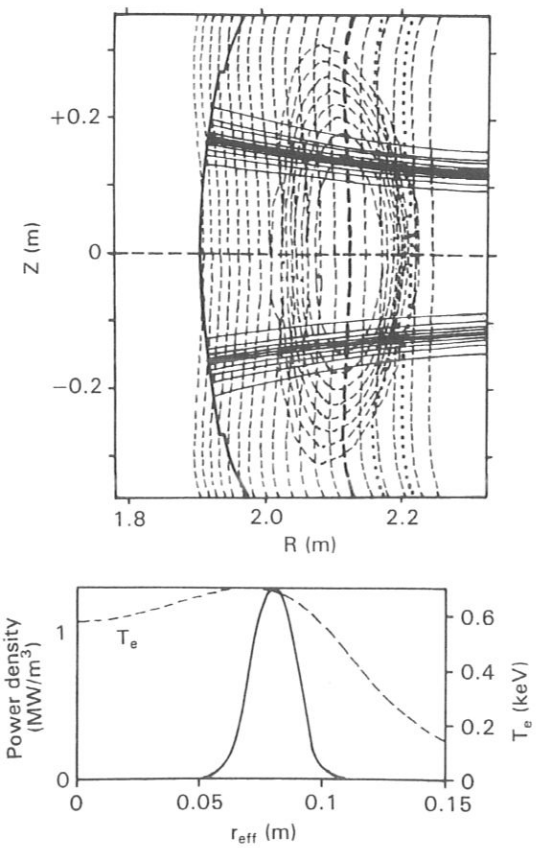

Fig. 7. Ray tracing calculations for heating with two rf beams directed ±130 mm vertically off axis. The horizontal lines are the rays. The resonant magnetic field layer (heavy dashed line) is centered on axis. The almost vertical dashed lines indicate constant $|B|$ contours intersecting the elliptically shaped flux surface contours. The power deposition profile (solid curve) and the measured electron temperature T_e (dashed curve) are shown as a function of the effective minor radius in the bottom figure.

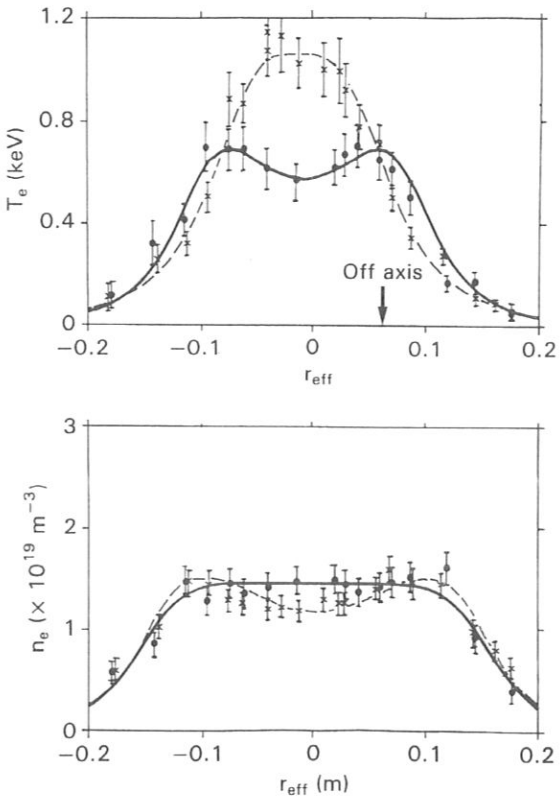

Fig. 8. Electron temperature and density profiles measured by Thomson scattering for off-axis (solid curves) and on-axis (dashed curves) plasma heating at an rf input power of 0.35 MW ($B_0 = 1.27$ T, second harmonic X mode). The off-axis case corresponds to the ray tracing calculations shown in Fig. 7.

similar to the one described in Sec. II.B to give sufficient flexibility for heating and current drive.

III. EXPERIMENTAL RESULTS

Some experimental results obtained during the first ECRH experimental campaign on W VII-AS with different kinds of wave launching are discussed in this section. The intention is to illustrate the usefulness of the flexibility of the electron cyclotron wave launcher rather than to provide a detailed discussion of the ECRH experiments, which would be beyond the scope of this paper.

III.A. On- and Off-Axis Heating

Off-axis ECRH and its effect on the electron temperature profile were already shown on the Wendelstein VII-A stellarator[10] by tuning the magnetic field and consequently shifting the electron cyclotron resonance layer radially in and out. Off-axis heating can also be achieved by adjusting the narrow rf beams geometrically off axis. As seen from Fig. 7, the ray tracing calculations, which take into account the complex stellarator magnetic field topology as well as the launching geometry in three dimensions, predict a power deposition profile that is ~2.5 cm wide and, for the given launching angles, ~8 cm off axis. This result is an important quantity for heat transport analysis and is obtained on the basis of measured profiles of electron density, which affects the ray bending and wave absorption, and electron temperature, which plays a key role in wave absorption. The measured

profiles of T_e and n_e are shown in Fig. 8 for on- and off-axis heating at the second harmonic X mode (perpendicular launch) with a heating power of ~0.4 MW. A clear dependence of the electron temperature and density profiles on the position of the rf power deposition is observed.

III.B. Electron Cyclotron Current Drive

Small net toroidal currents in the 1- to 4-kA range were measured on W VII-AS. The bootstrap current is a possible candidate for such net currents. Generally, net currents change the magnetic field configuration of the stellarator in an uncontrolled way. It is important for almost shearless magnetic field configurations such as W VII-AS to counteract such net currents to avoid deterioration of the global confinement by low-order rational surfaces appearing in the confinement region of the plasma and giving rise to magnetic island formation.[11]

The net plasma current can be kept close to zero by application of a proper toroidal loop voltage (ohmic transformer); however, future stellarators will not have an ohmic transformer. Thus, electron cyclotron current drive may be a powerful tool for net current control. In Fig. 9, an example is given where 200 kW of rf power is launched perpendicularly to the magnetic field, thus giving no electron cyclotron current drive contribution. The observed ~1-kA net current is attributed to the bootstrap current. Further increase in the current was suppressed while the stored plasma energy increased with application of a second rf beam later in the discharge with an angle of incidence of 14 deg with respect to the normal and in the opposite direction to the net current. If a second rf beam is launched in the perpendicular direction, the plasma current almost doubles compared to the application of only one rf beam. This means that the observed net current is counteracted by electron cyclotron current drive due to

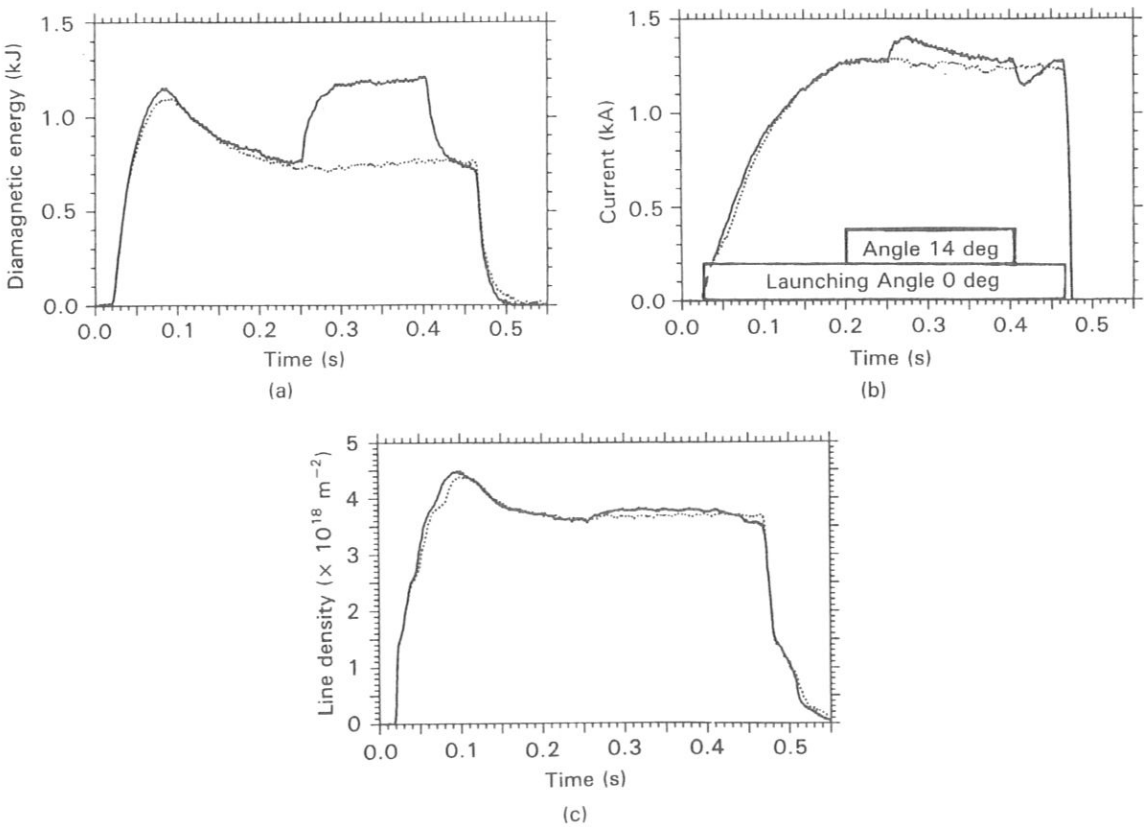

Fig. 9. (a) Total stored plasma energy from diamagnetic loop, (b) net plasma current, and (c) line integral of the density for ECRH-sustained discharges. The parameters obtained with perpendicular launch of one rf beam (dotted curves) are compared with an experiment, where a second beam is added later in the discharge at a 14-deg launch angle in the countercurrent direction (solid curves).

an appropriate choice of the angle of incidence of the rf beam and the applied rf power. This result was confirmed by numerous experiments where the beams were launched in both the co- and counterdirection with arbitrary angles of incidence and with different power levels.

III.C. Electron Cyclotron Wave Absorption

As pointed out in Sec. II.B, the waveguide array opposite the launching mirrors can be used to determine the single-pass absorption of the incident waves by a simple measurement of the fraction of the power hitting the inner wall mirror with and without plasma. An example is shown in Fig. 10a where an electron cyclotron wave in ordinary-mode polarization was launched. The three spatial channels across each rf beam in both the horizontal and vertical directions are fitted by a Gaussian function, which is justified by the calibration measurements shown in Fig. 10b with more data points. The total single-pass rf absorption derived by this measurement at the discharge time where the profile measurements were taken is 75 ± 5% for this particular temperature and density profile and was found to be in excellent agreement with the ray tracing calculation based on the measured profiles (70%).

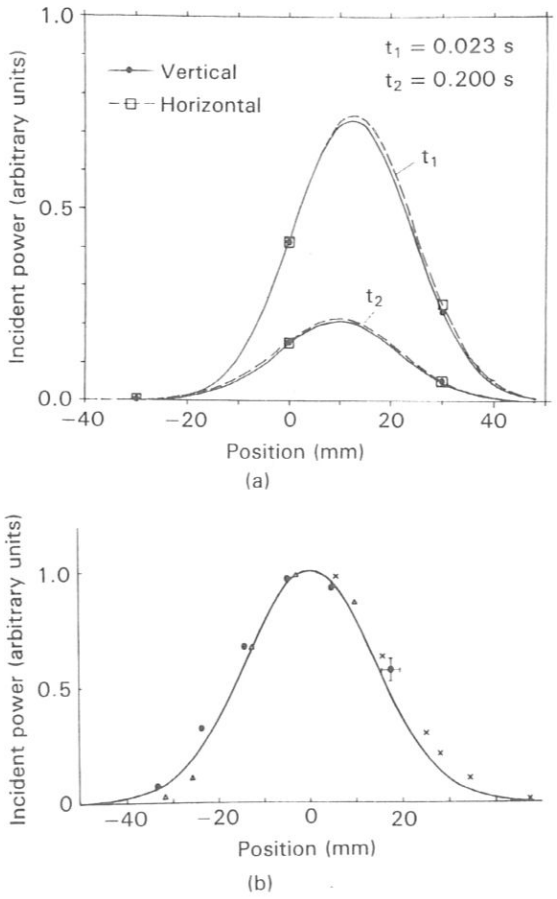

Fig. 10. (a) Measurement of the power incident on the inner wall mirror without (time t_1) and with plasma (time t_2) in both the vertical (solid line) and horizontal (dashed line) directions (the difference gives the single-pass absorption) and (b) comparison of the measured rf beam pattern at high power with the theoretical Gaussian beam pattern (solid curve).

IV. CONCLUSIONS

The combination of conventional oversized waveguide transmission lines for conversion of the gyrotron output mode into a linearly polarized wave and quasi-optical launchers was successfully operated under full-power conditions with a high transmission efficiency and mode purity. The quasi-optical microwave launcher allows rf power deposition at arbitrary positions of the plasma column by properly directing the narrow rf beams. Electron cyclotron current drive experiments were successfully performed by irradiation of the plasma at oblique angles. It was shown experimentally that the specially designed set of rf diagnostics inside the vacuum vessel and the transmission lines allows the *in situ* measurement of the beam quality. A direct measurement of the microwave single-pass absorption in the plasma was obtained.

ACKNOWLEDGMENTS

The following are members of the W VII-AS Team who also contributed to this paper: E. Anabitarte,[a] E. Ascasibar,[a] S. Besshou,[b] R. Brakel, R. Burhenn, G. Cattanei, A. Dodhy, D. Dorst, A. Elsner, K. Engelhardt, D. Evans, U. Gasparino, G. Grieger, P. Grigull, H. Hacker, J. H. Hartfuss, H. Jäckel, R. Jaenicke, S. Jiang,[c] J. Junker, M. Kick, H. Kroiss, G. Kuehner, I. Lakicevic, H. Maassberg, C. Mahn, R. Martín,[a] H. Münch, A. Navarro,[a] M. Ochando,[a] W. Ohlendorf, M. Pterov,[d] F. Rau, H. Renner, H. Ringler, J. Saffert, J. Sanchez,[a] J. Sapper, A. V. Saposhnikov,[e] F. Sardei, I. S. Sbitnikova,[c] I. Schoenewolf, F. Tabares,[a] M. Tutter, A. Weller, H. Wobig, E. Würsching, and M. Zippe.

The authors wish to thank U. Weber, J. Hofner, A.W. Hagemann, and J. Eischer for their help in getting the whole rf system running.

[a]From CIEMAT, Madrid, Spain.
[b]From Kyoto University, Japan.
[c]From Southwestern Institute of Physics, Leshan, China.
[d]From Ioffe Institute, Leningrad, USSR.
[e]From General Physics Institute, Moscow, USSR.

We wish to express our gratitude to the mechanical workshops at Max-Planck-Institut für Plasmaphysik and the Institut für Plasmaforschung at the Universität Stuttgart for their outstanding work in the manufacture and installation of the complex structures of the transmission lines and the in-vessel components.

REFERENCES

1. V. ALIKAEV et al., "Power Deposition Profile Effect on the ECH Efficiency in T-10," *Plasma Phys. Contr. Fusion*, **29**, 1285 (1987) and **30**, 381 (1988).

2. J. LOHR et al., "Observation of H-Mode Confinement in the DIII-D Tokamak with Electron Cyclotron Heating," *Phys. Rev. Lett.*, **60**, 2630 (1988).

3. V. ERCKMANN et al., "Electron Cyclotron Resonance Heating in the Wendelstein VII-A Stellarator," *Plasma Phys. Contr. Fusion*, **28**, 1277 (1986).

4. H. ZUSHI et al., "Heating and Confinement Studies of Electron Cyclotron Resonance Heated Plasmas in Heliotron E," *Nucl. Fusion*, **28**, 1801 (1988).

5. S. OKAMURA et al., "ECRH and ICRH Heating Experiments in CHS," *Proc. 16th European Conf. Controlled Fusion and Plasma Physics*, Venice, Italy, March 13–17, 1989, Vol. 13B, Part II, p. 571.

6. M. MURAKAMI et al., "Second Stability Studies in the ATF Torsatron," *Proc. 16th European Conf. Controlled Fusion and Plasma Physics*, Venice, Italy, March 13–17, 1989, Vol. 13B, Part II, p. 575.

7. H. J. HARTFUSS et al., "Evaluation of the Local Heat Conductivity Coefficient by Power-Modulated Electron Cyclotron Heating in the Wendelstein WVII-A Stellarator," *Nucl. Fusion*, **26**, 678 (1986).

8. W. KASPAREK and G. A. MUELLER, "The Wavenumber Spectrometer—An Alternative to the Directional Coupler for Multimode Analysis in Oversized Waveguides," *Int. J. Electronics*, **64**, 5 (1988).

9. H. J. BARKLEY, "The Direct Conversion to a Gaussian Beam from TE_{03} Gyrotron Modes," *Proc. 13th Int. Conf. Infrared and Millimeter Waves*, Honolulu, Hawaii, 1988, p. 467.

10. V. ERCKMANN et al., "Electron Cyclotron Resonance Heating Experiments in the Wendelstein VII-A Stellarator," *Fusion Technol.*, **7**, 275 (1985).

11. H. RENNER et al., "Initial Operation of the Wendelstein 7 AS Advanced Stellarator," *Proc. 16th European Conf. Controlled Fusion and Plasma Physics*, Venice, Italy, March 13–17, 1989.

PHYSICS AND ENGINEERING DESIGN FOR WENDELSTEIN VII-X

STELLARATOR SYSTEMS

KEYWORDS: *advanced stellarator, Helias, modular coils*

CRAIG BEIDLER, GÜNTER GRIEGER, FRANZ HERRNEGGER, EWALD HARMEYER, JOHANN KISSLINGER, WOLF LOTZ, HENNING MAASSBERG, PETER MERKEL, JÜRGEN NÜHRENBERG, FRITZ RAU, JÖRG SAPPER, FRANCESCO SARDEI, RUBEN SCARDOVELLI, ARNULF SCHLÜTER, and HORST WOBIG
Max-Planck-Institut für Plasmaphysik
IPP-EURATOM Association, D-8046 Garching bei München
Federal Republic of Germany

Received April 10, 1989
Accepted for Publication June 29, 1989

The future experiment Wendelstein VII-X (W VII-X) is being developed at the Max-Planck-Institut für Plasmaphysik. A Helical Advanced Stellarator (Helias) configuration has been chosen because of its confinement and stability properties. The goals of W VII-X are to continue the development of the modular stellarator, to demonstrate the reactor capability of this stellarator line, and to achieve quasi-steady-state operation in a temperature regime >5 keV. This temperature regime can be reached in W VII-X if neoclassical transport plus the anomalous transport found in W VII-A prevail. A heating power of 20 MW will be applied to reach the reactor-relevant parameter regime.

The magnetic field in W VII-X has five field periods. Other basic data are as follows: major radius $R_0 = 6.5$ m, magnetic induction $B_0 = 3$ T, stored magnetic energy $W \approx 0.88$ GJ, and average plasma radius $a = 0.65$ m. Superconducting coils are favored because of their steady-state field, but pulsed water-cooled copper coils are also being investigated.

Unlike planar circular magnetic field coils, which experience only a radially directed force, twisted coils are subject to a lateral force component as well. Studies of various superconducting coil systems for Helias configurations have shown that the magnitudes of these radial and lateral force components are comparable. Based on a support model, the mechanical stresses are calculated; all components of the stress tensor are of equal importance. Other studies being conducted are concerned with the many complex engineering aspects presented by the construction of nonplanar superconducting coils.

I. INTRODUCTION

Wendelstein VII-X (W VII-X) is a continuation of the advanced stellarator line, which has been developed at the Max-Planck-Institute für Plasmaphysik (IPP) and successfully inaugurated with the construction of Wendelstein VII-AS (W VII-AS). Wendelstein VII-X will go a step further than W VII-AS, planning to reach reactor-relevant parameter regimes and to demonstrate the reactor capability of modular stellarators. For this purpose, W VII-X has been chosen to be large enough to allow powerful heating and quasi-steady-state operation. The main goals of the W VII-X experiment are as follows:

1. to achieve quasi-steady-state operation in a reactor-relevant parameter regime with temperatures >5 keV and densities $>10^{20}$ m^{-3}
2. to demonstrate stable plasma equilibrium with $\langle\beta\rangle = 5\%$
3. to confine a plasma for a sufficiently long period of time, allowing extrapolation to reactor parameters
4. to control the plasma density and impurity content
5. to operate the magnetic field in steady state with a field generated by modular superconducting coils.

Wendelstein VII-X does not aim at ignition; therefore, deuterium-tritium reactions will not occur and provisions for handling radioactive materials need not be made. The temperature goal of 5 keV was chosen because in a reactor this temperature regime must be reached with auxiliary heating only, without the

assistance of the alpha-particle heating that becomes important at higher temperatures. The aim of a volume-average beta of $\langle\beta\rangle = 5\%$ results mainly from economic considerations; since fusion power output grows with $\langle\beta\rangle$, the limits of $\langle\beta\rangle$, set by plasma instabilities, must be pushed as high as possible and explored experimentally.

Confinement is also a critical issue facing stellarator reactors; even given the assumption of neoclassical losses, particle orbits and the magnetic configuration must be carefully optimized in order to reach ignition. Therefore, particular attention will be given to this topic in W VII-X.

Another important issue is steady-state operation, one of the principal advantages of stellarator reactors. In the W VII-X experiment, this means a pulse duration of 20 to 30 s, since all transient phenomena presumably have saturated and a steady state has been reached in this time. Such a state may be endangered by continuous impurity release from the wall and impurity accumulation in the plasma center; control of these effects and a careful examination of the underlying mechanisms are major goals of W VII-X.

The envisaged pulse duration of the plasma, the available space for coils, and relevance for future application in reactors has led to the decision to produce the magnetic field by modular superconducting coils. With a magnetic field of 3 T on axis and 6 T at the coils, it is possible to employ the existing technology of NbTi. Normal-conducting modular coils have been built already and are successfully in use on W VII-AS. Based on feasibility studies done by industry, it is believed that extending this technique to larger experiments and superconducting coils does not present insurmountable difficulties.

II. THE PRINCIPLES OF OPTIMIZATION

Since plasma confinement and stability depend mainly on the properties of the magnetic field (e.g., rotational transform, shear, magnetic well, and the structure of B on the magnetic surfaces), a careful optimization of the magnetic field and the modular coils is required to simultaneously achieve the following desirable properties:

1. High-quality magnetic surfaces: This implies a confinement region with good magnetic surfaces and an average aspect ratio $A = R_0/a \lesssim 10$. If low-order rational surfaces are avoided, field errors cause only small islands that are considered to be harmless. For this purpose, the shear must be small but finite. A typical value is $\delta\iota/\iota = 0.1$.

2. Good finite-β equilibrium properties: A small Shafranov shift and a small variation of the rotational transform with $\langle\beta\rangle$ for vanishing net toroidal current will yield a high equilibrium-$\langle\beta\rangle$ limit. This is possible when $\langle j_\parallel^2/j_\perp^2\rangle \leq 1$, which is primarily achieved by a suitable combination of helical curvature and elliptical flux surface cross section; see, for example, Refs. 1 and 2.

3. Good magnetohydrodynamic (MHD) stability properties: MHD stability in low-shear stellarators is mainly provided by a magnetic well. A vacuum field magnetic well of ~2% can be created by exploiting the helical curvature and suitably chosen indentation and triangularity of the flux surfaces. Magnetic well stabilization of resistive interchange modes at high $\langle\beta\rangle$ values requires sufficiently reduced parallel current density. Side conditions on the magnetic surfaces (aspect ratio, local curvature, local flux surface spacing) have to be observed to avoid ideal ballooning instabilities becoming more restrictive than Mercier instabilities.

4. Reduced neoclassical transport in the $1/\nu$ regime: Isodynamic configurations[3] have $j_\parallel = 0$ and classical rather than neoclassical losses, but apparently cannot be closely approximated at a finite aspect ratio because it is impossible to eliminate all poloidal variation from B in a curved system. The existence of quasi-helically symmetric stellarators[4] implies that toroidal stellarators without $1/\nu$ transport exist. The general nonaxisymmetric stellarator can be characterized by a normalized ripple transport coefficient $D_R = 1.65\delta_e^{3/2}L^*$ (L^* = normalized mean-free-path) with the magnitude of the equivalent ripple δ_e determined by Monte Carlo simulation of electron transport in the long-mean-free-path (lmfp) regime. This ripple must be kept small, typically 2% or smaller at half of the minor radius, to guarantee sufficiently good neoclassical energy confinement. This can be achieved by reducing the radial drift velocity of particles.

5. Small bootstrap current in the lmfp regime: The bootstrap current alters the rotational transform, and thus, it is particularly dangerous in low-shear stellarators. While axisymmetric configurations exhibit a bootstrap current that increases the rotational transform, quasi-helically symmetric stellarators show a "reversed" bootstrap current, i.e., one that decreases the rotational transform. It is possible to reduce the bootstrap current to a tolerable level by a proper combination of helical components and toroidal curvature effects in B on every magnetic surface.

6. Good modular coil feasibility: Generally, strong geometrical shaping of the plasma boundary will improve confinement and stability properties while it adversely affects coil feasibility. Thus, side conditions on the shaping parameters on the plasma boundary have to be used to qualitatively ensure coil feasibility. Important issues for selecting the coil geometry are the minimum distance between the coils and the plasma and the minimum radius of curvature of the coils.

A further necessary prerequisite for an experimental device is a sufficiently broad range of accessible and variable magnetic field parameters (e.g., field strength, rotational transform, and axis position).

In designing W VII-X, a simultaneous optimization of all properties mentioned above is possible; however, some compromises must be accepted. For example, the necessity of small bootstrap current requires some deviation from quasi-helical symmetry, resulting in an increase in neoclassical $1/\nu$ transport. In W VII-X, the resulting enhancement of the plasma losses is small; however, confinement of highly energetic trapped particles, e.g., alpha particles, may be strongly degraded by these asymmetries.

III. BASIC DATA OF W VII-X

The magnetic field configuration of W VII-X differs from W VII-AS mainly in the shape of the magnetic surfaces and in the existence of a helical magnetic axis. This Helical Advanced Stellarator (Helias) concept[1] extends the principle of minimum Pfirsch-Schlüter current to its maximum while it preserves MHD stability by maintaining a magnetic well. Helias configurations, which—as candidates for W VII-X—have been investigated for four, five, and six field periods,[5] are characterized by a small Shafranov shift and a small change in the rotational transform with finite $\langle\beta\rangle$. Configurations that are stable against resistive interchange modes up to an average $\langle\beta\rangle$ of 9% have been found. In the special case of quasi-helically symmetric configurations,[4] neoclassical transport is very low and comparable to axisymmetric configurations since the trapped particles are on confined orbits. Other Helias configurations are more of the "linked-mirror" type[1,2,6] with poloidally closed mod-B contour lines. Furthermore, Helias configurations with very small bootstrap currents for all plasma radii have been found.

For all these reasons, a Helias configuration with five field periods has been selected for W VII-X. The choice of five field periods is mainly dictated by resistive interchange and ideal ballooning modes, which lead to $\langle\beta\rangle$ limits $\leq 3\%$ for four-field-period configurations. Otherwise, the four-period case would be preferable due to the less complex geometrical properties of the coil system.

For the sake of experimental flexibility, provision has to be made for variation of the rotational transform. The rotational transform of five-period Helias configurations lies between 0.7 and 1.4 with a shear $\delta\iota/\iota < 0.2$. A variable rotational transform can be achieved by either dividing the modular coils into an upper and lower winding pack and feeding each one separately with current or by adding a separate coil system that superimposes a toroidal field parallel or antiparallel to the field of the modular coils. The latter solution has been chosen for W VII-X; by superimposing a 10% field, the rotational transform can be varied by $\pm 25\%$.

The number of modular coils per field period is driven in opposite directions by the desire for maximum distance between adjacent coils for heating and diagnostics purposes and the necessity to minimize the magnetic field ripple arising from these gaps. A compromise has been found with 12 coils per period.

A heating power of at least 20 MW is necessary to reach a reactor-relevant parameter regime in W VII-X. For this reason, the geometric dimensions of the device have been chosen to be large enough to allow heating schemes such as neutral beam injection (NBI) and for heat removal systems. Furthermore, the distance between the plasma and the wall must be made as large as possible to keep wall loading and impurity influx low.

Considering all physical arguments, a magnetic field on axis of 3 T and a major radius of 6.5 m (leading to an average plasma radius $a = 0.65$ m) have been chosen for W VII-X. A representative W VII-X coil system and magnetic surfaces are shown in Figs. 1 and 2 for the HS-5-8 configuration. In this specific version, the rotational transform on axis is $\iota_0 = 1.02$ and on the boundary $\iota_a = 1.18$. With slightly different geometrical parameters, another version, HS-5-7, with $\iota_0 = 0.75$ and $\iota_a = 0.95$ is obtained. Important parameters for W VII-X candidates are given in Table I.

TABLE I

Parameters for the W VII-X Candidates HS-5-7 and HS-5-8

	HS-5-7	HS-5-8
Average major radius, R_0 (m)	6.5	6.5
Average coil radius, r_c (m)	1.30	1.30
Radial coil height, t (m)	0.20	0.20
Lateral coil width, w (m)	0.18	0.18
Average coil volume, V_c (m^3)	0.33	0.33
Total coil volume, $n \cdot V_c$ (m^3)	19.7	19.8
Minimum radius of curvature, ρ_c (m)	0.27	0.28
Minimum distance between coils, Δ_c (m)	0.06	0.04
Coil number: total/per field period, n/np	60/12	60/12
Total coil current, I_c (MA)	1.73	1.73
Overall current density, j_c (MA/m^2)	48.6	48.6
Total inductance (one-turn), L (μH)	591	580
Stored magnetic energy, W (GJ)	0.88	0.87
Induction on axis, B_0 (T)	3.0	3.0
Maximum induction at coil, B_m (T)	5.7	5.8
Rotational transform on axis, ι_0	0.75	1.02
Rotational transform on boundary, ι_a	0.95	1.18
Average plasma radius, r_p (m)	0.65	0.70
Average force density, $\langle f\rangle$ (MN/m^3)	76	75
Local maximum force density, $\lvert f\rvert_m$ (MN/m^3)	274	282
Maximum net force (one coil), F_{res} (MN)	3.8	4.0
Virial stress, σ_i (MPa)	44.7	44.0

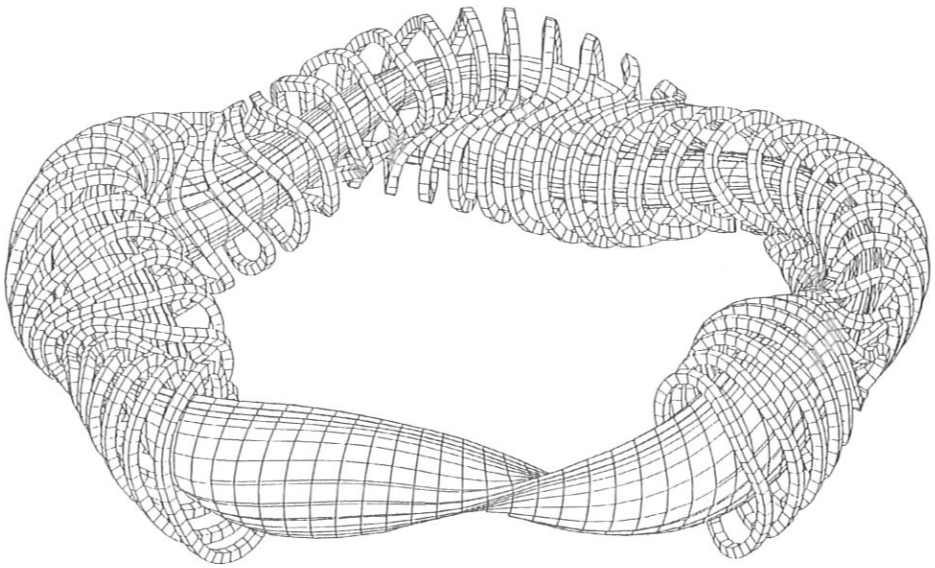

Fig. 1. HS-5-8 coil system with five field periods, 12 coils per period. The geometrical data are listed in Table I.

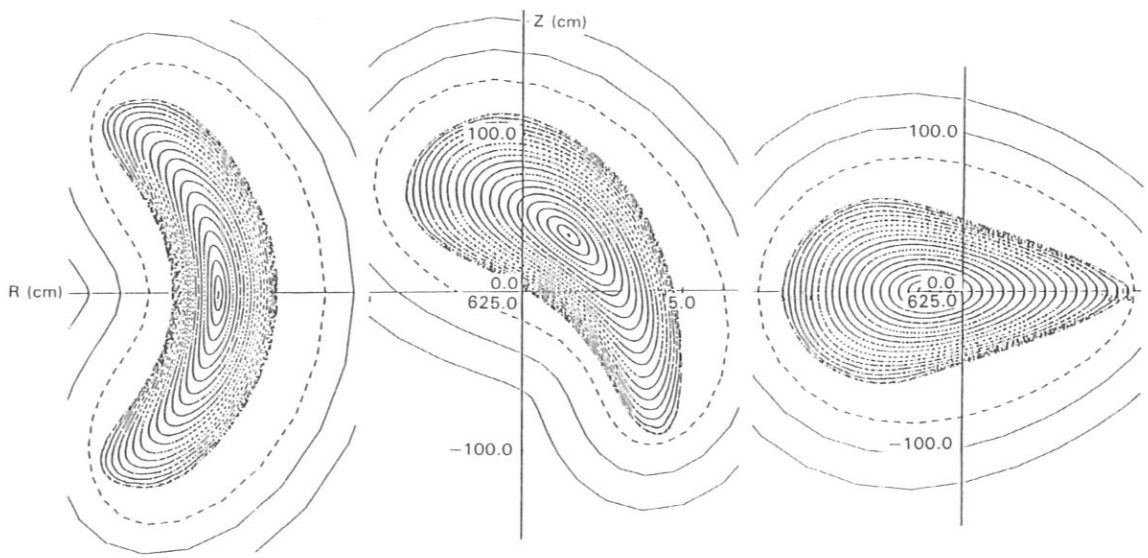

Fig. 2. Cross section of the vacuum magnetic surfaces of HS-5-8 at (left) the beginning of a field period, (center) one-quarter field period, and (right) one-half field period. Solid lines are the coil contours; the dashed line is the first wall.

IV. MHD EQUILIBRIUM AND STABILITY

Equilibrium in Helias configurations has been investigated using the VMEC code, which employs a fixed boundary.[7] Optimization of the shape of this boundary in a multidimensional parameter space with characteristically ten variables led to the Helias stellarator.[1] Various examples of Helias equilibria are given in Ref. 8.

A common feature of Helias equilibria is the small

Shafranov shift Δ, which in conventional stellarators is given by the simple estimate $\Delta/a \approx \langle\beta\rangle A/2\iota^2$. Figure 3 shows a five-period Helias equilibrium with $\langle\beta\rangle = 0.15$.

Another characteristic of Helias equilibria is that the rotational transform is only slightly modified by the finite-$\langle\beta\rangle$ effect; this is particularly important in low-shear stellarators. Helias-type free-boundary equilibria have been studied[9] using the NEMEC code. Due to the small Pfirsch-Schlüter current, the plasma pressure has little effect on the shape of the boundary. However, some questions still remain, particularly concerning the role of islands, stochasticity, and a self-consistent description of these phenomena. In selecting the W VII-X parameters, the importance of islands in the plasma region can be kept small by avoiding low-order rational magnetic surfaces where large islands could occur. On the plasma boundary, however, islands may actually be helpful in controlling plasma density and impurities.

The MHD stability of Helias configurations has been investigated mainly on the basis of localized resistive interchange modes and ideal ballooning modes[7]; the analysis of global modes is under study. Since the shear in Helias configurations is rather small, MHD stability relies on the depth of the magnetic well and on the reduction of the Pfirsch-Schlüter current, both of which appear in the resistive interchange criterion (which approximately coincides with Mercier's criterion). The magnetic well of a Helias vacuum field is rather small, typically <2%, so that $\langle j_\parallel^2/j_\perp^2\rangle \lesssim 1$ is necessary for stability against resistive interchange modes at sizable β values. The resistive interchange stability limits of various Helias configurations with four, five, and six field periods are given in Table II.

A somewhat lower limit is set by ideal ballooning modes. With respect to these modes, magnetic well, maximum field line curvature, shear, and connection length are the decisive governing quantities. With respect to the connection length, one has to expect higher $\langle\beta\rangle$ limits in five-period configurations than in four-period configurations, all other quantities being the same. In Table III, numerical results for the critical $\langle\beta\rangle$ values defined by MHD ballooning modes are listed. In four-period cases $\langle\beta\rangle = 3\%$ is the maximum stable value, whereas in five-period configurations $\langle\beta\rangle = 5\%$ can be achieved. This is the main reason for choosing five field periods in the design of W VII-X.

Below the ideal ballooning mode $\langle\beta\rangle$ limit, the plasma will be unstable against resistive ballooning modes. However, the growth of these modes occurs on the resistive time scale rather than on the Alfvén time scale, and it is generally believed that this instability leads to increased plasma losses instead of a violent destruction of the plasma column. Numerical studies of resistive ballooning modes in Helias configurations are in preparation.[10] Stability in Helias configurations is further endangered by drift modes excited by trapped particles.

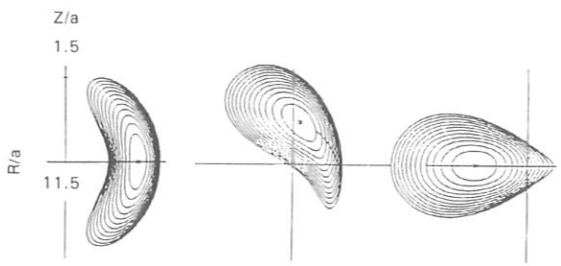

Fig. 3. Example of a five-field-period Helias equilibrium with $\langle\beta\rangle = 0.15$ (Ref. 7). The axes values are normalized to the average plasma radius a.

V. NEOCLASSICAL TRANSPORT

Particle orbits in a magnetic field are the basis of neoclassical transport, and therefore, extensive studies of particle orbits have been carried out. In magnetic

TABLE II

Various Helias Configurations Stable Against Resistive Interchange Modes

	Case[a]										
	4889	4978	4881	4081	4099	5081	5099	5281	5912	6081	6281
M	4	4	4	4	4	5	5	5	5	6	6
$A \approx$	8	9.5	8	10	10	10	10	12	10	10	12
ι_0	0.8	0.7	0.8	0.8	0.8	0.8	0.8	0.8	1.1	0.8	0.8
ι_a	0.9	0.8	1.0	1.0	0.9	1.0	0.9	1.0	1.2	1.0	1.0
$\langle\beta\rangle$	0.045	0.05	0.04	0.03	0.05	0.075	0.07	0.09	0.05	0.06	0.075

[a]The configuration label designates the number of periods (first digit), approximate aspect ratio (second digit), ι_0 in the vacuum field (third digit), and ι_a in the vacuum field (fourth digit).

TABLE III

Ballooning Mode Numbers n and m and $\langle\beta\rangle$ Values for Marginal Stability

	Case							
	5281	HS4V12	4881	4081	5081	5099	6081	6281
$\frac{n}{m}$	$\frac{7}{8}$	$\frac{5}{6}$	$\frac{7}{8}$	$\frac{7}{8}$	$\frac{7}{8}$	$\frac{7}{8}$	$\frac{7}{8}$	$\frac{7}{8}$
$\langle\beta\rangle$	0.05	0.03	0.023	0.02	0.047	0.047	0.03	0.047

coordinates (ψ = radial flux coordinate, and θ = poloidal and ϕ = toroidal angular variables), the scalar function $B = B(\psi,\theta,\phi)$ completely determines the particle orbits. An example of B = constant contours on a magnetic surface is given in Fig. 4.

Isodynamic configurations are characterized by $B(\psi,\phi)$, while in quasi-helically symmetric cases, $B = B(\psi,\theta - M\phi)$. Trapped-particle orbits are of particular interest since transport in the lmfp regime is determined by these particles. All banana orbits would be confined if $B = B(\psi,\theta - M\phi)$ were to hold. However, small symmetry-breaking terms $B_1(\psi,\theta,\phi)$ lead to neoclassical diffusion following the $1/\nu$ scaling. Concerning alpha particles in a stellarator reactor, a situation similar to ripple-induced stochastic orbit losses in tokamaks may arise. In general, the function $B(\psi,\theta,\phi)$ varies if the plasma pressure increases and particle orbits may change. However, this is not typical of Helias configurations, where it is found that the Fourier spectrum of B experiences only small variations with finite $\langle\beta\rangle$. Particle orbits, and consequently neoclassical transport, depend only slightly on finite plasma pressure.

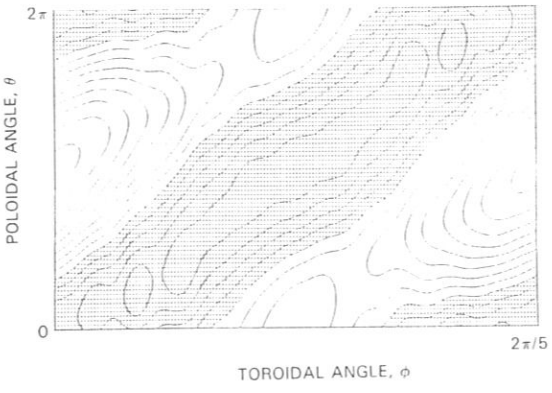

Fig. 4. Contour lines of $B(\theta,\phi)$ = constant on the magnetic surface at $r/a = 0.4$ are shown over one field period of HS-5-8. The horizontal axis is the toroidal angle and the vertical axis is the poloidal angle. The normalized mod-B contours range from 0.96 to 1.08 with the shaded area indicating mod-B <1.

Neoclassical transport in Helias configurations has been studied by various methods:

1. Monte Carlo techniques
2. analytical solution of the bounce-averaged drift kinetic equation
3. numerical solution of the drift-kinetic equation (DKES code).

The Monte Carlo code[11] calculates transport coefficients by convoluting monoenergetic results with a Maxwellian distribution and appropriate weighting factors. The same technique is used in the DKES code.[12] For neoclassical ion transport, configurational details are less important than the presence of a radial electric field ϕ', which in the case of $e\phi'/kT' \approx 1$ reduces the diffusion coefficient well below the plateau level. Therefore, electron behavior is of great importance since it is less affected by the electric field (electrons largely being in the $1/\nu$ regime). For conventional stellarators with

$$B = B_0[1 - \epsilon_t\cos\theta + \epsilon_h\cos(l\theta - M\phi)] \ ,$$

the diffusion coefficient in the $1/\nu$ regime is

$$D_{1/\nu} = \text{const}\cdot\epsilon_h^{3/2}\frac{\epsilon_t^2}{\nu} \ ,$$

where

ν = collision frequency

$\epsilon_t = r/R$ = inverse aspect ratio.

In Helias configurations, $D_{1/\nu}$ may be expressed in a similar manner with the helical ripple ϵ_h replaced by an "equivalent ripple" δ_e (see Sec. II), which is found to be ~0.01 for the Helias configurations under consideration. This result has been confirmed by each of the different methods listed above and demonstrates the strong reduction of neoclassical transport in Helias

configurations compared with nonoptimized stellarators, where this value may be as large as 0.1 or more.

Particles trapped in modular ripple wells do not experience a reduction in their radial drift; these losses can only be kept small by a small modular ripple. Extensive studies using the bounce-averaged drift-kinetic equation[13] were undertaken to calculate these losses, resulting in the conclusion that at least 12 coils per field period are required if modular ripple losses are to remain smaller than helical ripple losses for every flux surface in the plasma cross section.[14]

Diffusion in the plateau regime is determined by circulating particles. Since the toroidal harmonic of B is much smaller than the inverse aspect ratio in Helias configurations, these particles circulate on drift surfaces very close to magnetic surfaces, and therefore, a smaller radial diffusion is found than in standard stellarators. A reduction in plateau diffusion by a factor of 5 can be achieved; see Fig. 5. In summary, the W VII-X experiment is being designed in such a way that its performance will not be seriously limited by neoclassical transport.

VI. THE BOOTSTRAP CURRENT

Another neoclassical effect is the bootstrap current, which leads to a shift of ι with increasing plasma pressure. It is mainly this shift of ι across low-order rational surfaces, associated with deteriorated confinement, that requires the selection of Helias configurations with a greatly reduced bootstrap current. The lmfp regime is of particular interest because the bootstrap current is large here and nearly independent of the collision frequency, so that it has to be minimized by a proper choice of $B(\psi,\theta,\phi)$ in conjunction with the other principles of optimization. Helias configurations have been investigated using the Monte Carlo method[15] and the DKES code[12]; furthermore, the geometrical bootstrap coefficient C_b has been evaluated.[16] To compare various configurations, this factor is normalized to 1 in axisymmetric configurations.

In quasi-helically symmetric configurations, the bootstrap current is finite and opposite to that in axisymmetric tokamaks. With W VII-X parameters, the current could be as large as 250 kA, leading to a shift in the rotational transform of $\delta\iota = -0.3$, which is considered to be unacceptably large. For this reason, a certain deviation from quasi-helical symmetry is necessary:

$$B = B_0(\psi,\theta - M\phi) + B_1(\psi,\theta,\phi) \ .$$

The dominant term in the Fourier series of B_1 to compensate for the bootstrap current is the toroidal curvature term $C_{0,1}\cos\theta$, and it is found that $C_{0,1} \approx 1/3\,C_{M,1}$ is required to obtain nearly zero bootstrap current. Examples of Helias configurations with strongly reduced bootstrap currents are HS-5-7 and HS-5-8. In Fig. 6, the geometrical factor C_b is shown; in both cases $|C_b| = 0.05$ is found, which means that the expected bootstrap current is one-twentieth of the current in an equivalent axisymmetric configuration. Taking into account the achievable plasma parameters in W VII-X, this would lead to a maximum bootstrap current of 50 kA.

Because of the assumptions and approximations of the theory, a further optimization of the bootstrap current by field shaping is irrelevant. A small residual

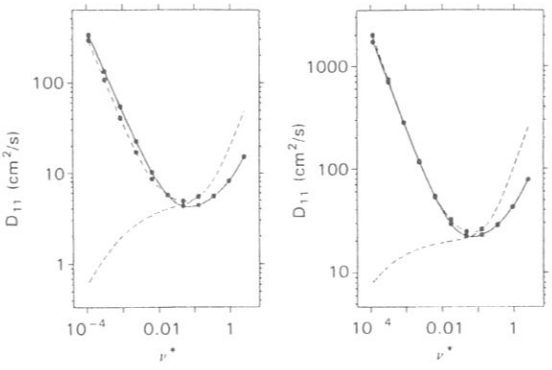

Fig. 5. Neoclassical diffusion coefficient for HS-5-7 versus collisionality: Solid line = result of the DKES code; dashed line = 0.2 $D_{H,H}$ (Hazeltine-Hinton); and dot-dashed line = Shaing-Houlberg approximation with $\epsilon_h = 0.005$, $\epsilon_t = 0.02$, and $\bar{r} = 0.55$ m (left) and $\epsilon_h = 0.006$, $\epsilon_t = 0.006$, and $\bar{r} = 0.2$ m (right). Simulation parameters are $B = 3$ T, $\iota = 0.82$, $T_e = 3$ keV (right) and $T_e = 1$ keV (left).

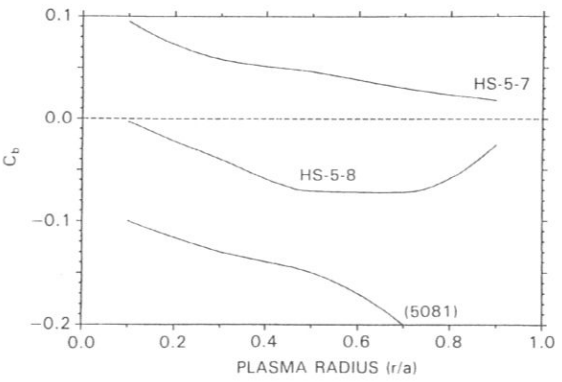

Fig. 6. Normalized geometrical bootstrap factor C_b of Helias configurations HS-5-7, HS-5-8, and HS 5081: $C_b = 1$ in an axisymmetric tokamak with the same aspect ratio and rotational transform.

bootstrap current can also be controlled experimentally by electron cyclotron resonance heating (ECRH) current drive, a technique that has been successfully demonstrated on the W VII-AS experiment.[17]

VII. BOUNDARY REGION

A generic feature of Helias configurations is the existence of a last magnetic surface surrounded by a region of stochastic field lines, between which small islands or remnants of islands may exist, and a region of open field lines. The stochastic region is usually very small, and field lines beginning outside this stochastic region intersect the vacuum chamber after a few toroidal transits. The distance between the last magnetic surface and the first material wall depends critically on the value of the rotational transform on this last surface; a minimum distance of 10 cm is required to yield sufficient decoupling of plasma and wall. Figure 7 shows the standard case of HS-5-7, where five islands with $\iota = 1.0$ exist at the boundary and the last magnetic surface is farther than 10 cm from the wall (dashed line). Field lines beginning in the ergodic region need several toroidal transits before they reach the wall; therefore, a scrape-off layer of cold plasma surrounding the last magnetic surface will exist. The width of this scrape-off layer is determined by radial diffusion competing with parallel plasma flow to the wall or neutralizer plates. This situation resembles the scrape-off layer in tokamaks with an open divertor, except for its three-dimensional geometry. Studies have been carried out to investigate the structure of the magnetic field in this boundary region and to identify the region of maximum wall loading by the outflowing plasma.[18]

Recycling of neutral particles has been investigated using the DEGAS Monte Carlo code.[19] Control of neutral gas is necessary to prevent sputtering of wall material by highly energetic neutrals. This occurs preferentially in the region of vertically elongated magnetic

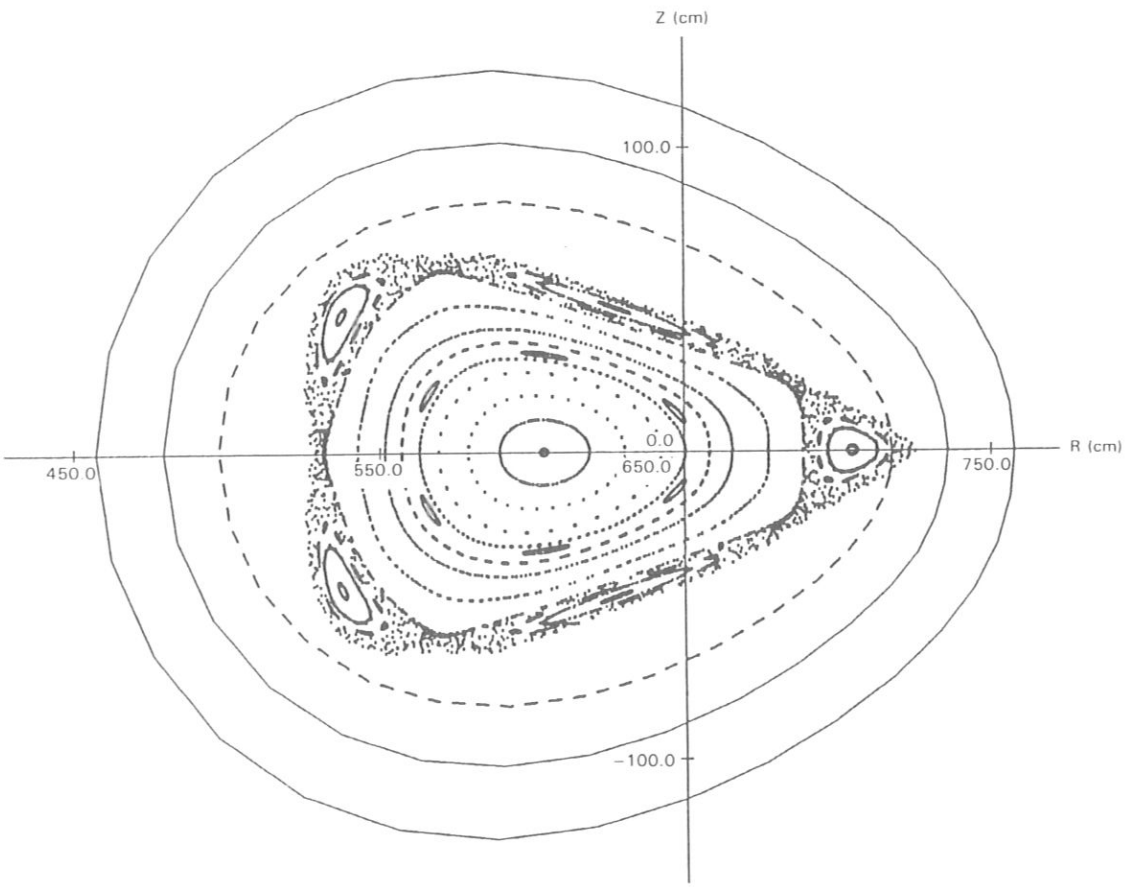

Fig. 7. Cross section of magnetic surfaces of HS-5-7. Islands at the boundary correspond to $\iota = 1.0$.

surfaces where a strong interaction between charge-exchange neutrals and the wall is possible at the inner indented position. The diffusion of neutrals into this region can be reduced by suitable divertor plates. Plasma outflow is expected on narrow fans along the separatrix of the boundary islands, which is similar to the plasma outflow into the open divertor of a tokamak, except for the three-dimensional geometry. Studies are ongoing with the goal of achieving a high density of neutrals in the boundary region and a high-recycling regime.

A critical issue for any approach that hopes to control the boundary region is the modification of the last magnetic surface by finite plasma pressure. This implies that any solution (divertor plates, neutralizer plates) must be designed to handle several different equilibrium configurations.

VIII. PREDICTION OF PLASMA PARAMETERS

To predict plasma parameters in W VII-X, a one-dimensional transport code has been developed that solves the combined equations of particle and energy transport for given radial source terms of particles and energy. The transport coefficients are modeled according to the results of neoclassical theory described in the previous sections. For this purpose, the analytic approximations of Shaing and Houlberg were used to describe lmfp transport with ϵ_h being replaced by δ_e; the reduction of the plateau transport coefficients is also accounted for at higher collision frequency. Furthermore, anomalous thermal conduction of electrons—as was found in Wendelstein VII-A (W VII-A) ($\chi_{e,an} \sim n^{-1} T_e^{-2/3}$)—has been taken into account. There is no theoretical explanation of this anomaly and further experiments in W VII-AS and other stellarators are necessary to determine the scaling laws for anomalous transport. If the anomalous thermal conduction $\chi_{e,an}$ scales inversely with temperature, its effect will be rather small in the expected parameter regime of W VII-X and confinement will be dominated by neoclassical transport. The other extreme is to predict plasma parameters on the basis of empirical scaling laws found in tokamaks under the assumption that these are universal and hence valid in currentless stellarators. This can be done with Kaye-Goldston scaling by replacing the plasma current I_p by the equivalent rotational transform. Another approach is that of the large helical system (LHS) group,[20] where an empirical scaling law for stellarators has been used:

$$\tau_E = 0.21 P^{-0.53} \bar{n}^{0.66} B^{0.53} a^2 R \ .$$

Both Kaye-Goldston and LHS scaling yield similar results.

On the basis of these transport models, the following results are obtained: With $B = 2.5$ T, $\bar{n} = 10^{20}$ m^{-3}, and a heating power $P = 10$ to 20 MW, the achievable average temperature is 4 to 6 keV (neoclassical transport) and 1 to 2 keV (LHS scaling). The energy confinement times are $\tau_E = 0.5$ to 1.0 s (neoclassical transport) and $\tau_E = 0.1$ to 0.3 s (LHS scaling). A $\langle\beta\rangle$ value of 5% can be reached if the confinement time is 1 s for $B = 2.5$ T. At a lower magnetic field, this $\langle\beta\rangle$ value is obtained for shorter confinement times. With anomalous transport following the LHS scaling, the achievable $\langle\beta\rangle$ remains $<2\%$.

In summary, on the basis of neoclassical transport plus anomalous transport as found in W VII-A, the plasma parameters listed in the goals of W VII-X can be reached at a heating power of 10 to 20 MW. Anomalous transport following the Kaye-Goldston L-mode scaling or LHS scaling would lead to much smaller values of achievable temperature.

IX. PLASMA HEATING

A heating power of 20 MW in W VII-X will be provided by various methods: ECRH, NBI heating, and ion cyclotron resonance heating (ICRH). The extent to which each method will contribute will be decided based on results obtained with current stellarator experiments.

Electron cyclotron resonance heating is necessary to provide a target plasma for NBI; for this purpose only a small power (1 MW) is needed. Neutral beam injection in W VII-X has been designed starting from the experience with Axially Symmetric Divertor Experiment (ASDEX)-Upgrade sources[21] (6-MW units, 55-keV full energy, 10-s pulse length). Since special coils of the type employed on W VII-AS are not foreseen for W VII-X, the injection angle is nearly perpendicular to the magnetic field. The available space between coils allows an injection angle of 20 deg, which is sufficient to ensure that most of the high-energy particles will be born on circulating orbits. The aim of NBI heating is to achieve a high-$\langle\beta\rangle$ plasma and to explore plasma stability at the stability limit. In this context, the density rise that is necessarily correlated with NBI (for the planned heating power, a particle influx of $\sim 10^{21}$/s is expected) is tolerable or even useful since high-$\langle\beta\rangle$ values can best be achieved at high density and low temperature.

Furthermore, testing $\langle\beta\rangle$ limits or stability limits do not require steady-state operation; therefore, the density rise and the associated power loss by impurity radiation is not considered a serious obstacle to this particular goal of W VII-X.

Electron cyclotron resonance heating is an appropriate heating scenario in W VII-X for quasi-steady-state operation at high temperature with the plasma in the lmfp regime. Calculations show that this can be reached at a heating power of 10 MW. Further parameters of ECRH are as follows: second harmonic heating at $f = 140$ GHz, $B = 2.5$ T, and a maximum plasma

density $n(0) = 10^{20}$ m^{-3}. Gyrotrons at this frequency are being developed for W VII-AS; further development toward power units of at least 1 MW each is necessary for application to W VII-X. A further application of ECRH is current drive, which has been investigated for W VII-X parameters.[22] These results indicate that at $\langle\beta\rangle = 5\%$, a current drive efficiency of 10 kA/MW heating power should be achievable, which is sufficient to control the residual bootstrap current.

As a third heating scenario, ICRH has been investigated.[23] The frequency regime is 38 to 76 MHz with units of 2 MW power. This allows second harmonic heating of hydrogen and deuterium and also minority heating of hydrogen in deuterium at a magnetic field of 2.5 T.

Geometrical access to W VII-X is provided for all heating schemes, since with 12 coils per field period the largest portholes are 40 × 80 cm. Therefore, application of all three heating schemes is planned in W VII-X, either each one separately or in combination. To a large extent, the planning will make use of the hardware and the expertise developed at IPP to avoid expensive research and development programs for new heating sources.

X. THE MODULAR COILS OF W VII-X

X.A. Methods for Finding Coils

The traditional approach to constructing stellarator fields begins with the coils. Prescribing the geometry of current filaments by a so-called "winding law," the magnetic field is calculated by using Biot-Savart's formula. A typical stellarator magnetic field with a twist in the field lines (rotational transform) can be generated either by helical toroidally closed coils ("helical windings") or by poloidally closed ("modular") coils with lateral excursions.[24] Even with planar coils,[25] a considerable rotational transform can be obtained. A winding law for modular stellarator coils is described in Ref. 26, which was used to compute classical $l = 2$ and $l = 3$ stellarator fields as well as configurations with helical magnetic axes. By varying the parameters of the winding law, the magnetic field can be optimized with respect to physics criteria, such as rotational transform, shear, magnetic well, MHD equilibrium, and stability properties, and with respect to technical constraints such as curvature of current filaments, current density, and optimum access to the plasma. Major limitations of this approach are that the functional space in which coil variations have to be considered is very large—a given confinement region can be realized with many coil systems—and parameter variations of the coils easily cause a deterioration of the aspect ratio.

In a second approach, which was used for W VII-AS (Ref. 27), the properties of the confinement region are optimized by composing the field from sets of harmonic functions, for example, Dommaschk potentials.[28] With this procedure, a surface current producing the optimized field can easily be determined on a surface bounding a toroidal domain. Coils are then obtained by discretizing the surface currents. Again, a major disadvatnage of this procedure is that variation of the amplitudes of the harmonic functions easily leads to an increase in aspect ratio.

A third approach tries to overcome the abovementioned limitations and starts from the observation that the magnetic properties of a stellarator equilibrium are completely determined by the geometry of the plasma boundary. Variation of this boundary led to the Helias stellarator (see Sec. II). In a practical sense, specifying this boundary also guarantees that magnetic surfaces will exist inside the boundary. Further, it decouples the discussion of the magnetic properties of a stellarator configuration from its realization by coils and so necessitates a new method of determining coils. For this purpose, the NESCOIL code[29] was developed to solve a Neumann problem at the plasma boundary in which a surface current is determined, such that the normal component of the field B produced by it is minimized at the plasma boundary. The input for the code consists of two toroidal surfaces: S_1, a magnetic surface at the plasma boundary, and S_2, an appropriately chosen surface outside of, and thus enclosing, S_1. Both surfaces are represented in Fourier series of two angular variables $0 \le u \le 1$ and $0 \le v \le 1$ in the poloidal and toroidal directions, respectively:

$$r = \sum_{m=0,n=-n_b}^{m_b,n_b} r_{m,n} \cos 2\pi (mu + nv) \ ,$$

$$z = \sum_{m=0,n=-n_b}^{m_b,n_b} z_{m,n} \sin 2\pi (mu + nv) \ ,$$

and

$$\varphi = \frac{2\pi}{M} v \ ,$$

where M is the number of toroidal periods, (r, z, φ) are cylindrical coordinates, and the usual stellarator symmetry $[r(u,v) = r(-u,-v)$ and $z(u,v) = -z(-u,-v)]$ is assumed. The code calculates a current distribution on S_2 such that the normal component of its field $\boldsymbol{B}$ on the surface S_1 is minimized. The surface current lines on S_2 are defined by $\phi(u,v) =$ constant, where ϕ can be written as

$$\phi(u,v) = \sum_{m=0,n=-N}^{K,N} \phi_{m,n} \sin 2\pi (mu + nv) - \frac{I_p}{M} v - I_t u \ ,$$

where I_p and I_t are the prescribed values for the net poloidal and toroidal surface currents, respectively.

The magnetic field in the domain bounded by S_2 depends only on the net poloidal current I_p and is independent of the net toroidal current I_t. This is because a current distribution with zero net poloidal and finite net toroidal current, which does not generate a field inside S_2, can be added to the solution. This property offers the possibility of producing the magnetic field either by poloidally closed modular coils ($I_t = 0$) or by torsatronlike toroidally closed coils (I_p/I_t rational). The best solution depends on the structure of the stellarator field to be realized; while it has been shown that toroidal Heliacs do not lend themselves to modular realization,[30] it turns out that Helias stellarators are quite well suited for this approach.

The approximate solution of the boundary value problem yields a vacuum field that is regular in the whole domain bounded by the outer surface S_2. The outer current-carrying surface can be shaped in such a way that the resulting surface current distribution is not too complicated and can be discretized into a finite number of feasible coils. Figure 8 shows a magnetic surface of a classical $l = 2$ stellarator with five field periods as well as a portion of the current lines determined by the NESCOIL code on a circular toroidal surface. Similarly, by using a torus with elliptic cross section rotating with the flux surfaces, the planar coils of the first "modular stellarator[25]" can be reproduced.

X.B. Optimization of the Coil System

The coils of W VII-X were calculated following the above procedure. The two surfaces S_1 and S_2 and a map of the current lines on S_2 are shown in Figs. 9 and 10. These current lines are considered as the central filaments of the finite-size coils. By varying the Fourier coefficients of S_2 and the number of Fourier harmonics in $\phi(u, v)$, the current lines can be improved according to the following criteria:

1. maximum distance between the plasma and the coils
2. maximum distance between two adjacent coils
3. maximum radius of curvature of the coils
4. quality of the resulting magnetic field with respect to the given field.

An extended version of the code systematically alters the coefficients of S_2 to obtain maximum distance between the plasma and the coils; constraints for coil curvature and maximum surface current density are also taken into account. The number of Fourier harmonics $\phi_{n,m}$ retained and the choice of S_2 mainly determine the quality of the approximation and the properties of the resulting magnetic field. In particular, these include the occurrence of magnetic islands on magnetic surfaces with low-order rotational transform. These natural islands are generic properties of stellarator fields (which are necessarily nonaxisymmetric) and not the result of symmetry-breaking error fields. In optimizing the geometry of S_2 and the spectrum of $\phi(u, v)$, this effect has been taken into account by appropriate modification of S_2. A small variation of surface S_1 may also be helpful in optimizing the magnetic field with respect to natural islands without adversely affecting the other properties of the magnetic field.

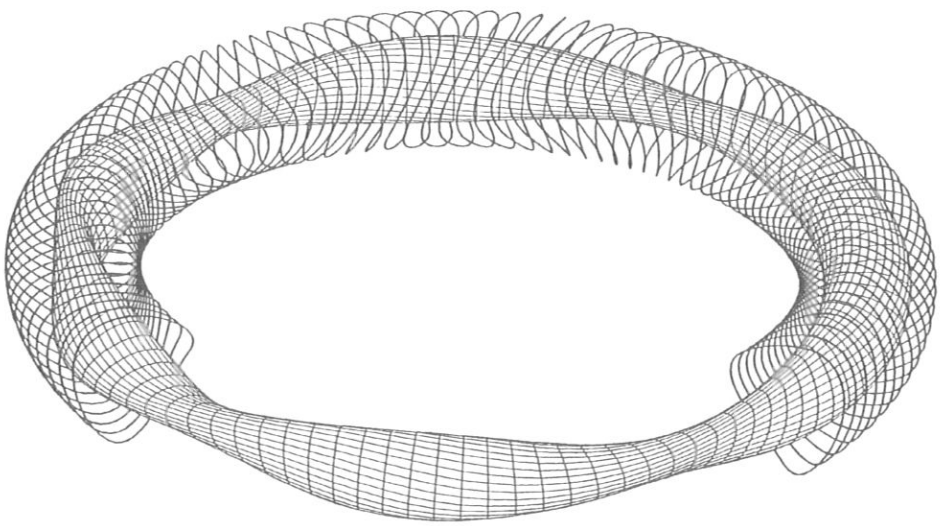

Fig. 8. Magnetic surface of a classical $l = 2$ stellarator with five field periods and a portion of the current lines on a circular toroidal surface determined by the NESCOIL code.

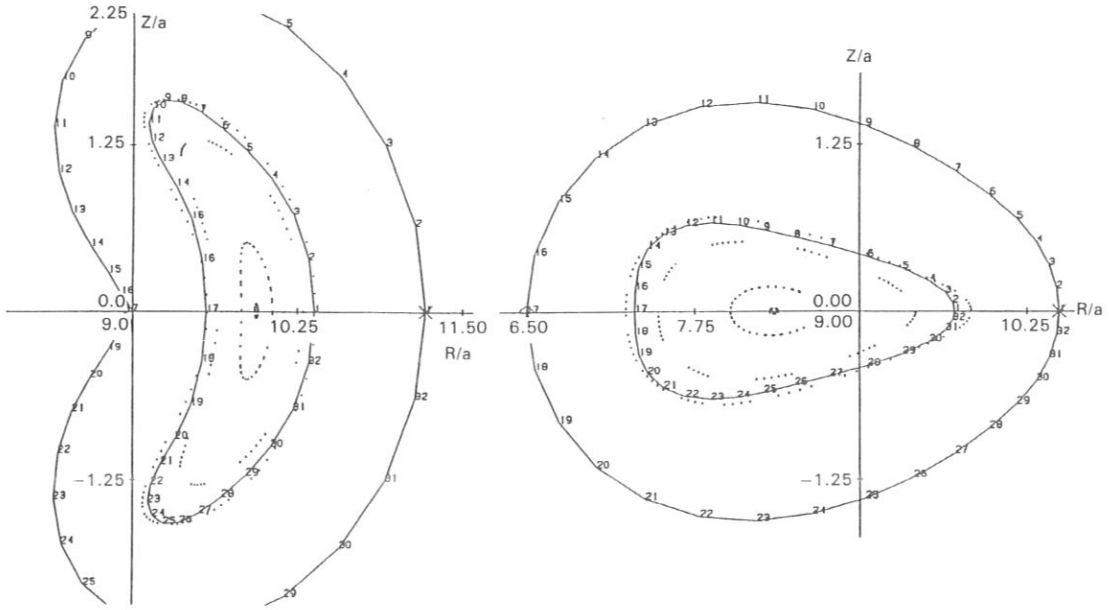

Fig. 9. Cross sections of the surfaces S_1 and S_2 (solid curves) at two toroidal planes and Poincaré plots (points) of the magnetic field produced by the current filaments shown in Fig. 10. The axes values are normalized to a.

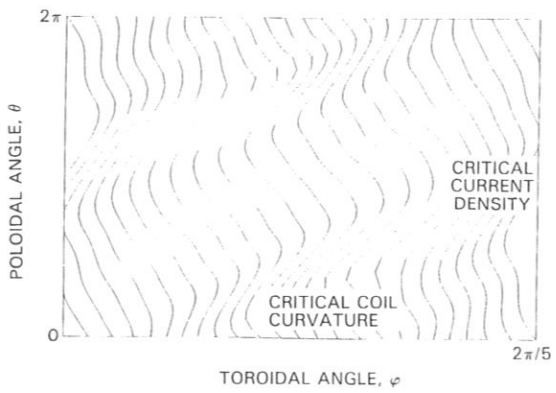

Fig. 10. Surface current lines on S_2 for HS-5-8 as calculated by the NESCOIL code. One field period is shown.

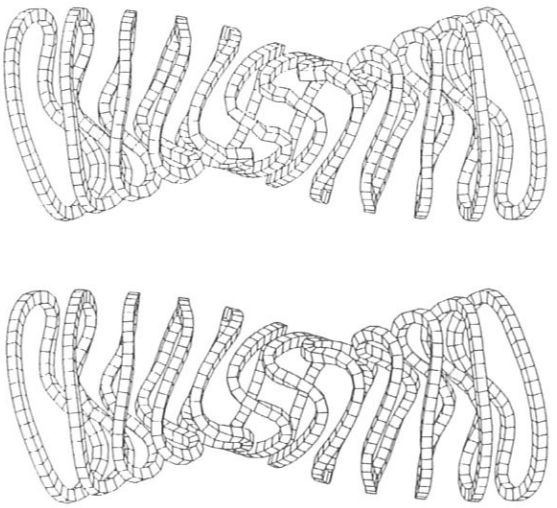

Fig. 11. Finite coils constructed from the current lines of Fig. 10: (top) before smoothing and (bottom) after smoothing.

Locally, the current lines calculated by NESCOIL may be too dense or too curved, and therefore, a local smoothing has been introduced. The deviation from the original field introduced by this smoothing has to be acceptable and limits this procedure. Such a coil set of one field period before and after smoothing is shown in the two parts of Fig. 11. The average major radius is $R_0 = 6.5$ m with the coils being arranged on a helical curve with a maximum distance of 0.2 m from this axis. Case HS-5-8, for example, has the following geometrical data: minimum radius of curvature of 30 cm, minimum lateral distance between coil

centers of 22 cm, and a minimum radial distance of 36 cm between the current surface (coil center) and a flux surface with an aspect ratio of 9.

X.C. Finite Coils

The current lines on S_2 represent the central filament of the modular coils. To construct the geometry of the finite-size coils, the tangential vector $\boldsymbol{t}$ of the central filament $\boldsymbol{x}(s)$, the normal vector $\boldsymbol{n}$ of the surface S_2, and the binormal vector $\boldsymbol{b} = \boldsymbol{t} \times \boldsymbol{n}$ are used. Here, s is the length along the central filament. The four curves at the edge of the rectangular cross section are defined by

$$y_i = \begin{cases} \boldsymbol{x}(s) + w\boldsymbol{b} + h\boldsymbol{n} \\ \boldsymbol{x}(s) + w\boldsymbol{b} - h\boldsymbol{n} \\ \boldsymbol{x}(s) - w\boldsymbol{b} - h\boldsymbol{n} \\ \boldsymbol{x}(s) - w\boldsymbol{b} + h\boldsymbol{n} \end{cases},$$

where $2h$ is the radial height of the coil and $2w$ its width.

Since the normal vector of the surface S_2, and *not* the normal vector of the central filament $\boldsymbol{x}(s)$, has been used to define the orientation of the coils, this method allows maximum utilization of the available space, especially where the coils come close together and the boundaries are nearly parallel. If the coils are nearly in contact, parallel alignment has to be made locally. The width and height of the winding pack are determined by the magnetic field and the maximum current density; these data are listed in Table I. After replacing the central filament with these finite coils, the real magnetic field deviates slightly from that of the filaments. However, this change is negligible in the region of closed magnetic surfaces, a result that has been tested by using several filaments instead of only one to calculate the field. In this region, the magnetic field can be well represented by a field of two current filaments located at different radial positions inside the finite coil. For force and stress analysis, the magnetic field inside the coils and nearby has been calculated using the EFFI code.[31]

X.D. Variation of the Magnetic Field

The modular coils described above generate a magnetic field with a fixed rotational transform. An experimental device, however, requires provisions for varying the rotational transform and for shifting the magnetic axis by use of a vertical field. Variation of the rotational transform can be achieved by an additional set of external coils or by radially divided coils where the lower and upper layers can be energized separately.[32] This double layer concept, however, is rather inefficient in a large coil system with relatively slim coils, and therefore, the other method, using four planar coils superimposed on the modular coils, is preferred. The arrangement is shown in Fig. 12.

Separate adjustment of the currents in coils A and B allows introduction of toroidal and vertical fields as well. The attainable range of ι is shown in Fig. 13; ι on axis, ι at the edge, and $\delta V'/V'(0)$ are plotted versus the current in the extra coils. A current of ± 0.5 MA per planar coil and of 1.75 MA in each modular coil changes the rotational transform by ~25%. Among the configurations obtained by varying the currents in the outer coils are those with $\iota = 5/4$ and $5/5$ at the boundary. In these cases 4 or 5 islands exist at the edge, which may be of interest for active control of the edge region.

By separately energizing the four coils in the outer system, vertical fields can also be superimposed. Opposite currents of 0.5 MA in planar coils A and B (see

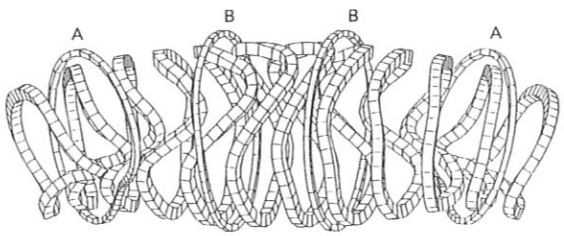

Fig. 12. One HS-5-8 field period showing modular coils and external planar coils A and B for varying the rotational transform and the magnetic axis position.

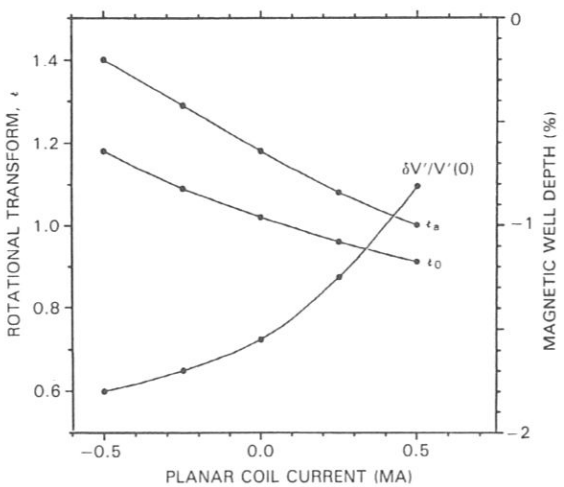

Fig. 13. Rotational transform ι_0 on axis, ι_a at the edge, and the magnetic well $\delta V'/V'(0)$ as functions of the current in the planar coils for HS-5-8. The current in the modular coils is 1.75 MA.

Fig. 12) shift the magnetic axis by ~1% of the major radius. The toroidal modulation of mod B introduced in this case can be reduced considerably if the modular coils carry different currents.

X.E. Coil Design

The choice of superconducting coils for W VII-X offers the possibility of steady-state operation, limited only by the capabilities of the heating systems and the heat removal system. (At the maximum heating power of 20 MW, a pulse duration of no more than 10 to 30 s appears possible; at reduced power, however, a truly steady-state experiment is possible.) The maximum field at the conductor is <6 T, allowing the use of NbTi for the superconducting material with a current density of 50 MA/m^2 averaged over the winding pack of the coils. The dimensions of the nearly rectangular coil cross section are 0.18 × 0.2 m, and the total current in each coil is 1.75 MA. Several options for superconducting cables have been investigated,[33] leading to a "cable-in-conduit" conductor as the optimum solution due to its high cryogenic stability. Cooling is provided by liquid helium and forced-flow cooling. The cross section of the superconducting cable is determined largely by the minimum radius of curvature—30 cm for HS-5-8, limiting the cross section to 2 cm^2 with a maximum current of 10 kA. The details of the superconducting cable are being investigated; the final choice will depend on performance tests of various cables and on the results of a test coil.

The technique to be employed in the winding of the coils is another important issue under investigation. Similar to the procedure applied to W VII-AS, the single cables must be bent in three dimensions and wound mechanically into a mold. Careful control of this process must be provided to minimize the springback effect. The cables are insulated by glass fiber tapes and impregnated by epoxy resin after completion of the winding process. Unlike the normal-conducting coils of W VII-AS, the coils of W VII-X must be enclosed in a stainless steel casing to give them sufficient mechanical stiffness. Geometric tolerances of 10^{-3} are required to avoid field errors; the experience with manufacturing the W VII-AS modular coils has shown that a precision of this order is feasible.

Strong transient magnetic fields are not expected in the coil system, and, therefore, eddy currents do not require enhanced cooling. Transient fields outside the plasma region do occur during the heating phase of the plasma; however, in the region of the superconducting coils, these time derivatives are not larger than $\dot{B} \approx 0.1\ \mathrm{T \cdot s^{-1}}$.

X.F. Normal-Conducting Coils

Normal-conducting coils in W VII-X would not present major technical difficulties since the same technique developed for W VII-AS could be applied. For comparison with the superconducting option, a normal-conducting version has been designed that shows the limitations and restrictions of this alternative. These limitations are consequences of the large ohmic power dissipated in the coils and the available electrical energy. The temperature rise in the coils limits the flattop time of the magnetic field to 10 s, which is considered to be too short for a steady-state experiment.

Parameter studies have been made with the major radius varying from R_0 = 5 to 7 m at constant coil aspect ratio $A_c = R_0/r_c = 5.55$. The pulse time is fixed at t_p = 10 s. In one case, the stored magnetic energy and the magnetic field on axis are kept constant while the current density inside the coils is minimized. In a second case, the current density is kept constant. The main results with respect to the electrical power needed, the total dissipated energy, and the temperature rise inside the coils are summarized in the following:

1. The lowest values are obtained by minimizing the current density in the coils. This means maximization of the coil cross sections and the copper volume of the coils. In the cases considered, the total copper volume of the system is between 28 and 78 m^3.

2. The minimum values were obtained for the R_0 = 7 m case: $P_{max} \approx 270\ \mathrm{MV \cdot A}$, $W_{tot} \approx 2550$ MJ, stored magnetic energy $E_{mag} \approx 600$ MJ, magnetic field on axis $B_0 = 2.4$ T, current density in the coils $j_c = 10.4$ MA/m^2, and total copper volume of 78 m^3. Only in this particular case are the power and energy of the present power supply sufficient to maintain the coil system.

3. With a reduced major radius $R_0 = 5$ m, $E_{mag} \approx$ 600 MJ, $B_0 = 4$ T, $j_c = 24$ MA/m^2, $P_{max} \approx 440$ MV·A, and $W_{tot} \approx 4400$ MJ.

4. With the power value kept constant ($P_{max} =$ 440 MV·A), the magnetic field on axis only decreases from $B_0 = 4$ to 3.4 T if the geometrical dimensions increase from $R_0 = 5$ to 7 m. For this case, the current density in the coils is a minimum.

5. The temperature rise in the cases considered is moderate and is between $\Delta\vartheta_{max} \approx 10$ to ≈ 47°C.

XI. ELECTROMAGNETIC FORCES

Magnetic forces on the modular coils are one of the main technical problems in W VII-X. These forces determine the geometry of the support system and the mechanical stresses, thereby setting the technical limits of the coil system. The magnetic field inside the coils and the magnetic forces are calculated using the EFFI code.[31] A complex magnetic field distribution exists inside the coils, which leads to an inhomogeneous force distribution and a resulting net force on each coil pointing not only in the radial direction but also in the

vertical and lateral directions as well. Figure 14 shows the contour lines mod B = constant in the $z = 0$ plane for two adjacent coils of HS-5-8; the maximum field at the coil boundary in this plane is 5.4 T. Forces and stresses have been calculated for the four-period HS-4-12 configuration (major radius of 5 m, $B_0 = 4$ T) and for HS-5-7 (major radius of 6.5 m, $B_0 = 3$ T; see Table I). To describe the forces, the local orthogonal coordinate system defined by the vectors $\boldsymbol{n}$, $\boldsymbol{b}$, and $\boldsymbol{t}$ of Sec. X.C is used. Hence, according to $\boldsymbol{f} = \boldsymbol{j} \times \boldsymbol{B}$, there are two components of the magnetic force density perpendicular to the direction of the current; f_R is the component in the direction of $\boldsymbol{n}$ (radial) and f_S the component in the direction of $\boldsymbol{b}$ (lateral). The component in the direction of $\boldsymbol{t}$ is zero ($f_T = 0$). Due to the fivefold symmetry of the magnetic field and the symmetry within one field period, there are only six different coils, which facilitates the analysis appreciably. As an example, the average force density for two coils in HS-5-8 is shown in Fig. 15. The magnitude of the lateral force density may be comparable to the radial force density. This, in particular, occurs in those coils with strong lateral excursions and strong local curvature.

For HS-5-8 with $R_0 = 6.5$ m, the toroidal excursions of the coils are increased in comparison with HS-4-12 with $R_0 = 5$ m. The result is an increase in the lateral force densities to levels where they can exceed the radial components; see Fig. 15. Although the magnetic field has been decreased from $B_0 = 4$ to 3 T in HS-5-8, the magnitude of the force densities is in the same range as for HS-4-12.

The moderate helicity of the magnetic axis of Helias coil systems causes a related helicity in the net coil force vector, corresponding to different coil forces in the radial and vertical directions. The resulting net forces are shown in Figs. 16 (HS-4-12) and 17 (HS-5-8). In the latter case, some coils even feel a force directed radially outward while others experience a force in the vertical direction that leads to a torque on the field period. The net force on the whole period is directed toward the torus center. As in the case of the local force densities, the maximum net forces are also comparable in HS-4-12 and HS-5-8. The maximum net force in both cases is 4 MN; under fault conditions—quenching of a coil—this force may increase to ~7 MN. It is of interest to compare these data with the centripetal forces of a system with equivalent circular planar coils; in such a case, the net radial force per coil would be 2.3 MN.

XII. SUPPORT CONCEPT AND MECHANICAL STRESS ANALYSIS

The forces described above are the input data for the stress analysis. Stresses depend on the support system of the coils, which must be optimized with regard to material limits, safety factors, and a maximum of accessibility. Unlike the normal-conducting coils of W VII-AS, the W VII-X coils must be surrounded by a stainless steel housing because the virial stress in W VII-X is roughly three times greater. Studies with various housing dimensions have been made; in the present results, a housing thickness of 8 cm at the outer coil face and 5 cm at the three other sides of the coil is assumed. Stress maxima tend to arise where the coils are curved; therefore, extra reinforcement is provided in these areas. Support elements are located between adjacent coils; these are mainly confined to the inner region, toward the torus center, thus leaving the outer region accessible for heating and diagnostic portholes. Figure 18 shows the arrangement of these support elements for HS-5-7. The system described here is not optimized; its purpose is to identify critical issues and to assess the data for a detailed design.

It is difficult to predict the material data for a winding pack that would consist of superconducting strands, copper, stainless steel, and insulating material. Tests must be made to obtain a reliable data base. For this reason, the elastic data of the Euratom LCT coil[34] are used as a first approximation:

Young's modulus (GPa)	$E_R = 62$, $E_S = 53$, $E_T = 120$
Shear modulus (GPa)	$G_{RS} = 10$, $G_{ST} = 26$, $G_{TR} = 21$
Poisson's ratio	$\nu_{RS} = 0.198$, $\nu_{ST} = 0.126$, $\nu_{TR} = 0.298$.

The elastic data of the coil housing and the support elements are those of stainless steel. The finite element SAP V(2) code is used to compute the stresses and strains in the winding pack. One period of the coil system (12 coils) is modeled by 6664 elements and 9600 nodes. Each individual coil is represented by 480 elements, 80 per winding pack and 400 per housing; the remaining elements model the support structure. Since gap elements cannot be treated by SAP V(2), the winding pack is rigidly connected to the coil housing. Fixed boundary conditions are defined at both ends of the period, thus balancing the net force on the coils and the torque in one period (see Fig. 18). Because of the nonplanar geometry of the coils and the inhomogeneous forces, all components of the stress tensor are equally important. The stresses are calculated in the center of each element; local stress maxima are approximately handled with this value as well, using a local enhancement factor of 2. Figures 19 and 20 give results for the van Mises stress σ_{vM} and the shear stress σ_{ST} of all 12 coils in one period. The maximum stresses are found to be $\sigma_{vM} \approx 140$ MPa and $\sigma_{ST} \approx 38$ MPa. The corresponding stresses in the four-period HS-4-12 configuration are $\sigma_{vM} \approx 115$ MPa and $\sigma_{ST} \approx 32$ MPa. The stress maxima are rather localized and it is expected that these stresses can be reduced by optimizing the support system.

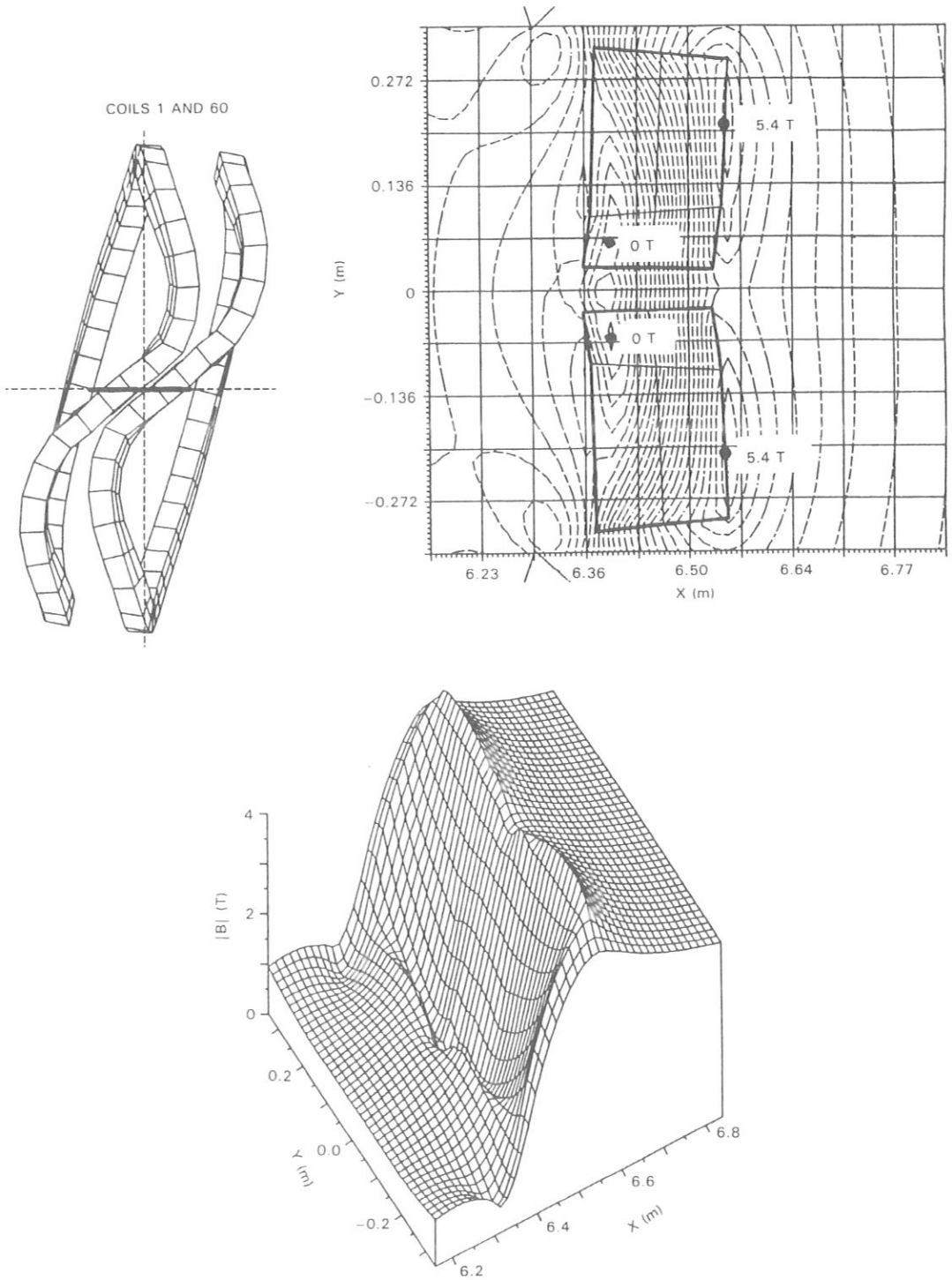

Fig. 14. Contour lines B = constant in the $z = 0$ plane at coils 1 and 60 for HS-5-8. The maximum field is 5.4 T. The lower picture is a three-dimensional plot of B in the same plane.

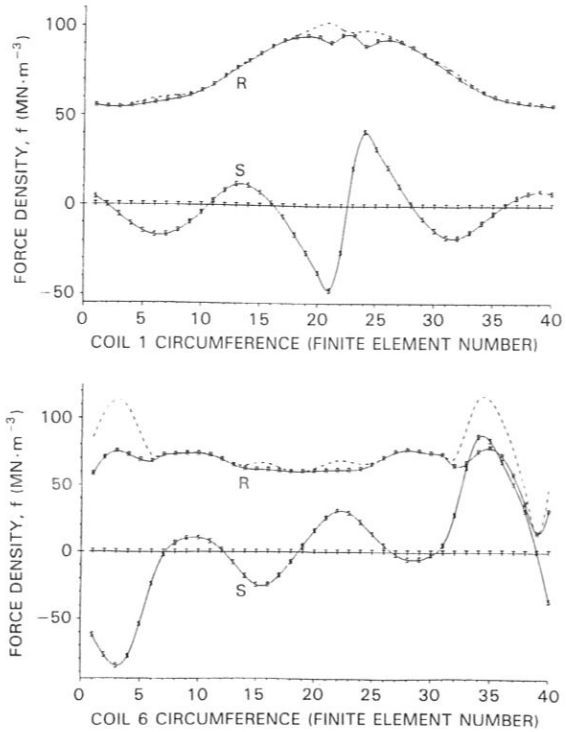

Fig. 15. Magnetic force densities in the radial (R) and lateral (S) directions for coils 1 (top) and 6 (bottom) as a function of the coil circumference (0 being the radial outside in the midplane of the coil) for HS-5-8. The dashed lines indicate the magnitude of the force density.

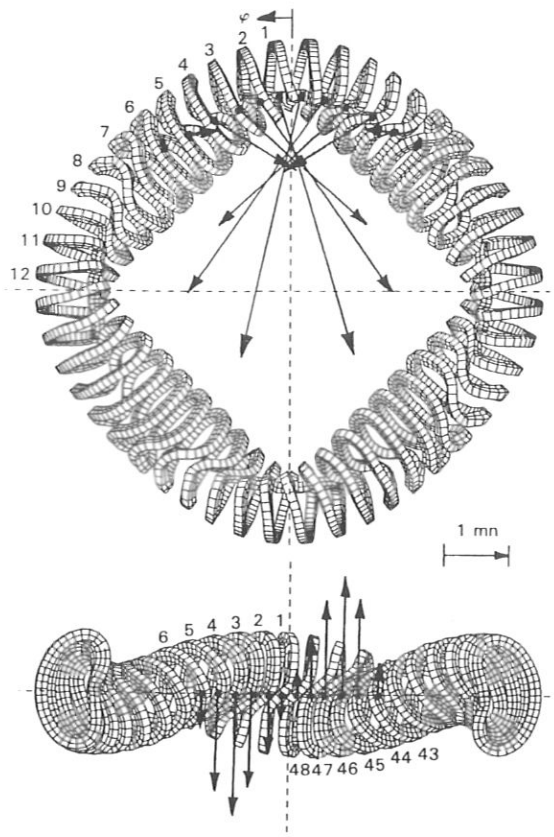

Fig. 16. HS-4-12 coil system with net radial and vertical coil forces.

In a further step, contact elements and gap elements between the winding pack and the coil housing will be introduced using the ANSYS and ADINA codes. First results obtained with a single coil indicate a 10% increase in the van Mises stress; separate stress components increase by 30% when more realistic boundary conditions are taken into account. The stresses described above arise from magnetic forces and thermal stresses; those caused by the manufacturing process have yet to be considered.

XIII. CRYOGENICS AND VACUUM VESSEL

The coils and the support system must be cooled with liquid helium at ~4 K. The overall mass to be cooled is ≈500 tonnes, which requires a 2- to 3-kW cooling system. A cryostat for the system is being developed; details are not yet available.

Another important component is the vacuum vessel, which consists of an outer vacuum chamber, surrounding the coils and mechanical supports, and the inner vacuum chamber between the plasma and the coils. The distance between the inner vacuum chamber and the winding pack of the coils is 14 cm; this space is needed for the coil housing, cooling pipes, and thermal insulation. The shape of the inner vacuum vessel is of similar complexity to the last magnetic surface S_1 or the current-carrying surface S_2. The manufacturing procedure developed for W VII-AS can also be applied to the vacuum vessel of W VII-X. The inner vacuum vessel must be protected against the radiation and thermal load from the plasma by a water-cooled liner, thus preventing the heating power to the plasma from being ultimately deposited in the cryostat.

About 150 portholes for various diagnostics, heating systems, and pumping are planned for W VII-X; the largest portholes are 40 × 80 cm. This section identifies only a few of the mechanical problems associated with the vacuum chamber; a detailed design is in preparation.

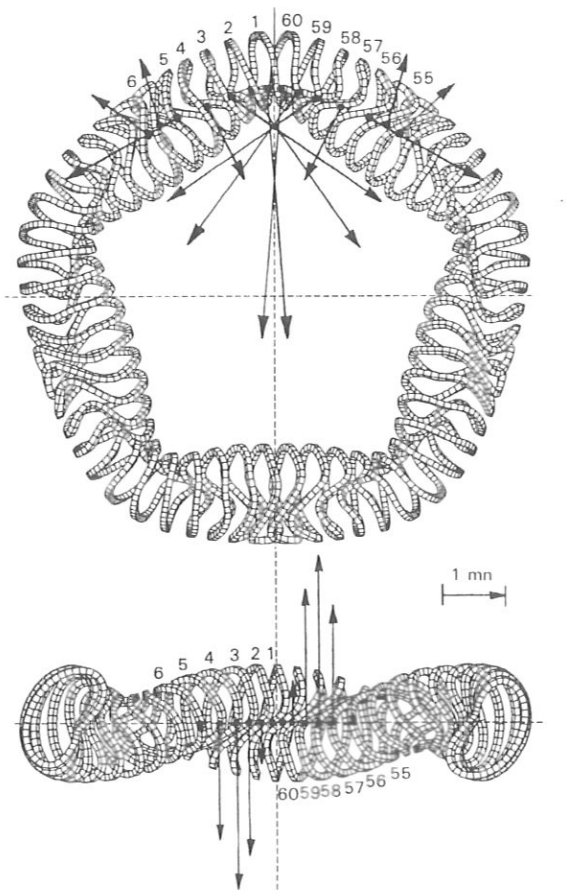

Fig. 17. HS-5-8 coil system with net radial and vertical coil forces.

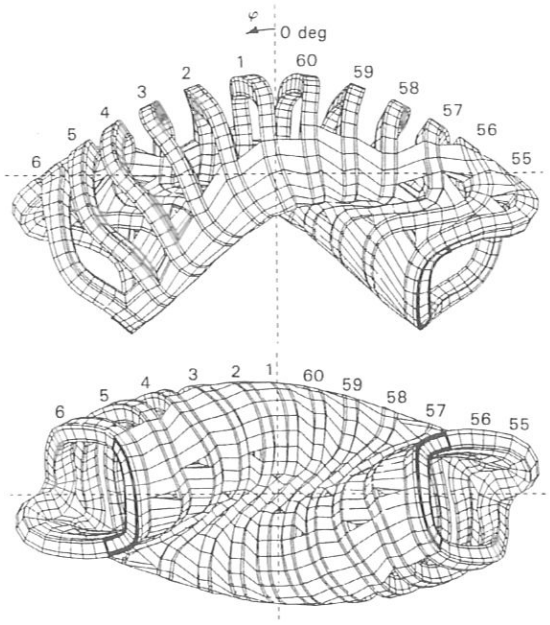

Fig. 18. Coils of one field period showing the coil housing and the support elements for HS-5-7. Fixed boundary conditions are placed on the solution at the end positions indicated by the heavier lineweight.

XIV. SUMMARY AND CONCLUSIONS

Optimization of stellarator equilibria has led to the Helias concept, which is characterized by a small Shafranov shift and MHD stability limits up to $\langle\beta\rangle \approx 5\%$. Neoclassical transport and the bootstrap current have been reduced to a tolerable level by optimization of the structure of B on magnetic surfaces. Based on these theoretical results, the W VII-X experiment is being planned with the goals of achieving reactor-relevant parameters and demonstrating the reactor capability of this stellarator line.

Reaching these goals requires a heating power of 20 MW; several heating scenarios with ECRH, NBI, and ICRH are envisaged. At present, a prediction of plasma parameters can be made only on the basis of neoclassical transport. Well-established empirical scaling laws of plasma confinement in stellarators do not exist, and it is questionable whether the empirical laws found for tokamaks also hold for stellarators. Neoclassical transport in W VII-X is small enough that the goals of the experiment can be reached. Physics studies for W VII-X have concentrated mainly on MHD effects, neoclassical effects, and coil finding procedures. Work is in progress on other important issues such as impurity behavior and nonideal instabilities.

Modular superconducting coils have been chosen mainly because of their reactor relevance and the ability to operate the experiment in quasi-steady state. The superconducting coils of W VII-X are the largest and most complex components of the experiment; for this reason, extensive studies have been made of the forces and stresses in this system. The net electromagnetic coil forces in modular Helias systems are inhomogeneous with components in all directions. Local lateral forces within a single coil can be as large as the radial components. This force inhomogeneity is not a serious obstacle and the stresses within the coils can be kept within technical limits by utilizing an optimized support structure. Details of the coil system including the manufacturing technique are being investigated under contracts with industry.

The design of the modular coil system will be based on the experience gained with the construction of W VII-AS. The expertise on superconducting coils

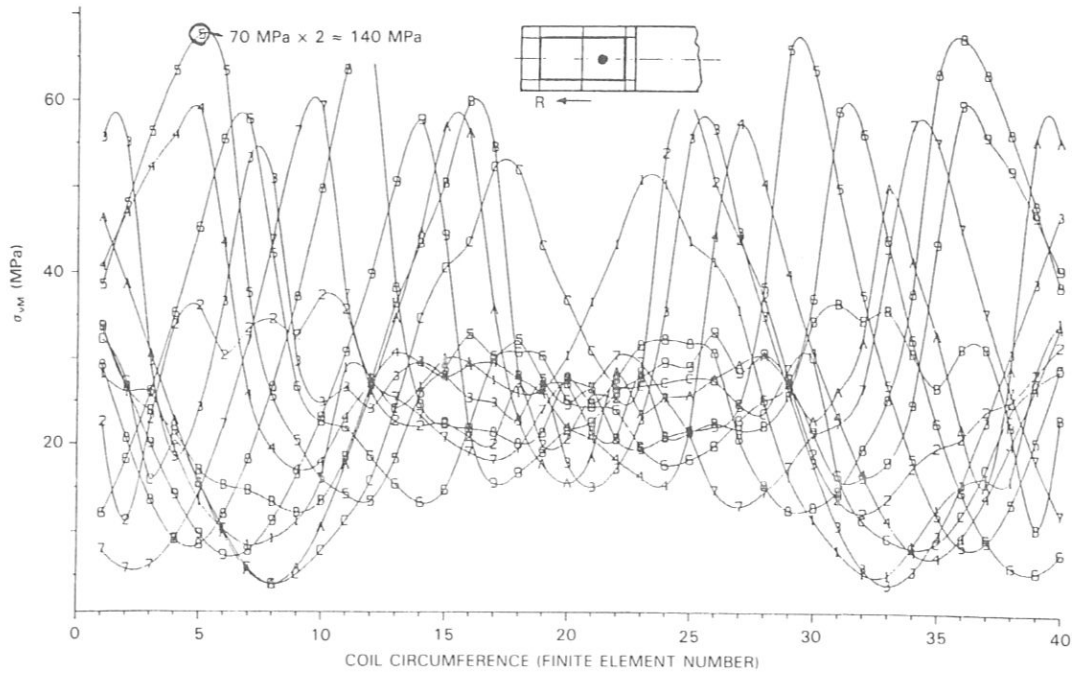

Fig. 19. Equivalent van Mises stress σ_{vM} along the coils of one field period for HS-5-7. The labels on each curve refer to the 12 coils of one field period; for example, the curve labels 1 through 9, A, B, and C correspond to the coils numbered 55 through 6 in Fig. 18. The insert indicates the stress output location.

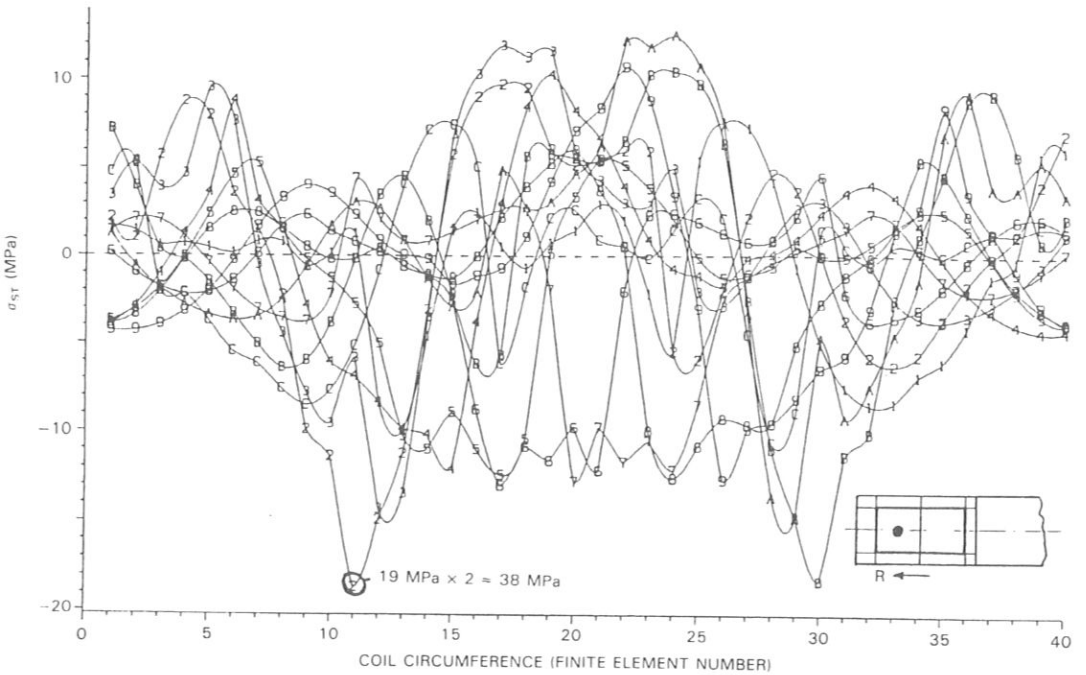

Fig. 20. Shear stress σ_{ST} along the coils of one field period for HS-5-7. The curve labels are as given in Fig. 19.

obtained in the LCT project will also be of great influence via cooperation with Kernforschungszentrum Karlsruhe.

In summary, the W VII-X experiment offers the opportunity for a new and promising stellarator line.

REFERENCES

1. J. NÜHRENBERG and R. ZILLE, "Stable Stellarators with Medium β and Aspect Ratio," *Phys. Lett.*, **114A**, 129 (1986).

2. W. DOMMASCHK, F. HERRNEGGER, W. LOTZ, P. MERKEL, J. J. NÜHRENBERG, A. SCHLÜTER, U. SCHWENN, and R. ZILLE, "Physics Studies for Advanced Stellarators," *Proc. 11th Int. Conf. Plasma Physics and Controlled Nuclear Fusion Research*, Kyoto, Japan, November 12–19, 1986, Vol. 2, p. 383, International Atomic Energy Agency (1987).

3. D. PALUMBO, "Some Considerations on Closed Configurations of Magnetohydrostatic Equilibrium," *Il Nuovo Cimento X*, **53B**, 507 (1968).

4. J. NÜHRENBERG and R. ZILLE, "Quasi-Helically Symmetric Toroidal Stellarators," *Phys. Lett.*, **129A**, 113 (1988).

5. G. GRIEGER, C. BEIDLER, E. HARMEYER, J. JUNKER, J. KISSLINGER, W. LOTZ, P. MERKEL, A. MONTVAI, J. NÜHRENBERG, R. RAU, A. SCHLÜTER, H. WOBIG, and R. ZILLE, "Physics Studies for Helical-Axis Advanced Stellarators," *Proc. 12th Int. Conf. Plasma Physics and Controlled Nuclear Fusion Research*, Nice, France, October 12–19, 1988 (to be published).

6. H. WOBIG, "Overview on Wendelstein VII-X," *Proc. 2nd Workshop on Wendelstein VII-X*, Schloss Ringberg, FRG, June 13–16, 1988, EUR 11705 EN, p. 3 (1988).

7. J. NÜHRENBERG and R. ZILLE, "Equilibrium and Stability of Low-Shear Stellarators," *Proc. Theory of Fusion Plasmas, Int. School of Plasma Physics Piero Caldirola*, Varenna, Italy, August 24–28, 1987, EUR 11336 EN, p. 3 (1988).

8. J. NÜHRENBERG and R. ZILLE, "Optimization of Helias for Wendelstein VII-X," *Proc. 2nd Workshop on Wendelstein VII-X*, Schloss Ringberg, FRG, June 13–16, 1988, EUR 11705 EN, p. 17 (1988).

9. P. MERKEL, "Applications of the Neumann Problem to Stellarators: Magnetic Surfaces, Coils, Free Boundary Equilibrium, Magnetic Diagnostics," *Proc. Theory of Fusion Plasmas, Int. School of Plasma Physics Piero Caldirola*, Varenna, Italy, August 24–28, 1987, EUR 11336 EN, p. 25 (1988).

10. H. P. ZEHRFELD, J. KISSLINGER, and H. WOBIG, "Resistive Ballooning Stability of Advanced Stellarators," *Proc. 16th European Conf. Controlled Fusion and Plasma Physics*, Venice, Italy, March 13–17, 1989, Vol. 13B, Part II, p. 591 (1989).

11. W. LOTZ, AND J. NÜHRENBERG, "Monte Carlo Computations of Neoclassical Transport," *Phys. Fluids*, **31**, 2984 (1988).

12. S. P. HIRSHMAN, K. C. SHAING, W. I. Van RIJ, C. O. BEASLEY, Jr., and E. C. CRUME, Jr., "Plasma Transport Coefficients for Nonsymmetric Toroidal Confinement Systems," *Phys. Fluids*, **29**, 2951 (1986).

13. C. D. BEIDLER, "Analytic Solution of the Bounce-Averaged Fokker-Planck Equation for Wendelstein VII-X," *Proc. 2nd Workshop on Wendelstein VII-X*, Schloss Ringberg, FRG, June 13–16, 1988, EUR 11705 EN, p. 121 (1988).

14. C. D. BEIDLER, "Modular-Ripple Transport in Stellarators," *Proc. 16th European Conf. Controlled Fusion and Plasma Physics*, Venice, Italy, March 13–17, 1989, Vol. 13B, Part II, p. 675 (1989).

15. W. LOTZ, J. NÜHRENBERG, and A. SCHLÜTER, "Neoclassical Energy Confinement in Stellarators," *J. Comput. Phys.*, **73**, 73 (1987).

16. K. C. SHAING and J. D. CALLEN, "Neoclassical Flows and Transport in Nonaxisymmetric Toroidal Plasmas," *Phys. Fluids*, **26**, 3315 (1983).

17. U. GASPARINO and H. MAASSBERG, "Sources of Toroidal Current in the Wendelstein VII-AS Stellarator," *Proc. 16th European Conf. Controlled Fusion and Plasma Physics*, Venice, Italy, March 13–17, 1989, Vol. 13B, Part II, p. 631 (1989).

18. C. D. BEIDLER, E. HARMEYER, F. HERRNEGGER, J. KISSLINGER, A. MONTVAI, F. RAU, R. SCARDOVELLI, and H. WOBIG, "On the Edge Structure of a Helias Configuration," *Proc. 16th European Conf. Controlled Fusion and Plasma Physics*, Venice, Italy, March 13–17, 1989, Vol. 13B, Part II, p. 699 (1989).

19. D. HEIFETZ, D. POST, M. PETRAVIC, J. WEISHEIT, and G. BATEMAN, "A Monte Carlo Model of Neutral-Particle Transport in Diverted Plasmas," *J. Comput. Phys.*, **46**, 309 (1982).

20. Design Group for the New Large Helical System Device, "New Large Helical System Device (Outline)" (Mar. 31, 1988) (English summary of the original Japanese).

21. F. P. PENNINGSFELD and E. SPETH, "Neutral Injection into Wendelstein VII-X," *Proc. 2nd Workshop on Wendelstein VII-X*, Schloss Ringberg, FRG, June 13–16, 1988, EUR 11705 EN, p. 215 (1988).

22. U. GASPARINO and H. MAASSBERG, "Considerations on ECRH Current Drive and Bootstrap Current for Wendelstein VII-X," *Proc. 2nd Workshop on Wendelstein VII-X*, Schloss Ringberg, FRG, June 13–16, 1988, EUR 11705 EN, p. 157 (1988).

23. F. WESNER, "ICRH for Wendelstein VII-X," *Proc. 2nd Workshop on Wendelstein VII-X*, Schloss Ringberg, FRG, June 13–16, 1988, EUR 11705 EN, p. 221 (1988).

24. H. WOBIG and S. REHKER, "A Stellarator Coil System Without Helical Windings," *Proc. 7th Symp. Fusion Technology*, Grenoble, France, October 24–27, 1972, EUR 4938 e, p. 345 (1972).

25. S. N. POPOV and A. P. POPRYADUKHIN, "Production of a Helical Magnetic Field," *Sov. Phys. – Tech. Phys.*, **11**, *2*, 284 (1966).

26. E. HARMEYER, J. KISSLINGER, F. RAU, and H. WOBIG, "A General Winding Law of Modular Stellarator Coils," IPP 2/274, Max-Planck-Institut für Plasmaphysik (1985).

27. U. BROSSMANN, W. DOMMASCHK, F. HERRNEGGER, G. GRIEGER, J. KISSLINGER, W. LOTZ, J. NÜHRENBERG, F. RAU, H. RENNER, H. RINGLER, J. SAPPER, A. SCHLÜTER, and H. WOBIG, "Concept of an Advanced Stellarator," *Proc. 9th Int. Conf. Plasma Physics and Controlled Nuclear Fusion Research*, Baltimore, Maryland, September 1–8, 1982, Vol. 3, p. 141, International Atomic Energy Agency (1983).

28. W. DOMMASCHK, "Representations for Vacuum Potentials in Stellarators," *Comput. Phys. Comm.*, **40**, 203 (1986); see also W. DOMMASCHK, "Solution to Stellarator Boundary Value Problems with a New Set of Simple Toroidal Harmonic Functions," *Z. Naturforsch.*, **36a**, 251 (1981).

29. P. MERKEL, "Solution of Stellarator Boundary Value Problems with External Currents," *Nucl. Fusion*, **27**, 867 (1987).

30. P. MERKEL, "Calculation of Coils for Stellarator Equilibria," *Proc. Workshop on Wendelstein VII-X*, Schloss Ringberg, FRG, March 18–20, 1987, EUR 11058 EN, p. 125 (1987).

31. S. J. SACKETT, "EFFI – A Code for Calculating the Electromagnetic Field, Force and Inductance in Coil Systems for Arbitrary Geometry," UCRL-52402, Lawrence Livermore National Laboratory (1978).

32. J. KISSLINGER, E. HARMEYER, A. MONTVAI, F. RAU, and H. WOBIG, "Magnetic Field, Force and Stress Calculations for Modular Helias Coil Systems," *Proc. 15th Symp. Fusion Technology*, Utrecht, The Netherlands, September 19–23, 1988, Vol. 1, p. 417 (1989).

33. W. MAURER, "General Aspects of Magnet Design for Wendelstein VII-X," *Proc. 2nd Workshop on Wendelstein VII-X*, Schloss Ringberg, FRG, June 13–16, 1988, EUR 11705 EN, p. 335 (1988).

34. A. MAURER, A. ULBRICHT, and F. WÜCHNER, "Effect of Azimuthal Dependence of Radial Young's Modulus on the Mechanical Behavior of the European LCT Coil," *Proc. 9th Int. Conf. Magnet Technology*, Zürich, Switzerland, September 9–13, 1985, p. 428 (1985).

Fusion Engineering and Design 11 (1990) 399–422
North-Holland

DESIGN AND ENGINEERING ASPECTS OF THE MAIN COMPONENTS FOR THE WENDELSTEIN VII-AS STELLARATOR EXPERIMENT

Reinhard MATHIS * and Jörg SAPPER

Max-Planck-Institut für Plasmaphysik (IPP) [Euratom association], D-8046 Garching b. München, Fed. Rep. Germany

Submitted 19 June 1989; accepted 13 September 1989
Handling Editor: P. Komarek

In this paper the design of the essential components of the newly constructed Wendelstein VII-AS stellarator experiment at Garching are described, and the first technical and experimental results are reported.

1. Introduction

Stellarators are an alternative line to tokamaks in the field of toroidal confinement systems for fusion machines. In contrast to tokamaks, they allow net-current-free plasma operation and are therefore inherently suitable for continuous performance in a reactor. During the development of fusion machines stellarators were characterised for a long time by their complex confinement coil configurations because of the additional helical winding system on the vacuum vessel. It was supposed that such a winding system could only be developed with inadequate expense to reactor size, and that a modular reactor design would be restricted by conditions adhering to the helical windings. In [1] it was shown that helical windings can be replaced by using nonplanar coils, which provide combination of poloidal and helical currents. When in 1982 the Wendelstein VII-A experimental stellarator at Garching was redesigned as an advanced version, such a modular coil system was used the first time for the confinement system in a larger machine. In the following, we describe the design of the essential components of the newly constructed Wendelstein VII-AS machine, and report on first technical and experimental results.

* Now with Balzers AG, Fürstentum Liechtenstein.

2. Magnetic confinement system of W VII-AS

2.1. Design and construction of the magnetic confinement system

The confinement field of the Wendelstein VII-AS experiment at Garching is exclusively generated by a coil set of modular design, composed of 45 nonplanar coils (Modular Field, MF-coils). Ten additional planar toroidal field coils merely serve to ensure the experimental flexibility of the system. The entire coil set consists of 5 equal field periods, each containing 9 nonplanar and 2 planar coils (see fig. 4). One of the MF-coils in each field period is enlarged to provide extensive (tangential or near-tangential) access to the plasma (e.g. for plasma heating by neutral beam injection and for diagnostics). The remaining 8 MF-coils are pairwise identical, with the two coils of each pair being assembled in symmetric position to the vertical midplane of a module and rotated by 180° on the horizontal coil axis [2] (fig. 1).

The applied magnetic forces and thermal loads impose high stresses on the coils and their support system. This together with physical and electrical requirements leads to specific problems in the manufacture and construction of the normal conducting Cu-coils:

- The dominating circumference stresses (typical average of 100 MPa over the coil cross-section) dictate the use of cold-hardened copper conductors.
- The generation of heat inside the coils requires an internal water cooling system.

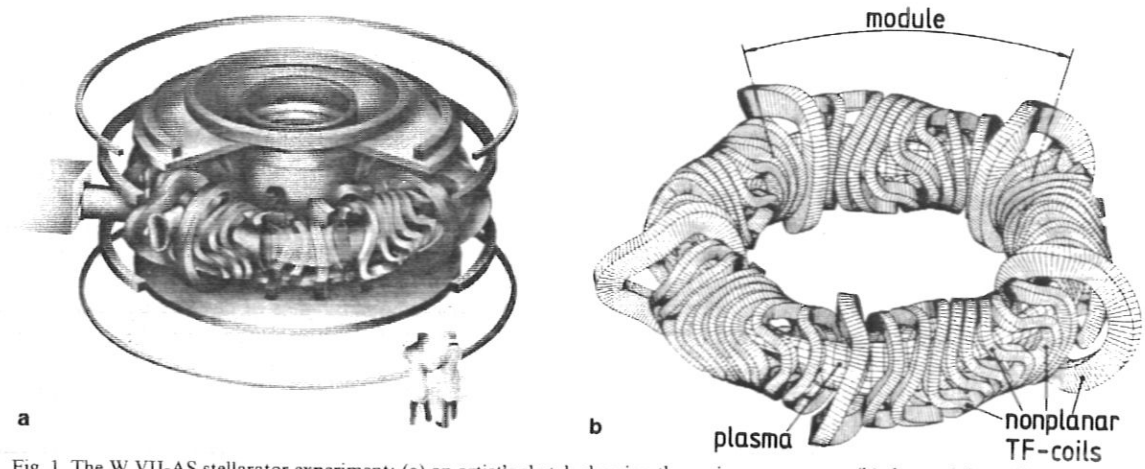

Fig. 1. The W VII-AS stellarator experiment: (a) an artist's sketch showing the main components, (b) the modular coil set only.

- The conductors must be three-dimensionally bent to radii of less than 0.1 m (minimum radius of curvature 0.08 m).
- For physical reasons the coil geometry must conform to strict tolerances. The error in the magnetic field principally has to be kept within a precision of 10^{-3} or better, referred to the theoretical field calculated from exactly located currents in the coil areas. The most sensitive influence is caused by deviations in the geometric symmetric conditions within the modules and from coil to coil. These deviations destroy the good confinement properties of the field. Therefore a high reproducibility of geometries has to be achieved. Against this the absolute coil contour deviation referred to a theoretical reference contour is of minor importance for a given machine because the wanted field configuration is not principally destroyed by a slightly altered coil set, yet the scientific goal of a machine might be depreciated if the field is modified significantly due to the contour deviations.
- An electrically and, owing to the applied loads, also mechanically reliable insulation system is necessary.
- The final mechanical and electric strengths of the coil have to be achieved by resin impregnation and curing in a high-precision mould.

The forming of rigid high-strength conductors capable of withstanding the applied mechanical stresses would involve the difficulty of appreciable conductor

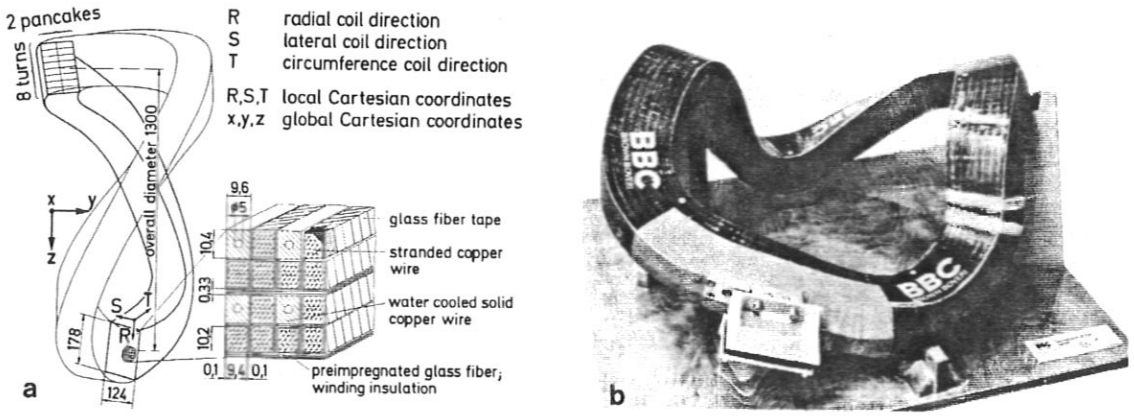

Fig. 2. Nonplanar MF-coils for W VII-AS: (a) coil concept composed of 2 pancakes and 16 copper turns separated by impregnated fibre-glass matting, (b) one field coil (number 1) before assembly.

"spring back" after coil forming and the possibility of insulation damage during coil forming (see, for example, [3]). To minimise these problems, the conductors are subdivided and each is built up from 160 single strain-hardened copper strands (0.8 mm in diameter each) joined together to a flexible, stranded copper wire and wrapped with glass-fiber tape. After extrusion (without using grease) the single copper strands are subsequently treated with an aliphatic polyamide primer (DZ80 from CIBA). This prevents oxidation and improves the adherence of the epoxy-resin to the wire surface. For cooling purposes solid, soft-annealed copper wires are added to the pack of stranded wires when they are wound into a mould to build up the coil. Oxides on the surfaces are removed by sandblasting and the primer painted on the surface. The inter-turn, pancake and surface insulation is provided by pre-impregnated high-strength glass-fibre tapes, composed of Silan-sized glass (fig. 2). Such an insulation system combines high dielectric strength and mechanical rigidity. To achieve mechanical rigidity, the coil is finally vacuum/pressure-impregnated with an epoxy resin system. The latter is a composition of Bisphenol A-type epoxy resin, MNA hardener and an accelerator. Before impregnation the conductor pack is pressed down to its final shape within the rigid mould [3]. After pre-drying, impregnation is carried out under vacuum, and finally the resin is polymerised (jellified and cured) [4].

The nominal magnet design parameters for the MF-coils are an operating time of 5 s equivalent rectangular current at full magnetic field – 3.0 T on plasma axis – with a duty cycle of 1 pulse every 180 s. The nominal coil current will be 592 kA and the copper cross-section is 14 640 mm^2. For the enlarged MF-coil the coil current is 1 480 kA, and the copper cross-section 36 600 mm^2 (filling factor appr. 67.5% related to an outside coil cross-section of 100%). Ohmic losses during the duration of the pulse (mean terminal resistance 1.21 mΩ). lead to a temperature rise of the coolant water along the cooling path relative to the coolant inlet temperature.

In spite of the pulsed operation of the magnet the maximum temperature rise within the coil was calculated for steady-state conditions using a finite-element program and a simplified equivalent model. This calculation permits a conservative evaluation of the maximum temperature rise for each point along the wire and across its cross-section relative to the water inlet position. The measured temperature rise per duty cycle of the coil is, as expected, lower than that calculated [5].

To limit mechanical stresses the nonplanar coils must be sufficiently well supported against the magnetic forces but, nevertheless, allow some relative motion of the coils within this support structure. A system comprising the coil arrangement, the support elements and the support structures was therefore selected to build up the confinement magnet [6].

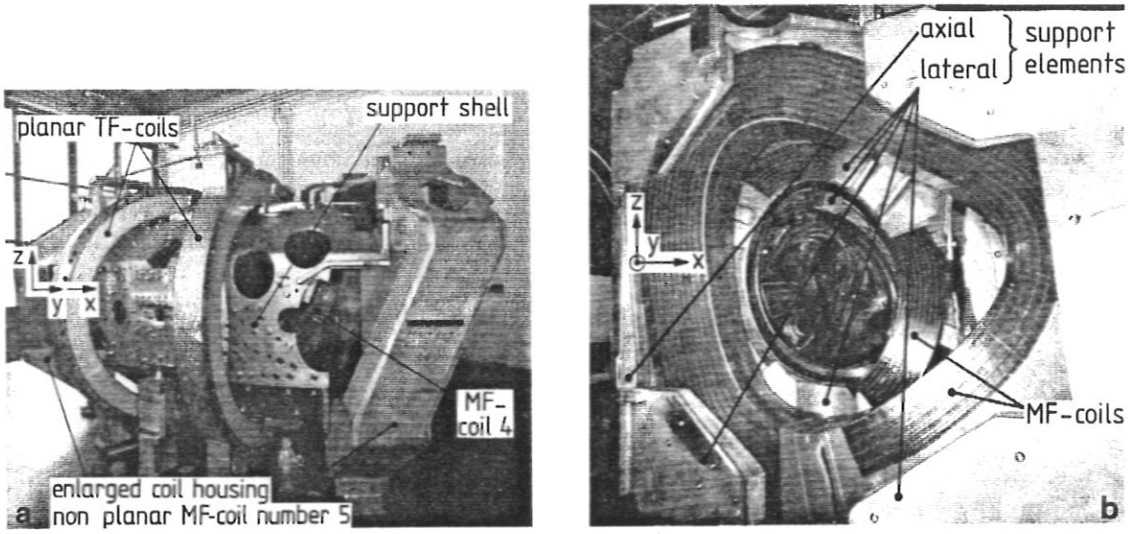

Fig. 3. An assembled module of the magnetic confinement system (only magnetic confinement system, vacuum vessel not installed): (a) seen from the outside, (b) view into one module.

The support structure for 8 of the nonplanar coils of one module is an external toroidal shell composed of two symmetric segments. It is a welded stainless-steel structure of 20 mm thickness (fig. 3a). Additional cast austenitic-steel support elements fix the lateral coil position (fig. 3b). Fiber slip coatings between the coil and the support elements considerably reduce friction if motion parallel to the surface occurs. The cast stainless-steel elements fixing the radial (R-direction) coil position are designed to support the coil on outside. This is done in the area determined by the sectional plane of the radial magnetic net force vector of one coil with the external shell, this force component being transmitted from the coil to the shell by pure pressure alone. All these structural members for one module are bolted together, forming the one part of the MF-coil support system. The second part of the system comprises single housings for each of the enlarged coils, these performing all of the functions already described (e.g. force transmission from the coil to the supporting structure (fig. 3).

Magnetically and thermally induced coil movements within these support systems are allowed in the radial and longitudinal coil directions and are prevented in the axial (lateral or toroidal) direction with respect to the coil plane. When the coil set is energised, the main magnetic force components are carried in different ways: the primary radial magnetic force is essentially carried by the cold-hardened copper conductor as (hoop) tension stress, while the lateral force component has to be transferred to the shell structure by support elements.

2.2. *Stress analysis – Magnetic confinement system*

The computational analysis of the structural mechanical behaviour for the W VII-AS MF-coils commenced by calculating the principal loads acting on the magnetic confinement system. The influence on displacements and stresses by the partially restrained coil movement described above is considered in the structural mechanical analysis, whereas (mutual inductance, electromagnetic fields and) magnetic volume forces for the single coils in the set arrangement are calculated in advance.

These calculations are done for critical magnetic force loading conditions occurring at a resulting magnetic field of 3.5 T on the plasma axis; an induction of 3 T is provided by loading the nonplanar MF-coils with their design current, and up to ± 0.5 T is provided in addition by the 10 additional planar TF-coils. The self and mutual inductances and electromagnetic forces for the coils were calculated with the EFFI (Electromagnetic Field, Force and Inductance) 3D computer program [7]. The magnetic field distribution or $\boldsymbol{B}$-vector field is computed by means of Ampere's law, and the magnetic pressure distribution by the vector cross product $\boldsymbol{J} \times \boldsymbol{B}$. Electromagnetic forces only act in the locally radial (R) and lateral (S) coil directions, whereas in the circumferential (T) direction (fig. 2a) no forces are induced owing to the electric current flow in this direction. These magnetic load calculations include the two principal components of the forces on these coils, coil self-forces on the individual coils and interactive forces between adjacent coils.

The basic model used for this electromagnetic calculation was the coil arrangement, the coils being represented as a series of connected, curved current density elements. The EFFI mesh discretisation depends on the mesh used for the structural mechanical analysis and will be shown later.

For mechanical reasons the coils must be allowed to expand in the radial and longitudinal directions by using antifriction coatings between the coils and support elements. Because thermally and magnetically induced movements in the lateral direction of these nonplanar coils are constrained, additional mechanical loads are applied. The influence of this load component on stresses and strains is considered in the the structural mechanical calculation.

The most critical load combination for the magnetic confinement system appears at the end of the flat-top time (to be precise: at the onset of de-energization of the coil set), at which:

- the maximum magnetic forces are applied,
- the maximum temperature difference between the coils and the support system appears (a conservative value being 55 K),
- the maximum coil temperature (worst case 80 °C → maximum temperature difference, maximum coolant temperature, steady-state conditions) with the lowest material strength values occurs.

If the expected safety margin at the end of this analysis were insufficient, the latter two temperatures and/or temperature differences would have to be restricted to less critical values.

First finite-element calculations using the SAP V code [8] together with material tests [9] demonstrated possible damage mechanisms (fatigue fracture or delamination of the copper wires and insulation system; permanent local deformation of the support structure). This knowledge served as a basis for a more detailed analysis using the MSC/NASTRAN code [10]. The inhomogeneous coil design leads to highly anisotropic and heterogeneous structural behaviour of this com-

posite system. For economic and numerical reasons, however, it is not possible to perform a 3D stress analysis giving separate consideration to each constituent of the coil. Instead, this system is replaced by an equivalent homogeneous orthotropic solid, whose material properties were calculated and/or measured (see Section 2.3). The overall material properties are described by nine engineering constants. Finally, the stress components for the constituent materials must be evaluated with due consideration of mechanical equilibrium and compatibility.

Three basic types of MSC/NASTRAN [10] finite-element structural models were used [11]. In a first model critical components of the coil support system had been selected. These results served as a basis for a detailed model of the most endangered component in this compound, the nonplanar coils. Special attention is directed to the coil with minimum radius of compound curvature (8 cm), which was found to be the modular field coil number 3 [12]. In a last step, this model is considerably refined in order to generate detailed stress tensors for those critical coil areas selected by comparing the results obtained from the FE analysis with the material behaviour of the coils.

If numerically possible, the geometry of the NASTRAN finite-element mesh for the coils or the coil cutout coincides with the EFFI current density element discretisation. This facilitates the transformation of the magnetic body forces (calculated with the EFFI code) to the kinematically equivalent nodal force components (volume forces) necessary as input data for the structural finite-element analysis.

2.2.1. Initial FE analysis

The initial model for the linear elastic FEM calculations was a 1/10 section of the assembly of all MF coils and their support system.

Restriction to such a reduced model is possible by utilising the given modularity of 5 and taking advantage of the geometry and magnetic load symmetries of the W VII-AS test device within one module. Gravity loads disturbing these load symmetries are negligible with respect to the magnetic loads. The enlarged coil, located in a single housing, is treated separately.

To generate the force data, an EFFI single-filament model representing each coil by 48 rectangular general current density elements (GCEs) was used (fig. 4). The coil geometry is described by the coordinates of the 4 coil edges at the boundaries of the GCEs. The NASTRAN mesh is achieved with different types of elements. The 4 nonplanar coils are meshed with 48 isoparametric 20-node solid hexahedron elements used

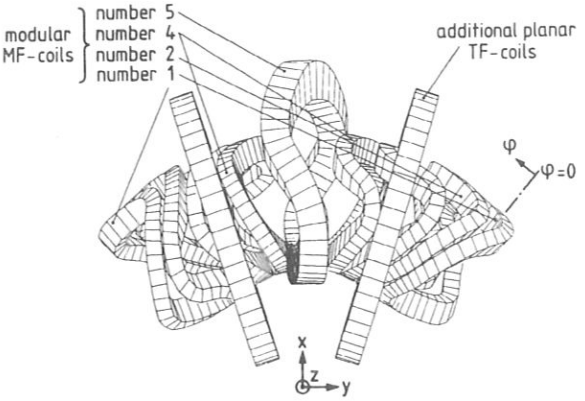

Fig. 4. Subdivision of one modular coil set into GCEs for the initial electromagnetic calculations.

for each coil (6912 d.o.f); for the support shell 653 quadrangular 8-node and 62 triangular 6-node plane-shell elements are used (11975 d.o.f); 298 hexahedron and 22 pentahedron solid isoparametric elements are used to model the support elements (6858 d.o.f); (e.g. figs. 5b, 5c and 6b for the FE subdivision).

The antifrictional coatings between the coils and their support elements in reality only allow the transmission of compressive (and shear, if $\mu \neq 0$) forces, but not of tension force components perpendicular to the sliding surface. On the contrary, after the first computer run tension forces appeared in the calculations between these two components. Thus, in a second run all activated rigid-body connections exhibiting tension force components (132 out of originally 512) are disconnected. After this second run only small tension force components appeared at very few coil lateral surface FE nodes. In the deformation plots no undue intersections of the coils and their support elements are detectable. No further calculation run was therefore necessary.

With this initial analysis it was primarily the mechanical behaviour of the external support structures that was examined. For these components (manufactured from isotropic material) we calculated the equivalent (Von Mises) stresses (fig. 5). It was then compared with S_m, the safe stress at room temperature for the materials used. The calculated equivalent stresses for the support elements as well as for the support structure are lower than S_m. For these parts of the magnetic confinement system the results obtained show that the stresses are acceptable.

Maximum equivalent stresses were analysed for the nonplanar coils with peak values of up to only 100 MPa (fig. 5). Nevertheless, the decision whether this stress is

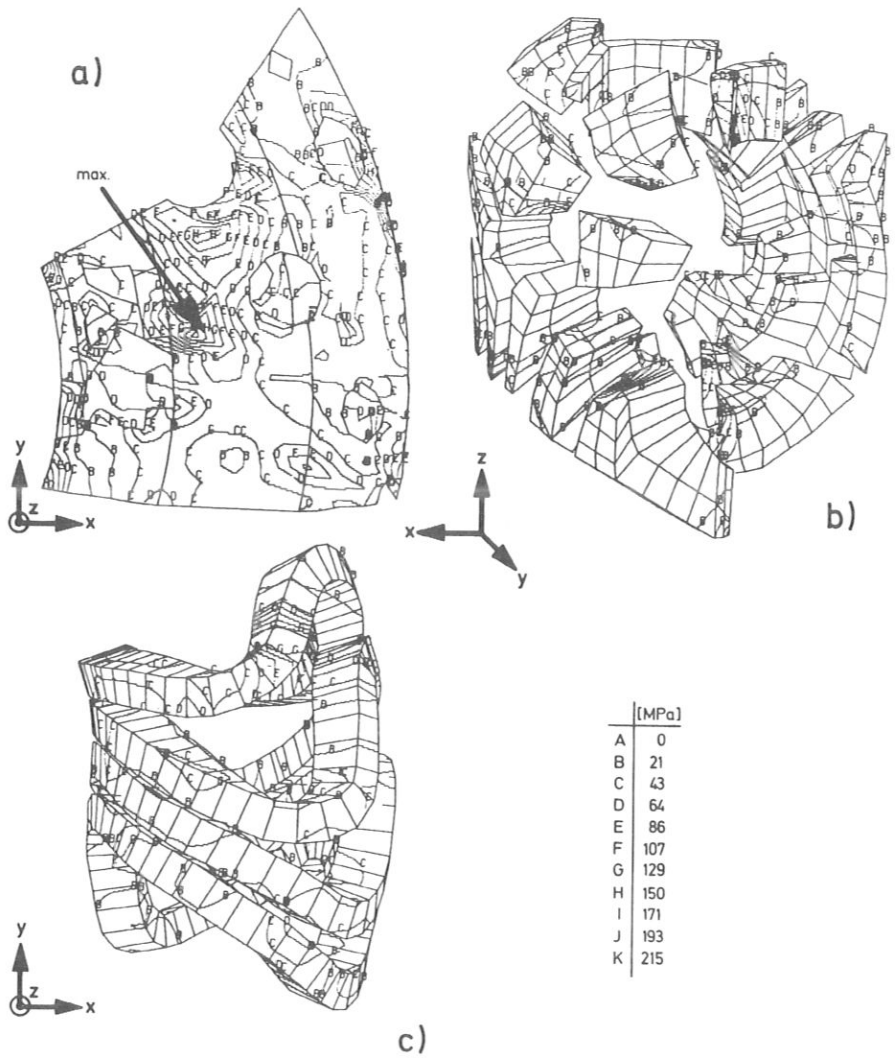

Fig. 5. Von Mises stresses from the initial stress analysis (1/10 section of the magnetic confinement system; isoequivalent stress contour plots): (a) support shell, (b) supporting structure, (c) nonplanar coil array.

admissible or not requires special attention due to the heterogeneous coil design with direction-dependent permissible stress values.

The maximum deflection of 1.17 mm for the support system occurs at the external shell (fig. 6).

2.2.2. Detailed FE analysis

In order to analyse more exactly the mechanical behaviour of the coils, each of the 5 geometrically different nonplanar coils was separately treated. Also included in the first FE models were all adjoining support elements [8,9,11]. As expected, the maximum critical stress components (primary shear and hoop stresses) occurred in the coil with minimum radius of curvature (8 cm) – viz. coil number 3 – and vice versa [11,12]. All investigations were thus focused on coil 3.

The electromagnetic force calculations were done with an EFFI multifilament model representing the analysed coil by 768 rectangular GCEs. The other 54 coils – 44 nonplanar and 10 planar – of the experimen-

posite system. For economic and numerical reasons, however, it is not possible to perform a 3D stress analysis giving separate consideration to each constituent of the coil. Instead, this system is replaced by an equivalent homogeneous orthotropic solid, whose material properties were calculated and/or measured (see Section 2.3). The overall material properties are described by nine engineering constants. Finally, the stress components for the constituent materials must be evaluated with due consideration of mechanical equilibrium and compatibility.

Three basic types of MSC/NASTRAN [10] finite-element structural models were used [11]. In a first model critical components of the coil support system had been selected. These results served as a basis for a detailed model of the most endangered component in this compound, the nonplanar coils. Special attention is directed to the coil with minimum radius of compound curvature (8 cm), which was found to be the modular field coil number 3 [12]. In a last step, this model is considerably refined in order to generate detailed stress tensors for those critical coil areas selected by comparing the results obtained from the FE analysis with the material behaviour of the coils.

If numerically possible, the geometry of the NASTRAN finite-element mesh for the coils or the coil cutout coincides with the EFFI current density element discretisation. This facilitates the transformation of the magnetic body forces (calculated with the EFFI code) to the kinematically equivalent nodal force components (volume forces) necessary as input data for the structural finite-element analysis.

2.2.1. Initial FE analysis

The initial model for the linear elastic FEM calculations was a 1/10 section of the assembly of all MF coils and their support system.

Restriction to such a reduced model is possible by utilising the given modularity of 5 and taking advantage of the geometry and magnetic load symmetries of the W VII-AS test device within one module. Gravity loads disturbing these load symmetries are negligible with respect to the magnetic loads. The enlarged coil, located in a single housing, is treated separately.

To generate the force data, an EFFI single-filament model representing each coil by 48 rectangular general current density elements (GCEs) was used (fig. 4). The coil geometry is described by the coordinates of the 4 coil edges at the boundaries of the GCEs. The NASTRAN mesh is achieved with different types of elements. The 4 nonplanar coils are meshed with 48 isoparametric 20-node solid hexahedron elements used

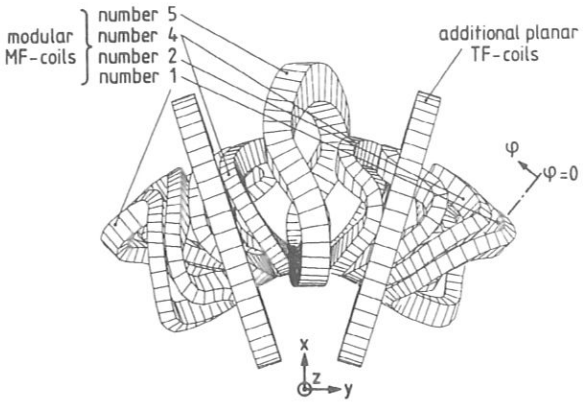

Fig. 4. Subdivision of one modular coil set into GCEs for the initial electromagnetic calculations.

for each coil (6912 d.o.f); for the support shell 653 quadrangular 8-node and 62 triangular 6-node plane-shell elements are used (11975 d.o.f); 298 hexahedron and 22 pentahedron solid isoparametric elements are used to model the support elements (6858 d.o.f); (e.g. figs. 5b, 5c and 6b for the FE subdivision).

The antifrictional coatings between the coils and their support elements in reality only allow the transmission of compressive (and shear, if $\mu \neq 0$) forces, but not of tension force components perpendicular to the sliding surface. On the contrary, after the first computer run tension forces appeared in the calculations between these two components. Thus, in a second run all activated rigid-body connections exhibiting tension force components (132 out of originally 512) are disconnected. After this second run only small tension force components appeared at very few coil lateral surface FE nodes. In the deformation plots no undue intersections of the coils and their support elements are detectable. No further calculation run was therefore necessary.

With this initial analysis it was primarily the mechanical behaviour of the external support structures that was examined. For these components (manufactured from isotropic material) we calculated the equivalent (Von Mises) stresses (fig. 5). It was then compared with S_m, the safe stress at room temperature for the materials used. The calculated equivalent stresses for the support elements as well as for the support structure are lower than S_m. For these parts of the magnetic confinement system the results obtained show that the stresses are acceptable.

Maximum equivalent stresses were analysed for the nonplanar coils with peak values of up to only 100 MPa (fig. 5). Nevertheless, the decision whether this stress is

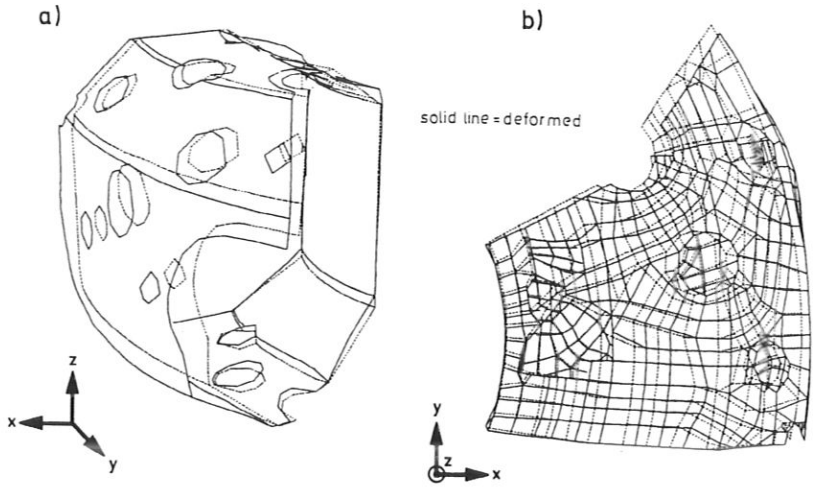

Fig. 6. Deflected and undeflected forms of a 1/10 section of the support shell (scaling factor = 100), initial stress analysis: (a) seen from outside the machine, only body edges considered, (b) top view, FE structural model.

tal device are less finely subdivided for economic (calculation time and available storage) reasons. Coil 3 is divided along its perimeter, into 96 sections or groups of GCEs (GGCEs), each section including 8 subcoils (2 by 4).

For the MSC/NASTRAN analysis the coil is idealised by means of 768 3D isoparametric 8-node solid hexahedron elements, the same subdivision being used as for the EFFI mesh. The adjoining support elements are idealised by 702 elements of the same type as used for the coil (fig. 7). To realise free coil movement between the lateral support elements and the coil for the calculations, there are in the interface two separate FE nodes for the two components, connected by multipoint

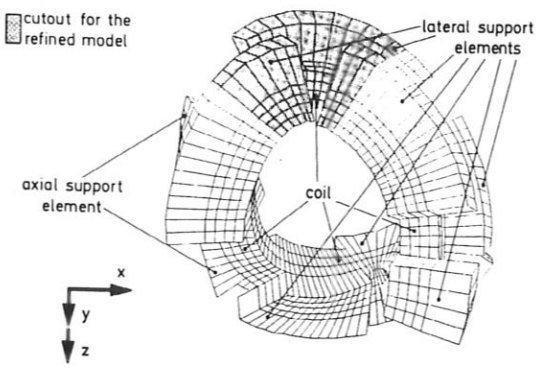

Fig. 7. FE structural model for the detailed stress analysis of modular field coil 3, including the adjoining support elements.

constrains [10]. Frictionless coil movement is realised by coupling just the two translational degrees of freedom normal to the interfaces. The whole model is thus built up from 3321 nodes. The kinematic support of the selected cutout (coil with adjoining support elements) was achieved by fixing the support elements in the connecting areas to the external support shell. A linear elastic analysis is made for a homogeneous solid with anisotropic material behaviour for the coil (isotropic for the support structure). Owing to the coil design (fig. 2a), the axes of anisotropy follow the edges of the coil and the edges of the normal cross-section.

The maximum deflection calculated is 2.8 mm and occurs at the coil in an area radially outside the W VII-AS device, of which 1.2 mm is due to thermal expansion (the rest being induced by the magnetic loads). The deflection on the inside of the device is negligible (fig. 8). This is because the magnetic force distribution results in a net force component towards the torus axis, thus pushing the coils against the very stiff support elements positioned inside which fix the radial coil position, and a second component which stresses the coil similar to a vessel under inside pressure.

As represented in the next section, the failure behavior of such a compound in a multiaxial stress field may be best described by separately considering the two main constituents of the coil, the copper wires and the insulation system. Only selected stress components of the analysed stress tensor will essentially contribute to the failure of these constituents. The impregnated copper wires are thus mainly endangered by circumference

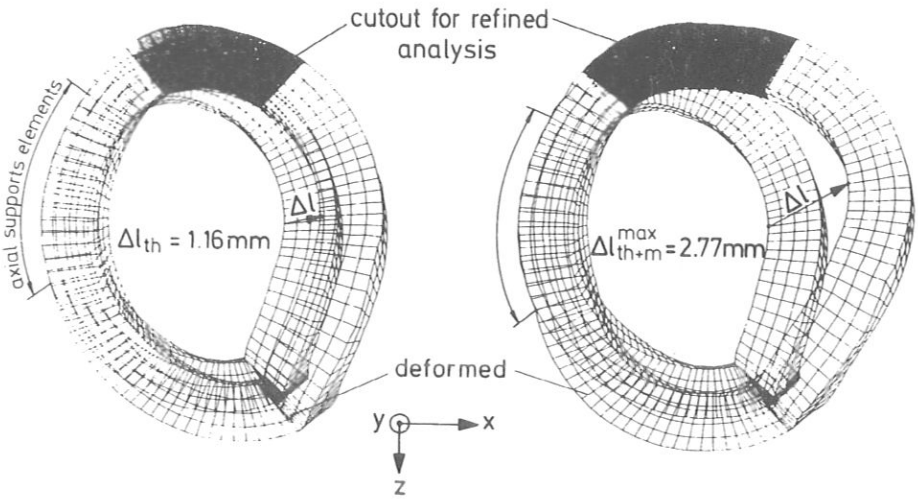

Fig. 8. Deflected and undeflected forms of modular field coil 3 (scaling factor = 100), detailed stress analysis: (a) deflection induced by thermal expansion, (b) superposed thermal and magnetic deflection.

(σ_T) and shear ($\tau_{R,T}$; $\tau_{S,T}$) stresses, the insulation system by out-of-plane direct (σ_T or σ_S) and in-plane shear ($\tau_{R,T}$ and $\tau_{R,S}$ or $\tau_{S,T}$ and $\tau_{S,R}$ respectively) stresses (for further details see Section 2.3 and [8,9,11,12,13,14]). On this basis, critical stress combination for these two constituents are selected from the FE analysis.

Comparison of these results with measured material strength values showed that two critical stress combinations endangering the impregnated stranded copper wires occurred:

(a) Superposed on the maximum hoop stress of σ_T = 105 MPa (applied to the whole coil cross-section) is a shear stress component of 12 MPa. The failure criterion with such a biaxial stress field (a first approximation) would be yielding of the copper wires; measurements distinctly indicated higher values for the yield strength – even on the assumption that only the copper wires will carry the hoop stresses (copper volume filling factor is $\geqq 0.63$).

(b) Superposed on the maximum shear stress of $\tau_{ST} = 55$ MPa in the copper wires is a direct stress component of $\sigma_T = 50$ MPa in the wire direction. The failure criterion here would be delamination in the impregnated copper wires. From the mechanical tests carried out it can be deduced that this load combination is more critical.

Based on adequate conclusions critical stress combinations for the insulation system and/or the adhesive interface plane are as follows:

(a) maximum in-plane shear stress of $\tau_{ST} = 55$ MPa with superposed out-of-plane direct (tension) stress of $\sigma_S = 13$ MPa,

(b) maximum out-of-plane tension stress of $\sigma_R = 20$ MPa with superposed in-plane shear stress of 18.5 MPa (resulting from $\tau_{R,T}$ and $\tau_{S,R}$),

(c) in-plane shear stress of 26 MPa with superposed out-of-plane tension stress of 10 MPa. The failure criterion for all three stress combinations would be delamination in the insulation system or adhesive/cohesive breakdown of the insulation/copper wire bond face. When comparing these results with measured strength values, one can conclude that all 3 cases are critical.

All critical stress combinations in the insulation system as well as the most critical for the copper wires are located in or around the coil area with maximum curvature. The accuracy of the calculated stresses can be estimated by, for example, checking the stress distribution at free surfaces and edges. It is then readily seen that the idealisation accuracy is not sufficient. Further mesh refinement is therefore necessary.

2.2.3. Refined FE analysis

The last step in the successive mesh refinement was to idealise the mechanically most endangered part of the coil separately. This selected cutout of the coil contains a strongly curved part of MF-coil 3 and will allow more detailed classification of the strain conditions.

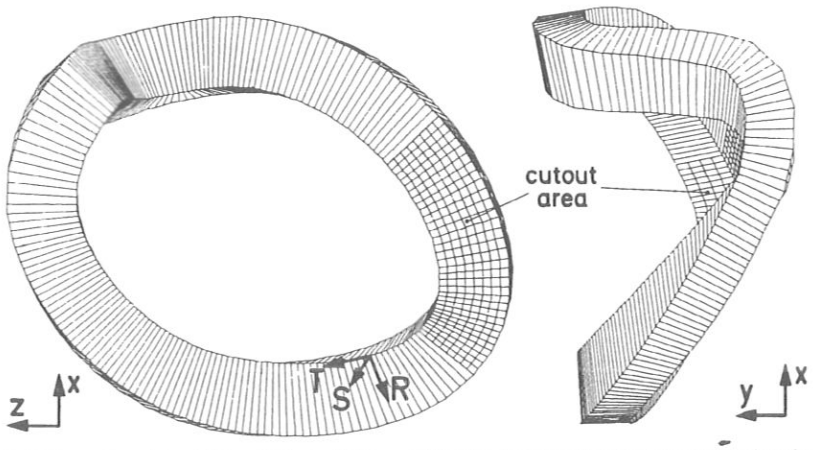

Fig. 9. Subdivision of modular field coil 3 into GCEs and GGCEs for the refined electromagnetic calculations.

The refined EFFI multi-filament model for the selected cutout contains along its perimeter 18 sections (114 for the whole coil; for the cutout each GGCE of the detailed FE analysis is divided into 2 new GGCEs), each section of the cutout including 60 subcoils (6 by 10). The rest of these coils and, as before, all adjoining coils are coarse-meshed (fig. 9). Because of the comparatively steep gradient in the magnetic volume loads in the coil cross-section – in contrast to the coil circumference direction – the mesh subdivision in the latter direction is less fine. The kinematically equivalent nodal force components at the NASTRAN nodes were computed by interpolating the body force values at the EFFI mesh (by BQUIN [15]).

The mesh for the structural analysis is achieved with the same element type as for the detailed FE analysis. The coil circumference direction is now meshed by 60 elements; in the coil circumference direction the cutout is subdivided into 30 sections (1 800 elements). The mesh of the adjoining support structure (440 elements) coincides at the contact faces with the coil mesh. Includes is now an elastic bed–meshed by 400 elements – built up from a glass/epoxy-resin composite and arranged between the coil and the support structure. The boundary conditions at the end sections of the cutout were derived from the detailed FE analysis, care being taken that the results from the latter were put in as prescribed displacements. All other boundary condi-

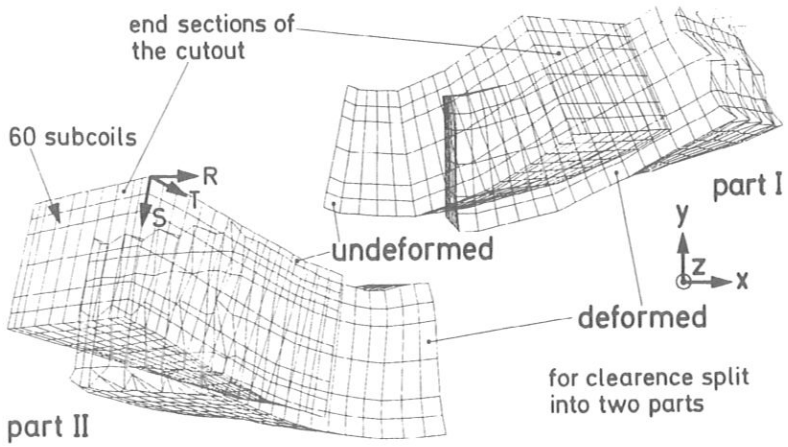

Fig. 10. Deflected and undeflected forms of the cutout of modular field coil 3 (scaling factor 10), refined stress analysis.

tions (e.g. realizing the coil movement; support conditions; material behaviour; two computer runs for realising force transmission from the coil to the support structure by compression loads only) are as before. The whole structure consists of 3763 grid points.

For the new calculations the resulting displacements from the coarse analysis are prescribed only at the grid points of the first analysis; no interpolation for the displacement tensor for any of the other nodes was carried out (fig. 10). All results at the end sections of the cutout are thus inaccurate; the influence of this simplification outside the end sections of the cutout is negligible.

The displacements calculated with the refined model are comparable to those obtained with the coarse model.

The critical stress combinations were selected on the same basis as described for the detailed analysis. For the impregnated, stranded copper wires the results obtained are not much different from those of the previous analysis (limited of course to the coil cutout): Superposed on the maximum hoop stress of $\sigma_T = 92$ MPa in the copper wire (all values applied to the whole coil cross-section) is a shear stress component of $\tau_{R,T} = 20$ MPa (previous analysis in the same area: $\sigma_T = 70$ MPa/$\tau_{R,T} = 16$ MPa). Superposed on the maximum shear stress in the copper wire of $\tau_{S,T} = 39$ MPa is a hoop stress of $\sigma_T = 37$ MPa (previously $\tau_{S,T} = 55$ MPa, $\sigma_T = 52$ MPa).

From many material tests and a prototype coil test (see Section 2.3 and [5,9,11,12,13,14,16]) no risk of fracture or delamination in the impregnated, stranded copper wires, even under fatigue loads is seen.

All critical stress combinations for the insulation system/interface planes detected from the detailed analysis are concentrated on the selected cutout. In this refined analysis these combinations are as follows:

(a) Maximum in-plane shear stress $\tau_{T,S} = 39$ MPa ($\tau_{RS} \approx 0$) with superposed out-of-plane tension stress of $\sigma_R = 15$ MPa;

(b) Maximum out-of-plane direct tension stress of $\sigma_R = 20$ MPa with superposed in-plane shear stresses of $\tau_{R,T} = 16$ MPa;

(c) out-of-plane direct compressive stresses in the analysed order of magnitude (up to 90 MPa, negligible shear) considerably reduce the risk of interface damage and delamination if in-plane shear stresses act simultaneously; the maximum combination of out-of-plane direct stress $\sigma_S = 60$ MPa and superposed in-plane shear stress $\tau_{S,T} = 20$ MPa will thus not cause damage to the insulation system.

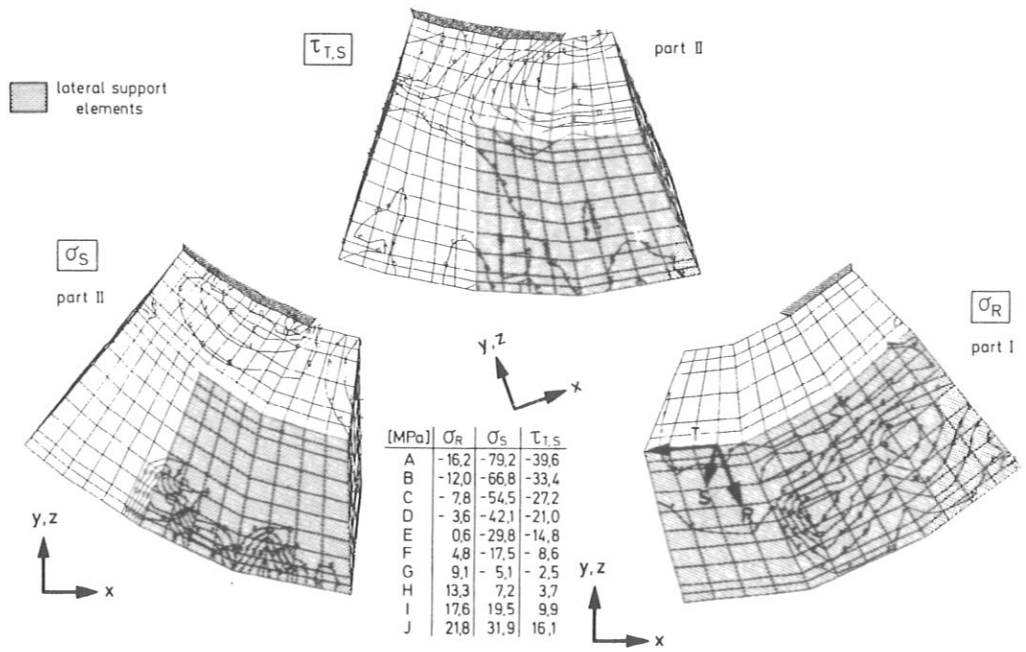

[MPa]	σ_R	σ_S	$\tau_{T,S}$
A	-16,2	-79,2	-39,6
B	-12,0	-66,8	-33,4
C	- 7,8	-54,5	-27,2
D	- 3,6	-42,1	-21,0
E	0,6	-29,8	-14,8
F	4,8	-17,5	- 8,6
G	9,1	- 5,1	- 2,5
H	13,3	7,2	3,7
I	17,6	19,5	9,9
J	21,8	31,9	16,1

Fig. 11. Selected stress components from the refined stress analysis for the cutout of modular field coil 3 (isoequivalent stress contour plots).

Most critical is the first-listed load combination, occurring in T–R planes (so-called pancake insulation layers, see fig. 2a). Normal insulation systems would not be capable of withstanding this load combination, but the special design selected for these planes with special insulation materials used (prepreg layers; see [9,16]) will considerably raise the limiting range of stresses. For manufacturing reasons this reinforcement is not possible in T–S insulation planes with the maximum load listed in second place. Nevertheless, the insulation system chosen will withstand this maximum load combination occurring in the insulation planes (direct tension 20 MPa, shear stress 16 MPa) for the envisaged lifetime of the W VII-AS device, 5×10^4 load cycles, at 80 °C.

One of the important problems in this analysis was to calculate very accurately the (comparatively small) stress components endangering the coil, whereas, for mechanical strength reasons, the dominant stress is not a limiting factor. But this is known to be difficult if displacement models are used. Especially for this refined analysis, it was found that boundary conditions, such as stress-free edges, disappearance of in-plane shear and out-of-plane direct stresses at free surfaces, or negative out-of-plane direct stresses and disappearance of in-plane shear stresses ($\mu = 0$ postulated) at sliding surfaces, are very accurately satisfied (fig. 11).

2.3. Material tests – Magnets

The maximum calculated Von Mises stress for the support shell – a welded stainless-steel structure – was 190 MPa, localized to a very small area (fig. 5a). The yield strength limit, which for an austenitic steel in a first approximation is equal to the fatigue strength limit, for type 304 LN (German Standard 1.4311) is 270 MPa. Because the cast austenitic support elements are less stressed than the shell (fig. 5b), there should be no fracture risk for this structural member of the confinement system either. Both of these components are designed for minimum deformation.

The elastic bed and antifrictional coating between the support elements and the coil are primarily stressed by compressive loads. They rise to 90 MPa. Neither the function of the fibre slip coatings – low coefficient of friction – nor that of the elastic bed (8 mm thick on average) – large area adaption of the steel elements to the nonplanar coils, which could possibly be made worse by creep processes – should be influenced.

More complicated is the mechanical valuation of the nonplanar coils because of the heterogeneous coil design exhibiting orthotropic material behaviour. For clarity, in a first step the two main constituents of the coil, the impregnated, stranded copper wires and the insulation system, are considered separately. Later on, the mutual interference of these two constituents is additionally investigated. Because strength values for this specific design of nonplanar coils are not available, an extensive test program for measuring material properties was carried out (see also [5,6,8,9,11,12,13,14,16]).

2.3.1. Stranded copper wire

The mechanical strength tests started with the single copper strands of the stranded copper wire. The material used for these strands is Ag-alloyed 0F-copper (0F–CuAg 0.1, German Standard DIN 1787/17666/40500), strain-hardened to a yield strength of $\geqq 230$ MPa. The silver content guarantees that there is no strength loss even under the final impregnation process at elevated temperature. The corresponding material tests were carried out after precipitation of the copper wires for 20 h at 150 ° and 1 h at 300 °C, and no strength reduction could be detected after this treatment. Complete and satisfactory priming of the strands was ensured by controlling the priming process (e.g. surface purity, extrusion velocity, primer bath viscosity, furnace temperature). The epoxy-resin used is described in Section 2.3.2.

The impregnated stranded copper wires are arranged within the coils in such a way as to be able to carry the dominating stress component occurring in such a construction unit, which is the hoop or tangential direct stress component. Besides this dominating stress component, there is also secondary an (external) shear stress $\tau_{R,T}$ and $\tau_{S,T}$ of up to 39 MPa endangering the nonplanar coils. Owing to the stranding angle of 10 ° of the single copper wires to the (tangential) T-direction and the inhomogeneous strand design (copper and epoxy-resin) the tangential direct stress component leads to micro-mechanical additional stress components of approximately $\tau_{internal} \approx 0.17\ \sigma_T$ occurring between single copper strands [9,14,17] which are superposed on the external shear stresses $\tau_{S,T}$ and $\tau_{R,T}$.

In order to find out whether or not the copper wires are mechanically endangered by the given (calculated) stress combinations, static and dynamic material tests with individual, vacuum-pressure-impregnated, stranded copper wires were carried out. Possible damage mechanisms occurring under the given mechanical loads are yielding, fracture or fatigue fracture of the single copper strands and static or fatigue delamination between the single copper strands within the epoxy resin or at the epoxy/copper interface. The tangential direct stress component σ_T in the first case and the superposition of external and internal shear stresses in the second case

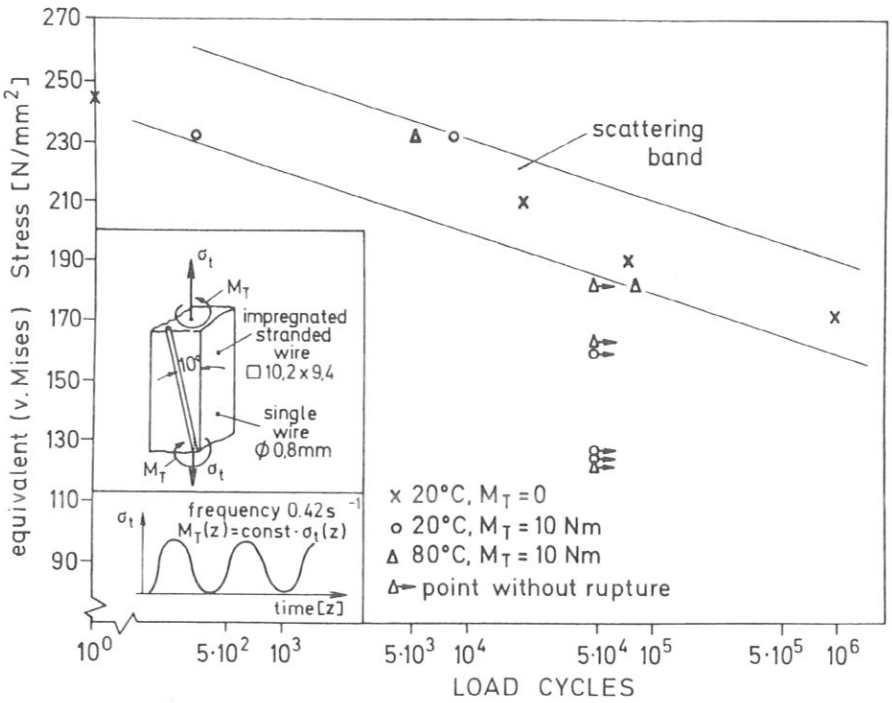

Fig. 12. Fatigue strength values under tension and combined tension–torsion loads for single-impregnated, stranded copper wires.

are the primary damage-inflicting loads. Static and dynamic tension and combined tension-torsion tests [9] were thus conducted (fig. 12).

The measured ultimate strength value in macroscopic pure static tension tests is 245 MPa, in pure fatigue tension tests at the envisaged lifetime of the test device (5×10^4 test cycles) appr. 190 MPa. The failure criterion is damage to the copper wires. Even under tension loads on which (external) torsional moments of 10 Nm are superposed, no delamination of the copper/resin interface or within the resin matrix occurs. The mechanical strength behaviour under these load combinations is essentially determined by the copper content. The results of the material tests are therefore summarised in a Wöhler Diagram, in which the maximum equivalent Von Mises stresses are plotted versus the load cycles (fig. 12). These equivalent stresses are calculated without taking into account the copper filling factor in the impregnated wire (app. 83%). The tests are carried out at 20 °C (room temperature) and 80 °C, the maximum temperature expected to occur in the nonplanar coils.

In this tension and combined tension/torsion fatigue tests the copper wires were undamaged after the envisaged lifetime of the device (5×10^4 cycles) with Von Mises stress values $\sigma_{vM} \leqq 190$ MPa. There is no significant difference in the lifetime of samples when the test temperature is varied between 20 ° and 80 °C, only the (dynamic) elongation and twisting amplitude are a little bit higher for the elevated temperatures. Contrary to this, the permanent twisting after the end of testing is at least 3 times as high at 80 °C. This is due to the elevated creep rate of the epoxy resin at this temperature.

From the FE calculations described in Section 2.2 and elsewhere [11,12] a maximum resulting equivalent stress in the stranded wire of 100 MPa can be calculated from the analysed stress tensors. This maximum stress value occurs in nonplanar field coil number 2 at maximum magnetic field values and maximum temperature. The value also takes into account the additional shear resulting from tensile stresses in the stranded wire. The available safety factor for the maximum load combination and an envisaged lifetime of the W VII-AS test device (5×10^4 full load pulses) is ≈ 1.9. The impregnated, stranded copper wires of the "compound" used in the coil should no be endangered under the given load combination.

2.3.2. Insulation system

The conventional vacuum-impregnated epoxy-glass insulation system chosen, Orlitherm OH 67-UM [19], is about the same as that used for the JET poloidal coils [20,21]. A primer is used to improve the adhesion of the resin matrix to the copper. The dielectric rigidity of the insulation system is ensured by the use of Silan-sized glass (pre-impregnated for use as insulation layers, dry glass tapes used to wrap the stranded wires). For such an insulation system the most critical stresses are in-plane shear (of the insulation layer) and out-of-plane direct tensional stresses or a combination of both. A special type of specimen (Type E, fig. 13), subjected to the same manufacturing processes as the nonplanar fields coils of W VII-AS has been developed.

First of all, these tests are useful for identifying strength-limiting components of all possible insulation/wire combinations of the insulation system. The result also serves to establish mechanical strength values. Tests have been carried out (see also [9,14]), using: (a) stranded wires only and dry glass; (b) solid wires only and dry glass; (c) stranded wires with one solid wire in the push-out position and dry glass; (d) stranded wires only and prepreg layers in selected positions; (e) stranded wires with one solid wire in the push-out position and prepreg layers in selected positions. The primer hardening conditions, the resin system combination as well as the impregnation and hardening conditions were identical in all 5 cases. In static tests the fracture load was first reached in samples built up from stranded copper wires only, wrapped with dry glass [9]. All other possible combinations – with solid wires and/or prepreg layers – show better mechanical resistance, with strength values up to 25% higher than the critical value. All further investigations were thus focused on these mechanically limiting wire/epoxy/glass combinations.

One of the problems of these E-type specimens (fig. 13) is the nonlinear shape of the in-plane shear and the additional appearance of out-of-plane direct stresses [13,14]. Thus, it is not readily possible to select the critical, failure-releasing stress combination.

Similar difficulties occur with B-, C- and D-type specimens [9,13,14,20] (fig. 13). The stress distribution for E-type specimens were calculated using finite elements, the results for the two most important stress components being shown in a simplified graph in fig. 14; for further information see [13,14]. $\bar{\tau}$ is the average shear stress, calculated from the applied load divided by the shear surface ($4\times$ the lateral surface of a stranded wire). Optimisation of the flexibiliser content and of the curing and hardening conditions of the resin as well as the use of accordingly tuned glass tapes improved the available fatigue strength of the insulation system for the envisaged lifetime of the device (5×10^4 load cycles)

specimen type	Ⓐ	Ⓑ	Ⓒ	Ⓓ	Ⓔ	Ⓕ
	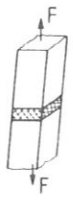	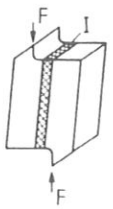	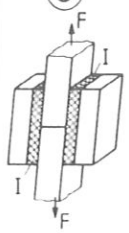	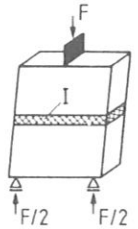	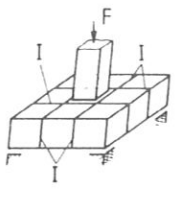	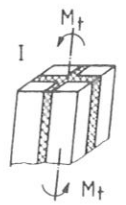
main insulation stress	tension	shear	shear	shear/pressure	shear	shear
main acting stresses	—	shear stress gradient in load-(insulation-) direction		add. out-of-plane pressure stresses	add. out-of-plane tension or compression stresses	shear stress gradient in cross section
wire type	not possible with stranded wires				for stranded wires	
references	Koch/Maix/Nylund; Last/Bond/Salpietro;	Koch/Maix/Nylund; Rauch/König/Schmid; Last/Bond/Salpietro;	Rauch/König/Schmid, Last/Bond/Salpietro;	Koch/Maix/Nylund; Rauch/König/Schmid; Last/Bond/Salpietro;	Mathis/Mukherjee/Sapper; Buck/Klee/Mathis; Buck/Osen/Bodisco/Winkler;	Buck/Klee/Mathis; Buck/Osen/Bodisco/Winkler;

Fig. 13. Different types of small test specimens (copper-insulation compound) used for measuring insulation strength values.

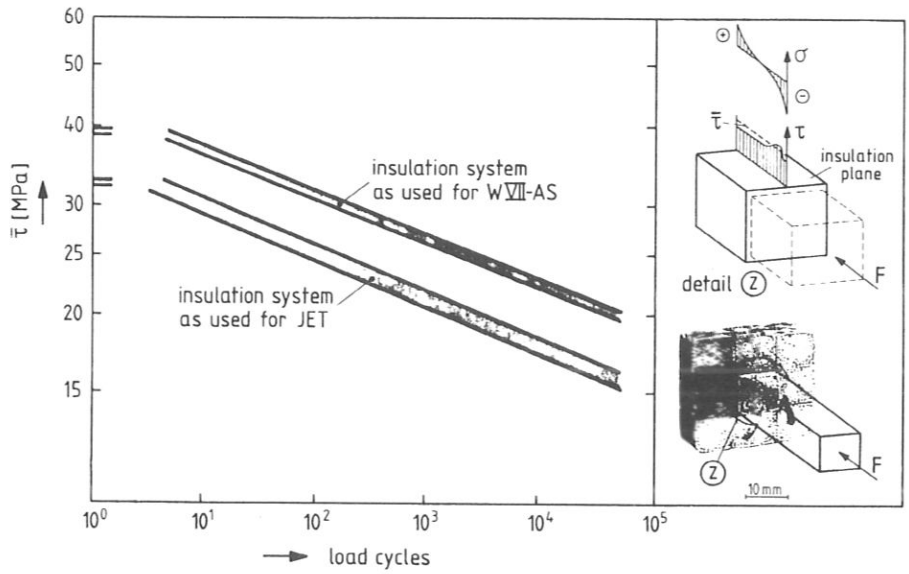

Fig. 14. Measured fatigue shear strength for two different types of insulation systems, ejection type test arrangement (80 °C, principal stress ratio $R = 0$, frequency 0.25 s^{-1}).

by appr. 30% (fig. 14). Test conditions such as temperature, frequency and so on have a decisive influence on the fatigue strength. For tests carried out using an F-type specimen, the optimised insulation system was found to have an endurable shear time strength after 5×10^4 load cycles of 20 MPa at 80 °C (for the shear stress distribution in this orthotropic compound torsion bar see [9,13,14]). Transferring these measured results to the coils is difficult because of some specimen-specific properties (e.g. occurrence of the shear stress peak at the surface – for the impregnation process different shrinkage conditions and different creep behaviour – or the shear gradient in the specimen cross-section – reduction of peak stresses by creep). Deducing a reliable strength value for such an insulation system in an approximately biaxial stress field is complicated by such specimen-specific shortcomings, e.g. in the shear stress distribution, in specimen preparation or through edge effects. This is reliable for all specimens given in fig. 13.

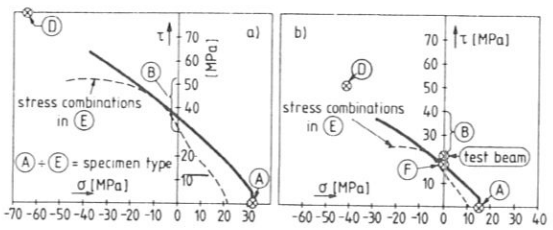

Fig. 15. Strength results obtained from different specimen types and deduced lowest damage limiting curve, shown in a biaxial strength field for "JET resin": (a) static loads, 80 °C; (b) fatigue limit, 5×10^4 load cycles, 80 °C, principal stress ratio $R = 0$, frequency ≈ 0.25 s^{-1}.

The results obtained from E- and F-type specimen tests can be transferred to a shear-/direct-stress time strength diagram. On the same basis – namely 5×10^4 load cycles, stranded copper wire with dry glass, resin as used for JET – additional strength values may be estimated from the measured values [9,14,16,19,20,21], converted with the knowledge resulting from E-type specimen tests (see [13,14] and fig. 13).

A range of safe working conditions in such a stress field may be defined on the basis of all these results (fig. 15). Similar considerations are possible for the optimised insulation system; for clarity, fig. 15 contains only measured values. The range of uncertainty for endurable strength values is wide. This is intensified by the problem of applying these values obtained from laboratory samples to the coil. The determined strength value with the uncertainty range is very close to analysed stress combinations in the coil. Further investigations are thus necessary for defining safe working conditions for the insulation system of the nonplanar coils.

2.3.3. Beam and prototype coils tests

Three straight models (beams) of exactly the same internal construction as the original coil with the original coil cross-section were made for material tests. They served for measuring the overall material properties of the inhomogeneous, orthotropic material as well as for measuring material strength values.

One model was first tested under pure static bending to measure Young's modulus in the coil circumference direction – the most important of the three E-moduli. In a second test these beams were subjected to torsion in order to analyse shear moduli, in which shear isotropy with reference to the shear moduli in the cross-sectional plane of the coil $G_{RT} = G_{ST}$ is given [9]. These measurements [9,14,18] together with small sample tests [5,9,14,18] and analytical calculations [9,13,14] serve to determine the nine engineering constants necessary to describe the mechanical behaviour of the homogeneous orthotropic equivalent system.

For mechanical fatigue tests the beams were loaded in a special test device – an excentrically supported bending beam, fitted with freely moving and twisting end sections [9,14]. This combined bending and torsion leads to stress combinations similar to those analysed for the nonplanar coils: see Section 2.2. The test temperature was 80 °C – the maximum working temperature of the magnet coils – and the test frequency 0.25 Hz (sinusoidal). The results of these tests are summarised in table 1 and fig. 15.

As expected after the laboratory tests there was no failure of the copper wires, either fracture of single wires or delamination within the stranded wires. The damage mechanism under the selected load combinations (test beam II and III) was delamination in the "insulation layer" between single wires [5,9,14,16]. Within the winding insulation, which is composed of prepreg layers, no delamination could be detected at the onset of failure start. This corresponds to the results described in Section 2.3.2. The beams had been produced by normal coil manufacturing techniques, but with "JET resin" (see Section 2.3.2) and component glass tapes in the impregnation process. The most important results of these beam tests may be summarised as follows:

- The mechanically limiting constituent in the coil is the insulation system.
- For the impregnated, stranded copper wire there is no danger of fracture or delamination under the expected stress combinations.
- For the optimized insulation system the admissible in-plane shear stress in the insulation should be approx. 30% higher, according to the results, described in 2.3.2. Thus the admissible in-plane shear stress for 5×10^4 full-load test cycles at 80 °C for a test beam with optimized resin system is expected to be also 30% higher than the values obtained from the original beams (see table 1).
- The fracture behaviour of this compound material is very goodnatured. After the first indications of delamination were detected, it took a long time (additional load cycles) for fracture propagation to occur; a total failure in the mechanical sense did not

Table 1
Results of combined tension/compression torsion fatigue tests with straight test beams having original coil cross-section (80 °C, principal stress ratio $R = 0$, frequency $\approx 0.25\ s^{-1}$)

	test number			test arrangement
	I	II	III	
τ_{max} [MPa]	16	28	22	
σ_{max} [MPa]	150	150	103	
$n_{delamination}$	$>5 \cdot 10^4$	$\approx 10^3$	$\approx 10^{4*}$	

F

orig coil cross-section

* initial loading (static): ≈ 60% above dyn. load

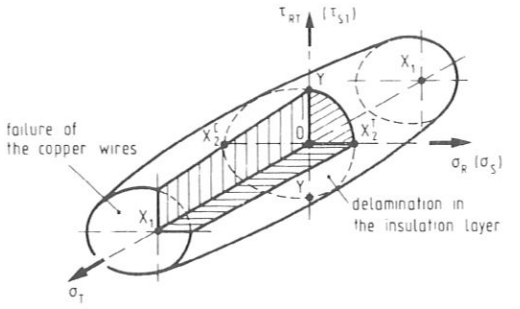

$$\frac{\sigma_T^2}{X_1^2} + \frac{\sigma_{R(S)}^2}{X_2^T \cdot X_2^C} + \frac{\tau_{RT(ST)}^2}{Y^2} - \frac{\sigma_T \cdot \sigma_{R(S)}}{X_1 \sqrt{X_2^T \cdot X_2^C}} + \frac{X_2^C - X_2^T}{X_2^T \cdot X_2^C} \sigma_{R(S)} \leq 1$$

X_1 fatigue strength for copper

X_2^T fatigue tensile strength perpendicular to conductor direction (out-of-plane direct strength of the insulation system)

X_2^C fatigue compressive strength perpendicular to conductor direction

Y fatigue in-plane shear strength in the insulation layer or in the impregnated conductor

Fig. 16. Approximate failure surface for the modular field coils.

occur (only increasing plastic deformation coupled with propagating delamination in the insulation layers).

From all these material tests it can be concluded that the failure behaviour of such a compound can be reasonably well described by the Tsai-Wu criterion [22;23,24,25], originally derived for undirectionally reinformed composites in a biaxial stress field (fig. 16). For the expected different local combinations of stress components this strength hypothesis is based on the fact that the coil or the two main constituents of the coil will be mechanically endangered only by selected stress combinations. The impregnated copper wires are thus subjected primarily to hoop or circumference stresses σ_T and secondarily to the shear stress components $\tau_{R,T}$, $\tau_{S,T}$. Other stress components of the local stress tensor are negligible. On the other hand, the glass/epoxy-resin insulation system and the insulation/copper adhesive interface are subjected primarily to direct stress acting in the insulation (interface) planes. In-plane direct and out-of-plane shear stress components are secondary effects.

For the envisaged lifetime of the test device (5×10^4 full load pulses) at maximum working temperature of the coils the fatigue strength limits are as follows (for optimised insulation systems): $X_1 > 150$ MPa (reference coil cross-section); $XT_2 \approx 21$ MPa; $|XC_2| > 55$ MPa; $Y \approx 27$ MPa (see fig. 16). On this basis, critical stress combinations are selected from the results obtained from the FE-analysis described in Section 2.2 and [10,11].

The maximum calculated hoop stress of $\sigma_T = 105$ MPa, on which a shear stress component of 12 MPa is superposed, appears in the detailed analysis of Section 2.2. These values are applied to the whole coil cross-section in accordance with fig. 2a, and they can be transformed to the impregnated and cured net conductor cross-section with a filling factor of ≥ 0.76. As shown in the analysis, for a more detailed finite-element model this dominating stress component in the tensor may increase. Anyway, the equivalent stress applied on the wires is less than the measured fatigue time strength for the impregnated copper wires (fig. 12) and considerably less than the hoop stresses applied to the prototype coil. Thus, under all boundary conditions described hitherto (worst-case analysis), the safety margin is above 1. Mechanically, the copper wires are not endangered.

The basis for a mechanical evaluation of the insulation system is the result obtained from the refined FE analysis. Out-of-plane direct compressive stresses, analysed up to 60 MPa, will not mechanically cause fatigue fracture of the system.

Furthermore the comparison of calculated stresses and experimental strength values are worst-case considerations, because:

(a) The maximum temperature rise under steady-state conditions of the coils is less than 55 K [5]. Approximately 30% of the stresses occurring in the nonplanar field coils are directly dependent on the temperature rise; see Section 2.2. Thus, the applied stresses are lower than the calculated values.

(b) The maximum temperature is less than 80 °C. This is also due to the reduced temperature rise within the coils and a reduced cooling water temperature under usual working conditions. Because of the heavily temperature-dependent material properties of the resin-impregnated compound material this temperature restriction will considerably raise the available (especially shear) strength values.

(c) The in-plane shear strength and the out-of-plane tensile strength for insulation planes perpendicular to the winding insulation are increased. This is due to the surface and winding insulation, which is analysed perpendicularly to the endangered breaking planes of the insulation system (fig. 2a).

(d) Only a part of the 5×10^4 pulses envisaged during the lifetime of this machine will be full power load cycles. Thus, in comparison with the above values, the fatigue strength values – given for 5×10^4 full load cycles at 80 °C – are increased, whereas the applied stresses – given for maximum magnetic field and a temperature rise inside the coil for steady-state conditions of 55 K – are decreased.

If necessary for special reasons, the available strength values and/or applied mechanical stresses may be further adapted by, for example such suitable conditions as extension of the pulse intervals or by working with the lowest possible cooling water temperature.

Finally, in a combined experimental and theoretical consideration, the assumptions, approximations, transformations and simplifications necessary to describe the behaviour of these nonplanar coils are rechecked. Especially the validity and accuracy of the mechanical and electromagnetic finite-element programs, of the calculated time-dependent thermal behaviour in the coil bulk, and of the assured material behaviour of the heterogeneous orthotropic composite material were verified. A prototype coil (shape as coil number 3 of the W VII-AS field coils) was therefore loaded by different electromagnetic forces in its self-field. The experimental tests were carried out without constraining the deformation of the prototype coil be means of the support structure, so that the effects of interaction of the nonplanar coils with other structural parts of the machine did not have

Table 2
Comparison of measured and calculated coil diameter deformation under magnetic loads, resulting from a prototype coil test in its magnetic self-field (coil number 3, side I)

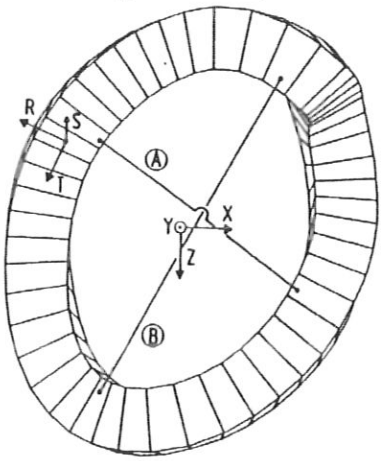

Δl [mm]		measurement	FE-analysis
minor diameter (A)	side I	1,8	2,0
	side II	1,9	2,2
major diameter (B)	side I	0,75	0,85
	side II	0,5	0,62

to be considered. The test procedure, the calculations and the measurements as well as an analysis of all the records obtained are described in detail [5,13,14,16] and may be summarised as follows:

(a) The measured electromechanically induced deformation in the quasilinear range of material behaviour at nominal current are compared for two diameters of the prototype coil with calculated values and show good agreement (table 2). The analysis carried out and the models used rested on the same basic foundations as for the non-sophisticated case of mechanically supported coils in a spatial arrangement with other magnets as described in Section 2.2.

(b) The measured temperature rise per duty cycle of the coil is lower than that predicted from conservative evaluations made by FE calculations [5]. But the calculated maximum temperature rise of 55 K was used as a basis for all calculations described in section 2.2.

(c) When the magnetic force is raised up to the onset of measurable material nonlinearities this onset shows good agreement with that predicted. The theoretical magnetic force for plastic yielding was predicted by comparing analysed local stress tensors – judged by the strength hypothesis already described – as a function of the applied loads (electric current flow) with the fatigue strength values described in Sections 2.3.2 and 2.3.3.

In these tests, carried out with a prototype coil, the comparison of measured data with predicted data resulting from calculations, material tests and the interpretation show good agreement. It therefore seems admissible to transfer this knowledge to the W VII-AS field coils.

3. Vacuum vessel

3.1. Design and construction of the vacuum vessel

A view of one modular section of the vacuum vessel is shown in fig. 17(a). It shows a test piece of original size undergoing the same manufacturing processes as envisaged for the W VII-AS vacuum vessel.

The design criteria for the vacuum vessel were as follows [e.g. 26, 27, 28, 29]:

- maximum distance between the plasma and inner vessel wall,

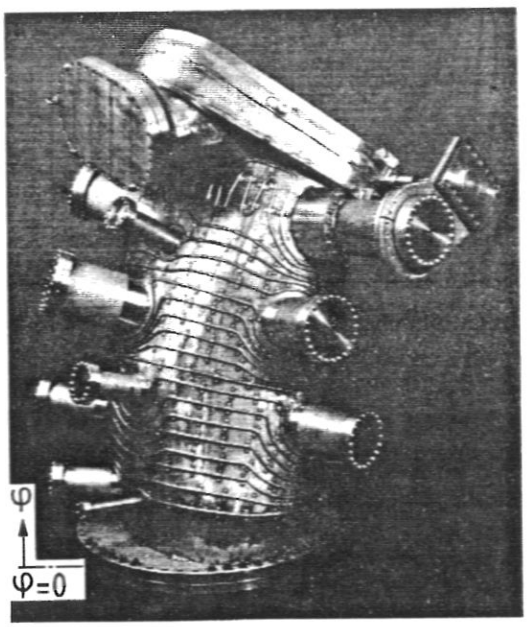

Fig. 17. The toroidal vacuum chamber: (a) test piece of a 1/10 section of the vessel, including a connection flange.

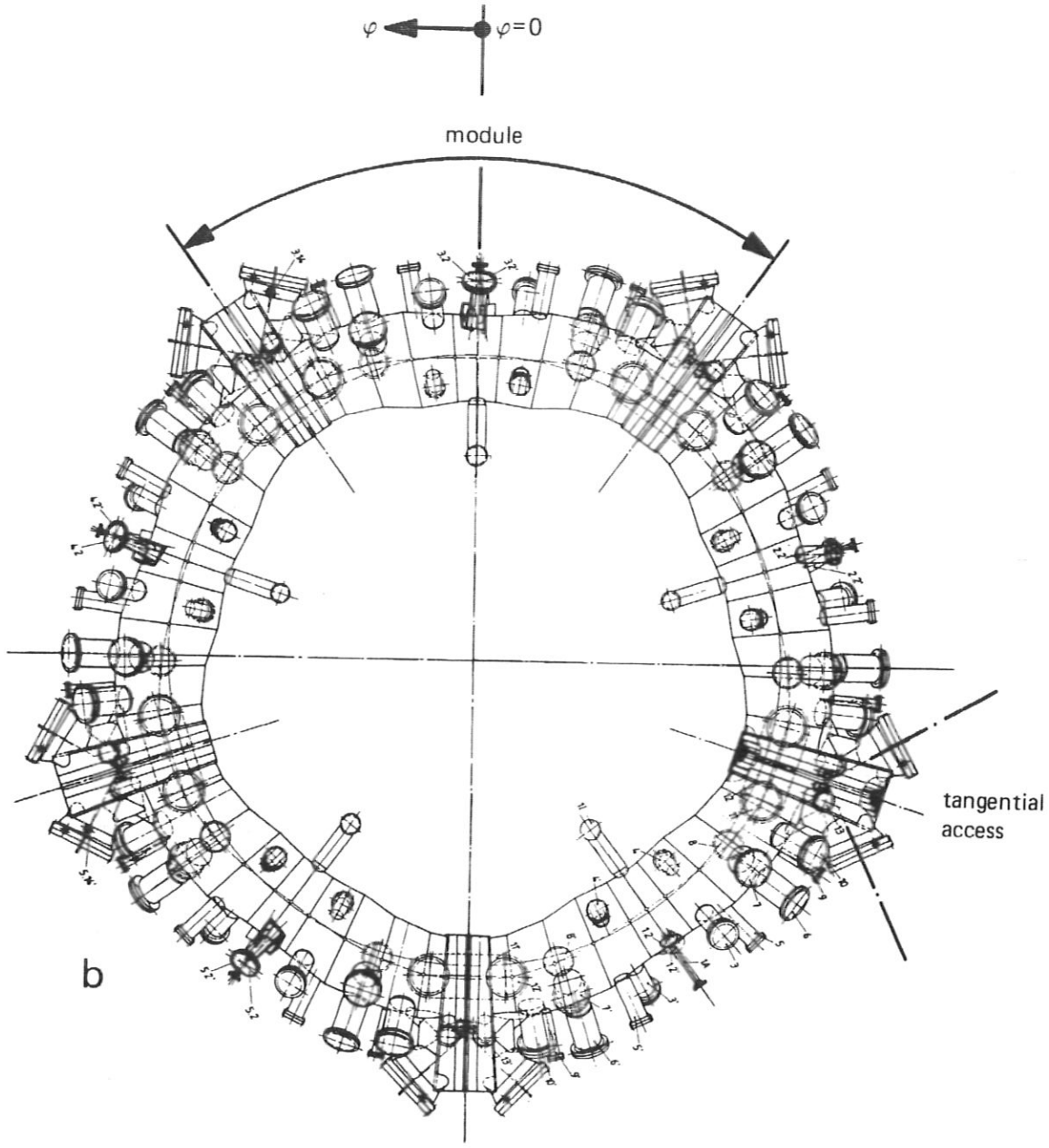

Fig. 17. The toroidal vacuum chamber: (b) plan view of the vessel, including all ports.

- minimum distance between the outer vessel wall and the MF-coils with a sufficient gap to allow radial expansion of the vessel when it is heated up, and with sufficient intermediate space for assembly,
- modularity,
- the number, size, and position of the portholes must meet the experimental requirements

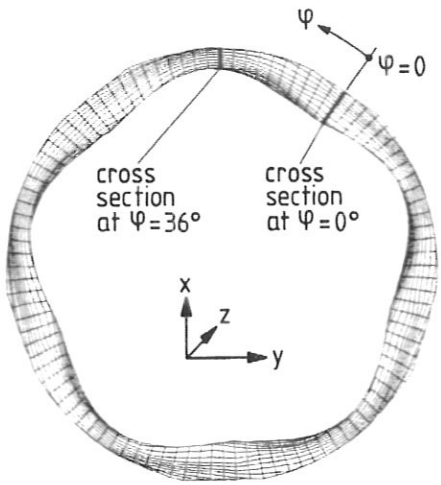

Fig. 18. Plasma column of the experiment.

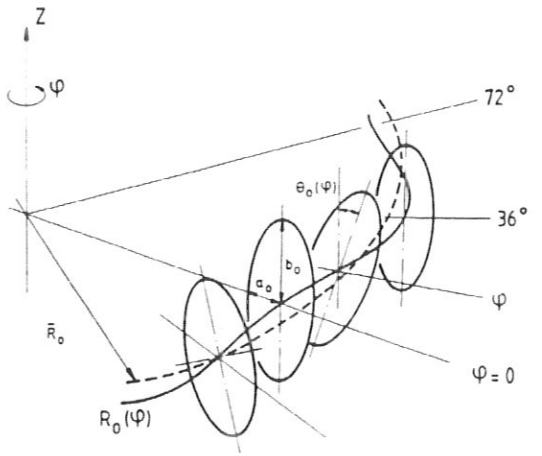

Fig. 19. Toroidal geometry of the vacuum chamber (theoretical envelope of the vacuum vessel):
$R_0(\phi) = 2000\ (1.02 - 0.03 \cos 5\phi)$ mm,
$\theta_0(\phi) = -22.5\ (\sin 5\phi + 0.5 \sin 10\phi)$ degrees.

– simplicity of the vessel geometry to limit manufacturing costs.

In fig. 17(b) the plan view of the final design of the vessel is shown. Figure 18 shows the plasma column of W VII-AS with a cross-section varying from a triangular shape at $\phi = 0°$ to a vertical elliptic shape at $\phi = 36°$. The cross-section of the vacuum vessel should closely match the inner bore of the MF-coils. The geometry was therefore derived from the surface current distribution [2,3,8,28] and is an approximation with

$$R_0(\phi) = 2000(1.02 - 0.03 \cos 5\phi)\ \text{mm},$$

$$\theta_0(\phi) = -\pi/8 \cdot (\sin 5\phi + 0.5 \sin 10\phi),$$

to the ellipse oscillating around the magnetic axis in the ϕ-direction (fig. 19). As described in the next section, a wall thickness of 12 mm was found to be sufficient. In accordance with the 5 field periods of the experiment, the vessel is divided toroidally into 5 modular sections. The volume of the vessel is approximately 7 m^3. Twenty-eight ports in each module allow abundance access to the plasma for heating and diagnostics.

The two oval-shaped special ports of a module allow nearly tangential access primarily for neutral beam injection.

For reasons of economic manufacturing, the shape of the torus surface in the toroidal and poloidal direction was approximated by polygons. The toroidal polygon divides the modules into segments. These segments are formed from plane plates on a hydraulic press. The intricately curved shape of a segment is formed by appropriate bending of sheet steel (fig. 20). The difference between this actual contour and the theoretical envelope is less than 5 mm. After being formed, each segment is individually fitted and then welded in the ϕ-direction. The segments can be welded together (in the θ-direction) into submodules, all the seams being welded through. The forming of one module of the

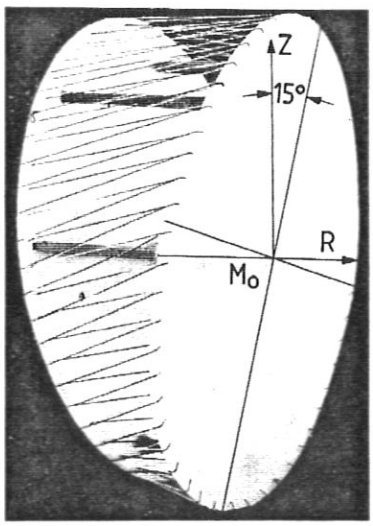

Fig. 20. Approximating the theoretical ellipse cross-section of the vacuum vessel by a polygon geometry resulting from an unroll process.

vacuum vessel is only possible after completion of the assembly of all parts of the magnetic confinement system, consisting of the MF-coils, support elements, and structure and the vessel submodules. The vacuum submodules are then welded together (seams only half-welded through to make repeated assembly possible) and finally all parts are welded into the module.

The overall construction thickness of the vessel after assembly is 20 mm. The vessel itself is a thin-walled type 304 LN stainless-steel torus, the steel wall thickness being 12 mm. The rest of the overall height is used for a pressurised hot water heating system combined with a thermal insulation system. This is necessary to produce clean vacuum conditions. To outgas the vacuum surfaces, the torus can be heated up to 150 °C by means of this system (glow discharge cleaning is envisaged to control light impurities). The thermostated water for baking the vessel circulates in copper pipes fastened to the outer torus surface. Good heat conduction to the torus is ensured by a special cement which fills the spacings between the pipes and the surface of the torus. Finally, the torus and piping system are covered by thermal insulation material (3 mm thick) to prevent excessive heat transfer to the modular field coils. All welded joints of the stainless torus are kept accessible to facilitate leak testing. When the torus is baked to 150 °C, the resulting thermal expansion is 12 mm in diameter. The rise time for the baking temperature is selected to be more than 6 h so that material stresses due to non uniform temperature fields are negligible. To prevent the deposition of unduly high heat flux from the plasma to the torus wall limiters are arranged inside the vessel.

Since a stellarator experiment does not involve induction of electric current flow in the plasma itself, the bellows necessary for tokamaks are not needed. Electrical insulation of the torus in the toroidal direction is provided in the separation planes of the 5 modules by enamel-coated sealing flanges. Vacuum sealing in the separation plane is made by helicoflex metal seals.

3.2. Stress analysis – Vacuum vessel

The vacuum vessel of W VII-AS is primarily subjected to gravity, vacuum, electromagnetic and thermal loads. Electromagnetic forces in a current-free stellarator, such as W VII-AS, act in the toroidal direction of the vessel during energising and de-energising of the coil system, whereas in the toroidal direction no electric current flow is induced. These electromagnetic forces – distributed over the torus surface – were calculated analytically and found to be less than 2.5×10^4 N/m^2 (fig. 21). A finite-element structural analysis in the final version carried out by the SULZER Comp. (manufacturers of the vessel) was made for static load conditions with the ANSYS code. The stress analyses were carried out for the following combined load case: (a) atmospheric pressure 1 bar; (b) net weight force of the vacuum vessel, which is 4.3 kN for a 1/10 section of the vessel; (c) weight force of auxiliaries limited to 30% of the vessel net weight force and distributed uniformly above the vessel (d) electromagnetic forces. The most critical loading condition occurs during de-energizing of the coil system, with an electromagnetic (pressure) force of 0.25×10^5 N/m^2 (a very low-frequency fatigue load) superposed on the load combination mentioned above. Owing to the modularity of the test device, combined with the given load and geometry symmetries, a stress analysis for just a 1/10 section of the vessel was made. For economic reasons, this was a simplified model taking into account only the large, oval-shaped outside port (fig. 22). The influence of the smaller ports was estimated by making the conservative assumption that the effects of additional ports, acting as stiffeners for the torus and thus reducing bending stresses, were neglected. On the other hand, the weakening influence of the diagnostic ports for the membrane stresses was taken into account. The structure of the vessel for the final ANSYS stress analysis was discretized by means of 506 isoparametric triangular and quadrilateral thin shell elements (522 nodes). They include both membrane and bending stiffness. For type 304 LN (X2CrNiN18 10) stainless steel the material data are as follows: Young's modulus 2×10^5 MPa, yield strenght 260 MPa (20 °C) and 180 MPa ($\approx$ 150 °C), isotropic material behaviour.

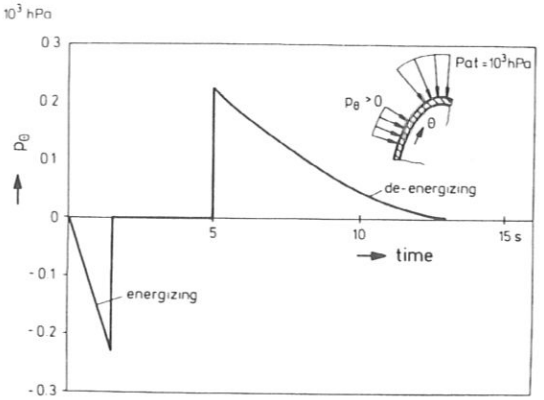

Fig. 21. Electromagnetic load on the vacuum chamber during energising and de-energising of the coil systems (vacuum field on torus axis max. 3.5 T).

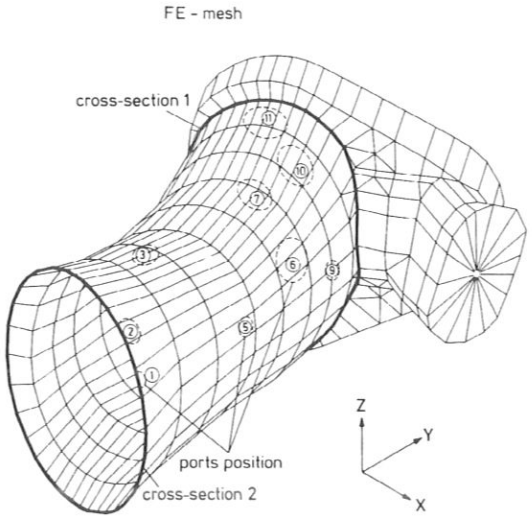

Fig. 22. FE structural model for the stress analysis of a 1/10 section of the toroidal vacuum chamber (for the cross-sections marked see fig. 23).

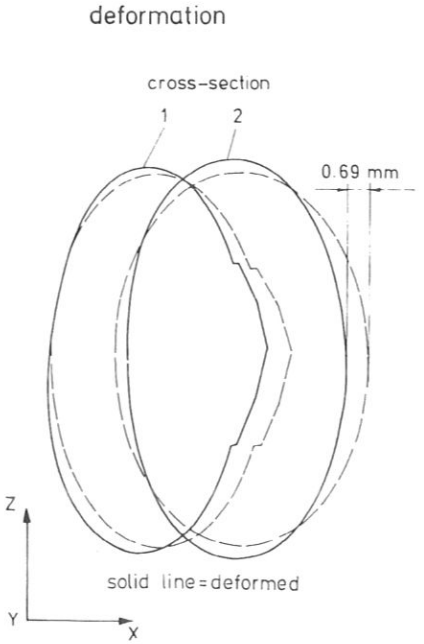

Fig. 23. Deflected and undeflected forms of two cross-sections of the toroidal vacuum chamber (scaling factor 100, only vacuum and electromagnetic loads).

Figure 23 shows the deformation of the vacuum vessel in cross-section. These deformations are small compared with the thermal expansion induced by heating the torus to 150 °C (< 6 mm maximum one side). The clearance between the torus and the MF-coils of more than 10 mm everywhere is thus sufficient with respect to the calculated displacement induced by combined magnetic, vacuum and gravity loads as well as those induced by unrestrained thermal expansion. The maximum displacement of 0.8 mm appears at the symmetry plane of the vessel model (fig. 23).

As derived from corresponding ASTM (American Society for Testing and Materials) regulations and AD specifications (German Arbeitsgemeinschaft Druckbehälter Merkblätter [30]), the safe working stresses for austenitic (stainless) steels must be below the following limits: (a) for membrane stresses $\sigma_m < s_M = R_{p,0.2}/1.1 = 164$ MPa (type 304 LN, 150 °C); (b) for linear stresses (membrane and bending) $\sigma_{m+b} < 1.5\ S_M = 245$ MPa.

The maximum equivalent (Von Mises) stresses obtained from the static structural analysis with the FE model described above are σ_{eq}^{m} (membrane) = 42.5 MPa and σ_{eq}^{m+b} (membrane + bending) = 84.6 MPa (table 3), localized in the transition region near the insulation flange of the module/torus. For only half welded through seams in the torus shell of the vessel the stresses were estimated on the basis of the FE calculations. The membrane stress component of the equivalent stress for half wall thickness is double the value obtained from the FE analysis, and the linear component is 4 times the value obtained from the analysis for σ_{eq}^{m+b}. The calculated maximum stress intensities for half welded through seams are $\sigma_{eq}^{m} = 76.8$ MPa and $\sigma_{eq}^{m+b} = 228$ MPa (table 3).

When comparing safe working stress limits with those stress values obtained from the FE analysis or derived from these results by adequate evaluations, one can see

Table 3
V. Mises stresses (membrane and bending component) in the toroidal vacuum chamber as obtained from the simplified FE analysis and estimated on this basis with allowance for ports and welded seams

v Mises stresses [MPa]	maximum value obtained from FE-analysis	estimated value for half-welded through seams	web between port 10 and 11		safe working limit s
			obtained from FE-analysis	considering weakening influence	
σ_{eq}^{m}	42,5	76,8	15,0	47,2	164
σ_{eq}^{m+b}	84,6	228,0	35,5	67,7	245

that the stresses determined are within the allowable levels for static loads (table 3). The safe working stresses are not heavily influenced (decreased) by fatigue loads resulting from the electromagnetic pulsed load. This is because this load component is comparatively small and the fatigue strenght of austenitic steel decreases only slightly from static (0.2% proof) strength values (especially for the lifetime of the machine envisaged, 5×10^4 load cycles). The W VII-AS vacuum vessel will thus be capable of withstanding the loads applied, even under fatigue loads. The critical buckling load of the (thick-walled) stainless-steel vacuum vessel, estimated by using the regulations given in [30] and formulas given in [31], is many times higher than the actual (primary vacuum) load.

4. Status of the experiment

4.1. First experimental results

The confinement system of the device, including the vacuum vessel, was assembled in early spring 1988 (fig. 24). Magnetic field mapping, succeeded in May and June 1988, first plasma operation of the experiment in Oct. 1988.

The evaluation of the field mapping experiments showed that in the W VII-AS Stellarator it has been demonstrated by means of modular field coils that it is possible to produce magnetic surfaces which are in very good agreement with the numerical predictions.

Also the first thousands of plasma discharges – preferrably heated with radio frequency power at the electron resonance frequency of 70 GHz and with some hundred kilowatts – showed expected performance. Experiments with enlarged heating power are planned, as well as the use of additional heating methods like neutral beam injection and ion cyclotron resonance heating. A mechanical problem appeared with one type of the small non-planar coils (No. 3) in the coil set: the displacements at nominal load are much higher than predicted in the FE-calculation and acting in other directions. Therefore it has to be assumed that the stress distribution and combination discussed earlier in that paper are not representative for that coil. To prevent predamaging of the insulation the allowed magnetic

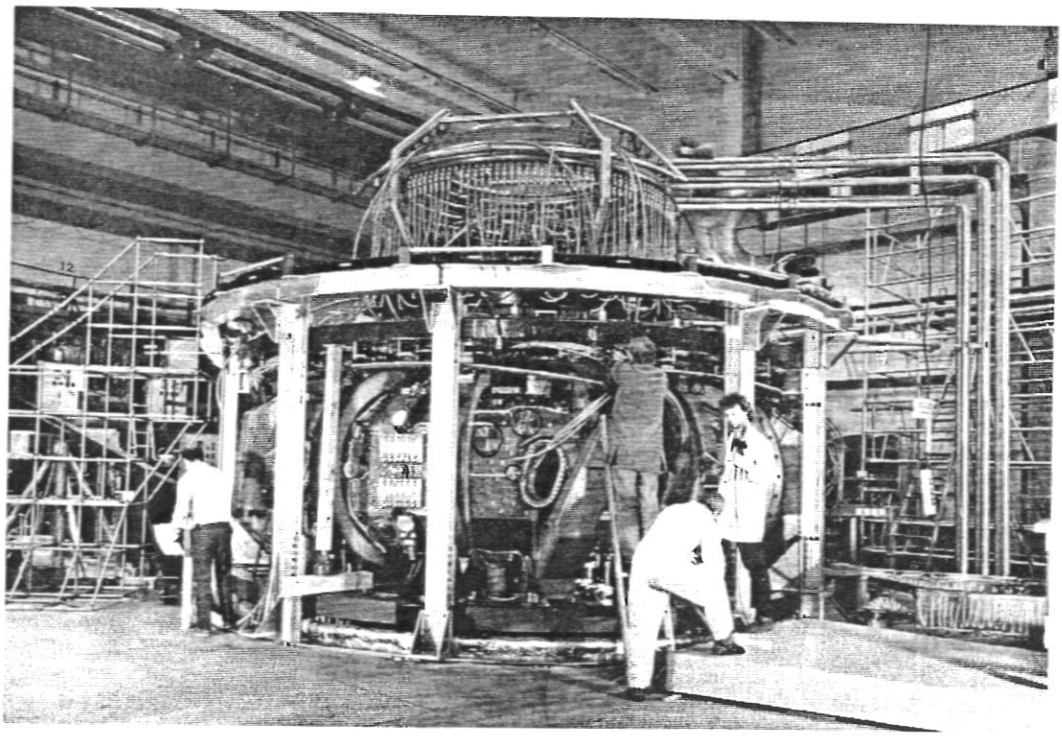

Fig. 24. Total view of the WENDELSTEIN VII-AS experimental device, status May 1988.

fields in the machine were limited to approx. 60% of nominal values. Investigations for detailed analysis are on the way and will be reported in a further publication after final evaluation.

Acknowledgements

Thanks for contributions to and support of this work are due to the W VII-AS project and design team of our institute (W. Bitter, U. Brossmann, D. Dorst, H. Gillhuber, A. Hasenmüller, E. Harmeyer, S. Huber, E. Katzmarek, F. Kerl, J. Kisslinger, T. von Larcher, W. Melchior, H. Münch, S.B. Mukherjee, H. Renner, I. Schoenewolf, B. Sombach and H. Wobig) and to our main contractors: BBC Company, Mannheim, F.R.G. (K.E. Buck, K.D. Huber and D. Klee), SULZER Company, Winterthur, Switzerland (R. Brook) and IABG Company, Ottobrunn, F.R.G. (G. Gröger and R. Schäfer).

References

[1] H. Wobig and S. Rehker, A Stellarator coil system without helical windings, Proc. of the VII SOFT, Grenoble, 1972, p. 345.

[2] J. Kisslinger, F. Rau and H. Wobig, Vacuum magnetic fields and modular coil system of the Wendelstein VII-AS advanced stellarator, Proc. 12th Symp. on Fusion Technology, Jülich (Pergamon Press, Oxford, 1982) pp. 1051–1057.

[3] K.E. Buck and J.W. Hammel, Fabrication effects on the structural behaviour of large coils for fusion experiments, Nucl. Engrg. Des. 54 (1979) 225–238.

[4] K.D. Huber, Modular coils for the Wendelstein VII-AS plasma experiment, Brown Boveri Review 74 (1987) 75–77.

[5] R. Mathis and J. Sapper, Comparison of measured and calculated behaviour of Wendelstein VII-AS components – First results, Trans. of the 9th Int. Conf. on Structural Mechanics in Reactor Technology, Lausanne, Switzerland (Balkema Publishers, Rotterdam, 1987) Part N, pp. 25–30.

[6] U. Brossmann, F. Kerl, W. Melchior, S. Mukherjee, J. Sapper and B. Sombach, Modular design of the W VII-AS advanced stellarator – Engineering details, Proc. of the 10th Symp. on Fusion Engineering, Philadelphia, USA, IEEE (1983) pp. 1569–1572.

[7] S.I. Sackett, EFFI – a code for calculating the electromagnetic field, force and inductance in coil systems for arbitrary geometry, Lawrence Livermore Laboratory, Report UCRL-52402 (1978).

[8] U. Brossmann, S. Mukherjee and J. Sapper, Mechanical stress analysis for the twisted coils of the Wendelstein VII-AS advanced stellarator, Proc. of the 12th Symp. on Fusion Technology, Jülich, FRG (Pergamon Press, Oxford, 1982) pp. 991–996.

[9] R. Mathis, S.B. Mukherjee and J. Sapper, Mechanical analysis and material tests of the twisted Wendelstein VII-AS coils, Proc. of the 8th Int. Conf. on Structural Mechanics in Reactor Technology, Brussels, Belgium (North-Holland, Amsterdam, Physics, 1985) Part N, pp. 23–29.

[10] C.W. McCormick, MSC/NASTRAN User's Manual, MacNeal-Schwendler Corp., Los Angeles, CA MSR 39 (1978).

[11] R. Mathis and J. Sapper, Application of finite-element methods to the design of a torus-shaped magnetic confinement system for fusion experiments, Int., Conf. on Computational Techniques and Applications 1987, Sydney, Australia, CTAC 1987 (North-Holland, Amsterdam, 1988) pp. 461–474.

[12] R. Mathis, Arbeitsbericht Projekt W VII-AS, Max-Planck-Institut für Plasmaphysik (1986).

[13] K.E. Buck, O. Osen, U. von Bodisco and K. Winkler, Structural analysis of large magnetic coils, Proc. Finite Elements in Engineering Application, Stuttgart (1987) pp. 173–192.

[14] K.E. Buck, P. Klee and R. Mathis, Festigkeitsnachweis für die großen Spulen des Plasmaexperimentes Wendelstein VII-AS, ABB-Technik, Heft 2 (1989) 17–24.

[15] Schrem et al., ASKA User's Ref. Manual, Rev. F, ISD-Report 73, Univ. Stuttgart (1979).

[16] R. Mathis and J. Sapper, Structural analysis of magnet coils, Proc. of the 3rd Int. Conf. on Cumputational Methods and Experimental Measurement, Porto Caras, Greece (Springer Verlag, Berlin, Heidelberg, 1986) pp. 229–249.

[17] J. Sapper, U. Brossmann, G. Grieger, J. Kisslinger, S. Mukherjee, F. Rau, B. Sombach and H. Wobig, The WENDELSTEIN VII-AS advanced stellarator, 12th Symp. on Fusion Technology, Jülich, FRG (Pergamon Press, Oxford, 1982) pp. 161–166.

[18] R. Mathis, J. Sapper and I. Schoenewolf, Engineering problems of the Wendelstein VII-AS experiment, Proc. of the 8th Int. Conf. on Structural Mechanics in Reactor Technology, Brussels, Belgium (North-Holland, Amsterdam, 1985) pp. 15–21.

[19] A.A. Koch, R.K. Maix and K. Nylund, Insulation systems for magnets used in experiments for nuclear fusion and high-energy research, Brown Boveri Review 65, No. 5 (1978) 326–333.

[20] J.C. Rauch, F. König and T. Schmid, Test program on the insulation system for the JET inner poloidal coils, Trans. 11th Symp. Fusion Technology (Pergamon Press, Oxford, 1980) pp. 449–454.

[21] J.R. Last; A. Bond and E. Salpietro, Mechanical tests on insulation systems for the JET poloidal coils, Proc. of the 10th Symp. on Fusion Technology, Padova, Italy (Pergamon Press, Oxford, 1978) pp. 1025–1031.

[22] S.W. Tsai and E.M. Wu, A general theory of strength for anisotropic materials, J. of Composite Materials 5 (1970) 58–80.

[23] A. Puck and H. Schürmann, Die Zug/Druck-Torsionsprüfung and rohrförmigen Probekörpen, Kunststoffe 72 (1982) 554–561.

[24] R. Bandenheier, Mechanisches Versagen von Kunststoffen – Anstrengungsbewertung mehraxialer Spannungszustände, Kunststoffe 72 (1982) 729–732.

[25] W. Knappe and W. Schneider, Bruchkriterien für unidirektionalen Glasfaser/Kunststoff unter ebener Kurzzeit- und Langzeitbeanspruchung, Kunststoffe 62 (1982) 864–868.

[26] D. Dorst, G. Grieger, R. Mathis and J. Sapper, The Wendelstein VII-AS experiment, Proc. of the 14th Symp. on Fusion Technology, Avignon, France (Pergamon Press, Oxford, 1986) Part 1, pp. 139–148.

[27] J. Sapper, U. Brossmann, G. Grieger and H. Wobig, Modular design of the W VII-AS advanced stellarator – Overview, Proceedings 10th Symp. on Fusion Engineering, IEEE, Philadelphia, USA, 1983, Paper 6 D 01.

[28] See ref. [6].

[29] R. Rau, J. Kisslinger, and H. Wobig, Vacuum magnetic field and modular coil system of the WENDELSTEIN VII-AS advanced stellarator, IPP Report 2/259 (1982).

[30] AD-Merkblatt B6, Berechnung von Druckbehältern, TÜV, FRG (1977).

[31] R.J. Roark and W.C. Young, Formulas for Stress and Strain (McGraw-Hill, New York, 5th edition, 1975).

CONFINEMENT STUDIES ON THE WENDELSTEIN VII-AS STELLARATOR

H. Ringler, U. Gasparino, G. Kühner, H. Maaßberg, H. Renner, F. Sardei
W VII-AS Team, NBI Team†*

Max-Planck Institut für Plasmaphysik
Association EURATOM-IPP, D-8046 Garching, FRG

ECRH-Group§

Institut für Plasmaforschung der Universität Stuttgart
D-7000 Stuttgart, FRG

Abstract

ECR heating at $B_0 = 2.5\,T$ has been extensively used in the 1990 experimental period of the W VII-AS stellarator. As it is a low-shear experiment the magnetic configuration (especially details of the rotational transform profile) depends sensitively on plasma currents (pressure driven, ohmic, EC driven, Ohkawa current) which in turn have a strong influence on energy and particle confinement properties. For the stationary phase a transport analysis has been performed, yielding the profiles of the electron heat conduction and the ion particle diffusion coefficients. The former was subjected to a statistical analysis resulting in phenomenological expressions for χ_e and τ_E. First experiments using neutral beam injection (ECRH target plasma) as well as combined heating (NBI+ECRH) will also be discussed.

Keywords: *Stellarator, W VII-AS, net current free operation, confinement, transport, electron heat conduction, ion diffusion, ECRH, NBI*

1. Introduction

Wendelstein VII-AS (AS is the abbreviation for Advanced Stellarator) is a low-shear, partially optimized, modular stellarator (major radius 2 m, minor radius 0.2 m), see Figure 1. It is one of the tasks of this experiment to show the importance of each of these attributes. The object of having a low-shear magnetic configuration is to avoid low order rational values of the rotational transform throughout the plasma confinement region, which are deleterious to the magnetic field structure as they cause the formation of islands or ergodic regions which in turn degrade the confinement properties. However, it is a natural property of such a configuration to react sensitively to currents flowing in the plasma (Pfirsch-Schlüter, bootstrap current) which may have a strong influence on the rotational transform, $\iota(r)$, and shear, ι', of the magnetic field structure. W VII-AS was designed to optimize the field structure such that the negative influence of the Pfirsch-Schlüter (PS) currents is reduced. In W VII-AS the PS currents are decreased by a factor of two as compared to an equivalent standard stellarator or tokamak, which leads to a reduction of the Shafranov shift and, consequently, to a reduced deformation of the $\iota(r)$ profile. The reduced outward shift of the plasma center was confirmed by both SX profile analysis (Weller, 1990) and magnetic measurements. W VII-AS is not optimized with respect to the bootstrap current. For current control, the bootstrap current has to be compensated by currents induced externally (Ohmic) or by the heating method (ECCD, Ohkawa) to conserve the edge value of rotational transform. In W VII-AS these currents have been widely used for shaping of the $\iota(r)$ profile in order to establish optimal confinement conditions.

---

*N. Beredin[1)], R. Brakel, R. Burhenn, G. Cattanei, A. Dodhy, D. Dorst, A. Elsner, K. Engelhardt V. Erckmann, U. Gasparino, S. Geißler, G. Grieger, P. Grigull, U. Gutarev[1)], H. Hacker, H.J. Hartfuß, R. Jaenicke, S. Jiang[2)], J. Junker, M. Kick, H. Kroiss, G. Kühner, I. Lakicevic, A. Lazaros, M. Liniers[3)], H. Maaßberg, C. Mahn, W. Ohlendorf, M.A. Ochando[3)], H. Renner, H. Ringler, J. Saffert, F. Sardei, M. Tutter, A. Weller, E. Würsching, M. Zippe, S. Zöpfel, H. Zushi[4)]
guests from: [1)] Institute of Physics and Technology, Kharkov; [2)] Southwestern Institute of Physics, Leshan (China); [3)] CIEMAT, Madrid; [4)] Kyoto University, Japan

† F.P. Penningsfeld, W. Ott, E. Speth

§ W. Kasparek, G.A. Müller, P.G. Schüller, M. Thumm, R. Wienecke

Furthermore, the reduced PS currents also give rise to a reduction of the neoclassical transport in both the plateau and the PS diffusion regime. As the electron heat and particle transport are strongly enhanced in these diffusion regimes (anomalous transport), this consequence of PS current reduction can hardly be checked in the experiment. The neoclassical transport properties in the long mean free path (LMFP) regime are determined by particles being trapped in local magnetic mirrors. In W VII-AS the neoclassical loss in the LMFP regime is dominated by particles being trapped in the regions with strong curvature (see Figure 1). The trapped particle drift orbits in the straight parts of the configuration, however, are rather close to the magnetic flux surfaces. Electron heat conduction, ion and impurity diffusion have been analyzed in a wide parameter range. Furthermore, a database has been accumulated to perform a statistical analysis of local χ_e which is very useful to find the leading parameter dependences as well as to compare present stellarator (W VII-AS, ATF, CHS, Heliotron-E) and tokamak experiments of quite different size.

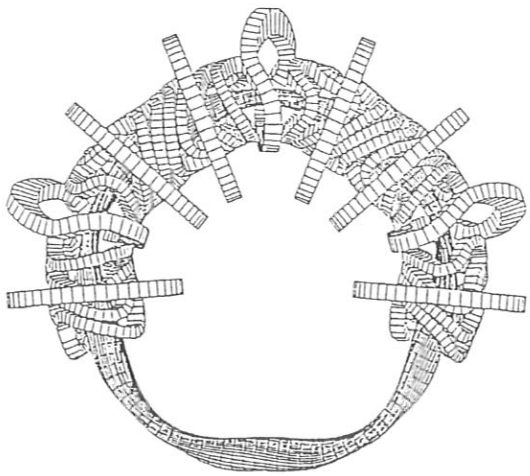

Figure 1 Schematic view of the coil system and the plasma column of W VII-AS: the magnetic field structure is realized by 45 non-planar modular field coils and 10 planar toroidal field coils.

An optimized configuration requires the engineering of a modular coil system which is a flexible tool for the appropriate realization of the magnetic flux surface geometry. The W VII-AS system was successfully built and is now routinely operated at full field parameters (2.5 T) after additional support structures had been introduced to limit elastic deformations of one of the coil-types.

Characteristics of the magnetic field: The magnetic field is generated by a modular system of coils which has fivefold symmetry (Fig. 1). The field is composed of two components: The "module" field consists of nine nonplanar coils per field period generating a shear free magnetic field with a rotational transform of $\iota = 0.39$. By superposition of a toroidal field generated by an addional set of two planar coils per field period, the edge value of the rotational transform, $\iota(a)$, can be varied in the range of $0.2 < \iota(a) < 0.7$. The magnetic flux surfaces are toroidally asymmetric, but exhibit the so-called stellarator symmetry. Thus, there are two planes of symmetry which are of particular interest for the experiments: the cross section of the magnetic flux surfaces in the region of maximum curvature has nearly elliptical shape, and the strong field gradient in major radius allows local heating under electron and ion cyclotron resonance conditions. The cross section in the second plane of symmetry (straight part) is triangular, the field gradient is small and inverted, thus providing the possibility of ECR heating with high field launch from the outer side. As the magnetic field topology of the W VII-AS stellarator is complex, a rigorous mapping of real space coordinates to magnetic flux coordinates (Boozer, 1981) was implemented. The TRANS code provides this coordinate transformation for all relevant vacuum and equilibrium configurations stored in Fourier representation. They were obtained by using GOURDON and KW (Kisslinger, 1985) codes. Experimental data taken at different poloidal and toroidal positions, which are nearly constant on flux surfaces, are reduced to a common radial representation, the effective radius.

ECRH: Four 70 GHz cw-gyrotrons (P = 200 kW, Δt = 3 s) have been installed for ECRH. A sophisticated transmission line (Kasparek, 1988) enables one to generate a completely polarized, almost divergence free EC wave which penetrates the plasma quasioptically. The angle of incidence of the EC wave can be varied in two directions by a set of movable mirrors, thus providing the possibility varying the location of power deposition (off-axis heating) as well as of introducing $k_{\|}$ components for EC current drive. ECCD has been clearly demonstrated by this technique (see left plot of Figure 5). Off-axis heating can also be achieved by tuning of the magnetic field. ECRH has be used in most of the present experiments and two scenarios have been extensively investigated: $B_0 = 1.25$ T with x-mode launch at 2nd harmonic at densities of $n_e < 3 \cdot 10^{13}$ cm^{-3} and $B_0 = 2.50$ T with o-mode launch at fundamental with densities of $n_e < 6 \cdot 10^{13}$ cm^{-3}. Maximum temperatures of $T_e = 2.8$ keV and $T_i = 0.4$ keV and plasma energies up to 8 kJ have been obtained.

NBI: Two long-pulse beam lines have been installed on W VII-AS, injecting neutral particles (H°: E = 45 keV, Δt = 3 s) tangentially into the plasma. By co- and counter injection the Ohkawa current can be compensated. Maximum heating power is about 1.5 MW (Feist 1984). Starting from an initially ECR produced target plasma, NBI heats a plasma at densities well above the cut-off density for ECRH. Maximum temperatures of $T_e \simeq T_i = 0.7$ keV, maximum densities $n_e \leq 10^{14}$ cm^{-3} and plasma energies up to 15 kJ have been achieved.

ICRH: The power supply which was installed for ICRH provides $P_{ICF} \leq 1.5$ MW RF-power in the frequency range of 30 to 110 MHz for a time duration of $\Delta t \leq 0.5$ s. A flexible experimental antenna system is installed in W VII-AS. It consists of two classical loops with Faraday shield which allow a variation of the k-spectrum (Wesner 1988). So far, ICRH has been used only for testing purposes.

OH current control: In addition the OH-transformer of W VII-A is still available. It is used to induce small currents, $I_p < 5$ kA, or to compensate currents occurring due to the plasma pressure (bootstrap) as well as to the heating method (ECCD, Ohkawa current) by applying small loop voltages, $U_{\rm loop} \leq 0.5$ V.

2. Configurational Effects

2.1. Rotational Transform at Plasma Edge

As was the case for the W VII-A stellarator (Wobig, 1987), the global confinement in W VII-AS depends strongly on the value of the boundary rotational transform, $\iota(a)$ (Renner, 1989). A degradation of both energy and particle confinement is found for low order rational values of the rotational transform at the plasma edge, $\iota(a)$, whereas optimum confinement can be established close to the resonances $\iota(a) \simeq 1/3$ as well as $\iota(a) \simeq 1/2$.

The W VII-AS magnetic field vacuum configuration is shearless at $\iota(a) = 0.39$. The vacuum rotational transform can be increased (decreased), introducing a very small positive (negative) shear. These vacuum configurations are modified by plasma currents: the PS current and the neoclassical bootstrap current generated by plasma pressure, currents driven by the heating method (ECCD and Ohkawa currents during NBI) or externally by the OH-transformer. For the ECRH discharges with moderate or low densities and high temperatures, the pressure effect on the ι profile is dominated by the bootstrap current, however, the PS contribution cannot be neglected in general. The bootstrap current always increases the rotational transform in W VII-AS and is localized in the T_e gradient region. The shear contribution is positive in the center and negative in the outer confinement region. Currents driven by the external loop voltage or by the heating method can be used to control $\iota(a)$ as well as the internal shear, thus current density control opens up a variety of scenarios for optimization of confinement.

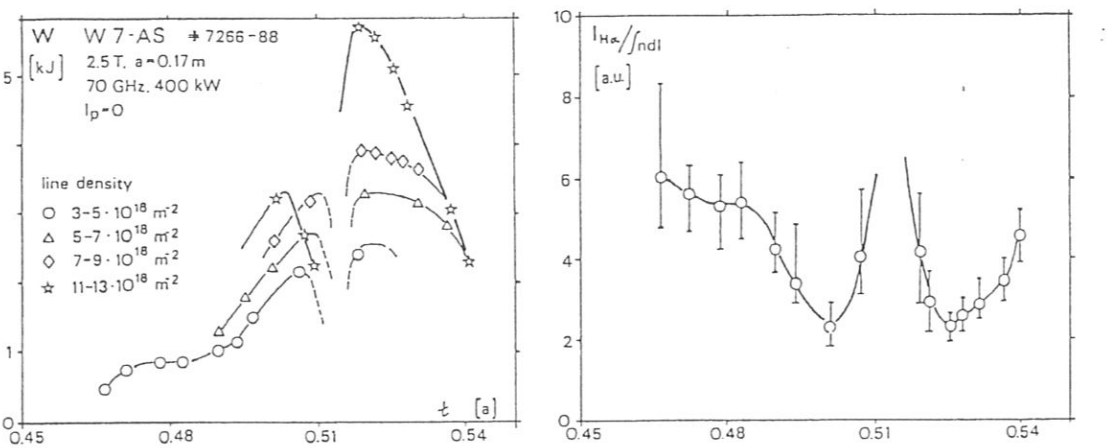

Figure 2 Total energy, W (left plot), and normalized H_α intensity, $H_\alpha/\int n\,dl \propto \tau_p^{-1}$ (right plot), versus the edge value of rotational transform, $\iota(a)$. Note that there is an uncertainty in the experimental estimation of $\iota(a)$ of about 0.01.

The global confinement properties depend sensitively on the rotational transform at the plasma edge. Figure 2 shows plasma energy, W, and the normalized H_α intensity as a measure of the inverse particle confinement time versus $\iota(a)$ in the vicinity of $\iota = 1/2$. Here, the vacuum value of $\iota(a)$ was changed shot by shot and the bootstrap current was balanced by the OH-transformer (net current-free discharges). A strong degradation of confinement is obvious at $\iota \approx 1/2$, the ι ranges for optimum confinement being very small, $\Delta\iota(a) \leq 0.01$. Above and below these two maxima, the natural islands with $\iota = 5/11$ and $\iota = 5/9$, respectively, enter the confinement region. These islands were directly observed in the vacuum magnetic field configuration (Renner, 1989). Typically, the internal contribution of the bootstrap current is much larger than the $\Delta\iota(a)$ windows for optimum confinement. Consequently, the total plasma current has to be controlled to avoid low order rational values of ι or to keep $\iota(a)$ within the range of optimum confinement. The line integrated electron density is given as a parameter in Figure 2 showing that both the energy content, W, and the energy confinement time, τ_E, increase with density for fixed heating power.

The intrinsic source for internal shear is the bootstrap current density with a maximum in the temperature gradient region and which develops as soon as the plasma pressure is built up. Typically, the other current contributions have different radial distributions. Current diffusion on the L/R time scale determines the time to reach stationary conditions. In order to analyze the confinement properties and to control the net plasma current as well as $\iota(a)$, 5 scenarios have been successfully used in W VII-AS :

a) No external loop voltage is applied: the total plasma current is driven by the bootstrap current and damped by an internal loop voltage (self-induction) on the L/R time scale. In this transient phase with a duration of up to 1 s,

the confinement properties were significantly affected by the ι profile developing with the bootstrap current, which itself depends on the confinement properties. Under stationary conditions, the shear changes sign with radius. For this scenario, a rather careful plasma operation was required, depending on the vacuum value of $\iota(a)$, and only in a few cases good confinement was obtained.

b) OH feedback: the bootstrap current was fully balanced by applying a small loop voltage, U_l, by feedback control of the OH-transformer. In the stationary phase, the Ohmic current density profile corresponds to the electrical conductivity which is concentrated in the central plasma region for the peaked T_e profiles whereas the bootstrap current is driven in the T_e gradient region. In this scenario (the one most commonly followed) $\iota(a)$ is fixed and positive shear is generated in the confinement region.

c) Electron cyclotron current drive: ECCD with a suitable $k_{||}$ spectrum (Gasparino, 1989) was used to compensate the bootstrap current completely. The current density profile driven by the ECRH is highly peaked, similarly to the power deposition profile. For central ECF power deposition, the ι profile with positive shear is comparable with the scenario of Ohmic current control. ECCD, however, offers the chance to control the rotational transform profile by adjusting the ECRH driven current density profile (partly off-axis power deposition, $k_{||}$ shaping). Only in this scenario can one generate a nearly shearless configuration with high plasma pressure.

d) The scenarios b) and c) are combined: by co- and counter ECCD with respect to the bootstrap current, both positive and negative internal shear can be generated depending on the $k_{||}$ spectrum (see Fig. 5).

e) Ohkawa currents: during NBI with co- and counter-injection, net current free discharges compensating the bootstrap current could be maintained by a corresponding mismatch of the Ohkawa currents.

2.2. Effect of Internal Shear

The effect of internal shear on the confinement had been analyzed in the predecessor W VII-A stellarator (Grieger, 1986 and Renner, 1986) which was also nearly shearless. For very low β with negligible pressure driven currents, moderate shear introduced by a small external loop voltage improved the confinement even in the degraded $\iota(a)$ regions up to the optimum values. For higher β, however, in the presence of pressure driven currents, the introduction of appropriate shear led to improved confinement only below and above the rational $\iota(a)$. By introducing stronger shear the confinement was degraded again and nearly independent of $\iota(a)$. Based on this experience, the investigation of ι profiles for "optimized" confinement properties is one main topic for W VII-AS .

The main operation in the W VII-AS with full compensation of the bootstrap current by external current control (OH-transformer or ECCD) leads to positive internal shear. The magnitude of this internal shear is related to the magnitude of the bootstrap current which depends on the energy content, especially on the electron temperature. In the transient phase of plasma build-up, the Ohmic current driven by the external loop voltage diffuses into the plasma center. Thus, the shear can be very small or even negative in this phase. Close to low order rational values of $\iota(a)$, unstable plasma evolutions (bifurcations) can appear. However, also transient maxima of the energy content were found in these phases with energy confinement times up to 30% higher than the ones in stationary phases. In the following, the effect of internal shear on the energy confinement is discussed only for stationary conditions with feedback control of the plasma current by the OH-transformer (scenarios b and d).

The regions with optimum energy confinement above and below $\iota(a) = 1/3$ are nearly equivalent. Internal shear, however, will change the situation: in discharges with $\iota(a)$ slightly above 1/3, the critical flux surface with $\iota = 1/3$ is located within the confinement region. For measured temperature and density profiles, the bootstrap current density and the electric conductivity are calculated (see Chap. 3.1.) and the internal ι profile is estimated. In these calculations, the currents are not completely balanced. These model calculations are based on Z_{eff} assumed to be constant in radius, the ion bootstrap contribution depending on the assumed T_i profile. For all ι profiles shown here the contribution of these residual currents was compensated. With sufficient internal shear depending on heating power and limiter radius, nearly identical discharges could be established above and below $\iota(a) = 1/3$, which means that the effect of island formation and ergodization at $\iota = 1/3$ could be suppressed by the internal shear. For lower heating power and small plasma radius ($a \simeq 12$ cm) in Figure 3, discharges with $\iota(a) > 1/3$ had degraded confinement properties. Even a flattening in the T_e profile was measured, indicating the $\iota = 1/3$ flux surface (Shots 8719-35 in Fig. 3). However, no degraded confinement was found for corresponding discharges with $\iota(a) < 1/3$ (Shots 8571-94 with slightly lower density), χ_e in the gradient region being more than a factor of 2 smaller than in the degraded case.

The profiles shown in Figure 4 (together with shots 8719-35 in Fig. 3) are part of an ECR-heating power scan with $\iota(a) = 0.34$ and equivalent densities. In these discharges the smallest possible limiter aperture corresponding to $a \simeq 12$ cm was used. For low heating power level (180 kW, shots 8763-78), the internal currents are very small and the internal shear in the plateau region in the T_e profiles is only weakly positive. Here, the confinement is significantly reduced, indicating island formation. Note that there is an offset of the ι-scale which is within the range of the experimental accuracy. For the higher heating power level (450 kW, shots 8638-58), however, the bootstrap current and the compensating Ohmic current are much higher, leading to stronger positive shear, $\iota' \approx 0.3$ m^{-1} at about half plasma radius. This improves the confinement, the $\iota \approx 1/3$ region is shifted outside and no flattening in the T_e profile is observed. For the two heating power levels of Figure 4, the energy content changes by a factor of 4 as compared to the power ratio of 2.5. Equivalent discharges at $\iota(a)$ slightly above 1/2 with $a = 12$ cm and with low heating power levels show that sufficient internal shear for good confinement is generated. Here, the shear in the vacuum configuration is already weakly positive which is contrary to the situation at $\iota \approx 1/3$. The scan of ECR heating power at $\iota \approx 1/3$ demonstrates a nonlinear mechanism of "self-stabilization" of the internal shear: both the

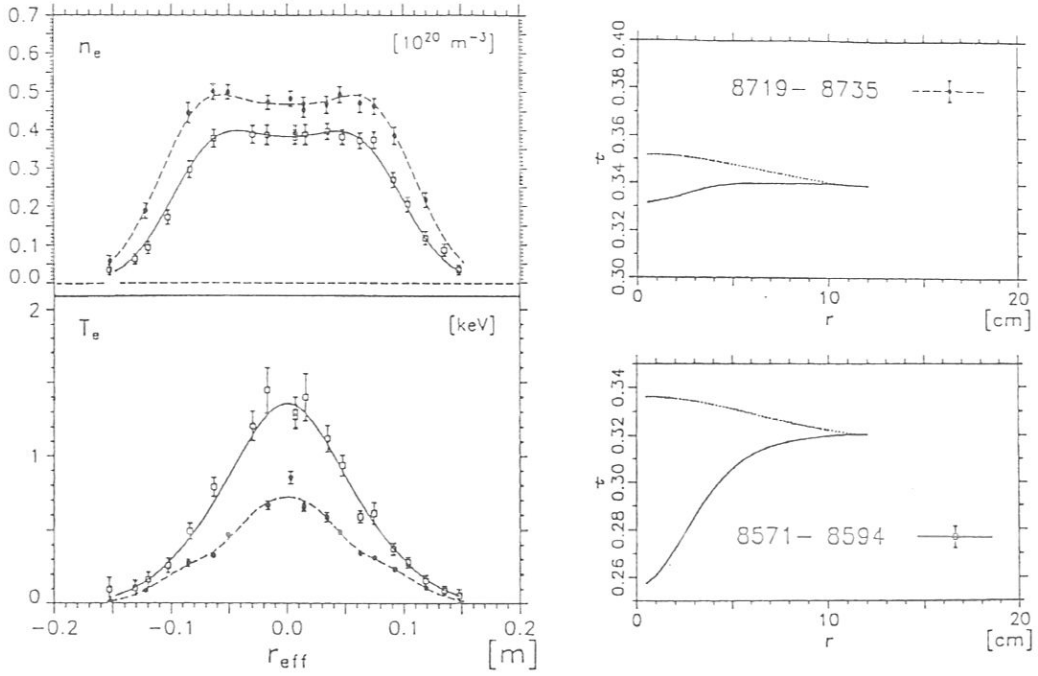

Figure 3 *Electron temperature, T_e, density, n_e, and rotational transform, ι, profiles for 2 discharge series with $\iota(a) < 1/3$ (shots 8571-94, solid lines) and with $\iota(a) > 1/3$ (shots 8719-35, broken lines), both with eqivalent ECR heating power ($\simeq$ 360 kW) and with plasma radius ($a \simeq 12$ cm). The dotted lines in the right plots represent the modified ι profiles due to the Pfirsch-Schlüter currents and the solid lines the $\iota(r)$ with bootstrap and compensating OH currents included.*

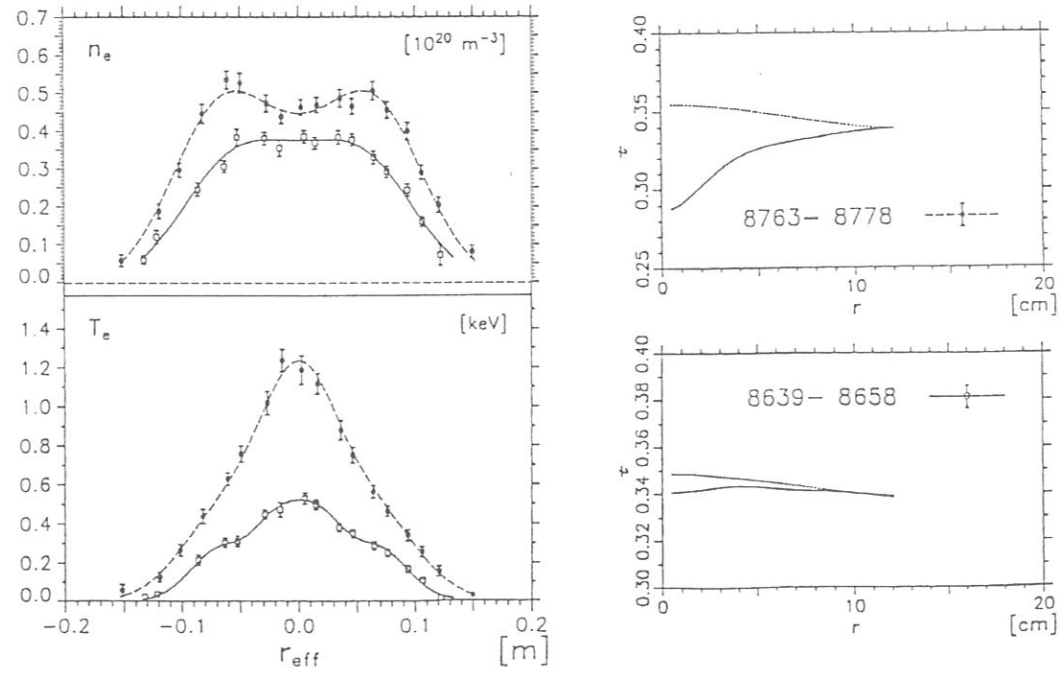

Figure 4 *Electron temperature, T_e, density, n_e, and rotational transform, ι, profiles for 2 discharge series with $P_{ECF} \simeq 180$ kW (shots 8763-78, solid lines) and with $P_{ECF} \simeq 470$ kW (shots 8739-58, broken lines), both with $\iota(a) > 1/3$ ($\simeq 0.34$) and with plasma radius ($a \simeq 12$ cm); compare Fig. 3.*

bootstrap and compensating Ohmic currents increase with the energy content, resulting in higher positive shear and in an improved confinement which leads to increasing energy content. The W VII-A experience indicates a degradation of confinement with strong internal shear. As a consequence, the optimization of energy confinement depends on the optimization of the internal ι profile.

ECCD was directly demonstrated (Erckmann, 1990). In stationary discharges ($n_e(0) \simeq 2.2\,10^{13}$ cm^{-3}) with 2nd harmonic ECRH, two rf-beams with perpendicular launching (no ECCD) were successively replaced by two other beams with oblique launching and equivalent power. The toroidal net current was feedback controlled by the OH-transformer. The change in the required loop voltage (with respect to perpendicular launch), $\Delta U_{\rm loop}$, is shown in Figure 5 (left plot) as a function of the launch angle. In the left and central plots, the solid lines represent the two rf-beam ECCD case and the broken lines the ECCD with one beam (perpendicular launching of the other one). With the plasma resistance, which was measured independently, fairly good agreement of $\Delta U_{\rm loop}$ was found with theoretical estimates on the basis of the adjoint approach (with trapped particle effects), which is included in the 3D ray-tracing code (Gasparino, 1990). The confinement properties are affected by the variation of toroidal launch angle (central plot in Fig. 5). The stored energy is decreased for co-ECCD with respect to the bootstrap current ($\varphi_{\rm tor} > 0°$) and increased for counter-ECCD ($\varphi_{\rm tor} < 0°$). The T_e profiles measured by the ECE diagnostic, however, are nearly unaffected. On the other hand, the change of stored energy can be related to changes in the density profiles. Corresponding modifications of the particle confinement properties are indicated by both H_α measurements and the external gas flux, which is required for feedback control of the line averaged density.

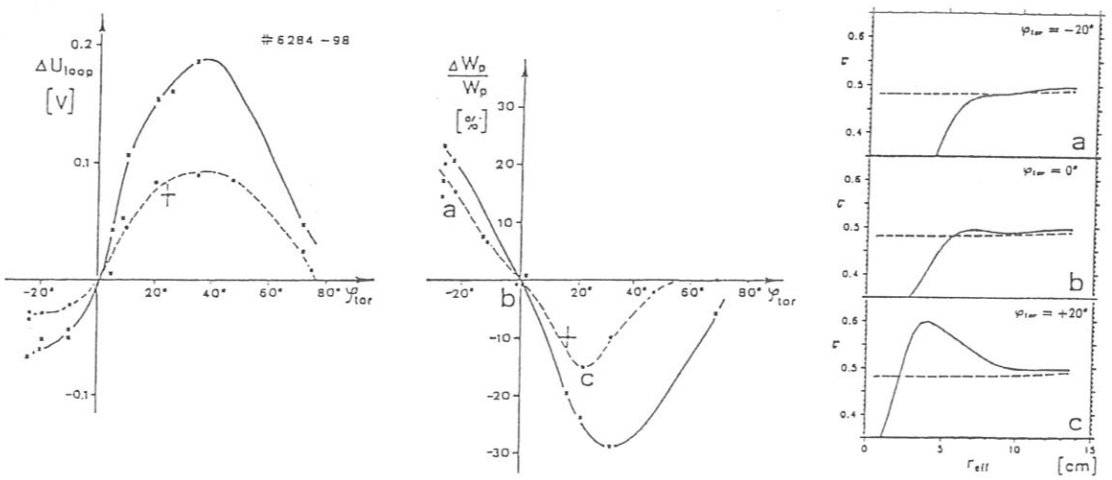

Figure 5 *Electron cyclotron current drive dependent on the toroidal launch angle, $\varphi_{\rm tor}$ ($k_\parallel$-spectrum), at 2nd harmonic ($B_0 = 1.25$ T) with nearly central deposition. The toroidal net current was completely balanced by the OH-transformer, the EC driven current is represented by the measured change in the loop voltage, $\Delta U_{\rm loop}$ (left plot). In the central plot, the change of stored energy, $\Delta W_p/W_p$, due to the different ι profiles is shown. The solid lines in these plots give the result of full ECCD with 2 rf-beams, the broken lines represent the ECCD with 1 beam where the other one being fixed (perpendicular launching, $\varphi_{\rm tor} = 0°$). In the right plots, 3 calculated ι profiles with one rf-beam ECCD are shown: for counter-ECCD (case a), no ECCD (case b) and for co-ECCD (case c). The solid lines give the estimates for the total ι profile, the broken lines the vacuum $\iota(r)$.*

These observations can be explained by changes of the rotational transform profiles which are shown in Figure 5 (solid lines in the right plots) for the one rf-beam ECCD case. In this series of discharges with nearly central ECRH power deposition, the EC driven current density profiles are highly localized and ι at outer radii is independent of details of the central ECCD profile. $\iota(a)$ is slightly below 1/2. The bootstrap current and the Ohmic current evaluated from measured profiles are not fully compensated leading to a small off-set in ι (solid lines). The case b corresponding to perpendicular launch ($\varphi_{\rm tor} = 0°$, no ECCD) is analogous to the discharges already described. The situation for counter-ECCD (case a) is similar to the case b, but the slightly increased positive shear improves the confinement. For the co-ECCD case c, however, the ι contribution of ECCD and bootstrap current is positive and the compensation by OH current results in negative shear in the confinement region. The shear is very small in the range $r > 10$ cm, the $\iota = 1/2$ resonance is within the region, which determines the global confinement properties. From both ECE and SX measurements electron temperature fluctuations (> 1 kHz) are derived only for the co-ECCD case. The fluctuation amplitudes are maximum at about 8 cm indicating the $\iota = 1/2$ resonance in agreement with the calculated ι profile (note the small off-set). In the corresponding 2 gyrotron co-ECCD case, the resonance is shifted outside (maximum of fluctuations at about 10 cm) and low frequency components (< 100 Hz) with broader radial resolution appear in the fluctuation spectrum. Furthermore, for both ECCD scenarios, equivalent fluctuation spectra are found in the H_α measurements at the limiters.

3. Transport

3.1. Electron Heat Conduction

For ECRH discharges, the electron densities were less than $5 \cdot 10^{13}$ cm^{-3}, so the collisional electron-ion coupling and the radiative losses were rather small, and the electron heat conduction was the dominant loss channel. Consequently, these discharges are the best candidates for electron energy balance analysis, which is based on density and temperature profiles measured by the Thomson scattering diagnostic. Furthermore, the n_e profiles were very broad and the T_e profiles highly peaked for central ECF power deposition.

For $B_0 = 2.5$ T, ECE electron temperature profiles are also available. In the central region of the plasma column, higher T_e values were indicated by the ECE measurements, the maximum T_e values from ECE were confirmed by continuum spectral analysis of SX measurements (PHA). For rotational transform $\iota \approx 1/2$, the difference between Thomson scattering and ECE data was much less than was the case for $\iota \approx 1/3$. The line of observation for Thomson scattering coincides with the calculated center of the vacuum magnetic surfaces. Due to the Shafranov shift which is larger for $\iota \simeq 1/3$ than for $\iota \simeq 1/2$, the Thomson scattering will miss the center of the plasma. Furthermore, there may be an additional outward shift of the magnetic axis. This will be cross checked by shifting the plasma by a vertical field. Up to now, only profiles from the Thomson scattering diagnostic have been used for the electron energy balance analysis. The central ion temperature was estimated by passive CX neutral particle diagnostic with T_i values up to 450 eV. As T_i-profile information was not available, the central T_i was assumed to be radially constant and the edge values were fitted to the measured T_e profile. These assumptions lead to low collisional coupling between electrons and ions. The total radiation loss was measured by bolometry. The normalized radiation profiles were modeled by a simple corona model.

The stationary electron energy balance equation with radiative losses and electron-ion power transfer is solved with the diffusive ansatz for the radial electron energy flux, $q_e = -n_e \chi_e T_e'$, and an analytic ECF power deposition model which is highly peaked in agreement with ray tracing calculations. Solving the electron energy balance equation, the measured T_e profiles are fitted by a least-squares technique using a power series of $log(\chi_e)$ in normalized radius, the power series coefficients being the fit parameters. This integration method of the electron energy balance equations leads to a smoothed representation of the electron heat conductivity, $\chi_e(r)$. For the n_e profiles, a standard fit function is used. With these T_e and n_e profiles, all neoclassical transport properties are estimated using the DKES-2 code (W.I. van Rij and S.P. Hirshman, 1989). The DKES code solves the monoenergetic drift kinetic equation for general magnetic field topology. Note that the W VII-AS field topology is quite different to that of standard stellarators. Energy convolution yields the full neoclassical transport matrix.

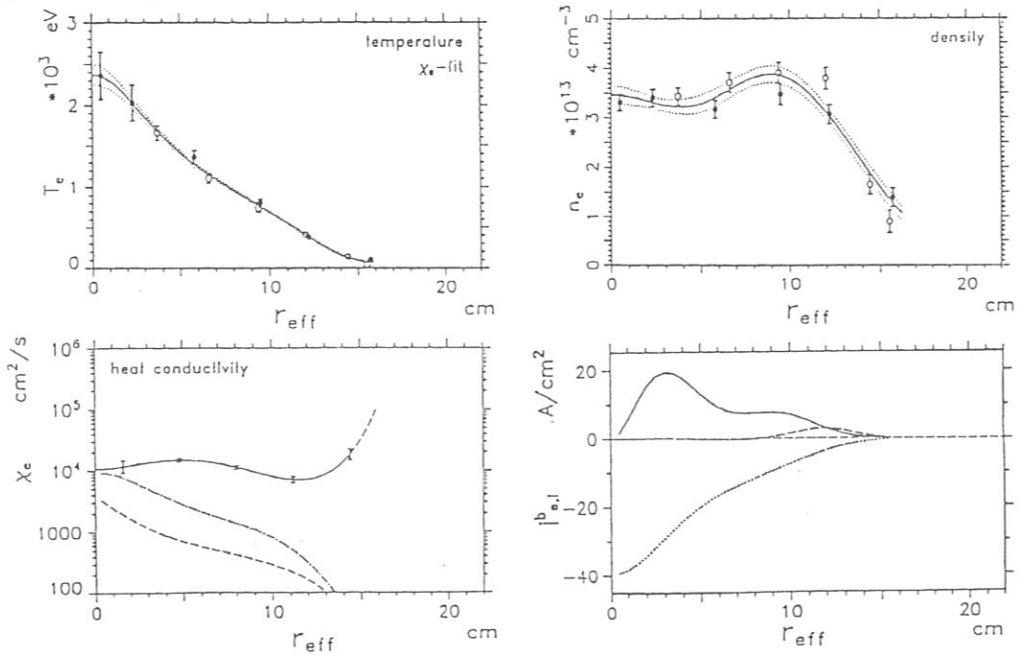

Figure 6 *Transport analysis for series 7545-57. Electron temperature, T_e, density, n_e, heat conductivity, χ_e, and current density profiles are shown for $B_0 = 2.5$ T and with $P_{ECF} \simeq 640$ kW input power. In the experimental χ_e (lower left plot, solid line) standard errors resulting from the least-squares fit of the T_e profile (upper left plot) are given, additionally, the χ_e from the DKES code (dot-dashed line) and from the Hinton-Hazeltine model (dashed line) are shown. The bootstrap current, see the profiles of j_{be} (solid line) and of j_{bi} (broken line) in the lower right plot, is compensated by an external loop voltage, see j_{OH} (dotted line).*

In Figure 6, the electron temperature, density, heat conductivity and current density profiles are shown for one of the high pressure ECRH discharges at $B_0 = 2.5$ T with 640 kW ECF input power (4 gyrotrons operating). The bootstrap current was compensated by an external loop voltage. The central β was about 0.5%. For this series of discharges with $\iota(a) \simeq 0.52$, the central T_e from ECE measurements was nearly 2.7 keV (2.4 keV from Thomson scattering). The T_e profile is highly peaked due to central ECF power deposition. For these high temperatures, the bulk part of the plasma is in the long mean free path regime (LMFP), the neoclassical transport being dominated by ripple losses. The neoclassical χ_e estimated by DKES code (dot-dashed line in Fig. 6) exceeds significantly the axisymmetric contribution (dashed line). Only in the innermost part does the neoclassical χ_e approach the experimental value. The error bars of the experimental χ_e-curve represent the standard errors of the fit given by the functional variance. Close to the effective limiter radius of 15.5 cm, the T_e profile becomes flat and the experimental χ_e increases strongly. Due to uncertainties in the outer T_e data, however, χ_e is reliable only up to 14.5 cm. In the major part of the plasma, χ_e is roughly constant (10^4 cm^2/s) and much larger than the neoclassical value. In the lower right plot, the internal current densities are shown: the electron and ion bootstrap current densities and the Ohmic current density, estimated using the measured loop voltage and the parallel electric conductivity, both current densities are estimated using the neoclassical DKES code. With an assumed value of $Z_{\text{eff}} = 4$, the total electron bootstrap current was calculated to be 4.1 kA (additionally, an ion contribution of up to 1 kA is expected) and the Ohmic current as -6.2 kA, the measured total plasma current being 0.2 kA. Typically, the agreement with the experimental data is not so good (Gasparino, 1990). This current distribution leads to a rather strong positive shear: $\Delta\iota = \iota(a) - \iota(0) \approx 0.2$, and the resonances $\iota = 1/2$ as well as $\iota = 5/11$ (natural islands in the vacuum configuration) are located within the confinement region (compare Chapter 2.1).

The series of discharges in Figure 6 is part of an ECRH power scan shown in Figure 7. In this scan, $\iota(a)$ was fixed at 0.52, the effective limiter radius was 15.5 cm and the central density was kept constant. Only for the lowest ECRH level (180 kW, solid lines in Fig. 7) was the half width of the n_e profile smaller. The T_e gradients (central plot) are only weakly dependent on heating power over the major part of the plasma column, the experimental electron heat conductivities, χ_e (lower plot) are significantly increased with heating power. The broader n_e profiles in Figure 7 at higher ECRH power levels (300 kW with 2 gyrotrons and 630 kW with 4 gyrotrons, dashed lines and dot-dashed lines, respectively) are related to a broader confinement regime with low χ_e in comparison to the discharges with low ECRH level. The χ_e profiles of this power scan with values much less than 1 m^2/s are some of the lowest values found in W VII-AS so far and of the order of the best χ_e values found in optimum Tokamak confinement.

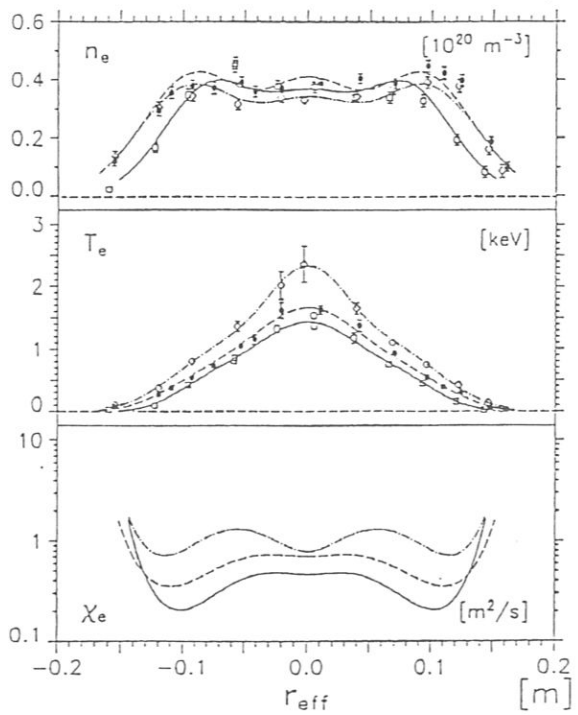

Figure 7 *Profiles of electron temperature, T_e, density, n_e, heat conductivity, χ_e, for an ECRH power scan at $B_0 = 2.5$ T, with plasma radius $a \simeq 15.5$ cm and $\iota(a) > 1/2$ ($\simeq 0.52$). The input power is $P_{ECF} \simeq 200$ kW (shots 7159-72, solid lines), $\simeq 340$ kW (shots 7333-48, broken lines) and $\simeq 640$ kW (shots 7545-57, dot-dashed lines), respectively.*

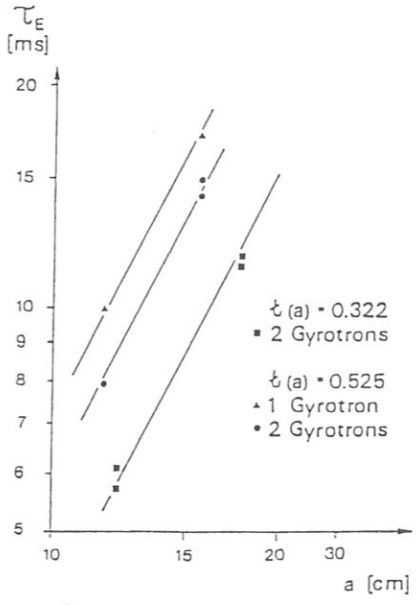

Figure 8 *Energy confinemt time, τ_E, as function of limiter aperture (plasma radius a) for ECRH with 1 and 2 gyrotrons and with $\iota(a) \simeq 0.32$ and $\iota(a) \simeq 0.52$, respectively. The slope of the straight lines corresponds to an a^2-scaling.*

. radius is typical for all discharges without degradation due to configurational egion, χ_e increases significantly (the n_e profiles are very broad). The electron shown in Figure 7 are nearly constant versus radius. This behaviour is only nement (high n_e, full field). Here, $n_e \cdot \chi_e$ is roughly constant in the outer part a^2 dependence of the global energy confinement time, τ_E, is found for fixed power, see Figure 8. This dependence can be directly explained from energy Figure 8 also shows that τ_E increases with $\iota(a)$ and decreases with ECRH n confinement, however, the T_e-gradients decrease and $n_e \cdot \chi_e$ increases close pendence of τ_E on a is found. The general trend of the energy confinement as resulting from the regression analysis in Chapter 4 shows that the dependence of τ_E on the plasma radius is weaker than a^2.

Due to ECRH cut-off, n_e at $B_0 = 1.25$ T was limited to $\leq 2.5\,10^{13}$ cm^{-3}. At high ECRH power levels, the generation of suprathermal electrons at low densities led to a broadening in the T_e profiles. Fokker-Planck model calculations indicated that ripple transport of suprathermal electrons would only result in a broadening of the effective power deposition, direct losses were negligible and a degradation of the effective heating power could be excluded. However, the minima values of the χ_e profiles were clearly higher (above 10^4 cm^2/s) for half field than for full field operation indicating an improvement of confinement with B_0 and n_e (see the regression analysis in Chapter 4).

3.2. Particle Transport

The particle confinement in W VII-AS was investigated for ECRH discharges at 1.25 and 2.5 T by coupling DEGAS code (Heifetz, 1982) simulations with H_α emissions measured at relevant toroidal positions. Radially resolved ion fluxes were obtained from calculated neutral particle distributions, after calibrating them with the H_α signals (Sardei, 1990). Estimated $Z_{\rm eff}$ were used to derive the electron particle fluxes and diffusivities.

The power scan at 2.5 T, $\iota(a) = 0.34$, $a = 12$ cm already discussed in Chapter 2.2., is characterized by electron density profiles which get more and more hollow as the heating power is increased, see Figure 9. In the central region the electron fluxes have been compared with neoclassical predictions. As T_i profile information is lacking, only the neoclassical electron fluxes can be estimated by DKES code. In the 4 gyrotrons case, for which the central hollow profile is most pronounced, the fluxes near the plasma center, $r = 2.5$ cm, are $\Gamma_e \simeq 3 \cdot 10^{15}$ cm^{-2}/s, and $\Gamma_e^{neo} \simeq 2 \cdot 10^{15}$ cm^{-2}/s. This fairly good agreement means that the observed hollow density profile can be explained reasonably well by the neoclassical temperature gradient driven particle flux (thermodiffusion), without need of additional anomalous contributions. This is consistent with the lack of major resonances in the central confinement predicted for large heating powers and fixed $\iota(a) \simeq 1/3$ (Chap. 2.2). There it is shown that the ohmic current needed to compensate the high bootstrap current leads to a strong positive shear which keeps the central region well below the $\iota = 1/3$ resonance (see Fig. 4). By reducing the heating power down to 1 gyrotron, the hollow density profiles disappear (Fig. 9) and the particle fluxes are enhanced by a factor of $\simeq 5$ over the neoclassical values. This poor particle confinement in the central region is consistent with a flattening of the measured T_e profile (see Fig. 4). In this case, an $\iota = 1/3$ transition in the main confinement region is predicted (see Chap. 2.2).

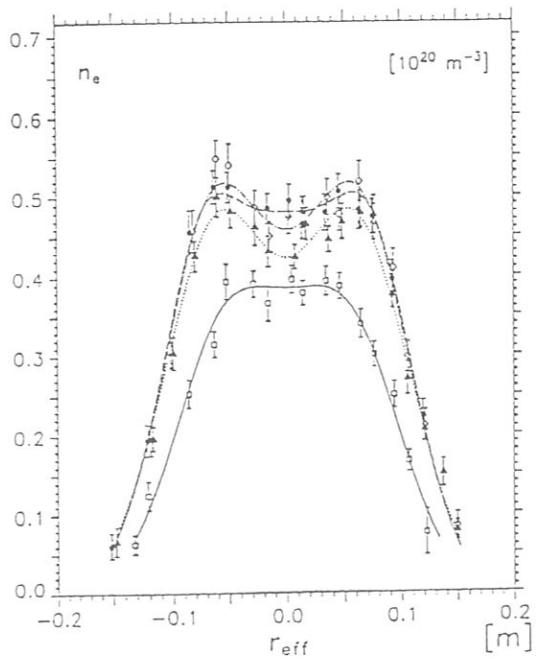

Figure 9 Electron density profiles for an ECRH power scan showing hollow profiles for high power level ($\iota(a) \simeq 0.34$ and $a \simeq 12$ cm). The ECF input power is $P_{ECF} \simeq 170$ kW (shots 8763-78, solid line), $\simeq 370$ kW (shots 8719-35, broken line), $\simeq 470$ kW (shots 8639-58, dot-dashed line) and $\simeq 640$ kW (shots 8668-95, dotted line), respectively.

In the density gradient region the particle fluxes strongly increase whereas the neoclassical fluxes are negligible with respect to the central region. For solving the particle balance equation the diffusive ansatz, $\Gamma = -Dn'$, is used for the particle fluxes. The particle diffusivities, D, have been evaluated for discharges operated at half and full field, and $\iota(a)$ values close to the major resonances 1/3 and 1/2, where optimum confinement has been found (see Fig. 2). The radial range of the diffusivities is restricted to the density gradient region up to the limiter (D cannot be determined for flat density profiles). Here, the density profiles can be explained by diffusive transport alone.

For the power scan at $\iota(a) = 0.34$ discussed above, the diffusivities in the outer confinement region ($r \simeq 10$ cm) increase with heating power for constant density ($D \simeq 1800 - 4000$ cm^2/s from 2 to 4 gyrotrons). The same behaviour is

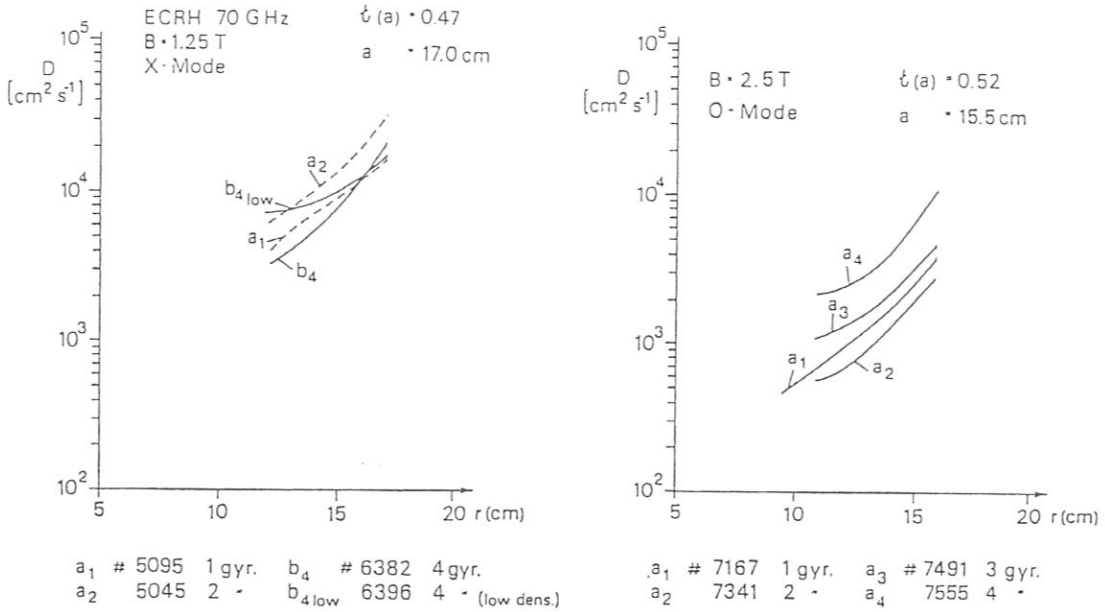

Figure 10 *Ion diffusivity profiles, D, for ECRH discharges at $B_0 = 1.25$ T (Fig. 10a, left plot) and at $B_0 = 2.5$ T (Fig. 10b, right plot) depending on ECR heating power (number of gyrotrons operating). In Fig. 10b the line averaged density is lower for the 1 gyrotron case.*

found for discharges operated at $\iota(a) \simeq 0.5$ for both 1.25 and 2.5 T, see the 1 and 2 gyrotron cases of Fig. 10a with $\bar{n}_e \simeq 10^{13}$ cm^{-3}, and the 2,3,4 gyrotron cases of Fig. 10b with $\bar{n}_e \simeq 2.8 \cdot 10^{13}$ cm^{-3}. D also increases with decreasing density for constant heating power, see the 4 gyrotron cases of Fig. 10a, with $\bar{n}_e \simeq 8.5 \cdot 10^{12}$ and $1.8 \cdot 10^{13}$ cm^{-3}, respectively. A similar behaviour was found for the electron thermal diffusivity, see Chapter 4. In the 1 gyrotron case of the 2.5 T, $\iota(a) = 0.52$ power scan shown in Fig. 10b, the expected reduction of D due to the small heating power is overcompensated by an enhancement due to a smaller local density. A comparison between the analyzed 1.25 and 2.5 T discharges indicate an average improvement of the particle confinement with the magnetic field by a factor of $\simeq 3$ throughout the density gradient region.

Figure 11 shows the ECRH power dependence of the diffusivities in the outer confinement region ($r/a = 0.8$) for the discussed 1,2 gyrotrons discharges at 1.25 T, the power scans at $\iota(a) = 0.52$ and 0.34 and 2 additional full field discharges at $\iota(a) = 0.52$, $a = 12$ cm. The lowest values of the diffusivity are found at full field, high ι operation. In the low ι power scan, the diffusivities are, on the average, twice as large as in the high ι power scan. This ι dependence of D is not distorted by density effects since, at each power level, the densities between the 2 power scans differ only by $\simeq 15\%$. The relatively high diffusivities in the 1 gyrotron case of both power scans can be explained by the local densities being 40% smaller than in the respective 2, 3, 4 gyrotron cases. All these results indicate that, at least in the outer confinement region, D scales positively with the heating power and negatively with B, ι and local plasma density. A comparison of D and χ_e for the analyzed discharges yields D/χ_e values between 0.1 and 0.3 in the outer confinement region at $r/a = 0.8$. Concerning the plasma refuelling sources, it should be mentioned that limiter recycling accounts for about 90% of the ion production in the small aperture, low ι case (optimal wall screening from ion impact) and only for about 20% in the large aperture, high ι case.

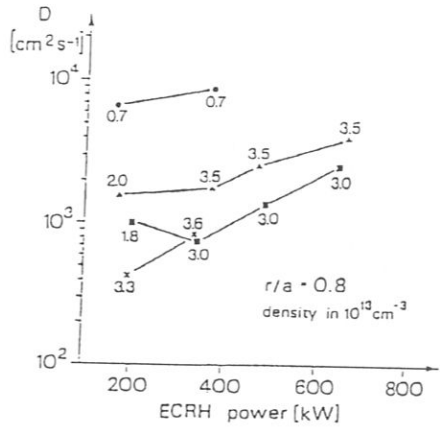

Figure 11 *Dependence of ion diffusivity, D, on ECRH power at fixed $r/a = 0.8$. The numbers in the plot give the local electron density, n_e, in units of 10^{13} cm^{-3}.*

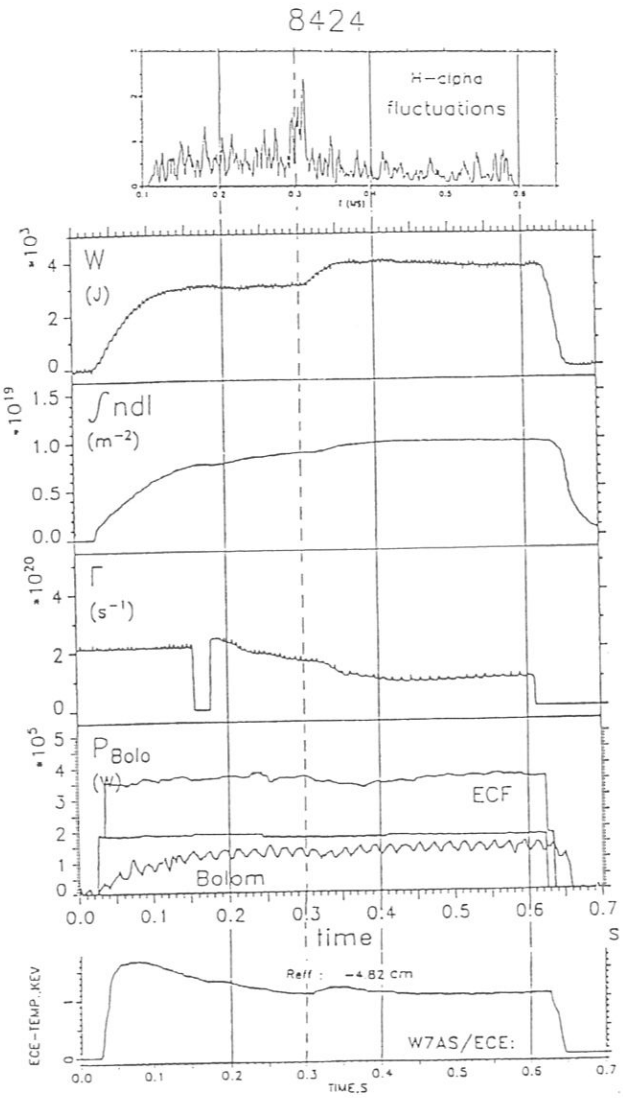

Figure 12 *Transition to improved confinement in shot 8424: the energy content, W, the line density, $\int ndl$, the gas flux, Γ, ECF input power and radiation loss, P, and, in the lowest plot, the ECE electron temperature at about $r \simeq 5$ cm are shown versus time. The H_α fluctuations (upper plot) peak at the transition (broken line) and decrease afterwards. T_e shows only a transient increase after the transition contrary to W and $\int ndl$.*

An interesting transition was observed in ECRH full field discharges at $\iota(a) = 0.32$ (Fig. 12). During the evolution of the electron density the energy content increases within 15 ms by about 30% without any measures being taken from the outside. The transition takes place at a line averaged density $\bar{n}_e = 1.8 \cdot 10^{14}$ cm^{-3} corresponding to $\int ndl = 7.5 \cdot 10^{14}$ cm^{-2} in Figure 12. The H_α signals show a maximum in the fluctuation level at the start of the transition and then relax to a lower level. From ECE measurements a small transient increase in T_e is seen during the transition at all radial positions. This indicates that this phenomenon is not just restricted to the plasma edge as one would conclude from the H_α signals alone. From Thomson scattering the temperature profiles during the steady phase after the transition turned out to be the same, but the electron density has increased, indicating better confinement, particularly as the external gas flux is even reduced. From energy and particle balance analysis, the transition to higher density is seen to correlate with an average reduction of χ_e by about 30% over the whole plasma column and with a decrease of D by about 50% in the density gradient region.

The impurity particle confinement in WVII-AS has been investigated by laser ablation of aluminium. Since hydrogen-like Al, which is peaked in the bulk plasma for ECRH discharges, can be assumed to evolve under ionization equilibrium conditions, the decay time of the Al-XIII line radiation during stationary plasma conditions is a measure of the central confinement time for this impurity. For moderate and high ECRH power, the decay time is found to increase from $\simeq 10$ ms at 1.25 T to $\simeq 40$ ms at 2.5 T. Also, it decreases with ECRH power for given limiter aperture. The time evolution of Al-XIII could be reproduced by transport simulations with the STRAHL code (Behringer, 1987), which uses a constant diffusion coefficient and an inward convective term $v = -(2D/a)\cdot(r/a)$. The corresponding D decrease from $5000 - 8000$ cm^2/s for 1.25 T to $1200 - 2000$ cm^2/s for 2.5 T. These numbers reduce by $\simeq 20\%$, if the velocity term is omitted. Discrepancies between the measured and simulated decay times are found, however, for the lower ionization stages. More experimental data, and more accurate simulations, including a spatial variation of D, are needed to improve the description of the impurity transport behaviour under different experimental conditions.

4. Transport Regression Analysis

The dominant parameter dependences of both the local electron heat conductivity, χ_e, and the global energy confinement time, τ_E, are given by multiple linear regression analysis. This standard procedure is only used to obtain the general trend in the confinement properties as well as the significant parameter dependences. About 40 series of discharges with $2nd$ harmonic ECRH as well as about 25 series of $1st$ harmonic ECRH were selected from a database system for this regression analysis. Only discharges with central ECF power deposition which is highly localized were taken into account (the database for off-axis heating is only small) and discharges with confinement degradation due to configurational effects were excluded. In most discharges at $B_0 = 2.5$ T the electron density is more than twice the density at low field, $B_0 = 1.25$ T, leading to a rather high correlation in the regressions with B_0 and n_e. Consequently, all regressions were tested separately on the reduced database with $B_0 = 1.25$ T and $B_0 = 2.5$ T, respectively. No significant modification in the regression coefficients was found.

First, the τ_E-regression results are described. The energy confinement time depends significantly on magnetic field strength, B_0, line averaged density, $\bar{n}_e$, ECF input power, P_{ECF}, and plasma radius, a. The edge value of rotational transform, $\iota(a)$, has a smaller significance, however, $\iota(a)$ is included in the regression.

$$\tau_E{}^{mlr} = (1.14 \pm .02)\, a^{0.83\pm.17}\, B_0{}^{0.51\pm.09}\, \bar{n}_e^{0.66\pm.07}\, P_{\mathrm{ECF}}^{-0.55\pm.05}\, \iota(a)^{0.26\pm.09}$$

with τ_E in ms, $\bar{n}_e$ in 10^{14} cm^{-3}, P_{ECF} in MW, B_0 in T and a in cm, a being the minimum of effective limiter and separatrix radius. For the selected database, the experimental $\tau_E{}^{exp}$ versus the result of the multiple linear regression, $\tau_E{}^{mlr}$, is shown in Figure 14. As a surprising result, these τ_E regression coefficients for B_0, $\bar{n}_e$ and P_{ECF} are identical to those found in Heliotron-E for ECRH discharges (Zushi, 1988). Also the energy confinement times estimated by means of the frequently used LHS-scaling (Sudo, 1990) are comparable. Furthermore, the regression coefficients for $\bar{n}_e$ and P_{ECF} are nearly identical to the LHS ones. However, the regression coefficients for B_0 and a are significantly smaller than those given by the LHS-scaling.

The relation of electron density in the bulk part of the plasma and line averaged density, $\bar{n}_e$, depends only slightly on plasma radius. Replacing $\bar{n}_e$ in the regression by the central electron density, $n_e(0)$, gives similar results. The general a dependence of τ_E in the regression is in contrast to the results shown in Figure 8 ($\tau_E \propto a^2$, see Chap. 3.1). For discharges with optimum confinement (e.g. those shown in Figure 7), the T_e profiles have nearly a triangular shape. However, for most discharges included in the database the T_e profiles are bell-shaped. For full limiter aperture at $\iota(a) \simeq 1/3$, $a > 18$ cm, the temperature gradient close to limiter is typically much smaller than for reduced limiter apertures, the edge electron densities being roughly comparable. Note that for $\iota \simeq 1/2$ the separatrix radius is less than 17 cm. This flattening of the T_e profile is consistent with a stronger increase of χ_e (and also $n_e \cdot \chi_e$) at the plasma edge. These findings indicate that the confinement is degraded in this region for most discharges.

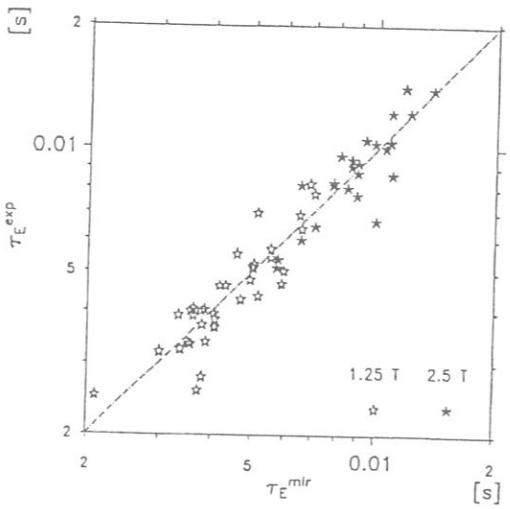

Figure 13 Experimental energy confinement times, $\tau_E{}^{exp}$, versus the values calculated by means of the multiple linear regression formula, $\tau_E{}^{mlr}$.

As the analysis of τ_E scaling laws is not very conclusive for describing the transport properties, a local χ_e regression is performed by using the χ_e profiles estimated from the electron energy balance analysis. For each χ_e profile a radial range of confidence was specified to exclude uncertainties depending on the quality of the measured profiles, especially near the plasma edge. In the central part of the plasma, the experimental χ_e can reach the neoclassical value for discharges with peaked T_e in the LMFP collisionality regime. Here, different T_e dependences must be expected. Furthermore, the χ_e profile from the electron energy balance analysis depends sensitively on the ECRH power deposition profile in the central region. Therefore, the plasma center with $r < 5$ cm was excluded from the regression analysis. For the gradient region, however, with $r > 5$ cm where the neoclassical χ_e is always small compared to the experimental one, the global regression analysis gives reasonable results.

As the experimental χ_e is roughly constant in the bulk part of the plasma and $T_e(r)$ varies strongly, a global χ_e regression must result in a very small T_e dependence of χ_e. Consequently, local regressions of χ_e (fixed plasma radius) with the local parameters B_0, n_e and T_e which are assumed to be dominant were performed. No conclusive results were found: the regression coefficients for B_0 and n_e were nearly independent of radius while the T_e dependence for $r > 8$ cm was rather small and the quality of these regressions was unacceptable. Adding a global heating power dependence leads to a significant improvement, however, the local T_e dependence remains to be rather small but is inverted: χ_e decreased with increasing T_e. Omitting the T_e dependence in local regressions has only a small effect on

ɜsion coefficients were roughly independent of radius. Contrary to what
ɪescribed (in sense of a best fit) by the global parameter P_{ECF} than by
ɜion of $\chi_e(r)$ with the parameters B_0, $n_e(r)$ and P_{ECF} which were the
ɪed. An additional $\iota(a)$ dependence was allowed to be consistent with

$$\sim n_e^{-0.60\pm.05}\, P_{ECF}^{0.76\pm.03}\, \iota(a)^{-0.49\pm.06}$$

ECF in MW, B_0 in T). The quality of this regression becomes obvious from
versus χ_e^{mlr}. The global standard error of the χ_e regression defined by means of the
ɪan 40%. The only radial dependence in this regression ansatz is given by the electron density
ɪnus, a remaining radial dependence is checked by analyzing the ratio $\chi_e^{exp}(r)/\chi_e^{mlr}(r)$ for all selected discharges. The mean value and the standard deviation are plotted versus radius in Figure 15. Obviously, no explicit radial weighting function is neccessary for this form of χ_e regression. Furthermore, the energy balance equation was integrated with this χ_e^{mlr} and when the resulting energy confinement times were compared with the experimental values, very good agreement was found.

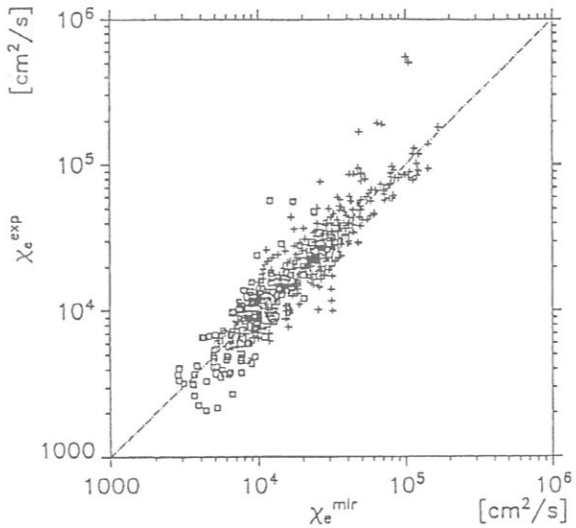

Figure 14 *Experimental electron heat conductivities, χ_e^{exp}, versus the values calculated by means of the multiple linear regression formula, χ_e^{mlr}.*

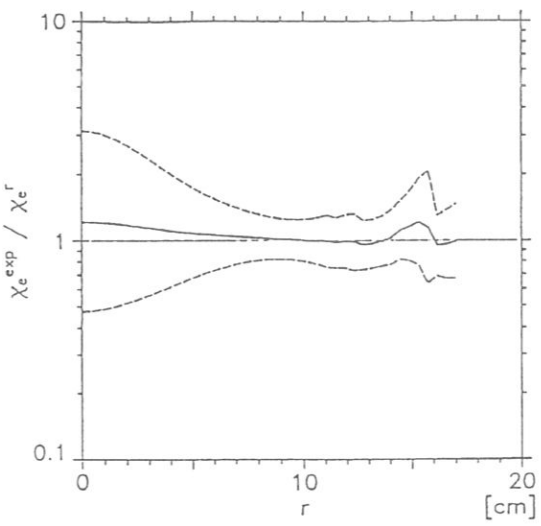

Figure 15 *Mean value (solid line) and standard deviation (broken line) of $\chi_e^{exp}/\chi_e^{mlr}$ estimated for 63 selected discharges of the database versus radius, r.*

The χ_e regression yields the analogous (inverse) parameter dependences as the τ_E regression. With a simplified integration of the electron energy balance based on χ_E^{mlr} a corresponding τ_E scaling formula can be derived. Thus, both the local and global transport regressions are consistent. The heating power dependence in the global χ_e regression can be qualitatively understood by means of the electron energy balance equation. Radiation losses and collisional electron-ion energy transfer can be neglected in this rough approach as the electron heat conduction is the dominant loss term. Outside of the ECRH power deposition zone ($r > 5\,cm$) the electron energy balance equations can be written in the form

$$-n_e \chi_e \frac{\partial T_e}{\partial r} \approx \frac{1}{4\pi^2 R r} P_{ECF}.$$

Typically, the density profiles are flat and very broad, and $n_e \cdot \chi_e$ is roughly constant. The shape of the T_e profiles does not change very much on variation of external plasma parameters. Within the important confinement region, the temperature gradient is only slightly affected by the heating power. These experimental findings reflect the basic physics of the electron energy transport. The parameter dependence of $\chi_e(r)$ follows directly: the strong relation of $n_e \cdot \chi_e$ to the heating power becomes obvious. The statistical significance shows this to be a general trend in all ECF heated discharges where electron heat conduction is the dominant loss channel. Consequently, on the basis of the electron energy balance the χ_e regression reflects the fact that only little variation is found in the electron temperature gradient. Furthermore, the dependences of χ_e on B_0 and $\iota(a)$ is given directly by the regression. A physical picture of this anomalous transport cannot be given by such a form of regression analysis. However, the fact that no local scaling of χ_e with T_e was found indicates two possible explanations. Firstly, the electron heat conduction cannot be treated by the specific form of regression ansatz as described in this Chapter or, secondly, the picture of transport being determined by only local plasma parameters is inadequate.

5. Combined ECRH and NBI Discharges

Most of the shots in W VII-AS have been oriented to the study of pure ECR heated plasmas. Two types of discharges have been investigated in connection with NBI.

a) NBI with ECR heated target plasma: the gyrotrons were only used to provide a target plasma and then shut off. The trapping of the neutral beams was improved in with additional pellet injection. The plasma parameters reached are $n_e(0) \simeq 10^{14}$ cm^{-3}, $T_e(0) \simeq T_i(0) \leq 0.7$ keV with an energy content $W \leq 15$ kJ and $\tau_E = 10$ ms. The discharges were always non-stationary and, due to good particle confinement, the fast density increase led to a radiative collapse.

b) Combined ECR and NBI heated plasmas leading to stationary discharges at moderate densities and radiation power levels. Similar experiments have already been reported from W VII-A (Ringler, 1986). An influence of ECRH on the time evolution of the density has been seen before (Alikaev, 1984 and Uo, 1986). Due to a reduction of the particle confinement as compared to purely NBI heated discharges, the density can even be feedback controlled by gas puffing. In Figure 16, shots are shown to illustrate this technique. Energy content, line density, gas flux and heating power are shown as a function of time. In the case of shot 9077, stationary conditions were reached using 3 gyrotrons with feedback control of the density. For shot 9079, however, one of the 3 gyrotrons failed with the result of a nonstationary discharge. The density reaches twice the ECRH cut-off without gas puffing. It turns out that the ECRH power necessary to reach stationary conditions has to be increased with NBI power. During the next experimental campaign these discharges with combined heating will be one of the focal points.

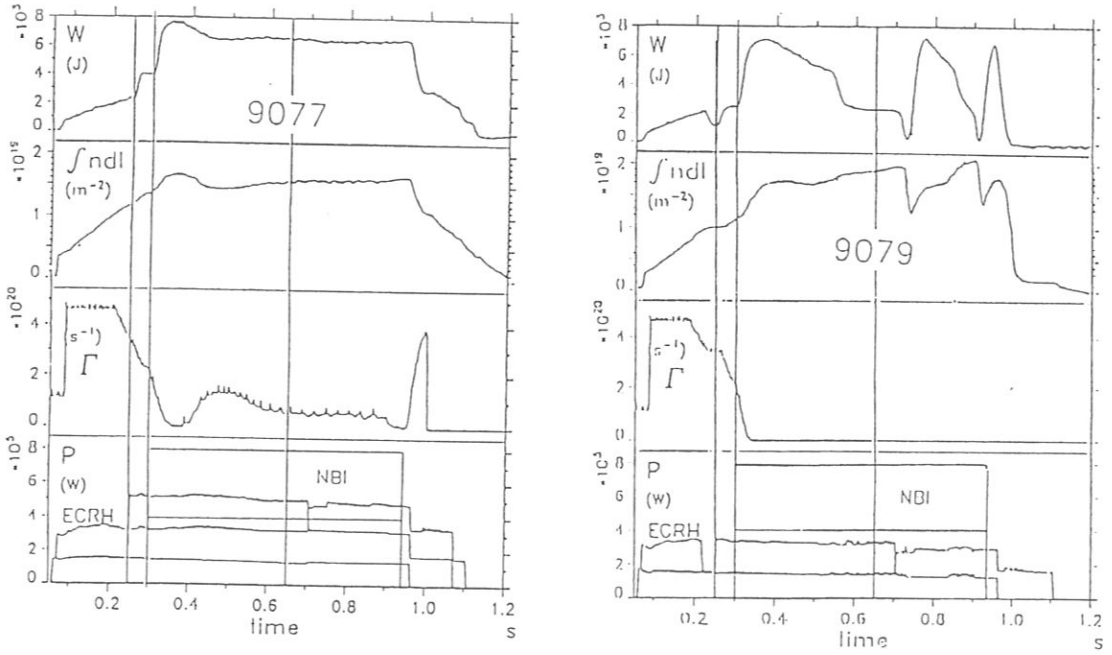

Figure 16 Density control in combined ECRH + NBI discharges: the energy content, W, the line density, $\int n\,dl$, the gas flux, Γ, and NBI and ECF input power, P, are plotted versus time. In shot 9077 with 3 gyrotrons operating, the density reamins below cut-off and even a small gas flux was neccessary for stationary conditions. In shot 9079 with only 2 gyrotrons operating, however, the density increases to cut-off, no gas flux was applied.

6. Summary and Conclusion

W VII-AS with its modular field system has operated routinely since January 1990 with full field parameters. From this experience one can draw the conclusion that also a large modular system can be realized, especially as the mechanical forces will not exceed values known from W VII-AS. In the 1st and 2nd experimental campaigns most of the investigations were devoted to ECR-heated plasmas (70 GHz) at 1.25 T and 2.5 T magnetic field with 2nd harmonic x-mode and fundamental o-mode launching. Maximum plasma parameters of $T_{eo} \simeq 2.5$ keV, $T_{io} \simeq 0.4$ keV, $n_{eo} \simeq 5 \cdot 10^{13}$ cm^{-3} and $\tau_E \simeq 10 - 20$ ms have been achieved with this technique. The expected reduction of the Shafranov shift by reducing the Pfirsch-Schlüter currents by a factor of two has been confirmed by the experiment.

The control of the rotational transform at the plasma edge, $\iota(a)$, works for all possible scenarios under consideration. For low internal shear operation, degraded confinement is found to be related to low order rational values of ι which indicates island formation and ergodization in the magnetic configuration. Even local flattening of the electron

or these conditions. Internal shear is generated by internal currents. In most
current which is experimentally confirmed is feedback-compensated by an
positive shear depending on the magnitude of the bootstrap current and
positive effect of internal shear on the energy confinement has been shown
ll be the study of confinement optimization by means of an appropriate
nsform profile using local ECCD.

uce analysis based on measured T_e and n_e profiles yields the electron heat conductivity, $\chi_e(r)$. χ_e values which have been achieved are well below 10^4 cm$^2/s$ which are in the range of the optimum χ_e ues found in tokamaks. For all analyzed discharges, the neoclassical transport coefficients were calculated by using the DKES code and compared to the experimental values. Due to the strong T_e dependence, the neoclassical χ_e values decrease rapidly with radius and are typically about one order of magnitude smaller than the experimental value at half plasma radius. The experimental χ_e, however, are roughly constant in the bulk part of the plasma and increase close to the plasma edge. The neoclassical χ_e come up to the experimental values only for central high ECF power deposition with peaked temperatures where the neoclassical ripple losses dominate. For discharges with $n_e > 3 \cdot 10^{13}$ cm^{-3} at full field optimum confinement properties were achieved, being characterized by $T_e' \approx const$ as well as $n_e \cdot \chi_e \approx const$ in nearly the whole confinement region. For these discharges, the global energy confinement time scales with a^2. With the present database a regression analysis of both τ_E and local χ_e has been performed. No significant T_e dependence was found in the local χ_e regression. χ_e scales with ECR-heating power and inversely with n_e, B and $\iota(a)$.

From the DEGAS code, particle fluxes and diffusivities have been derived using measured T_e and n_e profiles and absolute H_α intensities at relevant positions around the machine. The radial range of the diffusivities includes the density gradient region up to the limiter. Here, D is found to range between 500 and 10^4 cm^2/s for the discharges analyzed exceeding neoclassical predictions by more than one order of magnitude. D scales with ECR-heating power and inversely with n_e, B and $\iota(a)$. The ratio D/χ_e was between 1/10 and 1/3.

Density profiles were found to become hollow in the plasma center with increasing ECRH power (200 – 800 kW). For the hollow profiles at high power level, the central particle fluxes from DEGAS simulations agree fairly well with the neoclassical fluxes which are dominated by thermodiffusion. Consequently, the ECRH density pump-out in the central region is consistent with neoclassical transport in W VII-AS.

Future work will concentrate on NBI discharges. Firstly, there are two ways to avoid radiation collapse. Combined ECRH - NBI discharges have already been shown to reach a stationary state. However, the understanding of the density control by ECRH in NBI discharges is of dominant importance. Future experiments also at 140 GHz ECRH will concentrate on this topic. Furthermore, ECRH may also be used to avoid impurity accumulation. Secondly, the machine is now being carbonized and will be boronized later in the year. It should be noted that so far only glow discharges have been used for the conditioning of the machine. From the experience of other machines it is expected that these measures will reduce the radiation problem connected with the good particle confinement in pure NBI discharges.

References

Alikaev, V.V. (1985) Plasma Physics and Contr. Nucl. Fus. Res.; 1, 419

Behringer, K. (1987) JET-R (87) 08

Erckmann, V. et al. (1990) ECA, 17th EPS Conf. on Contr. Fus. and Plasma Phys., Amsterdam, 3, 1271

Gasparino, U. et al. (1989) ECA, 16th EPS Conf. on Contr. Fus. and Plasma Phys., Venice, 2, 631

Gasparino, U. et al. (1990) ECA, 17th EPS Conf. on Contr. Fus. and Plasma Phys., Amsterdam, 3, 1275

Grieger, G. et al. (1986) Plasma Physics and Contr. Fusion, 28, 43

Heifetz, D.B. et al. (1982) J. Comput. Phys., 46, 309

Horton, W. et al. (1989) Plasma Physics and Contr. Nucl. Fus. Res.; Proc. of the 12th Conf. (Nice), 2, 211

Kaneko, H. et al. (1987) Nuclear Fusion, 27, 1075

Kasparek, W. (1988) Proc. 15th Symp. on Fusion Technology (SOFT), Utrecht, B19

Kisslinger, J. and H. Wobig (1985) ECA, 12th EPS Conf. on Contr. Fus. and Plasma Phys., Budapest, 1, 453

Motojima, O. (1989) Proc. 1st Int. Tokei Conf. on Plasma Physics and Contr. Nucl. Fus., P3

Renner, H. (1986) ECA, 13th EPS Conf. on Contr. Fus. and Plasma Phys., Schliersee, 1, 287

Renner, H. (1989) Plasma Physics and Contr. Fusion, 31, 1579

van Rij, W.I. and S.P. Hirshman (1989) Phys. Fluids B, 1, 563

Ringler, H. et al. (1987) Plasma Physics and Contr. Nucl. Fus. Res.; Proc. of the 11th Conf. (Kyoto), 2, 603

Sardei, F. et al. (1990) ECA, 17th EPS Conf. on Contr. Fus. and Plasma Phys., Amsterdam, 2, 471

Sudo, S. et al. (1990) Nuclear Fusion, 30, 11

Uo, K. et al. (1987) Plasma Physics and Contr. Nucl. Fus. Res.; Proc. of the 11th Conf. (Kyoto), 2, 355

Weller, A. et al. (1990) ECA, 17th EPS Conf. on Contr. Fus. and Plasma Phys., Amsterdam, 2, 479

Wesner, F. et al. (1988) Proc. 15th Symp. on Fusion Technology (SOFT), Utrecht

Wobig, H. et al. (1987) Plasma Physics and Contr. Nucl. Fus. Res.; Proc. of the 11th Conf. (Kyoto), 2, 369

Zushi, H. et al. (1988) Nuclear Fusion, 28, 1801

TOMIC ENERGY AGENCY

'ATIONAL CONFERENCE ON
D CONTROLLED NUCLEAR FUSION RESEARCH

Washington, DC, United States of America, 1–6 October 1990

IAEA-CN-53/C-1-2

CONFINEMENT PROPERTIES OF THE "ADVANCED STELLARATOR" WENDELSTEIN W 7AS.

H. Renner, U. Gasparino, H. Maaßberg, G. Kühner,
H. Ringler, F. Sardei, A. Weller
and the W 7AS Team

V. Afanasiev*, R. Brakel, R. Burhenn, G. Cattanei, A. Dodhy, D. Dorst, A. Elsner, K. Engelhardt, V. Erckmann, U. Gasparino, S. Geißler, G. Grieger, P. Grigull, H. Hacker, H.J. Hartfuß , A. Izvozchikov*, R. Jaenicke, S. Jiang**, J. Junker, M. Kick, H. Kroiss, G. Kühner, I. Lakicevic, A. Lazaros, H. Maaßberg, C. Mahn, W. Ohlendorf, M.A. Ochando***, F. Rau, H. Renner, H. Ringler, J. Saffert, J. Sanchez***, F. Sardei, M. Tutter, A. Weller, E. Würsching, M. Zippe, S. Zöpfel, H. Zushi****

guests from:
* IOFFE-Institute, Leningrad, USSR;
** Southwestern Institute of Physics, Leshan (China);
*** CIEMAT, Madrid;
**** Kyoto University, Japan

NBI Group
F.P. Penningsfeld, W. Ott, E. Speth

Pellet Injection Group
K. Büchl, R. Lang

Max-Planck Institut für Plasmaphysik
EURATOM-IPP, D-8046 Garching, FRG

ECRH Team
W. Kasparek, G.A. Müller, P.G. Schüller, M. Thumm

Institut für Plasmaforschung der Universität Stuttgart,
D-7000 Stuttgart, FRG

ABSTRACT

An extended parameter range ($T_e \leq 3$ keV, $T_i \leq 0.7$ keV, $n_e \leq 2.5\ 10^{20}$ m^{-3}) was explored in the new modular stellarator Wendelstein W 7AS using ECRH and NBI. At 2.5 T main field central values of ß up to 1.5 % were achieved. A reduced Shafranov shift as consequence of the reduced Pfirsch-Schlüter currents for the advanced stellarator concept is verified. Depending on the plasma parameters a net current is observed and identified as the bootstrap current. At the low shear stellarator W 7AS the magnetic configuration and the the confinement depends sensitively on the plasma currents. Thus a control of the configuration by small currents (OH, ECCD, Ohkawa current) is applied to maintain optimum confinement.

Based on profile measurements the electron heat conduction and the ion particle diffusion coefficient were evaluated for ECRH plasmas. As result of statistical analysis a phenomenological expression for the energy confinement time τ_E is derived.

After carbonization the high Z impurities (Fe, Ti) and radiation losses were significantly reduced. At first experiments with NBI ($P_{IN} \leq 1.5$ MW) discharges at density $n_e \leq 2.5\ 10^{20}$ m^{-3} could be maintained and an energy replacement time of up to 30 ms was achieved.

1. INTRODUCTION

The new stellarator at Garching, W 7AS "Advanced Stellarator" (major radius 2m, plasma radius ≤ 0.17 m) [1] is being operated since summer 1988. The experimental programme is devoted to the new possibilities offered by the concept of optimization and guides further theoretical models. The configuration of W 7AS with m=5 periods, similar to 5 toroidally linked mirrors, is produced by a system of modular coils. Each period consists of 9 individually shaped nonplanar coils [2]. The innovative engineering of the magnetic system is testing a technique for the realization of favourable magnetic configurations even for dimensions of a reactor. The improved equipment for heating includes ECRF (electron cyclotron heating: 4 gyrotrons at 70 GHz with 200 kW each), NBI (neutral beam injection heating: tangential injection with 1.5 MW), ICRF (ion cyclotron heating: "experimental antenna" with 1 MW) and allows more flexible operation of the device compared to the previous conventional stellarator W 7A [3]. Especially, the sophisticated ECRF system enables a quasioptical power launch by adjustable mirrors to vary the power deposition profiles and apply for local current drive by introducing k_{II} components [4].

PARAMETER RANGE

More than 10,000 plasma discharges have been recorded up to now, nearly half of them at full field of 2.5 T. Plasma build-up by ECF waves (70 GHz) works routinely for both fundamental and 2nd harmonic launching. In the first experimental periods of W 7AS stellarator, investigations have centered mainly on ECR heated discharges at Bo =1.25 T (2nd harmonic

x-mode) and B_0=2.5 T (fundamental o-mode). In these quasi-stationary ECRH discharges, the maximum densities were limited by the cut-off condition to < 3 10^{19} m^{-3} for B_0=1.25 T and to < 6 $10^{19}m^{-3}$ for B_0=2.5 T. Up to 800 kW ECF power was launched. Maximum electron temperatures of up to nearly 3 keV were measured. Typical energy exchange times of 5 up to 20 ms were evaluated. For these ECRH discharges with a duration of up to 1.5 seconds, the L/R -times were very large and up to 1 second was necessary for establishing of a stationary internal current density profile. The global confinement can depend sensitively on the internal rotational transform profile, and unstable plasma evolutions (bifurcations) were observed in phases with stored energy and line density being constant [5]. NBI heated discharges in the first experimental phase without wall conditioning were dominated by radiative losses and, in most cases, terminated by radiative collapse. After carbonization, the radiation loss mainly due to heavy impurities (iron and titanium) was significantly reduced and operation at high density became possible.

2. MAGNETIC CONFIGURATION
EQUILIBRIUM AND STABILITY

Excluding the direct vicinity of $\iota = 1/2$ and $\iota = 1/3$, very good agreement of all measured flux surfaces with code simulations was found on the plane where the cross section has a triangular shape [6]. Flux surfaces were also measured in one elliptical plane, where the deviation of the

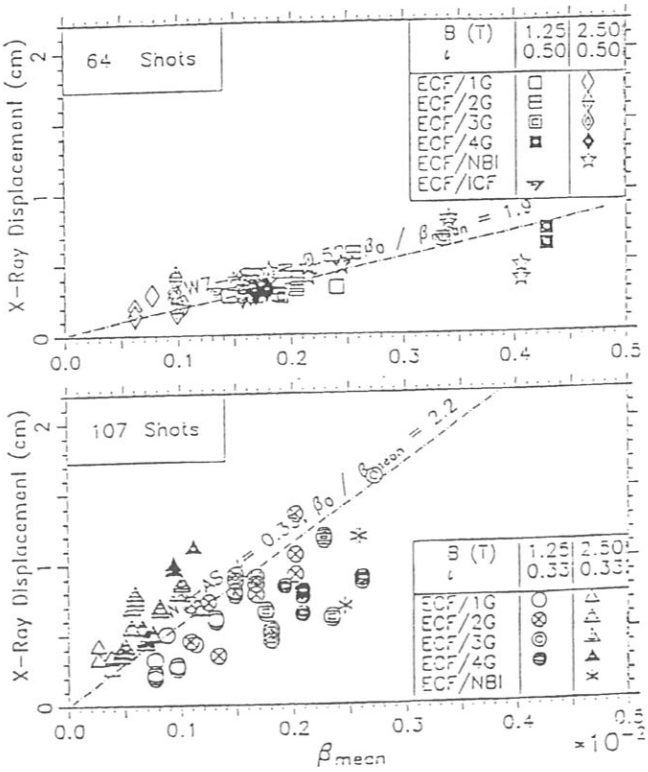

Figure 1

The horizontal shift of the magnetic axis versus the volume averaged < ß > from X-ray profile analysis for $\iota \approx 1/2$ (upper plot) and for $\iota \approx 1/3$ (lower plot). The straight lines result from equilibrium calculations (KW code).

measured to the predicted position of magnetic axis was within the accuracy of the method. Electron temperature profile measurements (Thomson, ECE and SX) at different toroidal positions indicate an average accuracy of the magnetic axis position of roughly 1 cm.

One of the aims of the partly optimized W 7AS field configuration was the reduction of the Pfirsch-Schlüter (PS) currents. From the W 7AS optimization, a PS current reduction by a factor of 2 was expected with respect to a standard stellarator. This leads to a reduced Shafranov shift. The outward shift of the magnetic axis with β_0 is confirmed by soft-X observations. In ECRH discharges with highly localized central power deposition, the electron temperatures are peaked. Figure 1 shows the outward shift of the measured central X-ray profile as a function of $<\beta>$ for $\iota \approx 1/2$ and $\iota \approx 1/3$. Note that the shift of the magnetic axis depending on the shape of the pressure profile is about three times larger for $\iota \approx 1/3$ than for $\iota \approx 1/2$. The comparison with predictions based on the KW equilibrium code [7] verifies the PS current reduction by a factor of 2. In addition, the B_z field component originating from the PS currents, which is related to the volume averaged $<\beta>$, is measured directly with magnetic loops and agrees with the relation $B_z \sim <\beta> B_0/\iota$ as simulated by the VMEC equilibrium code [8]. Volume-averaged β values, $<\beta>$, of up to 0.16 % and 0.28 % were found using ECRH for B_0=2.5 T and B_0=1.25 T, respectively. The maximum peak β_0 values were 0.52 % and nearly 0.8 %. Maximum values of $<\beta>$ = 0.62 % and β_0=1.5 % were found with NBI. So far, the maximum values of β seem limited only by the available heating power. The experimental $<\beta>$ values were much lower than the predicted $<\beta>$ limit of about 2 %. However, localized fluctuations and mode activities were found by the SX and the ECE diagnostics, from reflectrometry and from H_α measurements. These activities are mainly related to configurational effects for discharges with resonances $\iota=1/2$ or $\iota=1/3$ within the confinement region. Current profile analysis indicates that these fluctuations and mode activities not related to the stability limit are stabilized by sufficient internal shear as generated by the internal currents.

BOOTSTRAP CURRENT

The magnitude of the bootstrap current in W 7AS is comparable with the equivalent tokamak value, and the bootstrap current increases the rotational transform. In the ECRH discharges, bootstrap currents of several kA were measured which, in most cases, were fully balanced by applying a small loop voltage, U_l, by feedback control of the OH transformer. Without current control, the edge value of the rotational transform can be modified significantly leading to confinement degradation due to configurational effects. In ECRH discharges with typically very broad n_e and peaked T_e profiles, the neoclassical bootstrap current is mainly driven by the electron temperature gradient, the ion contribution being rather small because $T_i << T_e$ under these conditions.

For each magnetic configuration in W 7AS, the bootstrap current is calculated using the DKES code. Based on measured T_e and n_e profiles, the total bootstrap current as well as the plasma resistance are calculated. In Figure 2, the neoclassical predictions for the dominant electron component, I_b^e, are compared with the experimental values defined by I_p-U_l/R for ECRH discharges. The agreement with the neoclassical predictions is very good.

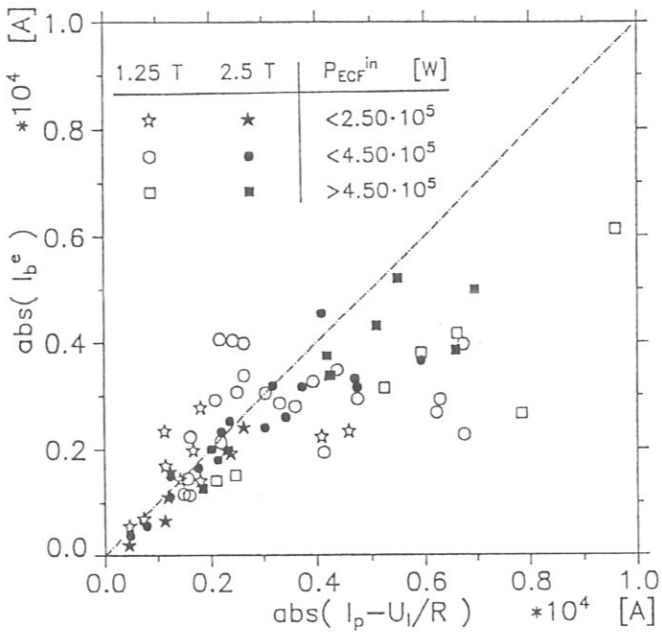

Figure 2
The electron component of the bootstrap current, I_{be}, calculated from the DKES code versus the experiment value, I_p-U_l/R, for ECRH discharges (without ECCD) with central deposition.

For higher heating power levels and lower densities, suprathermal electrons will contribute to both the bootstrap current and the plasma resistance. For ECRH discharges without ECCD, the dependence of the experimental value of the bootstrap current, I_p-U_l/R, on global plasma parameters is found by multiple linear regression. I_p-U_l/R scales linearly with the effective plasma radius, a, and nearly quadratically with the volume averaged temperature defined by W_{dia}/ n . A slightly negative B and nearly no ι dependence was found. These findings are consistent with the neoclassical predictions for which the temperature dependence of the bootstrap current coefficients is dominant. DKES calculations [9] show that the bootstrap current is rather insensitive to the different magnetic field configurations characterized by vacuum ι, B_z field and field ripple which can be modified by varying the currents in the modular coil system. This result of bootstrap current being roughly the same for different W 7AS configurations is in contrast to the situation in the ATF experiment where the existence of the neoclassical bootstrap current was confirmed by changing the additional quadrupole field.

CONFIGURATIONAL EFFECTS ON CONFINEMENT

As was the case for the W 7A stellarator, the global confinement in W 7AS depends strongly on the boundary value of the rotational transform, $\iota(a)$ [5]. A degradation of both energy and particle confinement is found for low order rational values of the rotational transform at the plasma edge, $\iota(a)$, whereas optimum confinement can be established in narrow ι-windows close to the resonances $\iota(a)\approx 1/3$ as well as $\iota(a)\approx 1/2$. The nearly shearless vacuum configurations are modified by plasma currents: the PS current and the neoclassical bootstrap current generated by plasma pressure, currents driven by the heating method (ECCD and Ohkawa currents during NBI) or externally by the OH-transformer. As the contribution of the bootstrap current to the rotational transform is much larger than the narrow ι-windows for optimum confinement, the total plasma current was controlled to avoid low order rational values of ι or to keep $\iota(a)$ within the range of optimum confinement. Current diffusion on the L/R time scale determines the time to reach stationary conditions. In most ECRH discharges, the bootstrap current was fully balanced by applying a small loop voltage, U_l, by feedback control of the OH-transformer. In the stationary phase, the Ohmic current density profile is concentrated in the central plasma region for the peaked T_e profiles whereas the bootstrap current is driven more outside in the T_e gradient region. For $\iota(a)$ being fixed, positive shear is generated in the confinement region. The situation for counter-ECCD with central power deposition is similar, the shear also being positive. For stronger co-ECCD, however, negative shear can be generated in the whole confinement region. For low internal shear operation, degraded confinement is found to be related to low order rational values of $\iota(a)$ which indicates island formation and ergodization in the magnetic configuration. Even a local flattening of the T_e profile has been resolved for these conditions. With sufficient internal shear nearly identical discharges could be established above and below both $\iota(a)=1/3$ and $\iota(a)=1/2$. Current profile estimates clearly show that the low order rational values are within the confinement region. By a scan of ECR heating power a nonlinear mechanism of "self-stabilization" of the internal shear was demonstrated [5]: both the bootstrap and compensating Ohmic currents increase with the energy content, resulting in higher positive shear and in an improved confinement which leads to increasing energy content. The W 7A experience, on the other hand, indicates a degradation of confinement with strong internal shear. As a consequence, the optimization of energy confinement depends on the optimization of the internal ι profile. First experiments using local ECCD for the ι profile shaping show promising results.

3. TRANSPORT

ELECTRON HEAT CONDUCTION

For ECRH discharges, the electron densities were less than $5\ 10^{19}\ m^{-3}$, so the collisional electron-ion coupling and the radiative losses were rather small, and the electron heat

conduction was the dominant loss channel. These discharges are the best candidates for electron energy balance analysis, which is based on density and temperature profiles measured by the Thomson scattering diagnostic. Furthermore, the n_e profiles were very broad and the T_e profiles highly peaked for central ECF power deposition. With increasing power density the density profiles become hollow. The central ion temperature was estimated by passive CX neutral particle diagnostic with T_i values up to 450 eV. As T_i-profile information was not available, the central T_i was assumed to be radially constant and the edge values were fitted to the measured T_e profile. The total radiation loss was measured by bolometry. The radiation profiles were modelled by a simple corona model.

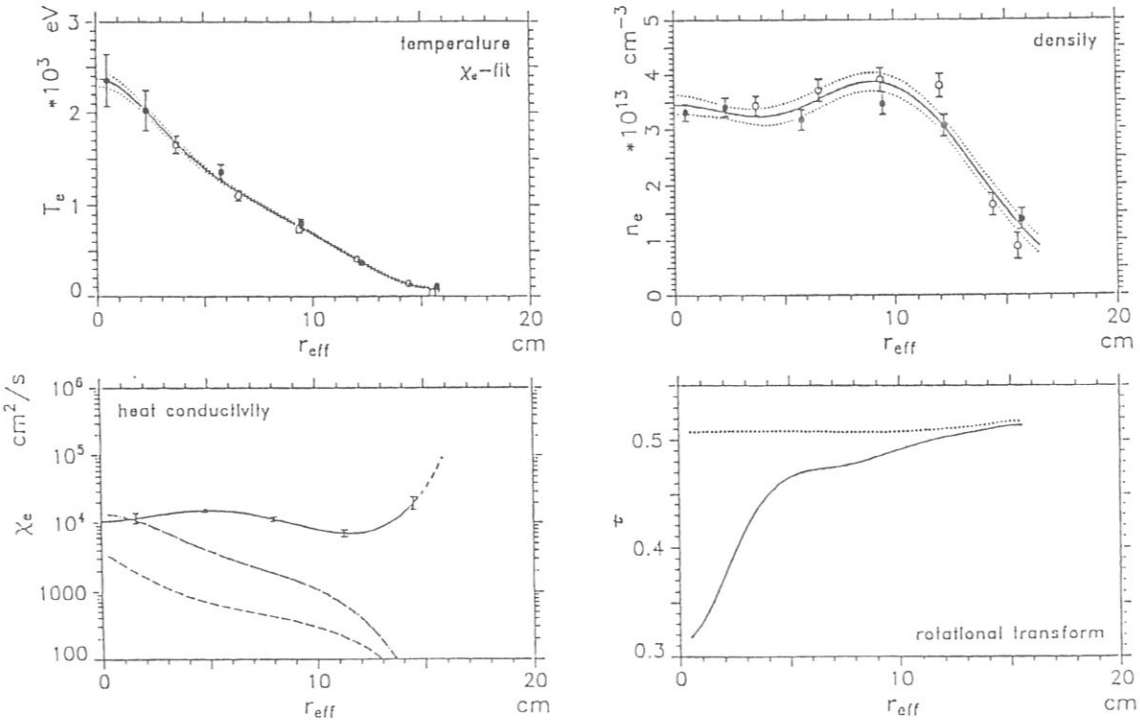

Figure 3

Transport analysis for series 7545-57. Electron temperature, T_e, density, n_e, heat conductivity, χ_e, and rotational transform profiles are shown for B_0=2.5 T and with $P_{ECF} \approx 640$ kW input power. In the experimental χ_e (lower left plot, solid line) standard errors resulting from the least-squares fit of the T_e profile (upper left plot) are given, additionally, the χ_e from the DKES code (dot-dashed line) and from the Hinton-Hazeltine model (dashed line) are shown.The rotational transform, ι, is shown in the lower right plot, the resulting $\iota(r)$ due to internal currents (solid line) and without internal currents (dotted line). collisionality : $\nu_e^* \geq 3\ 10^{-3}$

The stationary electron energy balance equation with radiative losses and electron-ion power transfer is solved with the diffusive ansatz for the radial electron energy flux, $q_e = -n_e\ \chi_e\ T_e'$,

and an analytic ECF power deposition model which is highly peaked in agreement with ray-tracing calculations. Solving the electron energy balance equation, the measured T_e profiles are fitted by a least-squares technique using a power series of log(χ_e) in normalized radius, the power series coefficients being the fit parameters. This integration method of the electron energy balance equations leads to a smoothed representation of the electron heat conductivity, χ_e. For the n_e profiles, a standard fit function is used. With these T_e and n_e profiles, all neoclassical transport properties are estimated using the DKES code [10]. In Figure 3, the electron temperature, density, heat conductivity and rotational transform profiles are shown for typical one of the high pressure ($<\beta> = 0.14$ %) ECRH discharges at B_o=2.5 T with 640 kW ECF input power (4 gyrotrons operating). The bootstrap current was compensated by an external loop voltage. For the highly peaked T_e profile due to central ECRH, the bulk part of the plasma is in the long mean free path regime (LMFP), the neoclassical transport being dominated by ripple losses. The neoclassical χ_e estimated by the DKES code (dot-dashed line in Figure 3) exceeds significantly the axisymmetric contribution (dashed line). Only in the innermost part does the neoclassical χ_e approach the experimental value. Close to the effective limiter radius of 15.5 cm, the T_e profile becomes flat and the experimental χ_e increases strongly here. In the major part of the plasma, χ_e is roughly constant (1 m^2/s) and much larger than the neoclassical value. With an assumed value of $Z_{eff} = 4$, the total electron bootstrap current was calculated to be 5.2 kA nearly compensated by the ohmic current. In the lower right plot, the resulting ι profile is shown. The resonances ι=1/2 as well as ι=5/11 (natural islands in the vacuum configuration) are located within the confinement region. At reduced power χ_e values much less than 1 m^2/s were deduced which are of the order of the best χ_e values found in optimum Tokamak confinement. A minimum in the χ_e profiles at about 2/3 plasma radius is typical for all discharges without degradation due to configurational effects. For most discharges with optimum confinement, $n_e \chi_e$ is roughly constant (or even decreasing) over the whole plasma cross section. For maximum limiter aperture, however, the increase of $n_e \chi_e$ indicates a degradation of the confinement due to the magnetic topology at the outermost radii.

PARTICLE TRANSPORT

The particle confinement in W 7AS was investigated for ECRH discharges at 1.25 T and 2.5 T by coupling DEGAS code [10] simulations with H_α emissions measured at relevant toroidal positions. Radially resolved ion fluxes were obtained from calculated neutral particle distributions, after calibrating them with the H_α signals. Estimated Z_{eff} were used to derive the electron particle fluxes and diffusivities. Central electron density profiles were found to get more and more hollow as the ECR heating power with central deposition is increased. For an ECRH power scan at 2.5 T the electron fluxes in the central region have been compared with neoclassical predictions. As T_i profile information is lacking, only the neoclassical electron

fluxes were estimated by the DKES code. For the higher heating power levels, for which the central hollow profiles are more pronounced, the fluxes near the plasma center are in fairly good agreement. This means that the observed hollow density profiles can be explained reasonably well by the neoclassical temperature gradient driven particle flux (thermodiffusion), without need of additional anomalous contributions. Reduction of the heating power down to the lowest level (1 gyrotron) yields density profiles that are flat and particle fluxes much larger than the neoclassical values. In the density gradient region, as compared to the central region, the particle fluxes strongly increase whereas the neoclassical fluxes are negligible due to the neoclassical T_e dependence. The particle diffusivities, D, have been evaluated for discharges operated at half and full field, and $\iota(a)$ values close to the major resonances 1/3 and 1/2, where optimum confinement has been found. Concerning the plasma refuelling sources, it should be mentioned that limiter recycling accounts for about 90 % of the ion production in the small aperture, low ι case (optimal wall screening from ion impact) and only for about 20 % in the large aperture, high ι case. A comparison between all analyzed 1.25 T and 2.5 T ECRH discharges indicate an average improvement of the particle confinement with the magnetic field by a factor of ≈ 3 throughout the density gradient region. A comparison of D and χ_e for the analyzed discharges yields D/χ_e values between 0.1 and 0.3 in the outer confinement region.

The impurity particle confinement in W 7AS has been investigated by laser ablation of aluminium. Since hydrogen-like Al, which is peaked in the bulk plasma for ECRH discharges, can be assumed to evolve under ionization equilibrium conditions, the decay time of the Al-XIII line radiation during stationary plasma conditions is a measure of the central confinement time for this impurity. For moderate and high ECRH power, the decay time is found to increase from $\approx$10 ms at 1.25 T to $\approx$ 40 ms at 2.5 T. Also, it decreases with ECRH power for given limiter aperture. The time evolution of Al-XIII could be reproduced by transport simulations with the STRAHL code [11] which uses a constant diffusion coefficient and an inward convective term $v=-(2D/a)(r/a)$. The corresponding values of D decrease from 5000-8000 cm^2/s for 1.25 T to 1200-2000 cm^2/s for 2.5 T. On the other hand, if the velocity term is omitted, these numbers reduce by only $\approx$ 20 %. Discrepancies between the measured and simulated decay times are found, however, for the lower ionization stages. More experimental data and more accurate simulations, including a spatial variation of D , are needed to improve the description of the impurity transport behaviour under different experimental conditions.

FIRST RESULTS WITH NEUTRAL INJECTION (NBI).

During July 1990 the investigations at W 7AS were concentrated on experiments using neutral beam injection. After carbonization by glow discharges with a mixture of He and 30% CD_4 (or CH_4) the content of high Z material (Fe und Ti) was significantly reduced. With reduced radiative losses the parameter range of plasmas was extended to much higher densities than

before and pulse duration up to 300 ms. The target plasma is produced by ECRH 70 GHz at main field 2.5T or 1.25 T. The full power of NBI ($P_N \leq 1.5$ MW) at W 7AS injecting H^0 with an accelerating voltage of 45 kV was used for further heating, see Fig. 4.

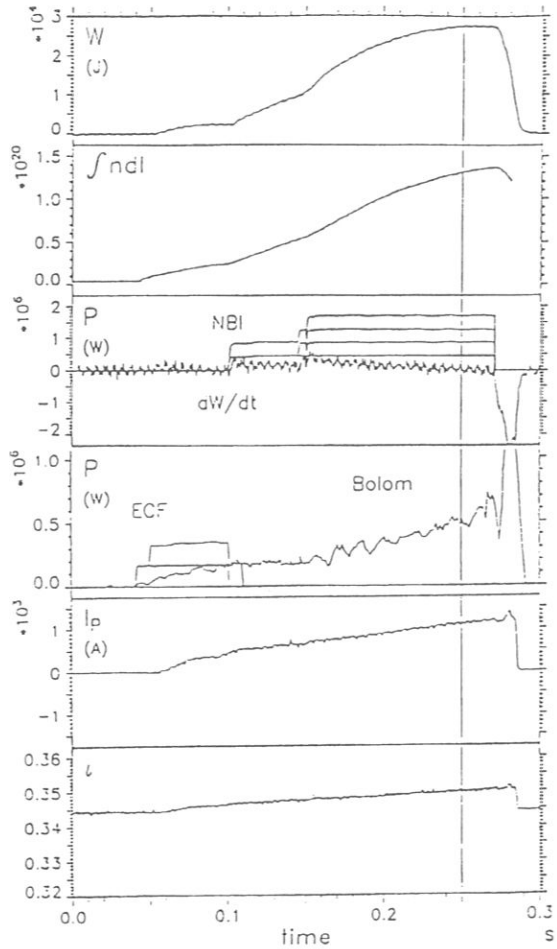

Figure 4
NBI injection after carbonization : shot 9901, 2.5 T. ι = 0.34, balanced injection using 4 beams with P_N = 1.5 MW. Development of global parameters: energy content W, line density (m^{-2}) at the elliptical plane with L=0.63 m by HCN-interferometer, input power : ECF and NBI, radiative power by bolometer, time derivative of W, plasma current, rotational transform.

With carbonized walls the recycling coefficient is larger than 1 and the evolution of the discharge is characterized by a steady increase of density. Before saturation the rate of density increase is determined by gas released by plasma/wall interaction rather than by the flux associated to NBI. The maximum energy content was 28 kJ ($\beta_0 \approx 1.5$ %) at 1.4 MW absorbed power was achieved at field 2.5 T and plasma radius 0.176 m for the rotational transform ι = 0.34. With balanced injection the observed bootstrap current of 1.2 kA agrees well with the calculated value. Unbalanced injection generates a variation of the net current by some kA depending on the density. Unfortunately, no ion temperatures could be measured at these high densities since the diagnostic beam and the CX flux from the center were completely absorbed. However, electron and ion temperatures should be equal at this very high density. The maximum obtainable density, and consequently ß, seems related to the absorbed power, as long

the electron temperature stays above 350 eV to minimize the radiative losses and prevent a radiative collapse.

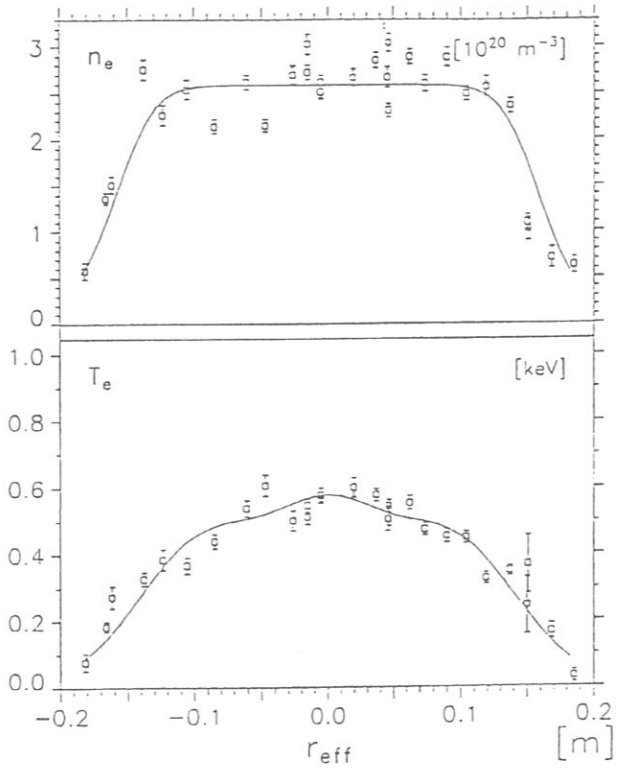

Figure 5
Density and temperature profiles for the discharge of Figure 4 at $\Delta t = 0.25$ s (series 9866-9897).

Fig. 5 presents the measured profiles. Compared to the typical situation for the ECRH discharges the ion heat losses should be significantly enlarged. More detailed information is necessary to evaluate local experimental data and deal with the influence of electric fields. Presently only a global description of the energy confinement is possible. He glow discharges and the reduction of the input power allow to stabilize the density close to $n_{eo} = 1\ 10^{20}\ m^{-3}$. At these densities with $T_{eo} \approx 0.75$ keV, $T_{io} \approx 0.6$ keV a maximum replacement time of 30 ms was achieved.

Operating at low field 1.25 T discharges at similar densities and slightly reduced temperature could be maintained. Using only 3 injectors ($P_N \leq 1.1$ MW), plasmas with an averaged $\langle ß \rangle = 0.65\%$ and a replacement time of typical 10 ms were produced.

ENERGY CONFINEMENT SCALING

The dominant parameter dependence of the global energy confinement time, τ_E, is given by multiple linear regression analysis. This standard procedure is used to obtain the general trend in the confinement properties as well as the significant parameter dependences.

About 86 series of discharges with 2nd and 1st harmonic ECRH as well as 14 series with NBI were selected from a database system for this regression. Discharges with confinement

degradation due to configurational effects were excluded. The energy confinement time depends significantly on magnetic field strength, B_0, line averaged density, n, absorbed power, P_{abs}, and plasma radius, a. The edge value of rotational transform, $\iota(a)$, was found to have a smaller significance.

$$\tau_E^{W\,7AS} = (1.68\pm .02)\ 10^{-8}\ a^{1.28\pm.16}\ B_0^{\,0.716\pm.06}\ n^{0.53\pm.03}\ P_{abs}^{-0.56\pm.03}\ \iota(a)^{0.23\pm.08}$$

with τ_E in ms, n cm^{-3}, P_{abs} in W, B_0 in T and a in cm, a being the minimum of effective limiter and separatrix radius. The experimental τ_E versus the result of the regression, $\tau_E^{W\,7AS}$, is shown in Figure 6.

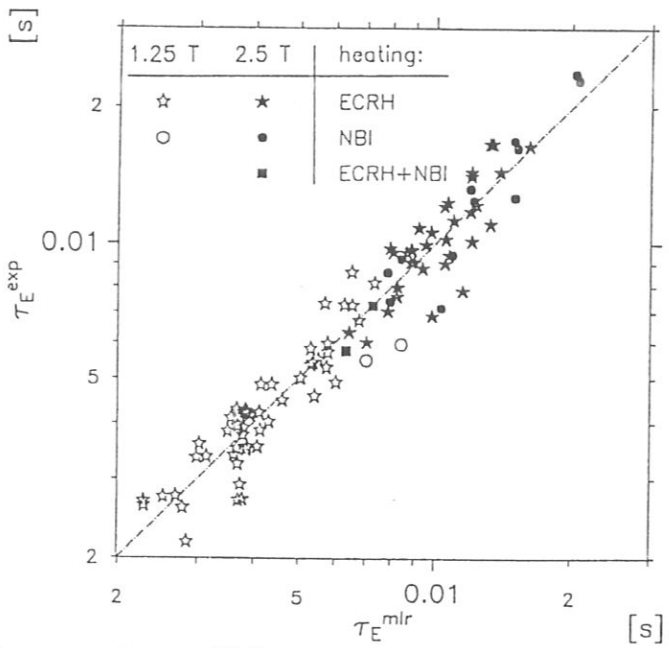

Figure 6
Experimental energy confinement times, τ_E^{exp}, versus the W 7AS regression result, $\tau_E^{W\,7AS}$ (τ_E^{mlr}) for ECRH and NBI heated discharges without confinement degradation due to configurational effects.

The regression coefficients for n and P_{abs} are very similar to those of the LHS or "gyro-reduced Bohm" scalings. In spite of the differences in the parameter range for ECF ($\nu_e^*(0) \geq 10^{-3}$) and NBI discharges ($\nu_e^* \approx 0.1$), the different power deposition and different power losses by electrons, ions and radiation there is no significant deviation in such a global scaling. For pure ECRH discharges in W 7AS, where the density profiles are flat and very broad, $n_e \chi_e$ was found to be roughly constant. The shape of the T_e profiles does not change very much on variation of external plasma parameters. Within the important confinement region, the temperature gradient is only slightly affected by the heating power. A physical picture of this anomalous transport cannot be given by such a form of regression analysis. However, the fact that no local scaling of χ_e with T_e was found indicates two possible explanations. Firstly, the electron heat conduction cannot be treated by a regression ansatz as used so far for the accessible parameter range, or, secondly, the picture of transport being determined by only

local plasma parameters is inadequate. ECRH related effects (distortion of the energy distribution, localized power deposition) must be eliminated by application of different heating methods and a more detailed local transport analysis.

4. CONCLUSIONS

The "advanced stellarator" W 7AS is being sucessfully operated. To date there have been about 4000 plasma discharges at full field parameters with a duration of up to 1.5 s. This experience allows the conclusion that also a large modular coil system can be realized, especially as the mechanical forces will not exceed those in W 7AS. Together with the promising results of the first experimental period a good basis for the further development of the "Advanced stellarator" concept to Wendelstein W 7X [12] which shall include all theoretical improvements is obtained.

The predicted reduction of the Pfirsch-Schlüter currents by a factor of 2 has been verified by measurements of the Shafranov shift. The achieved pressure was much below the predicted stability limit, and no significant mode activity related to the stability limit was observed. However, local mode activity and fluctuations which are related to low order rational values of the rotational transform were detected. The effect of these activities on transport is not yet analyzed.

The neoclassical bootstrap current is quantitatively confirmed in W 7AS. The bootstrap current with several kA affects significantly the rotational transform profile and dominates the Pfirsch-Schlüter contribution. It depends sensitively on the average temperature. In order to avoid a strong modification of the ι profile, the bootstrap current has to be controlled. The control of rotational transform at the plasma edge worked well for all scenarios under consideration. Internal shear is introduced by the bootstrap current depending on the energy content achieved. A future task of W 7AS will be the analysis of confinement optimization by means of an appropriate shaping of the whole rotational transform profile using local ECCD.

For ECRH discharges, electron energy balance analysis based on measured T_e and n_e profiles yields the electron heat conductivity, $\chi_e(r)$. The best χ_e values which have been achieved are well below 10^4 cm^2/s which are in the range of the optimum χ_e values found in tokamaks. For all analyzed discharges, the neoclassical transport coefficients were calculated by using the DKES code and compared to the experimental values. Due to the strong T_e dependence, the neoclassical χ_e values decrease rapidly with radius and are typically about one order of magnitude smaller than the experimental value at half plasma radius. The neoclassical χ_e comes up to the experimental value only for central high ECF power deposition with peaked temperatures where the neoclassical ripple losses dominate. Further investigations of transport in an extended parameter range with different heating methods are necessary to discriminate effects related to particular heating scenarios.

The regression analysis of the global energy confinement time agrees rather well with predictions based on the LHS- and the "gyro-reduced Bohm" scalings.

From the DEGAS code, particle fluxes and diffusivities have been derived using measured T_e and n_e profiles and absolute H_α intensities at relevant positions around the machine. The radial range of the diffusivities includes the density gradient region up to the limiter. Here, the value of D exceeds neoclassical predictions by more than one order of magnitude. The ratio D/χ_e was between 1/10 and 1/3. For the hollow profiles at high power level, the central particle fluxes from DEGAS simulations agree fairly well with the neoclassical fluxes which are dominated by thermodiffusion. Consequently, the ECRH density pump-out in the central region is consistent with neoclassical transport in W 7AS.

Some preliminary results are obtained for NBI heated discharges. With carbonization, the very high wall recycling lead to a strong density increase, and stationary conditions could not be obtained. The radiation losses, however, were significantly reduced, and the discharges were terminated by edge cooling at very high densities. Only limited by the available heating power discharges at densities up to 2.5 10^{20} m-3 with favourable confinement were obtained. Acceptable discharge conditions with low radiation levels and lower recycling could be realized shortly after helium glow discharge cleaning. Boronization and the installation of pump limiters positioned in regions with high outward fluxes [13] may help to reduce the impurity production and to lower recycling (perhaps due to partial Ti-gettering).

REFERENCES

[1] Brossmann,U. Dommaschk,W. et alt., Plasma Physics and Controlled Nuclear Fusion Research (Proc. 9th Conf. Baltimore 1982), **Vol. 3**, IAEA, Vienna (1983), p.141

[2] Sapper, J. et alt. Transactions 8th Int. Conf. Structural Mechanics in Reactor Technology, Amsterdam (1985), **N**, p.15

[3] Renner, H. et alt., Plasma Physics and Contr. Fusion, **31**, (1989), p. 1579-1596

[4] Erckmann, V., et alt., 17th Europ. Conf. on Contr. Fusion and Plasma Physics, **14B**, p. 1271, Amsterdam 1990

[5] Ringler, H. et al., 17th EPS Conf. on Contr. Fus. and Plasma Phys., invited paper, Amsterdam, 1990

[6] Jaenicke, R., et alt., 16th Europ. Conf. on Controlled Fusion and Plasma Physics, Venedig (1989), **P8 B3**

[7] Kisslinger, J. and H.Wobig, ECA, **9F I** , p. 453, 1985

[8] Gardner, H.J., 2nd Workshop on Wendelstein VII-X, **EUR 11705 EN**, p. 51, 1988

[9] Hirshman, S.P., et alt., Phys. Fluids **29** (1986), 2951

[10] Heifetz, D.B., et alt. J. Comp. Phys. **46** (1982), 309

[11] Behringer,K., **report JET-R (87) 08** , 1987

[12] Grieger, G., et alt. , Proc. of the 13th Intern. Conf. on Plasma Phys. and Contr. Nucl. Fusion, Washington 1990, **G-1-6**

[13] Grigull, P. et al., Proceedings of the 9th Int. Conf. on Plasma Surface Interaction, Bournemouth, 1990.

INTERNATIONAL ATOMIC ENERGY AGENCY

THIRTEENTH INTERNATIONAL CONFERENCE ON
PLASMA PHYSICS AND CONTROLLED NUCLEAR FUSION RESEARCH

Washington, DC, United States of America, 1–6 October 1990

IAEA-CN-53/ C-3-1

ELECTRON CYCLOTRON CURRENT DRIVE AND WAVE ABSORPTION EXPERIMENTS IN THE W 7-AS STELLARATOR

V. Erckmann, U. Gasparino, H. Maaßberg, H. Renner, M. Tutter,
W VII-AS Team+)
Max-Planck-Institut für Plasmaphysik,
EURATOM Association, D-8046 Garching, FRG

W. Kasparek, G.A. Müller, P.G. Schüller, M. Thumm
Institut für Plasmaforschung, Universität Stuttgart, FRG

+)W 7-AS-Team

V. Afanasiev*, R. Brakel, R. Burhenn, G. Cattanei, A. Dodhy, D. Dorst, A. Elsner, K. Engelhardt, V. Erckmann, U. Gasparino, S. Geißler, P. Grigull, H. Hacker, H.J. Hartfuss, A. Izvozchikov*, R. Jaenicke, S. Jiang**, J. Junker, M. Kick, J. Kißlinger, H. Kroiss, G. Kuehner, I. Lakicevic, A. Lazaros, H. Maassberg, C. Mahn, M. Ochando***, W. Ohlendorf, F. Rau, H. Renner, H. Ringler, J. Saffert, J. Sanchez***, F. Sardei, M. Tutter, A. Weller, H. Wobig, E. Würsching, M. Zippe, S. Zöpfel, H. Zushi****

* Guest from *IOFFE-Institute, Leningrad, USSR*
** Guest from *Southw. Institute of Physics, Leshan, China*
*** Guest from *Ciemat, Madrid, Spain*
**** Guest from *Kyoto University, Kyoto, Japan*

IAEA-CN-53/C-3-1

ELECTRON CYCLOTRON CURRENT DRIVE AND WAVE ABSORPTION EXPERIMENTS IN THE W 7-AS STELLARATOR

ABSTRACT

Experiments on non-inductive current drive by electromagnetic waves in the vicinity of the 1st and 2nd harmonic of the electron cyclotron frequency (ECCD) were performed at the W 7-AS stellarator with up to 1 MW rf-power at 70 GHz in long-pulse operation (< 1.5 s). The single pass absorption as an important input quantity for current drive investigations was directly measured for 1st harmonic O-mode and 2nd harmonic O- and X-mode operation, respectively in a wide plasma parameter range. A good agreement with a 3-D ray tracing model was found.

ECCD was investigated by

a) a toroidal launch angle variation of the microwave-beams while the total net current was kept close to zero ($I_P < 0.2$ kA) by beedback control of the OH-transformer. The change of the required loop voltage with respect to perpendicular launch (no ECCD) was measured as a function of the launch angle
b) the adjustment of the launch angle of the microwave-beams to balance the bootstrap current without making use of the OH-transformer (counter current drive). Here the EC-wave driven current is measured in units of the bootstrap current.
c) a perturbation experiment at up/down shifted frequencies, where 0.2 MW were launched at a fixed toroidal angle and the EC-resonance layer was shifted out of the confinement region (B_0 - variation). The loop voltage change required for compensation of the EC-driven current was measured as a function of the magnetic induction.

The parameter dependence on the launch angle, the electron temperature, the plasma density and the microwave-power for all types of ECCD experiments is in good agreement with a linear theoretical model, which takes into account quasilinear and trapped particle effects. The results are confirmed by Fokker-Planck calculations.

1. INTRODUCTION

Experiments on current drive by electromagnetic waves in the vicinity of the electron cyclotron frequency and the comparison with theory attract increasing interest for both, tokamak as well as stellarator research to provide a reliable data-base for Electron Cyclotron Current Drive (ECCD) scenarios in next step devices such as NET and WVII-X. The high localization of the driven currents and the capability to penetrate the plasma centre even in large machines together with the technical advantage of a simple remote launching structure may overcompensate the disadvantage of a small ECCD efficiency (compared to Lower Hybrid Current Drive) for particular applications such as MHD-mode control, current profile shaping or, especially for stellarators, bootstrap current compensation. Basic experiments were performed at the W VII-AS stellarator, where the small EC-driven currents are not masked by large inductively driven currents as in tokamaks. The control of a pressure driven net current was experimentally demonstrated and is mandatory in low vacuum shear configurations such as W VII-AS to maintain good confinement properties [1].

The theoretical treatment of ECCD would require a Fokker Planck solution in full phase space, which is out of scope. In a first approach, we compare the experimental results with a theoretical model, which in the simpliest version neglects trapped particle effects [2]. In a second step, we have analysed the sensitivity of this model with respect to simplified assumptions on trapped particle and quasi-linear effects [3,4]. The experimental investigation of the single pass absorption of a microwave beam in the electron cyclotron frequency range is of crucial importance as an input quantity for CD-calculations. Measurements of the single pass absorption are compared to ray tracing calculations.

2. WAVE ABSORPTION

Plasma build up and heating is achieved at W 7-AS with a 1 MW, 70 GHz ECRH system. The resonant magnetic field and the cutoff densities are 2.5 T and $n_{e,crit} = 6.2 \cdot 10^{19}$ m^{-3} for the 1st harmonic and 1.25 T and $n_{e,crit} = 3.1 \cdot 10^{19}$ m^{-3} for the 2nd harmonic experiments, respectively.The single pass absorption was directly measured for perpendicular launch by a 35 channel pick-up wave guide array mounted opposite to the launching mirrors at the inner vacuum vessel wall. In the investigated electron temperatures range of 0.6 keV < T_{eo} < 1.8 keV total absorption of the waves in a single transit through the plasma was found in all cases with 2nd harmonic X-mode launch, whereas for 2nd harmonic

O-mode the plasma is optically thin (single pass absorption < 7 %) in agreement with theory. A deviation from total absorption is expected for 2nd harmonic X-mode at a central electron temperature of $T_{eo} < 200$ eV. For 2nd harmonic O-mode $T_{eo} > 4$ keV is required to obtain considerable absorption.

For 1st harmonic O-mode heating, however, the single pass absorption is sensitive to the electron temperature and density in the experimentally accessible parameter range of 0.6 keV $< T_{eo} <$ 2.7 keV and $1 \cdot 10^{19} < n_{eo} < 5 \cdot 10^{19}$ m^{-3}. The single pass absorption for a density scan at fixed central electron temperature of 1.5 keV and a temperature scan at fixed electron density of $2.5 \cdot 10^{19}$ m^{-3} was measured ranging from 60 % ± 3 % up to 95 % ± 5 %. A comparison of the measurements with a 3-D ray tracing model based on measured spatial profiles of T_e and n_e (Thomson-scattering, ECE) shows an excellent agreement within the experimental error bars.

3. ELECTRON CYCLOTRON CURRENT DRIVE - EXPERIMENTS

The ECCD-experiments were performed at the W VII-AS stellarator with up to 0.7 MW rf-power in long-pulse operation (< 1.5 s). Up to four linearly polarized rf-beams were launched at both the 1st harmonic ordinary and the 2nd harmonic extraordinary wave polarization,respectively, from the low field side. The rf-beams were directed towards the plasma at arbitrary toroidal launch angles by a set of independently movable focussing mirrors mounted inside the vacuum chamber [5].

In a first experiment, the toroidal launch angle of the rf-beams was varied while the total net plasma current was kept close to zero (I < 0.2 kA) by feedback control with the OH-transformer. The measured change of the required loop voltage ΔU with respect to perpendicular launch (no ECCD) is plotted in Fig. 1(a) as a function of the launch angle at the resonance-layer for constant input power of 0.35 MW in 1st harmonic O-mode. The dots refer to experiments with one beam (0.17 MW) at perpendicular launch (no ECCD) and one beam (0.17 MW) at oblique launch angles. The crosses refer to a variation of the launch angle of both beams. The right wing of the curve with positive loop voltage increment corresponds to a situation, where the bootstrap current has the same direction as the EC-driven current. The left wing of the curve corresponds to ECCD in counter direction to the bootstrap current. Equivalent experiments at $B_o = 1.25$ T show similar results [6]. The change of the internal current distribution results in a change of the total stored plasma energy of about 20 %. The influence on the confinement is explained by magnetic field configuration and internal shear

effects [7]. The ECCD efficiency is evaluated in a 3-D ray tracing code by means of the adjoint approch [8]. In the limit of low collisionality, the evaluation of the local efficiencies was generalized to include trapped particle effects in W 7-AS magnetic configurations [4]. A comparison of the experimental data with this linear model [3] is shown in Fig. 1(b). The calculations are based on the measured n_e-profiles and the measured change of the T_e-profiles for each launch angle. The experimental findings are well described by the model. In particular, the launch angle for maximum current drive and the linear increase of ECCD with rf-power agree well. The absorption layer is shifted radially outward with increasing oblique launch. The current drive efficiency decreases for large launch angles (far in the Doppler regime) because the absorption depends sensitively on T_e and the absorption layer is then within the T_e gradient region. Furthermore, the number of trapped particles increases and the mismatch of the incident linearly polarized waves is no longer negligible [6]. It should be noted that the measured current inversion at large launch angles is also found in the calculations and is related to the particilar W 7-AS magnetic field topology. The absolute value of the EC-driven current at maximum launch angle derived from the experiment is about 3 - 5 kA, which is in satisfying agreement within the simplified assumptions of the theory and the experimental error bars.

In a second experiment, the launch angle of up to 4 microwave-beams (0.7 MW) was adjusted to balance the bootstrap current without making use of the OH-transformer (counter current drive). The net plasma current was kept below ± 0.3 kA under all plasma conditions. The EC-wave driven current is then measured under steady state conditions in units of the bootstrap current, which is varied by a variation of the plasma parameters with increasing microwave power. The dominant electron component of the bootstrap current ($T_e >> T_i$) was calculated by the DKES code for the measured spatial profiles of n_e and T_e. Scanning the rf-power from 0.17 - 0.7 MW, the electron temperature from $0.8 < T_e < 1.9$ keV and the electron density from $1.1 < n_{eo} < 2.8 \cdot 10^{19}\ m^{-3}$, the bootstrap current varies from $0.8 < I_{Boot} < 4.3$ kA (2^{nd} harmonic X-mode). The current drive model overestimates the EC driven current by typically a factor of 3, if trapped particles are neglected. If trapped particles are taken into account, this discrepancy almost vanishes within the experimental accuracy and the uncertainties to derive the bootstrap current from the measured plasma profiles.

In a third experiment, ECCD in the UP/DOWN SHIFTED REGIME was investigated by making use of a peculiarity of the magnetic field configuration of W 7-AS, i.e. wave launching at a poloidal plane with an almost vanishing magnetic field gradient. Under such conditions, a sufficiently high single pass absorption is obtained even at moderate electron temperatures of about 2 keV. Here one microwave beam (0.2 MW) is launched at a fixed angle

of 11^{o} with respect to perpendicular incidence. A magnetic field variation from 2.4 up to 2.6 T shifts the EC-resonance completely out of the confinement region in this poloidal plane as seen in Fig. 2(a). The target plasma is maintained by 0.7 MW at perpendicular launch (no ECCD) in

a poloidal plane with a strong tokamak-like magnetic field gradient, where the EC-resonance layer remains well within the confinement region for the given magnetic field variation. The calculated spatial current density distribution is given in Fig. 2(b) for the three cases of B_o = 2.4 T (up-shifted), 2.5 T (resonant), and 2.6 T (down-shifted). For the resonant case (Fig. 2(b), middle) an almost zero net current is found because the vanishing magnetic field gradient and the corresponding broad power deposition profile create counterstreaming currents on both the low and the high field sides of the resonance layer. The current inverses the sign while varying the magnetic field from an upshifted scenario (Fig. 2, top) to a downshifted scenario (Fig. 2, bottom). The measured loop voltage increment required to balance the EC-driven current is given in Fig. 3(a) for the full magnetic field scan. The change of the sign as well as the transition through zero loop voltage increment at the resonant magnetic field is in agreement with theory as shown in Fig. 3(b), where the EC-driven current is normalized to the launched microwave power. We assume, however, that only the first transit absorption, which is given in Fig. 4(a) as a funtion of the magnetic induction, contributes to current drive. The relevant EC-current drive efficiency is then obtained by normalizing the total current to the power absorbed in a single pass, which is shown in Fig.4(b). In all calculations trapped particle effects are taken into account. An improved current drive efficiency as compared to the two experiments mentioned first is clearly deduced.

4. CONCLUSIONS

Fundamental experiments on wave absorption and ECCD were performed in the W 7-AS stellarator. The single pass absorption of the microwaves was measured at perpendicular launch for 1^{st} harmonic O-mode and 2^{nd} harmonic O- and X-mode launch respectively. An excellent agreement with ray tracing calculations was found. The parameter dependence of ECCD on the launch angle of the incident waves, the electron temperature, the electron density and the microwave power was investigated for both 1^{st} harmonic O-mode and 2^{nd} harmonic X-mode operation. Perturbation experiments at up-/down-shifted resonance for first harmonic ECCD were performed by shifting the resonance layer across the confining region of the plasma. The experiments are in good agreement with a linear theoretical model and Fokker-Planck calcuations if trapped particles are taken into account.

REFERENCES

[1] H. Renner et al., Initial Operation of the WENDELSTIEN 7-AS Advanced Stellarator, Plasma Physics and Contr. Fusion, 31, (1989), 1579-1596

[2] U. Gasparino et al., Sources of Toroidal Current in the WENDELSTEIN 7-AS Stellarator, Proc. 16th Europ. Conf. on Plasma Physics and Contr. Fusion, Venice, Italy, Vol. II, 631

[3] U. Gasparino et al., Non inductive current in W 7-AS, 17th EPS Conf. on Contr. Fusion and Plasma Heating, Vol. 14B, III, p. 1275, Amsterdam, The Netherlands, 1990

[4] M. Taguchi, ECRH Current Drive in Tokamak Plasmas, Plasma Physics and Contr. Fusion 31 (1989), 241

[5] V. Erckmann et al., Electron Cyclotron Resonance Heating transmission line and launching system for the W 7-AS stellarator, Fusion Technology, Vol. 17, (1990), 76

[6] V. Erckmann et al., Current Drive experiments at the Electron Cyclotron Frequency, 17th EPS Conf. on Contr. Fusion and Plasma Heating, Vol. 14B, III, p. 1271, Amsterdam, The Netherlands, 1990

[7] H. Ringler et al., Confinement Studies on the WENDELSTEIN 7-AS Stellarator, 17th EPS Conf. on Contr. Fusion and Plasma Heating, Amsterdam, The Netherlands, 1990

[8] S.P. Hirshman, Classical collisional theory of beam-driven plasma currents, Phys. Fluids 23 (1980), 1238

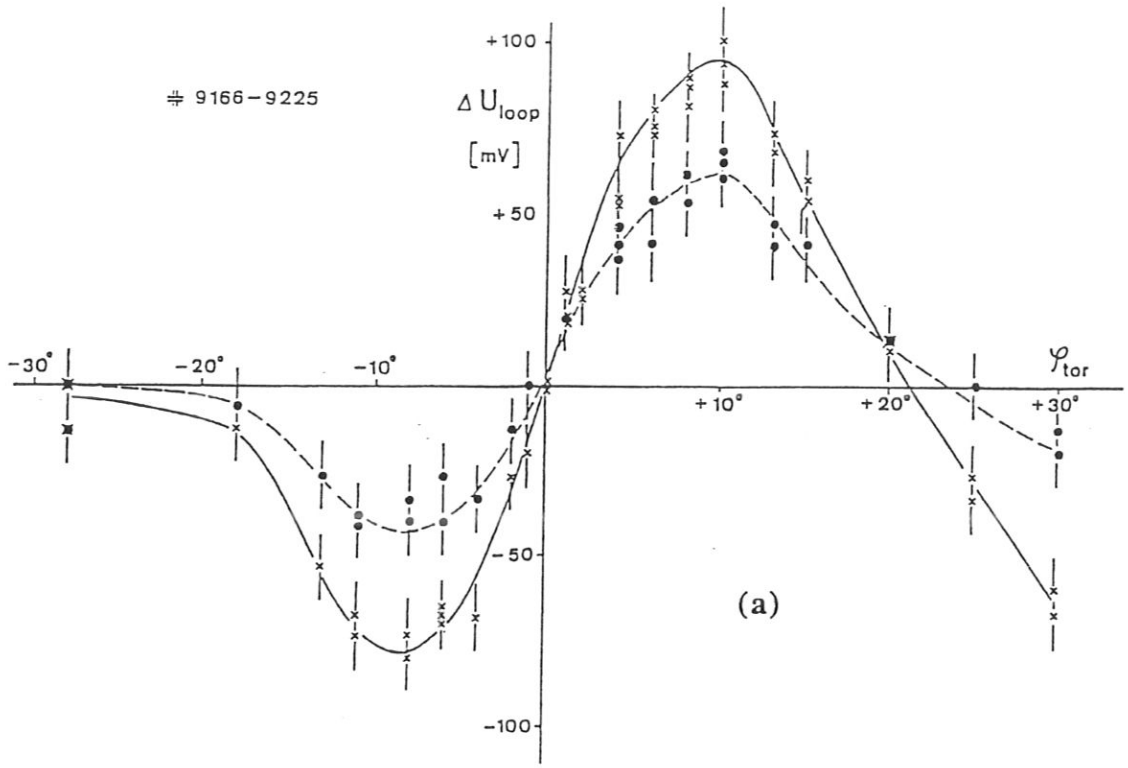
≒ 9166–9225
Δ U loop
[mV]
+100
+50
−50
−100
−30°
−20°
−10°
+10°
+20°
+30°
φtor

(a)

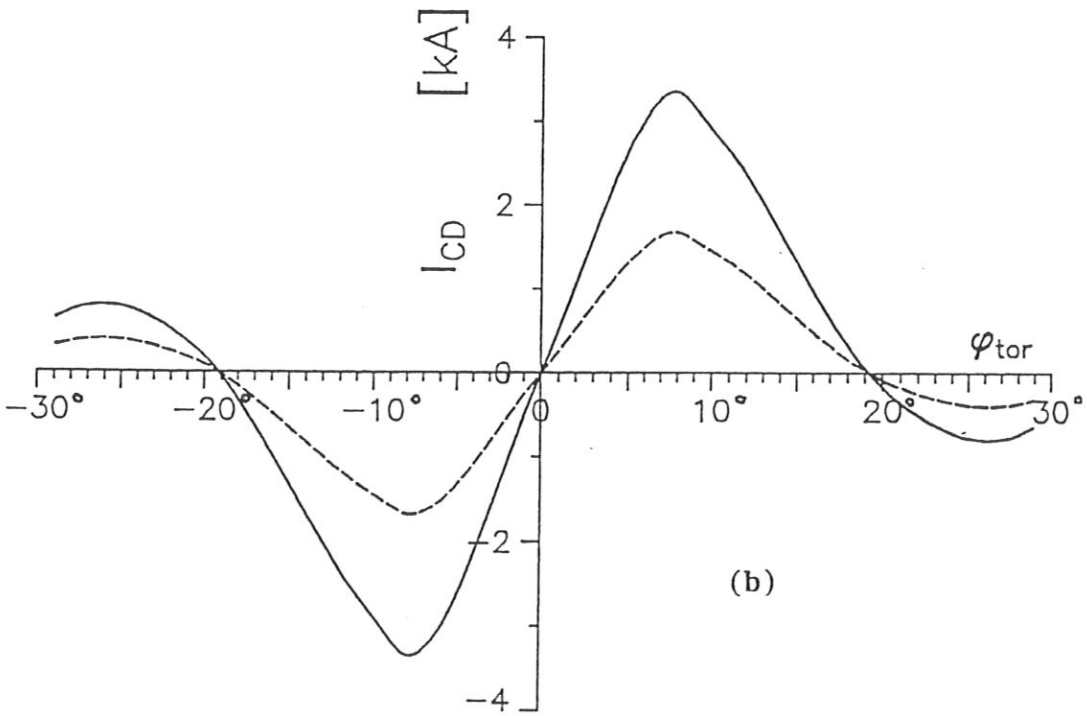
[kA]
ICD
4
2
0
−2
−4
−30°
−20°
−10°
10°
20°
30°
φtor

(b)

FIGURE CAPTIONS

Fig. 1(a) Loop voltage increment ΔU as a function of the launch angle for 0.17 MW (dots) and 0.35 MW (crosses) ECCD power. The EC-driven current is balanced by inductive curent drive (OH-transformer feedback). The total input power for both cases is 0.35 MW.

(b) EC-Current Drive Modelling based on the measured n_e- and T_e-profiles for the same discharges at 0.17 MW (dashed curve) and 0.35 MW (solid curve).

Fig. 2(a) Position of the resonance layer (dotted line) in a poloidal cross-section with small magnetic field gradient at Bo = 2.4 T (top), Bo = 2.5 T (middle) and Bo = 2.6 T (bottom). The solid lines indicate /B/ = const. contours, the dashed lines give the nested flux surfaces.

(b) EC driven current density distribution from 3-D ray tracing calculations for 0.1 MW microwave power at the upshifted resonance (top), the resonant case (middle), and for the downshifted case (bottom).

Fig. 3(a) Loop voltage increment ΔU_{loop} required to balance the EC-driven current as a function of the magnetic induction on axis. The left part ($B_o \sim 2.4$ T) corresponds to an upshifted, the right part ($B_o \sim 2.6$ T) to a downshifted scenario.

(b) EC-Current Drive modelling of the experiment. The current-drive efficiency η_{in} is defined as the driven current I_{CD} normalized to the launched power P_{in}

Fig. 4(a) The single pass absorption P_{abs} normalized to the launched power P_{in} from ray tracing calculation for the same discharges.

(b) EC-Current Drive efficiency η_{abs}, with the driven current I_{CD} normalized to the single pass absorption P_{abs} for the same discharges.

(a)

(b)

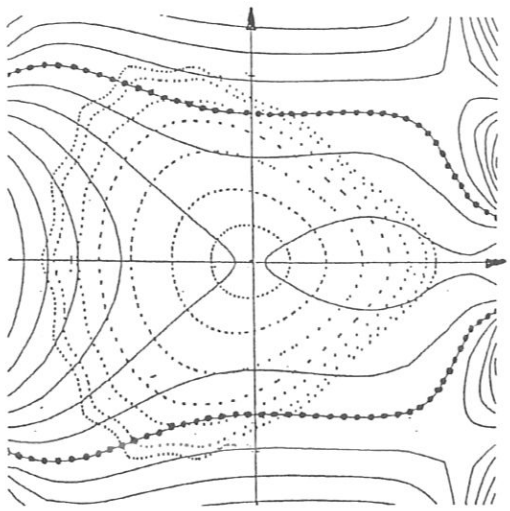

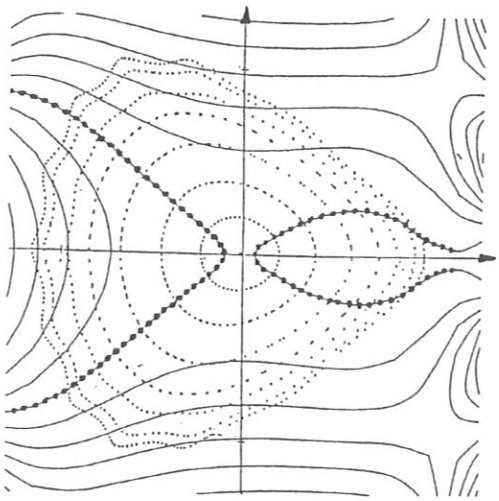

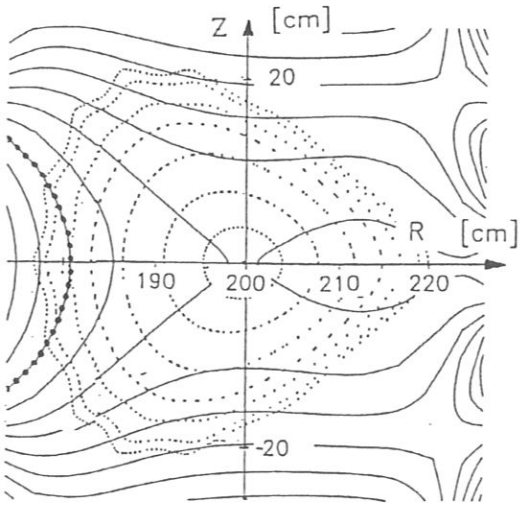
Z [cm]
20
R [cm]
190
200
210
220
-20

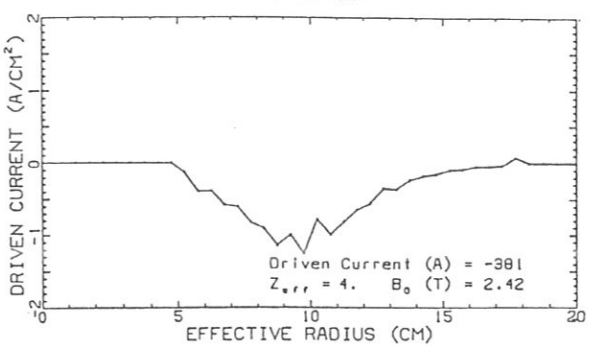
DRIVEN CURRENT (A/CM²)
2
1
0
-1
-2
0
5
10
15
20
EFFECTIVE RADIUS (CM)
Driven Current (A) = -381
Z_eff = 4. B_o (T) = 2.42

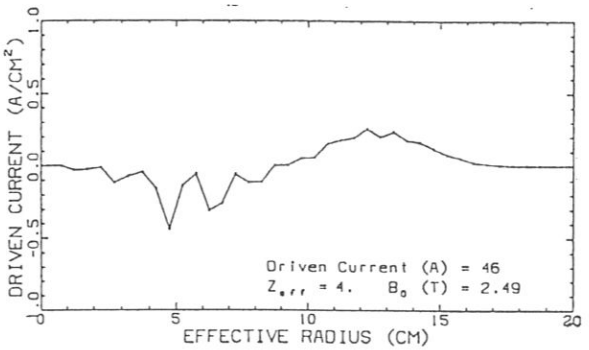
DRIVEN CURRENT (A/CM²)
1.0
0.5
0.0
-0.5
-1.0
0
5
10
15
20
EFFECTIVE RADIUS (CM)
Driven Current (A) = 46
Z_eff = 4. B_o (T) = 2.49

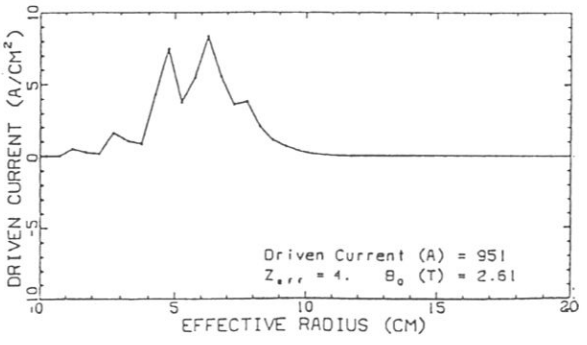
DRIVEN CURRENT (A/CM²)
10
5
0
-5
-10
0
5
10
15
20
EFFECTIVE RADIUS (CM)
Driven Current (A) = 951
Z_eff = 4. B_o (T) = 2.61

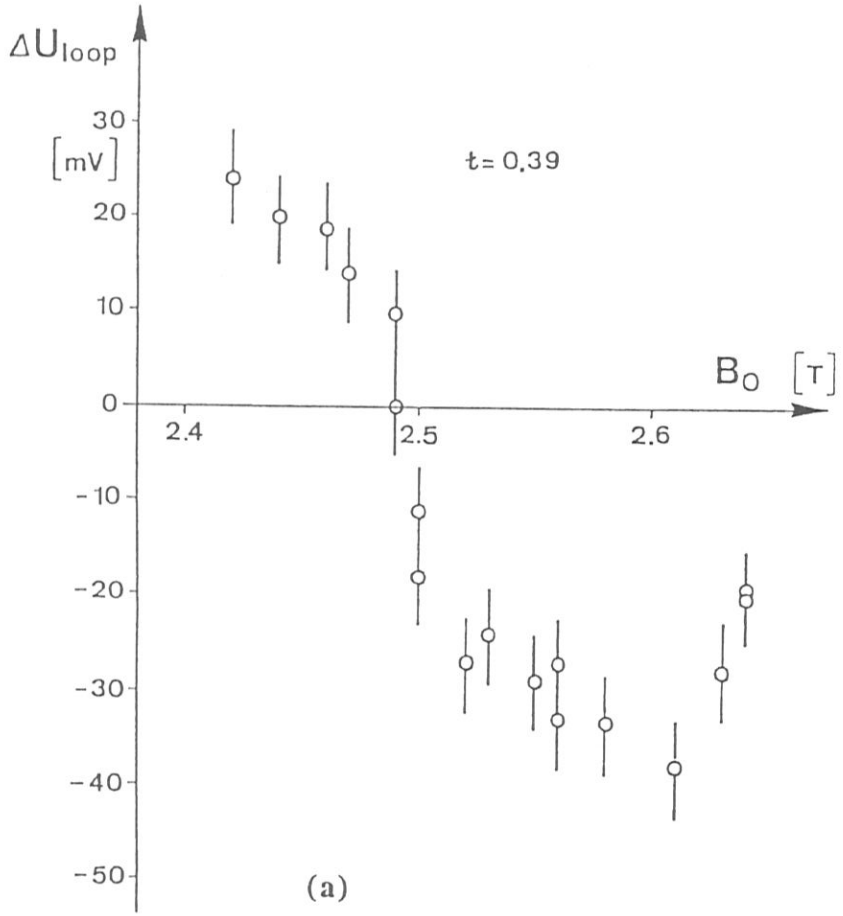
ΔU loop
[mV]
30
20
10
0
-10
-20
-30
-40
-50
t= 0.39
B0 [T]
2.4
2.5
2.6

(a)

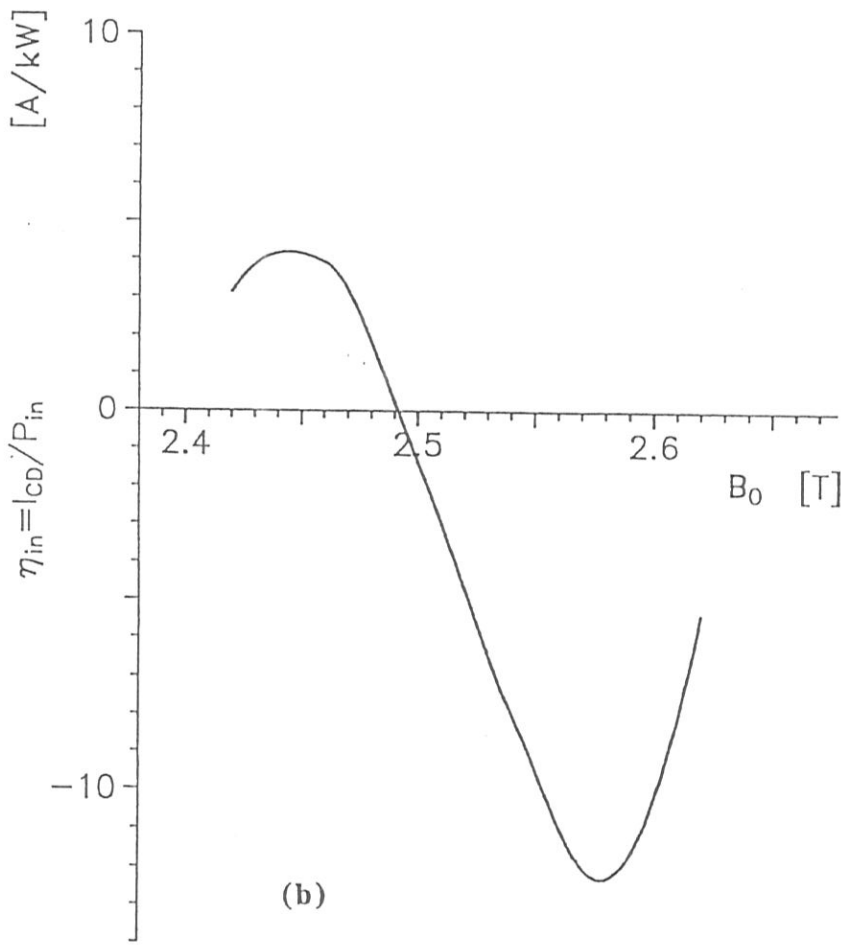
[A/kW]
10
0
-10
ηin=ICD/Pin
2.4
2.5
2.6
B0 [T]

(b)

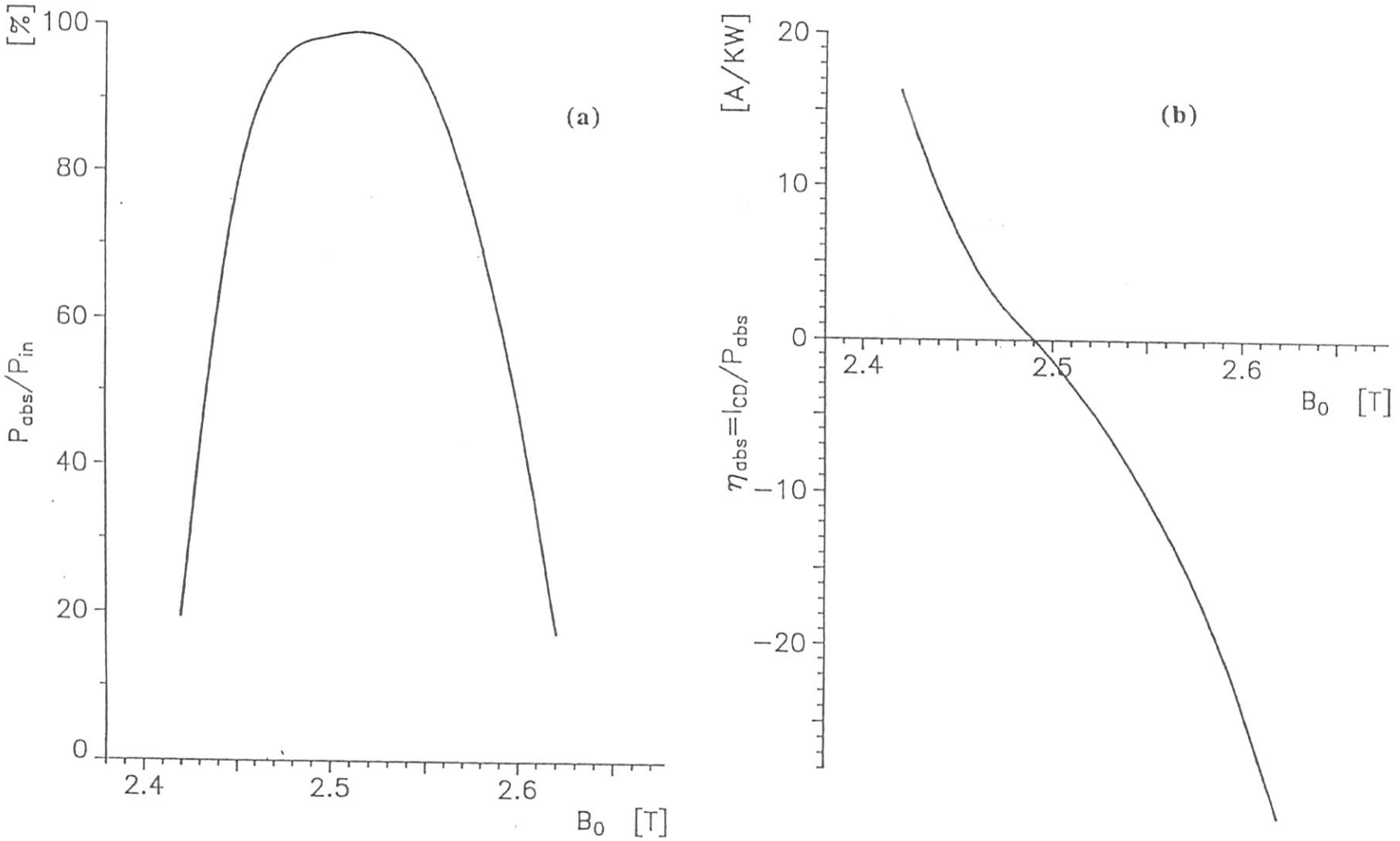
[%]
100
80
60
40
20
0
P_{abs}/P_{in}
2.4
2.5
2.6
B_0 [T]
(a)
[A/KW]
20
10
0
−10
−20
$\eta_{abs}=I_{CD}/P_{abs}$
2.4
2.5
2.6
B_0 [T]
(b)

INTERNATIONAL ATOMIC ENERGY AGENCY

THIRTEENTH INTERNATIONAL CONFERENCE ON
PLASMA PHYSICS AND CONTROLLED NUCLEAR FUSION RESEARCH

Washington, DC, United States of America, 1–6 October 1990

IAEA-CN-53/ G-1-6

PHYSICS AND ENGINEERING STUDIES FOR WENDELSTEIN 7-X

G. GRIEGER, C. BEIDLER, H. MAASSBERG, E. HARMEYER F. HERRNEGGER, J. JUNKER, J. KISSLINGER, W. LOTZ, P. MERKEL, J. NÜHRENBERG, F. RAU, J. SAPPER, A. SCHLÜTER, E. SARDEI, H. WOBIG

Max-Planck-Institut für Plasmaphysik
IPP-EURATOM Association
D-8046 Garching bei München
Federal Republic of Germany

PHYSICS AND ENGINEERING STUDIES FOR WENDELSTEIN 7-X

G. GRIEGER, C. BEIDLER, H. MAASSBERG, E. HARMEYER F. HERRNEGGER, J. JUNKER, J. KISSLINGER, W. LOTZ, P. MERKEL, J. NÜHRENBERG, F. RAU, J. SAPPER, A. SCHLÜTER, E. SARDEI, H. WOBIG

IPP-Euratom Association,
Max-Planck-Institut für Plasmasphysik,
Garching, Federal Republic of Germany

Abstract

PHYSICS AND ENGINEERING STUDIES FOR WENDELSTEIN 7-X

Results from experiment, theory and engineering have now yielded a detailed concept for WENDELSTEIN 7-X (W 7-X), an Advanced Stellarator of the Helias type. This concept satisfies the criteria for stable confinement of reactor relevant plasmas of sufficient pressure. W 7-X is designed to explore under reactor relevant plasma conditions whether transport and β-limits will agree with the expected values, and to develop exhaust technologies appropriate for steady state operation. Use of DT is neither necessary nor foreseen for this purpose. The device will be based on a superconducting magnet system. Additional coils will allow the exploration of a wide parameter range around the optimum configuration. Design studies in industry have yielded feasible engineering solutions. Experiments in W 7-AS, done so far, support the physics and engineering picture underlying W 7-X.

1. INTRODUCTION

With the WENDELSTEIN line, IPP is exploring the reactor potential of Advanced Stellarators, a concept for confining toroidal plasmas with magnetic fields generated exclusively by external, modular coils. A net toroidal plasma current, as needed in Tokamaks, is not required in Stellarators. Thus, Stellarators without this current are inherently capable of steady state operation without disruptions, without request for an external current drive system, and without need for more than one single modular coil system. These properties are of major importance for fusion reactors. After ignition, a Stellarator reactor with proper edge control would work continuously on refuelling and exhaust alone. Absence of a net plasma current also minimizes the free energy available for driving instabilities. – It is thus important to check to which extent this concept holds its promises.

Progress in Stellarator development has been large. Stellarator optimization predicts for Advanced Stellarators of the Helias type [1, 2] that in contrast to classical Stellarators they can be designed to satisfy the criteria one would establish for stable confinement of plasmas of sufficient pressure. In essence, these criteria are [3]:

- high quality vacuum magnetic surfaces, $\rightarrow$ shear as large as compatible with this condition,
- good finite-β equilibrium properties, $\rightarrow$ minimum sensitivity of configuration to β,
- good MHD stability properties, $\rightarrow \langle\beta\rangle \gtrsim 0.05$,

- small neoclassical transport in the lmfp regime, $\rightarrow$ equivalent field ripple ≤ 0.02,
- small bootstrap current in the lmfp-regime, $\rightarrow$ minimum effect on configuration,
- good collisionless alpha particle containment at operational values of β,
- good modular coil feasibility.

The configuration of W 7-X has been selected according to this set of criteria.

2. EXPERIMENTAL RESULTS FROM WENDELSTEIN 7-AS

W 7-AS is the first Advanced Stellarator, with a limited degree of optimization though. Plasma operation has begun about one and a half year ago. Latest experimental results are published in two other papers [4, 5] to this conference. With respect to both, engineering and physics, W 7-AS has already yielded the following results of basic importance to W 7-X:

- A modular coil system for Stellarators is feasible and cost-effective in construction.
- The accuracy of the generated field configuration is proven to be high.
- It is supported that major resonances in field line twist have to be avoided and shear has to be maximized within this constraint.
- The concept of an improved plasma equilibrium is confirmed by the observation of the reduced Shafranov shift.
- The measured bootstrap current agrees with calculations; EC current drive is verified.
- Plasma operation of up to 1.5 s has confirmed internal time constants of this duration.
- Using up to 0.8 MW ECRH and up to 1.3 MW NBI, plasma temperatures in the keV range, line average densities of 2×10^{20} m^{-3}, and confinement times of 25 ms have been reached. These are significant achievements in view of the device parameters of W 7-AS.

These results support the physics and engineering picture underlying Wendelstein 7-X.

3. PROGRAMMATIC OBJECTIVES OF WENDELSTEIN 7-X

It is now timely to undertake an integrated concept test for producing convincing predictions on the properties of ignited plasmas in Advanced Stellarators. DT operation is neither foreseen nor necessary for this purpose. Thus, the programmatic objectives of W 7-X are:

- achievement of adequate confinement and investigation of plasma transport under reactor relevant conditions,
- effective heating methods for plasma generation and heating to temperatures of some keV,
- investigation of impurity transport and development or adaptation of means for its control,
- achievement of $\langle\beta\rangle$-values of about 0.05 and analysis of the β-limit,
- long-term and quasi-stationary operation,
- study of refuelling, exhaust and plasma wall interaction under steady state conditions,
- development of proper means for control of plasma edge conditions.

4. DEFINITION OF WENDELSTEIN 7-X

The theoretical and experimental studies and the planning activities over several years have now resulted in the completion of the concept of Wendelstein 7-X. It will employ the full potential of the Helias concept and will utilize a modular coil system. The optimization procedure mentioned above has yielded the W 7-X configuration, as displayed in Fig. 1, without noticeable ambiguity. It satisfies all criteria listed above. Some characteristic nondimensional data of W 7-X are listed in Table I.

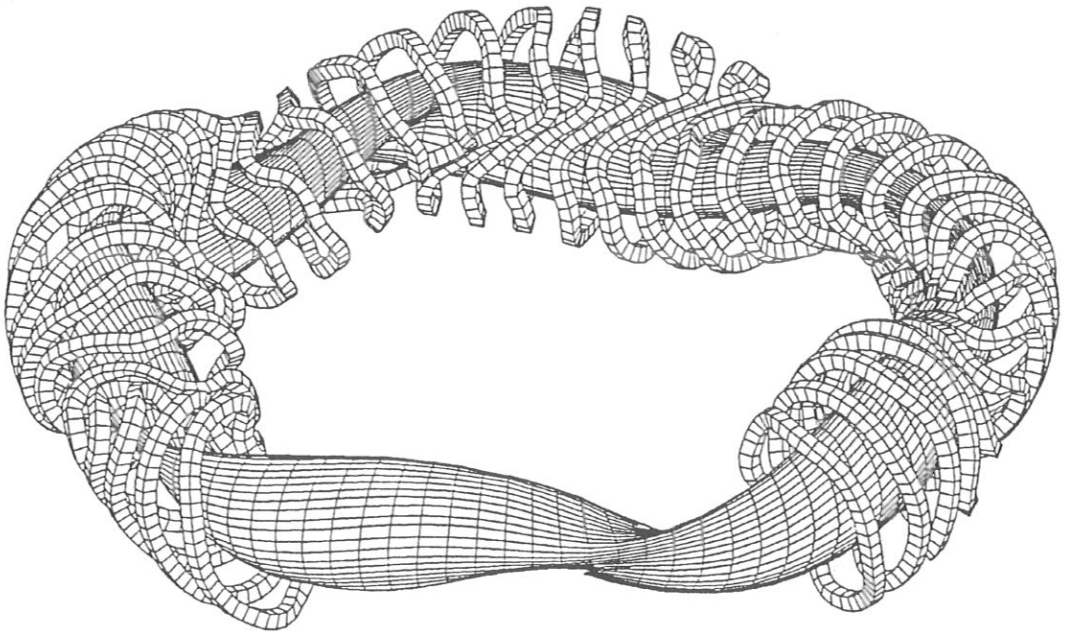

Fig. 1: Sketch of WENDELSTEIN 7-X basic configuration. The lines on the plasma surface indicate the magnetic field lines and meridional sections, respectively.

Rotational transform, ι, on axis/boundary	0.84/0.99
Variation of ι	± 0.2
Variation of shear	± 0.1
Variation of mirror field	0.1
Pfirsch-Schlüter currents, $\langle j_{\parallel}^2 / j_{\perp}^2 \rangle$	0.5
Magnetic well depth	0.01
MHD stability limit, $\langle \beta \rangle_{st}$	0.043
Equivalent ripple, δ_e	0.015
Ratio of bootstrap currents, $J_{BS,stel}/J_{BS,tok}$	$\lesssim 0.1$

Table I: Characteristic Nondimensional Data of the Experiment W 7-X

The absolute dimensions of W 7-X follow from the programmatic objectives together with physical and technical constraints. The first one is the use of ECRH because this is the only proven method for allowing both generating plasmas in Stellarators by starting

...the gas phase and heating them to high temperatures. In order to have the cut-off density not too far below the highest operating density, a frequency of 140 Ghz, twice the frequency used on W 7-AS, has been selected. This frequency is compatible with a field strength of 2.5 T. The required experimental flexibility to be able to create ECRH resonance conditions at any desired position in the plasma then leads to a maximum operating magnetic field of 3 T. Experience from W 7-AS requests the minimum flat top time of the magnetic field to be well above 10 to 20 s. This cannot reasonably be managed anymore with water-cooled copper coils. The magnet has therefore to be superconducting, but NbTi conductors are fully sufficient for this kind of application. The maximum current density of 50 MA/m^2 and a minimum distance between plasma and wall of at least 0.1 m, and larger, where particle and power sinks have to be introduced, then lead to the characteristic dimensional data of W 7-X listed in Table II. A smaller device is not compatible with the above constraints. The fusion diagramme comparing the projected performance of W 7-X with those of various other devices is shown in Fig. 2.

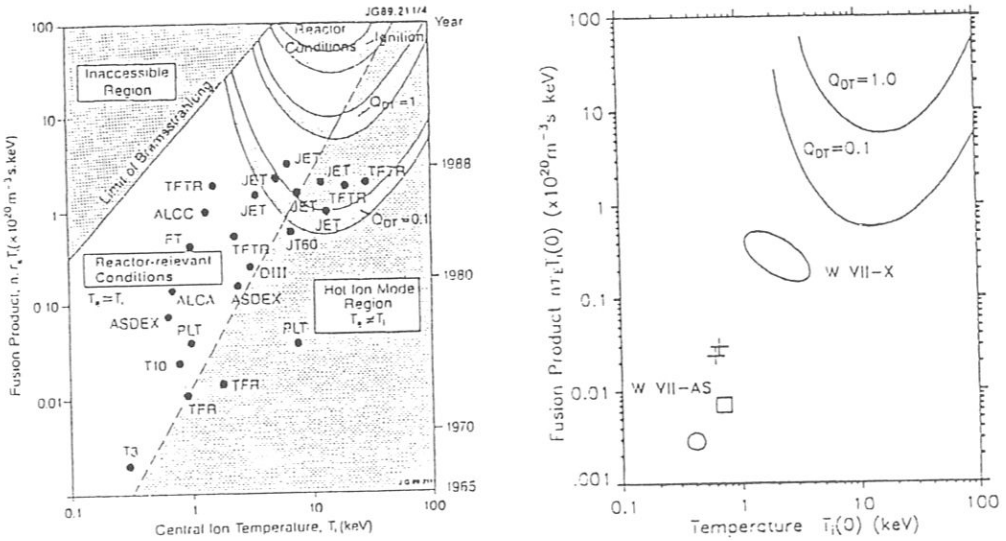

Fig. 2: Fusion diagram comparing the projected performance of WENDELSTEIN 7-X (right) with those of various other devices (left). The prediction for WENDELSTEIN 7-X is obtained with a specific assumption on the anomalous electron heat conductivity (Lackner-Gottardi modified plateau scaling) and ECRH and NBI power ranges of 2 – 10 MW and 5 – 20 MW, respectively. A reduction of the anomalous electron heat conductivity by a factor of 8, as considered possible for the WENDELSTEIN 7-X design, would lead to increases of $n\tau T$ by a factor of about 3 and of $T_i(0)$ by a factor of about 1.5. The Japanese LHD project aims at the same region in the above $T - n\tau T$ diagram. For W 7-AS: o ECRH result: □ preliminary result of initial NBI experiments; + preliminary NBI results after first carbonization.

Average major radius, R_0	5.5 m
Average plasma radius, r_a	0.53 m
Average coil radius, r_c	1.14 m
Min. distance plasma – coils, Δ_{pc}	0.29 m
Min. distance plasma – wall, Δ_{pw}	0.12 m
Induction on axis, B_0	3.0 T
Max. induction at coils, B_m	6.1 T
Total magnetic energy, W_m	600 MJ
Max. net force (one coil), F_{res}	3.6 MN

Table II: Characteristic Dimensional Data of the Experiment W 7-X

5. TRANSPORT PHYSICS AND EXHAUST EXPERIMENTATION

An important task for W 7-X is to investigate the contributions of anomalous transport in a reactor relevant configuration and under reactor relevant conditions. In this context it is very promising that the stellarator optimization concept used also removes or at least reduces most of the candidate causes of anomalous transport, such as stochasticity in vacuum and finite-β fields, instabilities such as tearing, ballooning, trapped-particle drift modes, and trapped-orbit widths. This results from the regularization of the magnetic surfaces and the avoidance of major resonances, from the large reduction of the parallel-current density, from the absence of large net toroidal currents, from the small shear, from the trapped particles being removed from the strong-curvature regions, and from the largely reduced step width in the gyro-reduced Bohm model. The possibility to explore transport properties under such conditions might even shine some light on the origin of anomalous transport in toroidal configurations in general.

The development of a proper exhaust technology is another important task for W 7-X. The separatrix region of the configuration selected for W 7-X inherently provides basic divertor properties favourable for this purpose and is found to be reasonably insensitive to variations of β because of the small parallel current density. This is a necessary prerequisite for proper divertor action whose details will depend on the "island" structure at the edge of the plasma. Basic properties of this concept will be tested in W 7-AS, which has already shown the expected concentration of particle and power fluxes in half-helix like stripes at the outboard side of the configuration [6,7].

6. CONFIGURATIONAL FLEXIBILITY

For an experiment like W 7-X, it is necessary to explore the confinement properties in a wide range around the optimum configuration. This is achieved by a relative variation of the currents in the individual modular coils and by superimposing to the basic coil system a second one, not shown in Fig. 1, allowing the addition of toroidal and vertical field components. As follows from Table I, this provides the necessary variation of such important quantities as iota, shear, mirror field, and well depth.

7. ENGINEERING

By means of two study contracts launched with industry, a conceptual design has been made and found to be feasible. By proper design of the superconducting cable, the coil winding technology successfully developed for W 7-AS can also be applied for the production of the superconducting coils of W 7-X. The maximum magnetic field at the coils is sufficiently low to allow conventional NbTi superconducting technology to be used, the operational reliability of which is demonstrated by many applications.

The magnet consists of 50 non-planar coils, 10 per field period, with geometrical characteristics less demanding than those of W 7-AS. There are only five geometrically different coil types. Separate current feeds, five in total, and a system of 20 superimposed planar coils, four per field period, provide the configurational flexibility described above. Each coil is surrounded by a stainless steel housing; the whole magnet, including its internal support structure, is embedded in a cryostat. The total cold mass is about 350 tons. The refrigerator will work at 4 K, the same temperature as that of the LCT project. The experience gained with LCT is fully accounted for by the IPP-KfK collaboration. With a magnetic energy of about 600 MJ, the magnet system of W 7-X is also comparable with that of the TF magnet of Tore Supra. It is now intended to produce a representative length of the superconducting cable, to fabricate a demonstration coil [8], and one sector of the vacuum and cryostat system. When starting construction at the beginning of 1993, the device could be ready for operation five years later.

8. SUMMARY AND CONCLUSIONS

WENDELSTEIN 7-X is designed to undertake an integrated concept test for producing convincing predictions on the properties of ignited plasmas in Advanced Stellarators but without using DT plasmas. The magnetic configuration results from a Stellarator specific optimization procedure and satisfies all criteria established for this purpose. Essential tasks for W 7-X are to explore whether the expectations for both sufficiently low anomalous transport and a sufficiently high β-limit are justified and to develop proper means for impurity control and exhaust to allow stationary operation. When starting construction at the beginning of 1993, the device could be ready for operation in 1998.

REFERENCES

[1] NÜHRENBERG, J., ZILLE, R., Phys. Letters 114A (1986) 129.

[2] LOTZ, W., NÜHRENBERG, J., SCHWAB, C., C-3-5, these Proceedings.

[3] GRIEGER, G., et al., "Physics Studies for Helical-Axis Advanced Stellarators", Plasma Physics and Controlled Nuclear Fusion Research 1988 (Proc.12th Int. Conf. Nice, 1988) Vol. 2, IAEA, Vienna (1989) 369.

[4] RENNER, H., et al., IAEA-CN-53/C-1-2, these Proceedings.

[5] ERCKMANN, V., et al., IAEA-CN-53/C-3-1, these Proceedings.

[6] GRIGULL, P., et al., to be published in Proc. of the 9th Int. Conf. on Plasma Surface Interaction, Bournemouth, 1990.

[7] BEIDLER, C., et al., Proc. 17th EPS Conf. on Contr. Fus. and Plasma Heating, Amsterdam (1990), Vol. 14B, part II, 517.

[8] HARMEYER, E., et al., "Force and Stress Calculations for a Non-Planar W 7-X Demonstration Coil", Proc. 16th Symp. on Fus. Techn., London (1990).